Cranfield University

David Roberts

Analysis and Control of Resonant Cavity Flows

School of Engineering

Academic year: 2012 – 2013

Supervisor: Dr D G MacManus

Submitted for the degree of PhD

Abstract

Recently, the trend for the internalisation of stores within an aircraft fuselage has led to a renewed interest in the field of cavity aero-acoustics. Many modern military aircraft, including recent unmanned combat configurations, are designed with internal stores carriage. Housing stores within a weapon bay cavity has the two fold benefit to the aircraft: reduced excrescence drag, and a smaller radar signature. However, open cavities exposed to a grazing flow can exhibit large resonant pressure fluctuations which may damage stores or components within the cavity. The aim of this research is to investigate the fundamental flow characteristics of open cavities and to develop passive palliative concepts to control the unsteady pressure fluctuations within resonant cavity flows.

The fundamental flow characteristics of two scale cavities were investigated experimentally: a $1/40^{th}$ scale model under transonic conditions ($0.80<M_{\infty}<0.95$) and a $1/20^{th}$ scale configuration under both transonic ($M_{\infty}=0.70$) and supersonic ($M_{\infty}=1.5$) freestream conditions. Cross-correlation and auto-correlation analyses were used to identify the fundamental time signatures, which are related to the generation of the unsteady pressures within the cavity. The key features within the spectra were identified through Fourier analyses and this assisted in the development of a passive control concept based on resonant absorbers.

The temporal characteristics identified from the correlation analyses were linked to a previously proposed generation mechanism for the unsteady pressure modes within the cavity flow. This mechanism links the characteristic travel time of the vortices shed from the cavity front wall, the pressure waves within the cavity, and the frequency of the high intensity modal peaks recorded within the unsteady pressure spectrum. The current work provides the first experimental evidence to support this proposed modal generation mechanism under transonic conditions ($0.85<M<0.95$).

The modal attenuation from a series of passive acoustic absorbers, primarily based on arrays of Helmholtz type resonators, has been investigated and analytical design rules have been developed based on both the wind tunnel test results and separate impedance tube investigations. Within the cavity flow, resonant arrays have demonstrated significant peak attenuation levels with up to 15dB for transonic (M=0.95) conditions and up to 26dB for supersonic (M=1.5) conditions. These new results demonstrate the potential of resonant arrays as passive palliative devices. The attenuation under supersonic conditions is of particular interest, as resonant arrays could support the more widely used spoiler palliatives under the supersonic conditions where spoilers can be less effective. A preliminary investigation into the feasibility of resonant arrays for a full-scale application has also demonstrated the potential of the devices for full-scale use.

Acknowledgments

Firstly, I would like to thank my supervisor David MacManus for the large amount of support he has offered me throughout my studies. From improving my writing to developing my analytical thinking, the skills I have learned will be invaluable for my future career. Alongside the support David's continued interest in the project has led to many unique opportunities through the successful proposals submitted to the sponsors. Also at Cranfield, I would like to thank Kevin Garry, Jenny Holt and Paul Dancer for the use of the wind tunnel facilities and for the manufacture of my cavity models. Outside of Cranfield I would like to thank Phil Rubini and Qin Qin at the University of Hull for the use of their acoustic impedance tube facilities and for useful discussions about the project. Also, I would like to thank Paul Murray of Morrisbrand Ltd for carrying out the high SPL impedance investigation using high SPL impedance measuring equipment

I would also like to thank the sponsors involved in the work. These were: the UK MoD (DSTL) through the Centre for Defence Enterprise (CDE) and the US Air Force through the European Office of Aerospace Research & Development (EOARD). This work has been partially funded by the UK MoD through the Centre for Defence Enterprise Contract: RT/COM/7/53 and DSTLX1000053780. Part of the material presented here arose from research arranged through the European Office of Aerospace Research and Development (EOARD). Effort sponsored by the Air Force Office of Scientific Research, Air Force Materiel Command, USAF, under grant number FA8655-11-1-3025. The U.S. Government is authorized to reproduce and distribute reprints for Governmental purpose notwithstanding any copyright notation thereon.

As well as the organisations I would also like to thank both Trevor Birch and Ross Chaplin of DSTL for their support and helpful guidance throughout the work. The input and discussions from the interested parties greatly improved both the quality and enjoyment of the work. Furthermore, I would like to thank both Rudy Johnson and Jim Grove of AFRL in the US. Their kind facilitation of the use of their supersonic wind tunnel facility added far more to the project than we could have expected. The week of testing at Wright Patterson Air Force Base was an unexpected and unique opportunity, which I greatly enjoyed.

Finally, I would like to thank everyone I have met at Cranfield along the way. Both the people I have lived with at the farm, and those who are more than happy to have a cup of tea and talk about cars, F1 and anything non-work related.

Contents

List of figures

List of tables

Nomenclature

LATIN CHARACTERS

a	Freestream speed of sound
a_0	Speed of sound within cavity (ms^{-1})
C_n	Generic n^{th} constant
Cp	Pressure coefficient
d	Resonator orifice diameter (m)
D	Resonator orifice pitch spacing (m)
d_S	Rod spoiler diameter (m)
f	Generic frequency (Hz)
f_a	Fundamental aeroacoustic loop frequency (Hz)
f_b	Modulating frequency for amplitude modulation mechanism
f_n	Frequency of the n^{th} Rossiter mode (Hz)
H	Boundary layer shape factor ($H=\delta^*/\theta$)
h	Cavity depth (m)
h	Impedance tube height (m)
H_1	Impedance tube incident pressure transfer function
H_{12}	Impedance tube total sound field transfer function
H_R	Impedance tube reflected pressure transfer function
H_S	Spoiler height (m)
h_S	Step height (m)
H_T	Sawtooth spoiler tooth height (m)
k	Ratio of vortex convection speed to freestream velocity ($k=V_V/ U_\infty$)
k_0	Acoustical wave number
l	Cavity length (m)
L	Resonator backing length (m)
m	Rossiter mode number or Mass of oscillating air mass (Kg)
M_0	Mach number based on Static temperature within cavity
M_∞	Freestream Mach number
O_S	Spoiler offset (m)
P_0	Total pressure (Pa)
P_{stat}	Static pressure (Pa)
r	Impedance tube reflection factor
Re	Reynolds number ($Re=\rho UL/\mu$)
Re_ω	Unsteady Reynolds number
s	Impedance tube microphone spacing (m)
St	Strouhal number
t	Resonator faceplate thickness (m)
T*	Non-dimensionalised travel time ($T^*=T_{()}/t_{ref}$)
t’	Resonator faceplate thickness with end correction (m) or Arbitrary time (s)
T_0	Total temperature within cavity (K)
T_a	Time period of fundamental aeroacoustic loop (s)
T_c	Static temperature within cavity (K)

T_P Time for a pressure wave to travel over one cavity length (s)
t_{ref} Reference time (s) ($t_{ref}=U_\infty/l$)
T_S Spoiler thickness (m)
T_V Time for a vortex to convect over one cavity length (s)
U_∞ Freestream velocity (ms^{-1})
U_n Velocity normal to resonator orifice within cavity (ms^{-1})
U_o Velocity within resonator orifice (ms^{-1})
w Cavity width (m)
W_L Sawtooth spoiler tooth spacing (m)
x Cavity length ordinate (m)
y Cavity width ordinate (m)
z Cavity depth ordinate (m)
Z* Normalised impedance
Z_0 Characteristic impedance ($Z_0=\rho_\infty a_\infty$)
z_n Impedance tube distance from sample (m)

GREEK CHARACTERS

α Rossiter phase constant (α=0.062l/h) or Absorption coefficient
β Resonator absorption coefficient bandwidth (%)
γ Ratio of specific heats (γ=1.4)
δ Boundary layer thickness (m)
δ* Boundary layer displacement thickness (m)
ε Porosity of resonator faceplate (%)
ζ Modulation frequency ratio for amplitude modulation mechanism ($\zeta=f_b/f_a$)
θ Boundary layer momentum thickness (m) or Cavity wall sweep angle (°) or Cavity wall chamfer angle (°)
λ Acoustic wavelength (m)
λ_P Pressure wave spacing (m)
λ_V Vortex spacing (m)
μ Dynamic viscosity ($kgm^{-1}s^{-1}$)
ν Kinematic viscosity (kgm^{-3})
ρ Density (kgm^{-3})
Φ Impedance tube diameter (m)
ω Angular frequency ($rads^{-1}$)

ABBREVIATIONS AND ACRONYMS

DAQ Data acquisition
DES Direct eddy simulation
FPL Fluctuating pressure level (dB)
FW Cavity front wall
Im Imaginary part of a complex number
LS Large scale

OASPL	Overall sound pressure level (dB)
RE	Cavity rear wall
Re	Real part of a complex number
SCFH	Standard cubic feet per hour
SPL	Sound pressure level (dB)
STFT	Short term Fourier transform
TGF	Trisonic Gasdynamics Facility

1 Introduction

1.1 Introduction to cavity noise

Design requirements for modern day combat aircraft such as aerodynamic efficiency and low observability have led to the internalisation of stores (*Figure 1*). Consequently, the use of weapon bays has renewed interest in the field of cavity aero-acoustics. The presence of an open cavity exposed to high speed flows encountered by aircraft can cause further issues for the aircraft designer. For example, it is well known that a weapon bay cavity with open doors may experience high intensity modal pressure fluctuations [1] [2]. These fluctuations can reach intensities of up to 165dB and may cause damage to both the aircraft and to sensitive stores or components carried within the cavity.

Figure 1 – F-35 lightning II A-variant with stores carried within weapon bay cavities [3]

Flow over cavities can be broadly categorised into two different regimes referred to as open and closed flows (*Figure 2*) [2]. In the case of open flows the boundary layer at the front of the cavity detaches and forms a shear layer which then spans the length of the cavity. This shear layer then reattaches at, or downstream of, the cavity rear wall (RW) (*Figure 2*a). Vortices are formed within the shear layer and are convected downstream from the front wall (FW) and eventually impinge at the rear wall stagnation point. This process results in the upstream propagation of pressure waves within the cavity and these in turn trigger the shedding of further vortices. This process sets up a feedback loop within the cavity. For closed flows, the shear layer from the front wall reattaches

on the cavity ceiling and the undesirable pressure fluctuations are typically avoided (*Figure 2b*). However, cavities with closed flow properties exhibit an adverse pressure gradient which can greatly affect store separation characteristics by creating a nose up pitching moment on the store (*Figure 3*). Therefore, closed flow type cavities are usually avoided. A typical open flow cavity has a length (l) to depth (h) ratio of less than 6. Whereas, closed flow cavities have an l/h ratio which is greater than 10. A transitional boundary between the two flow regimes also exists, which also depends on the Mach number of the approaching flow [2].

The focus of this work is on the more problematic open flow configuration. The feedback loop within an open flow cavity sets up a series of modal pressure fluctuations. A typical modal cavity spectrum is shown in *Figure 4*. The frequencies at which the modal peaks occur are sometimes calculated using the modified Rossiter equation (*Equation 1*) [2] [4]. However, there is no such simple and reliable method for the prediction of the peak magnitudes.

$$St = \frac{fl}{U_\infty} = \frac{m - \alpha}{M_\infty \left(1 + \frac{\gamma - 1}{2} M_\infty^2\right)^{-\frac{1}{2}} + \frac{1}{k}}$$

Equation 1

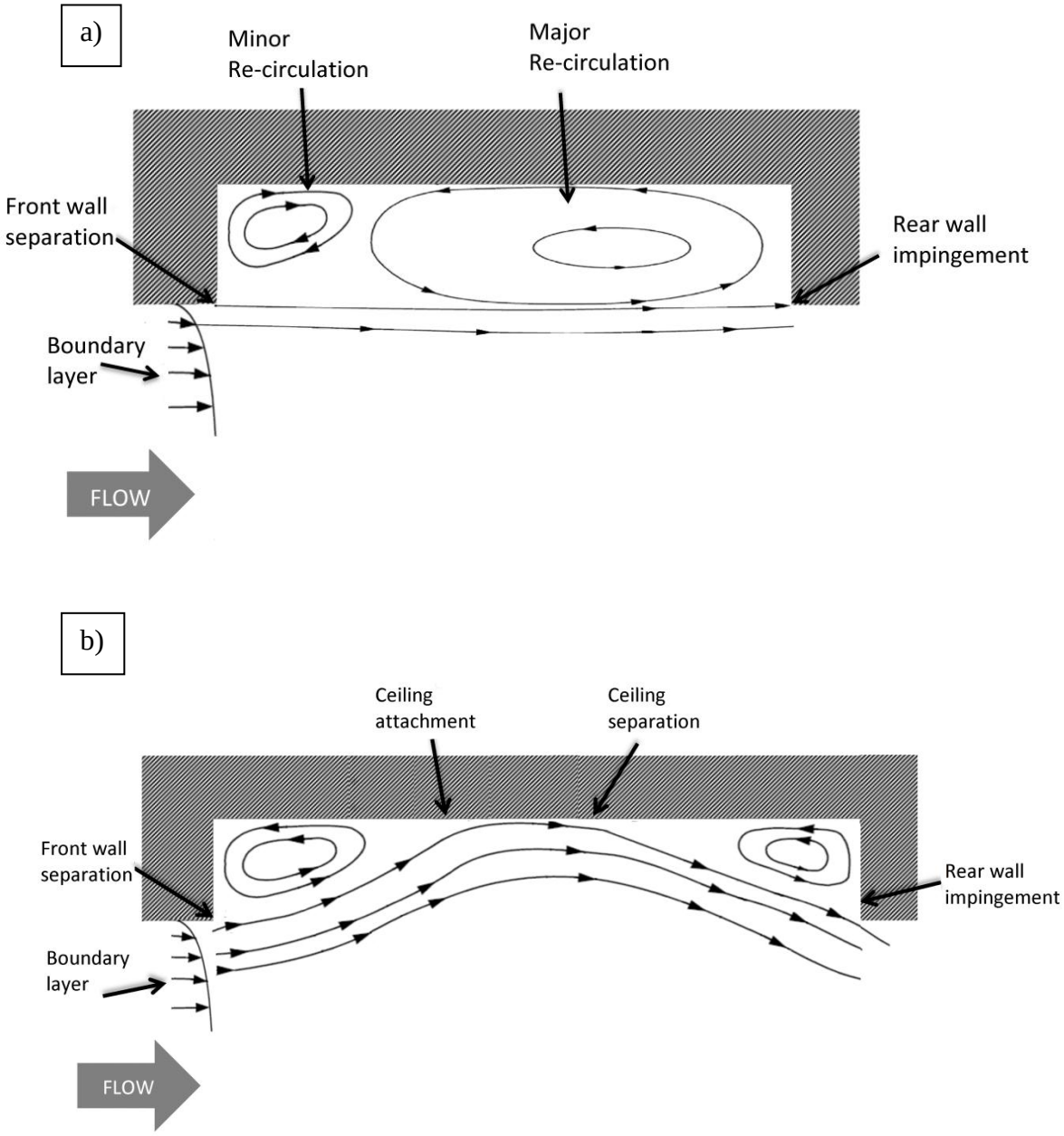

Figure 2 – a) Sketch of an open flow cavity mean flow [2], b) Sketch of a closed flow cavity mean flow [2] .

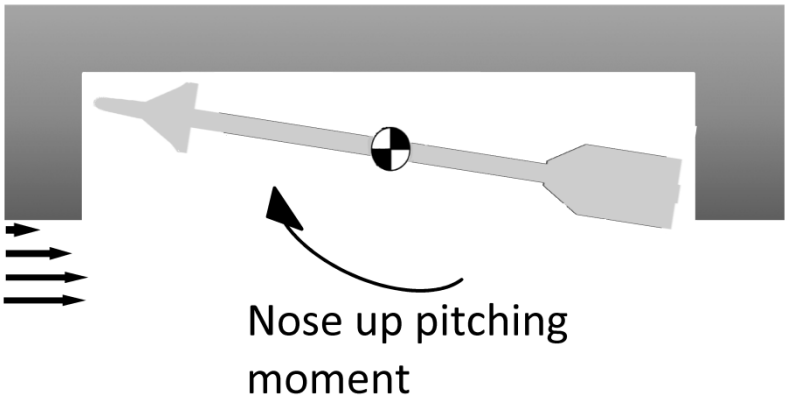

Figure 3 – Sketch of nose up pitching moment on a store created by the adverse pressure gradient within a closed flow cavity. (see *Figure 9*)

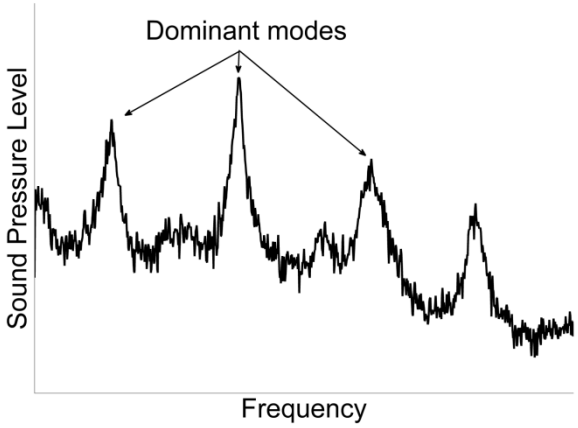

Figure 4 – A typical open flow cavity acoustic spectrum

1.2 Current technologies for cavity noise attenuation

The current state of the art concerning the attenuation of cavity aero-acoustics covers a wide variety of techniques which use both active and passive control methods. One definition of a passive control system is that which does not add energy into the cavity flow [5] and are typically formed from a fixed geometry. This provides the benefits of simplicity and reduced costs. However, due to the fixed nature of the geometry the attenuation of the acoustic modes may only be viable for certain sections of an aircraft's flight envelope. Active control systems, whether they are open-loop or closed-loop, require energy to both function and to attenuate the noise. Open-loop system typically operate at a fixed pre-prescribed condition, whereas, closed-loop systems can adapt to the changing flow conditions experienced in flight. Overall, closed-loop active control systems are costlier and more complex to implement when compared with passive systems, but will provide attenuation over a wider range of flight conditions.

The most widely used method for cavity noise attenuation is the leading edge spoiler or fence (*Figure 5*). Spoilers disrupt the airflow over the cavity and divert the detached shear layer so that it no longer impinges at the cavity rear wall (*Figure 6*). This removes the main source of unsteadiness within the cavity and can reduce modal amplitudes by up to 20 dB [6]. To avoid excess excrescence drag, spoilers are actuated to only deploy when required and this adds complexity and an extra space requirement to the simple passive spoiler approach. A more detailed examination of the current state of the art is provided in the literature review in *section 2*. The attenuation from typical spoiler devices can also be limited by the flow regime in which they are operated. Although, under subsonic and transonic conditions spoilers can provide high levels of modal attenuation [6], under supersonic conditions the attenuation level can be significantly reduced and, in some supersonic cases spoilers can amplify the modal amplitudes [7]. Therefore, there is a strong requirement for palliative devices which can be installed into an aircraft with minimal volume and also a device which can provide high levels of modal attenuation under both transonic and supersonic conditions.

Figure 5 – Spoilers installed upstream of the weapon bay cavity on an F-117 aircraft

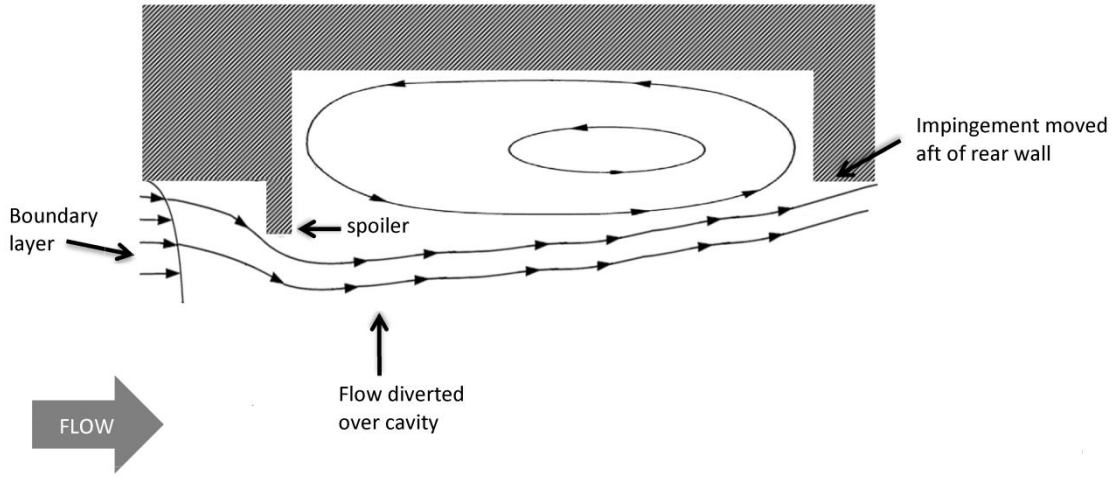

Figure 6 – Sketch of diverted mean flow over a cavity caused by an upstream spoiler (based on figure from reference [8])

1.3 Aims and objectives

The overall aims of this study were to investigate methods to reduce cavity aero-acoustic noise levels and also to investigate the fundamental flow mechanisms within the cavity flowfield. This was achieved by setting the following objectives:

- To establish an appropriate test facility including the following aspects:
    - Determination and implementation of the test instrumentation requirements.
    - An assessment of the suitability of the facility for the acoustic investigation of the cavity noise.
    - The design and commission of a new small scale cavity model to enable the performance of palliative configurations for the side wall and ceiling of the cavity.

- To investigate the fundamental mechanisms within the cavity flowfield including the following:
    - Cross-correlation analysis to establish the characteristic speeds of the main flow features.
    - Auto-correlation analysis was used to assess whether the fundamental components required for the generation of the modal acoustics supported a recently proposed modal generation mechanism.
    - The fundamental cavity loop frequency in conjunction with a previously proposed modal generation mechanism.

- The main focus of the palliative development is the use of tuned resonant absorbers for the attenuation of cavity modes and this process involved the following:
    - Design a series of resonant arrays to target the cavity modal frequencies for small ($1/40^{th}$) scale transonic tests and medium ($1/20^{th}$) scale transonic and supersonic freestream conditions.
    - Propose and validate an analytical model to tune the arrays and to calculate their relative performance within the cavity environment.
    - Conduct small ($1/40^{th}$) scale cavity tests to assess the palliative performance under transonic ($0.8<M<0.95$) conditions and medium ($1/20^{th}$) scale cavity tests under supersonic ($M=1.5$) conditions.
    - To conduct a preliminary assessment of the suitability of the proposed devices for use within a full scale operational weapon bay cavity.

- Assess the attenuation performance of several alternative palliative approaches.
    - It was of interest to see if acoustic foam, which is used in a wide variety of environments, was applicable for the attenuation of cavity acoustics.
    - Bias flow has been previously shown to improve the attenuation from resonant absorbers, therefore the effect of bias flow on the attenuation performance was investigated.

1.4 Scope and research roadmap

The overall aim of this research was to investigate the use of tuned absorbers as passive palliatives within a resonant cavity and the work presented within this thesis focuses on both analytical and experimental studies. The overall structure of the work and the links between the various activities, are shown in the research roadmap (*Figure 7*). The research activities can be split into three sections referred to as: initial design, design development, and final recommendations (*Figure 7*). Work conducted under the initial design period was focussed on the use of existing models and techniques to assess both the modal generation process and the designs of the palliatives. The findings from this initial phase were then used to direct the research conducted under phase two, where significant advances in both the understanding of the cavity modal generation process and palliative attenuation mechanism were made. The final recommendations are based on the series of experimental results from the phase two investigation into the effect of the cavity environment on the array performance (*Figure 7*).

Three major streams of investigation were conducted simultaneously. These were: wind tunnel testing, analytical work, and impedance tube testing. The analytical work focussed on both gaining a fundamental understanding of the modal generation process within the cavity, and the calculation of the palliative performance within the cavity environment. The design process within this stream was initiated from existing models for both the palliative performance and cavity modal generation process. The results from this investigation fed into both the wind tunnel and impedance tube investigations.

The impedance tube investigations were primarily used to provide experimental support of the analytical models used for the design of the resonant absorbers. The impedance tube enabled the effects of the high SPL environment within a resonant cavity on the performance of the arrays to be measured and also enabled a preliminary investigation into the suitability of resonant arrays for use within a full scale weapon bay. The results from this stream of work are of great use to the conclusions made within this study.

The third work stream comprised the various wind tunnel tests which were conducted to investigate both the modal generation process and the effectiveness of the palliative devices designed within the study. The small scale, transonic, investigation of the palliative effectiveness was initiated from the beginning of phase one and were conducted through to phase three, where the results and conclusions were used to design arrays for the transonic and supersonic medium scale investigations. Within this process the effect of array location, Mach number, and combined configurations on the attenuation performance were assessed to aid the development of effective devices for both transonic and supersonic experimental investigations. The effect that the cavity environment had on the array performance was investigated within the three work streams. The high SPL impedance tube results provided information which was used to assess the most suitable design metric for future arrays. This information was used for the design of the most effective arrays for both the transonic and supersonic investigations.

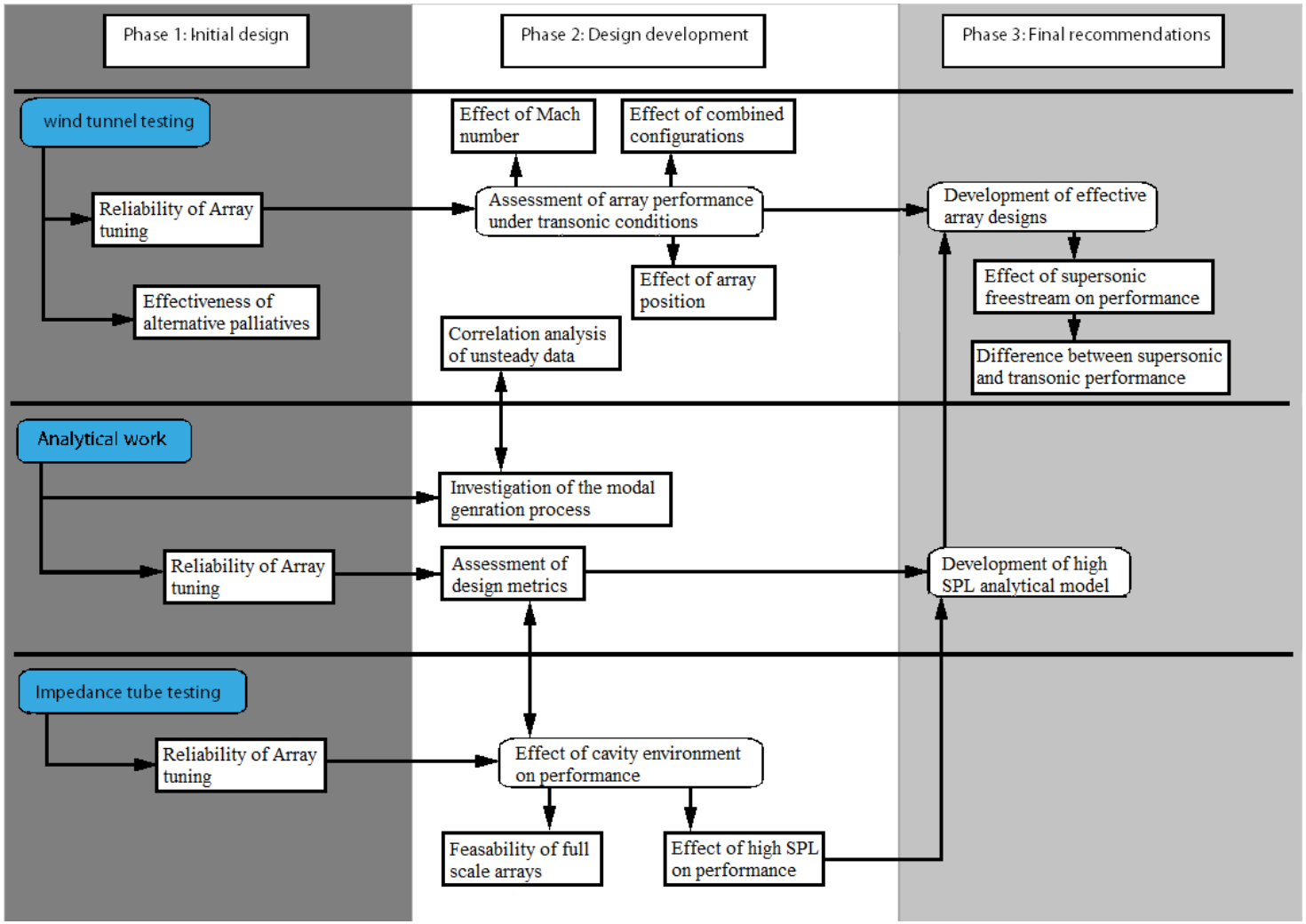

Figure 7 – Research roadmap

2 Literature review

It is important to recognise that the overall field of cavity aero-acoustics and acoustic control has received a large amount of interest ever since the initial weapon bay related studies, which were conducted in the mid twentieth century. This section presents a concise review of the published literature pertaining to the research contained within this body of work. Previous studies have investigated both the fundamental aspects of the cavity mode generation as well as control, through both passive and active methods and these previous studies provide contrast and comparison for the investigations contained within the current body of work.

The first section of this review covers the background of the cavity acoustics problem and discusses the fundamental studies, which investigated the modal generation process, and the characteristics of the flow within a resonant cavity. The second section presents the previous research which is related to the passive control of the acoustic modes within resonant cavities. This section on passive control is especially pertinent to the current research as this is the domain in which the proposed palliative devices within this body of work belong. The third section provides information on active palliative devices. Whilst, active devices are expected to provide greater attenuation levels when compared with passive alternatives, they sometimes have a higher cost implication and are therefore included to provide comparative level of attenuation for the proposes passive devices. Finally, a summary of the current palliative technology is included along with a discussion of how the current research is innovative in light of the previous work that has been undertaken within the field of cavity aerodynamics and acoustics.

2.1 Cavity aero-acoustics background

The introductory chapter provided a brief discussion of cavity flows and the potential issues which may arise during their operation. The focus of this discussion is on weapon bay configurations which are exposed to high transonic and supersonic flows. Firstly, this section provides a more detailed narrative about the criteria required for cavity resonance and also provides details of the differences between the various cavity environment classifications. Secondly, this section discusses how various factors, such as the cavity geometry or freestream flow conditions, can affect the acoustic characteristics within the cavity. Finally, a discussion is provided on the methods which are commonly used to calculate the frequency of the modal peaks within a cavity acoustic spectrum.

2.1.1 Criteria for cavity resonance

The flow over cavities can be categorised into two broad classifications, which are referred to as open and closed flows [9]. A typical open flow cavity has a length (l) to depth (h) ratio of l/h<6, whereas, for closed flow a cavity will typically have an aspect ratio l/h>10 [9] (*Figure 8*). These two regimes are classified by the acoustic characteristics, where only open cavity flows exhibit the high intensity unsteady pressure peaks. The flowfield within the two different cavity regimes can be described by the profile of the mean streamlines down the centreline of the cavity (s*ection 1.1*). Away from the cavity centreline the flow will exhibit three-dimensional effects, which are discussed in *section 2.1.2*. Between the open and closed flow regimes a transitional classification exists and the characteristics of the flow within this transitional regime depends on the freestream Mach number over the cavity [10].

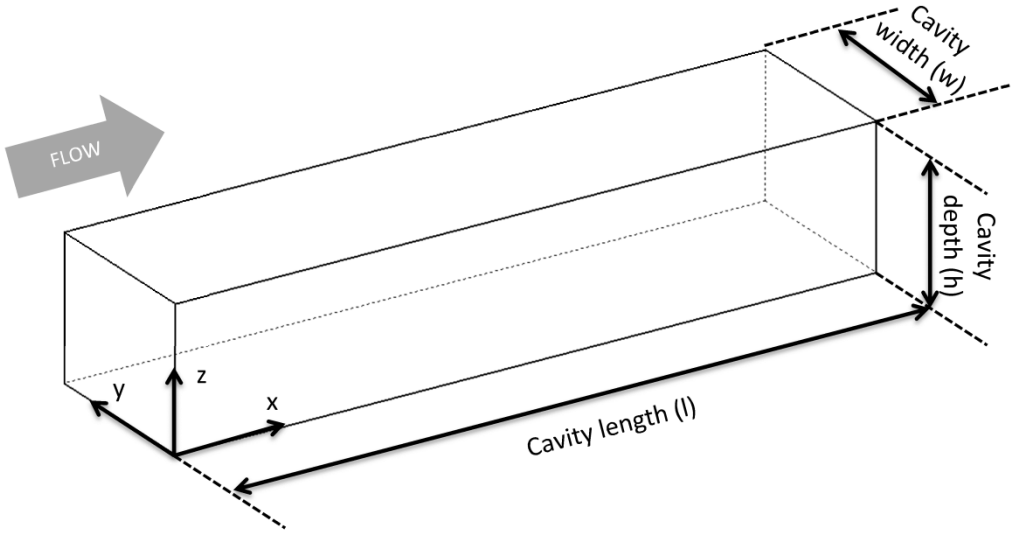

Figure 8 – Schematic of a rectangular planform cavity with the defining dimensions and coordinate system labelled

2.1.1.1 Closed cavity flows

The closed flow condition for cavity flows typically occurs when the length to depth aspect ratio of the cavity is l/h>10, which results in a relatively long and shallow cavity. In general, for closed flow, the shear layer over the cavity separates at the cavity front wall before reattaching to the cavity ceiling (*Figure 2b* (*section 1.1*)). Further downstream, the flow again separates from the cavity ceiling and exits the cavity over the rear wall. An impingement area exists at the rear wall and two separate recirculation zones exist within the upstream and downstream corners of the cavity (*Figure 2b* (*section 1.1*)). In the central portion of the cavity (x/l=0.5) freestream flow enters into the cavity volume due to the attachment and separation of the shear layer on the cavity ceiling (*Figure 2b* (*section 1.1*)). The increase in the local flow velocity and Mach number within the cavity, due to the freestream incursion, disrupts the upstream

propagation of pressure waves within the cavity and results in a non-modal cavity spectrum. Despite this, closed flow cavities are seldom used for weapon bays.

The typical static pressure coefficient profile for a closed flow cavity is shown in *Figure 9* [11]. The longitudinal distribution (x/l) of the static pressure coefficient (Cp) along the ceiling centreline, shows three distinct regions within the cavity. Initially, there is a rise in Cp with increased x/l, which is followed by a plateau region in the centre of the cavity x/l=0.5 where the freestream flow is attached to the cavity ceiling. However, towards the rear of the cavity, there is a rapid rise in Cp caused by the freestream flow as it detaches from the cavity ceiling and impinges on the rear wall. In general, as x/l is increased from the front wall the pressure coefficient rapidly rises and reaches a maximum level at the rear wall. This adverse static pressure gradient can cause a nose up pitching moment (*Figure 3*) [12] which severely affects the release characteristics of stores and is the major reason why closed flow cavities are generally avoided for weapon bay configurations.

Away from the cavity centreline two longitudinal vortices are entrained within the detached shear layer which enters the cavity volume. These entrained vortices are carried along the cavity sidewalls before they exit over the rear wall of the cavity with the shear layer and freestream flow which was also inside the cavity volume [13]. These vortices typically follow the path of the stream lines shown in *Figure 2b* and are expected to reach a maximum depth aft of the cavity centre (x/l=0.5) before exiting the cavity over the rear wall. On either side of the front wall recirculation zone, two vortices which stand vertically within the cavity, are present and this feature is also observed for open cavity flows. Whilst the characteristic velocities of disturbances within the cavity are not related solely to the vortical properties of the cavity flow, the presence of vortical structures with varying strengths throughout the cavity would be expected to affect the flow velocities within the cavity.

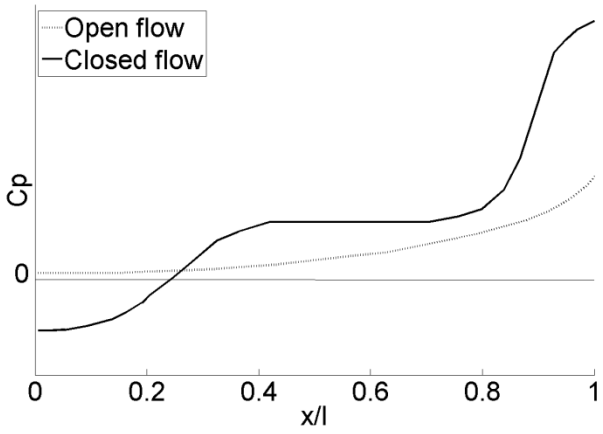

Figure 9 – Typical static pressure coefficient (Cp) profiles over a cavity ceiling for a closed and open flow cavity. (x/l denotes position from front wall of cavity across the ceiling surface (*Figure 8*)) [2]

2.1.1.2 Open cavity flows

Open cavity flows usually occur for cavities with aspect ratios of l/h<6 [14]. This creates a short, relatively deep cavity where the detached shear layer spans the cavity length and impinges upon the rear wall of the cavity (*Figure 2a* (*section 1.1*)). Vortices are shed from the front wall of the cavity and convect downstream within the shear layer where they impinge upon the rear wall stagnation point. This process results in the upstream propagation of unsteady pressure waves within the cavity [1] which trigger more vortices to be shed from the front wall [1]. The combination of both of these processes sets up a feedback mechanism within the cavity which has been identified as the cause of the unsteady spectra and high modal SPLs associated with open cavity flows (*Figure 4*) [1] [15]. Within the cavity, two areas of recirculation are typically established, where the major recirculation zone occupies around 70% of the aft portion of the cavity. A minor recirculation also zone exists in the front corner of the cavity and the centreline profiles for these two zones are shown in *Figure 2a* (*section 1.1*) [13]. These assumptions generally hold for rectangular planform cavities with open flow and dimensions of l/h>2.5, w/h>1.5, and w/l<l [13].

The major benefit of open cavity flows over the closed flow regime for weapon bay operations can be seen from the pressure coefficient (C_p) profile in *Figure 9*. Compared to the C_p profile for closed flows (*Figure 9*) the open flow case has a much lower gradient over the cavity length and a lower maximum value at the rear wall (x/l=1). Therefore, open cavity flows do not exhibit the strong adverse pressure gradients which can affect the separation characteristics of stores. This makes the open flow regime an attractive choice for the designer of weapon bays. However, as has been previously mentioned (*section 1.1*), open cavity flows exhibit a largely modal pressure spectrum with several high intensity modal peaks (*Figure 4*). These modal peaks can cause damage to both the aircraft and to stores carried within the bay. This potential for damage has driven the wide variety of investigations which have been undertaken into palliative devices designed to attenuate the damaging pressure peaks.

2.1.2 Factors which affect the modal characteristics of open flow cavities

This section discusses how the modal characteristics of an open cavity can be affected by both geometric and environmental factors. The effects on the modal characteristics are defined as changes to their respective frequencies and peak amplitudes. Based on these effects several models have been developed which calculate the modal frequencies for a cavity with a given geometry and flow conditions. These models are discussed in *section 2.7*.

2.1.2.1 Cavity geometry

The cavity geometry is perhaps the most intuitive factor which affects the modal characteristics. Typically the cavity length (l) is non-dimensionalised by the cavity depth (h) to yield the aspect ratio l/h (*Figure 8*). The main effect of l/h on the cavity acoustic signature has already been discussed in regard to the open and closed flow regimes (*section 2.1.1*). Briefly, as l/h increases, the modal amplitudes decrease as the cavity flowfield moves from the open to the closed flow regime [9]. Also, as l/h increases the frequencies of the modal peaks decrease. This decrease in frequency is linked to the greater travel times for the vortices and pressure waves over the extended cavity length and therefore, the modal frequency (f) is inversely proportional to the cavity length (l) ($f \propto 1/l$) [2].

The cavity width (w) (*Figure 8*) is typically non-dimensionalised by the depth (h) to yield the width aspect ratio w/h and changes to w/h affect both the modal frequencies and amplitudes. For both subsonic and supersonic freestream conditions the modal frequencies are weakly affected by increases in w/h [14]. For example, when w/h increases from w/h=1 to w/h=4 the modal frequencies of multiple modes could be raised by around 2% [14]. With regard to the modal amplitude the same increase in w/h from 1 to 4 raised the peak SPL by around 5dB. Interestingly, for a cavity with an l/h=10 aspect ratio, which would not be expected to exhibit modal characteristics, an increase in w/h from 1 to 4 changed the acoustic spectrum from a flat non-modal profile to a highly modal spectrum typical of open flow type cavities. This demonstrates that whilst the main property related to the cavity acoustic characteristics is the l/h ratio the w/h ratio is also important and can have a bearing on whether the cavity will exhibit modal characteristics.

Perhaps one of the major discrepancies between academic investigations into cavity acoustics and operational cases is the planform shape. Typically, wind tunnel or numerical investigations into cavity acoustics use a rectangular cavity planform. Whereas, an operational cavity may have a trapezoidal planform, due to the incursion of engine intakes or other critical aircraft structures into the bay. This will result in a cavity where an end wall may not lie orthogonally to the cavity length. If the front wall of the cavity is swept the phase of the vortex shedding will differ across the cavity span. This will affect the modal generation process as the phase of the vortices impinging upon the rear wall will vary and this will weaken the feedback mechanism. Indeed, a swept cavity front wall has been discussed as a possible cavity palliative [16] and has demonstrated a reduction in modal SPL of around 10dB. Cavities with non-rectangular planforms also exhibit modal peaks at lower frequencies when compared with rectangular cavities. Non-rectangular planform cavities have demonstrated decreases in modal frequency of around 1% compared to comparable rectangular cavities. The reduction in modal frequency can be attributed to the greater travel distance between the furthest part of the swept front wall and the cavity rear wall.

2.1.2.2 Approaching boundary layer state and thickness

The effect of the approaching boundary layer thickness (δ) can be non-dimensionalised by the cavity depth (h) and the relationship between the cavity acoustic characteristics and δ/h are investigated. Previous investigations have found it difficult to differentiate between the effects of boundary layer state and thickness. However, data exists for an l/h=3.75 open flow cavity where δ/h was increased from 0.14 to 0.25 through the use of a backwards facing step upstream of the cavity for Mach 0.4 freestream conditions [17]. This change equates to a twofold increase in δ ahead of the cavity and for this previous experimental case [17] the upstream boundary layer was determined to be turbulent. Initially, with δ/h=0.4 the cavity was highly modal with 4 clear modal peaks with SPLs typically 20dB higher than the broadband level. When δ/h was increased to 0.25, the modal peaks were completely removed from the spectrum. This indicates that a thick turbulent boundary layer can effectively damp out the oscillations within a cavity and prevent the high intensity modal peaks associated with typical open flow cavities.

The state of the approaching boundary layer also plays an important role in the generation of the modal acoustic characteristics within a resonant cavity. Both laminar and turbulent boundary layers are capable of exciting resonant conditions within a cavity [18] [19] and in some cases laminar boundary layers produce the largest modal amplitudes [20]. The majority of the previous work has concentrated on cases with turbulent boundary layers as this is the most likely case for an operational cavity. Within these previous cases there is evidence that by thickening the approaching turbulent boundary layer the modal intensities can be reduced by around 24dB (*Figure 10)* [21] [22].

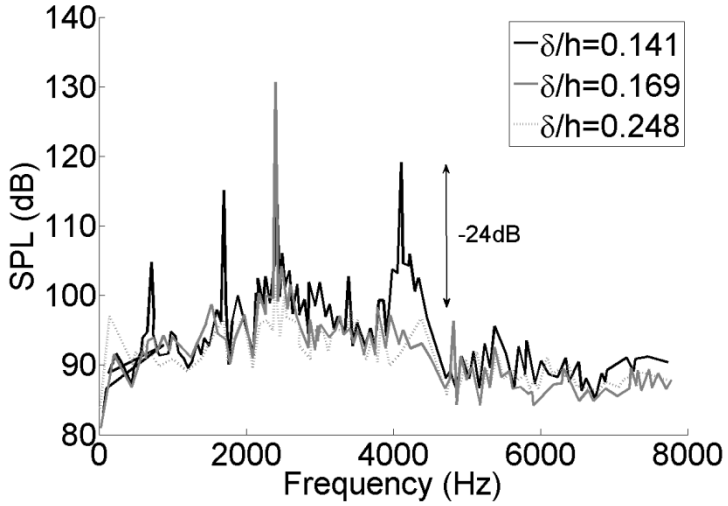

Figure 10 – Effect of increased δ/h on the modal amplitudes [21]

2.1.2.3 Freestream Mach number and Reynolds number

The freestream Mach number over a cavity is linked to both the frequency and amplitude of the modal peaks within the cavity spectrum (*Equation 1*). In general, for both subsonic and supersonic flows, as Mach number is increased the frequency of the modes also increases [2].

The relationship between the modal amplitudes and the Mach number is slightly more complicated. The amplitudes of the modal peaks are not only affected by the flow properties, but also by the acoustic characteristics of the cavity itself. For instance, if the modal frequency of a Rossiter mode coincides with one of the natural acoustic frequencies attributed to the cavity geometry that modal amplitude will undergo amplification due to the coupled cavity geometry resonance. This causes different modes to be dominant under different flow conditions. In general, for subsonic flow, as Mach number is increased the modal amplitudes will rise [2] [14]. This relationship has been attributed to the cavity flow classification switching from closed or transitional flow at lower Mach numbers ($M<0.2$) to open flow for higher Mach numbers. At these higher subsonic Mach numbers ($M\approx0.9$) the feedback mechanism responsible for the generation of the cavity modes is stronger and therefore generates modes with higher amplitudes. Under supersonic conditions the relationship is different, where an increase in Mach number causes the modal amplitudes to reduce [2]. This reduction in modal amplitude has been attributed, by Unalmis [23]. to the larger amount of fluid with a high momentum which is entrained into the cavity at lower Mach numbers compared with higher Mach number conditions [23]. The reduction in modal amplitude with increased supersonic Mach number is also accompanied by a substantial reduction in the broadband cavity noise [2].

Reynolds number, related to the cavity length, is reported to have little or no effect on either frequency or amplitude of the Rossiter modes [2] and this assumption is used throughout this body of work. Under both subsonic and supersonic conditions, variations in Reynolds number over the range $1x10^6$ to $8x10^7$ have demonstrated no effect on the modal frequencies [2] [24]. However, the evidence is less clear with regard to the effect of Reynolds number on the modal amplitudes. Typically, modal spectra are presented in terms of SPL which is referenced to a standard level ($2x10^6$Pa) and this does not take into account any changes to the tunnel operating conditions. Reynolds number is often varied through changes to the air density within the tunnel brought about through changes to the tunnel dynamic pressure and this then affects the amplitudes of the SPLs recorded. For cases where the data are presented in terms of fluctuating pressure levels (FPL), where the pressures are normalised by the freestream dynamic pressure, any effects due to increased dynamic pressure, which is often used to vary the Reynolds number, can be accounted for. Such investigations demonstrate that changes in Reynolds number have no effect on the modal amplitudes under subsonic conditions [24]. Data for supersonic cases is presented in terms of SPL and so the conclusion is less clear. However, if the expected increase in SPL due to the changes in

dynamic pressure are considered, then Reynolds number appears to have little or no effect on the modal amplitudes under supersonic conditions [2] [25].

2.2 Prediction of open cavity flow characteristics

For cavity applications it is important to be able to calculate not only the onset of the problem acoustic modes, but also the frequency and intensity of the unsteady modal peaks. Since the early cavity investigations in the mid twentieth century [1] [18] simple semi-empirical models have existed for the calculation of the modal frequencies. Perhaps the most widespread and well known model is that which was first proposed by Rossiter [1]. This model was later adapted for use under transonic and supersonic Mach numbers [20]. As this approach is the most commonly used within the published literature it is discussed in *section 2.7.2*. Alternative methods [26] [27] which are also based on Rossiter's work and measurements have also been proposed, but are not discussed in this study. A mechanism through which the modal frequencies are generated [15] is also discussed alongside Rossiter's original and updated model (*section 2.7.4*).

Whilst there are numerous reliable approaches to estimate the modal frequencies within a cavity there are no simple, reliable techniques which can be used to estimate the modal intensities. It has taken until recently, with the use of DES numerical methods to be able to reliably calculate the modal amplitudes [28]. No further discussion is included here on the calculation of the modal amplitudes and for additional information the reader is directed to reference [2].

2.3 Passive approaches to cavity noise attenuation

Passive approaches to the modal attenuation are categorised by the use of devices where no energy is imparted to the freestream or cavity flow [5]. This excludes consideration for the actuation of devices which need to be moved into place for operation. For example, a palliative is not required if the cavity doors are closed and the device can be accommodated within the aircraft fuselage until required. The majority of passive palliatives, once deployed, are fixed structures or devices which have been designed to attenuate a specific frequency or range of modal frequencies at a given flow condition. This leaves passive designs with the issue that they may not work well under off-design conditions and have to be designed with compromise in mind.

Passive devices provide attenuation through several mechanisms which can be broadly generalised as either a flow manipulation or energy absorption processes. Examples of flow manipulation type devices are spoilers [16] [29] [30] [31] [32] [33] and other cavity geometry changes [31] [34] [35] [36]. These devices aim to alter the way in which the cavity flow field interacts with the cavity structure and therefore to reduce the amplitude of the modal peaks. There are fewer examples of absorptive approaches, but these could include absorptive material [37] or tuned resonant absorbers [38]. Absorptive methods are typically designed to attenuate one or more of the cavity modal peaks by absorbing

energy at that modal frequency. The following sections discuss a variety of passive control techniques including the current state of the art and devices which are comparable to the resonant arrays proposed within the current body of work. For further information regarding the performance of a wide range of passive palliative devices the reader is directed to reference [2].

2.3.1 Spoilers

Perhaps the most widely used and investigated passive attenuation approach is a spoiler installed upstream of the cavity (*Figure 6* and *Figure 12*) [2] [4] [7] [16] [17] [29] [30] [31] [32] [33] [39] [40] [41] [42] [43]. The discussion of the performance of passive attenuation approaches starts with a look at the various types of spoiler devices which have been developed. The role of a simple upstream spoiler is to reduce the interactions between the vortices within the shear layer and the rear wall of the cavity. A simple spoiler will achieve this by two means. Firstly, the spoiler diverts the incoming air flow over the cavity which moves the shear layer reattachment point downstream of the cavity rear wall and this is known as lofting (*Figure 6*) [32]. Secondly, by raising the shear layer into the freestream flow it is expected that the convection speed of the vortices increases in comparison with the untreated case. If vortices still impinge at the rear wall this will occur at a higher frequency compared to the untreated case and this should result in the cavity being driven at a slightly higher frequency. The cross-correlation investigation in the current work examines these aspects for the effect of the spoiler on the cavity flow field (*section 5.1.1*).

The effect of spoiler shape on attenuation has previously been investigated by using saw tooth design spoilers or rod type spoilers ahead of the cavity [30] [31]. These devices are designed to not only deflect the detached shear layer over the cavity, but also to introduce additional streamwise vorticity into the shear layer and to disrupt the spanwise coherency of the vortices (*Figure 11*). This can force the shear layer at frequencies above the untreated vortex shedding frequency and this is expected to stabilise the shear layer [32]. The following sections discuss some of the key results from previous experiments which have investigated the performance of spoiler palliatives.

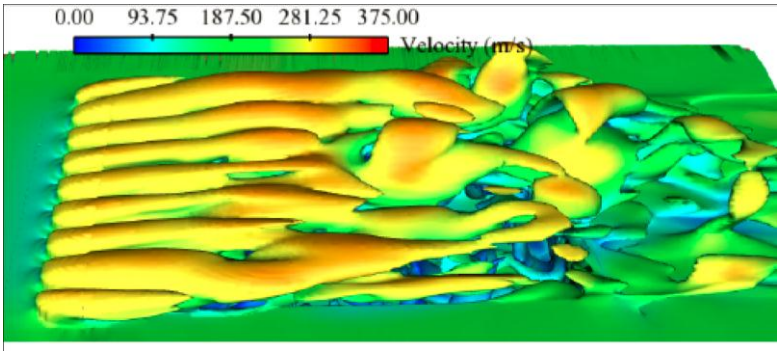

Figure 11 – Velocity contours of vorticity iso-surfaces over a cavity to show the streamwise vortices shed from a sawtooth spoiler. (reproduced from reference [16])

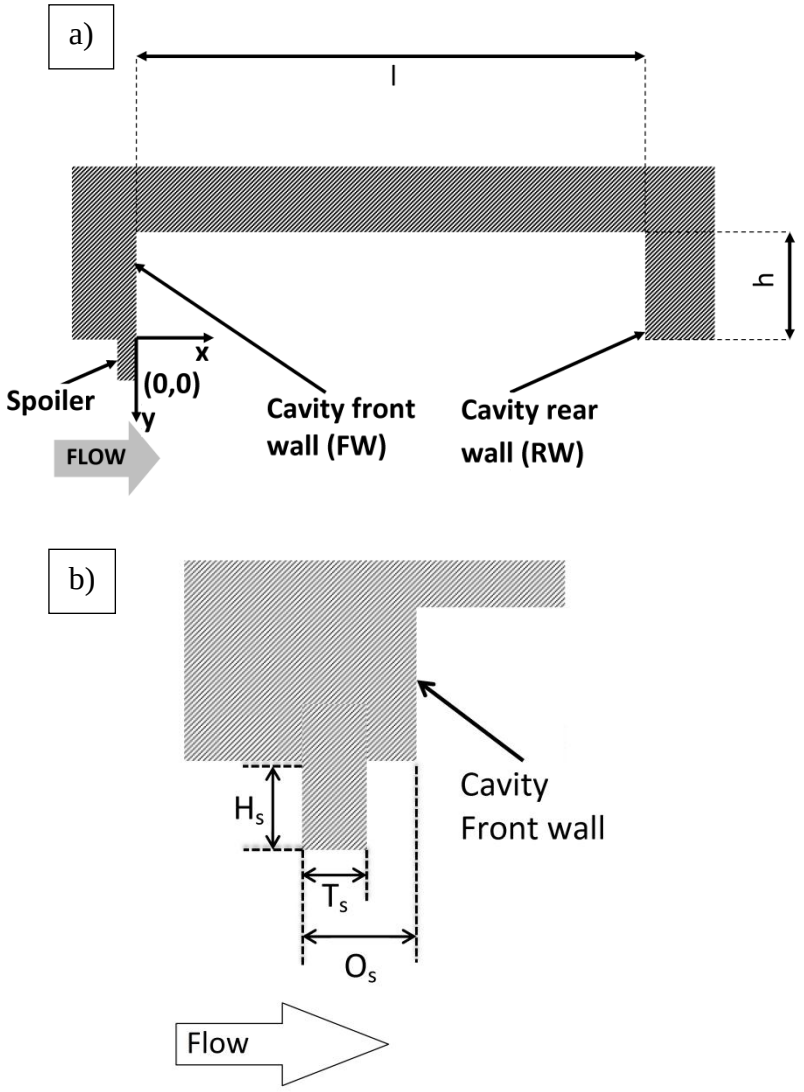

Figure 12 – a) Sketch of a spoiler installed at the cavity front wall, b) Sketch of the characteristic spoiler dimensions (H_S= Spoiler height, T_S= Spoiler thickness, and O_s= Spoiler offset)

2.3.1.1 Plain rectangular and sawtoothed spoilers

Spoilers are typically classified by the ratio of their height (H_s (*Figure 12*b)) and thickness (T_s (*Figure 12*b)) with respect to the approaching boundary layer (δ). The offset of the front wall from the cavity (O_s (*Figure 12*b)) is also often indicated. Serrations can be added to a spoiler design to add vorticity into the shear flow over the cavity (*Figure 13*): these serrations are characterised by the ratio of spacing (W_L (*Figure 13*)) to the cavity width (w), and by the ratio of the serration height (H_T (*Figure 13*)) to δ.

Numerous investigations have taken place which focussed on either the effects of spoiler geometry or freestream Mach number. With respect to geometry, plain spoilers demonstrated the best attenuations when $H_S/\delta \approx 1$ [2] [30] [33]. Under transonic conditions 1δ solid spoilers have achieved attenuation levels of up to 27dB from modal peaks (*Figure 14*) [2] [30] [33] when installed directly at the cavity front wall ($O_S/l=0$). This attenuation level reduces as the spoiler is moved further upstream of the cavity with the level around 50% of the front wall case when the spoiler was installed $O_S/l=0.08$ upstream of the cavity front wall [33]. A thicker spoiler also with $O_S/l=0.08$ provided a similar level of attenuation and it was proposed that the reduced attenuation performance from upstream spoilers was due to the location of the shear layer impingement point aft of the cavity. If this point is not deflected far downstream of the cavity then vortices will still impinge upon the corner of the rear wall and the modal generation loop will be remain within the cavity [32] [33].

Sawtoothed spoilers are designed such that they impart vorticity into the detached shear layer over the cavity. The first aim of this process is to stabilise the shear layer by reducing the tendency for the growth of the spanwise vortical structures within the shear layer [16]. The second aim is to reduce the coherence of any large scale structures which may form in the shear layer and convect downstream [30]. Both of these effects are designed to break up the mechanism through which the Rossiter modes are generated. Typically, sawtoothed spoilers have a greater height than solid spoilers with $H_S/\delta \approx 1.2$ devices providing a similar level of attenuation compared with solid configurations [2] [17] [33] [35]. This extra height is required to achieve the same lofting effect due the reduced frontal area created by the spacing of the teeth. Overall, the levels of attenuation which can be achieved under transonic conditions are relatively similar for both solid and sawtoothed spoilers. However, when the attenuation levels from spoilers of the same height are compared the attenuation from solid spoilers can be around 5dB greater than the equivalent sawtoothed device [35]. Therefore, transonically sawtoothed devices do not offer a distinct performance benefit over solid devices.

Under supersonic conditions the attenuation potential of both solid and sawtoothed spoilers is less clear. Previous work generally agree that spoiler attenuation performance reaches a maximum in the Mach number region $0.9<M<1.1$ and also that as Mach number is increased to higher supersonic conditions the attenuation levels, of both the

modal peaks and broadband noise, will decrease (*Figure 14*) [2] [7] [17] [43]. However, some spoiler configurations under supersonic conditions can cause a greater amplification to cavity modes with the greatest amplification of around 13dB, for a $H_S/\delta<1$ spoilers at Mach 1.5 [2] [7]. Other configurations have been used under higher supersonic conditions of up to Mach 3 with similar amplification effects [43]. The relationship between reduced performance and increased supersonic Mach number has been demonstrated for both solid and sawtoothed spoilers, where both devices have demonstrated modal amplifications of between 5dB and 10dB [2] [43]. This issue of reduced attenuation performance under supersonic conditions could be a problem for the application of spoilers as palliatives for operational cavities. An alternative approach or a combination between a spoiler and another palliative may be required for reasonable attenuation levels across an aircraft's flight envelope.

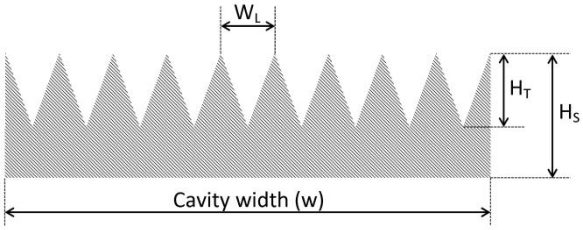

Figure 13 – Sketch showing the defining dimensions for a sawtoothed spoiler

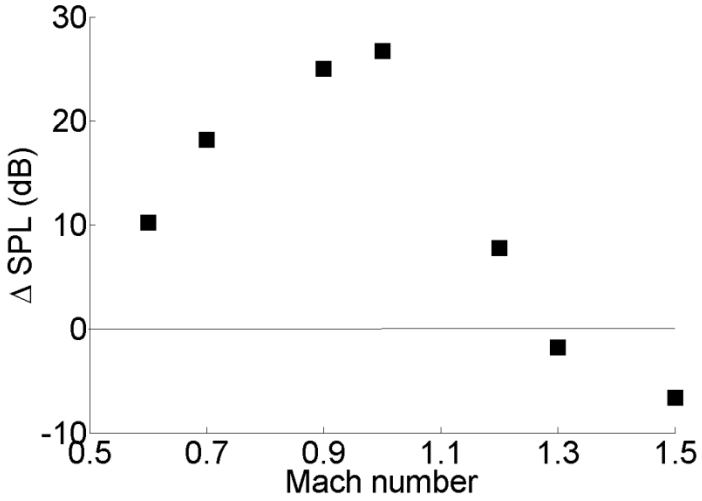

Figure 14 – Attenuation of the first cavity mode (ΔSPL) from a solid spoiler installed upstream of a cavity for various transonic and supersonic Mach numbers [6]

2.3.1.2 Rod in cross-flow

The vortex shedding properties of the flow past a cylinder are well known [44] and this can be used to affect the shear layer at the front wall of a cavity. These vortex shedding properties are linked to the Strouhal number (St (*Equation 2*)), where f is a frequency (Hz), d_s is the diameter of the rod (m), and U is a velocity (ms^{-1}). Previous studies have assumed a constant Strouhal number of around St = 0.2 for a cavity control rod [32].

$$St = \frac{fd_s}{U}$$ **Equation 2**

This type of cavity flow control is known as forcing the shear layer where it is most receptive to small perturbations [32] [45]. This concept is typically used by active flow control techniques, which will be discussed in *section 2.4*. This process involves exciting the shear layer at frequencies above those associated with the generation of the vortices, which are responsible for the initialisation of the feedback mechanism for the unsteady pressure fluctuations [1]. A rod in the crossflow presents an obstacle to the oncoming flow and it can be assumed that a certain level of attenuation is achieved through the diversion of the shear layer over the cavity, much like the lofting effect for regular spoilers [32] [45]. The characteristic dimensions of a rod in the crossflow type device are shown schematically in *Figure 15*, where h_S is equivalent to the height of a spoiler and d_S is the diameter of the rod. Both of these are typically non-dimensionalised by the height of the approaching boundary layer (δ).

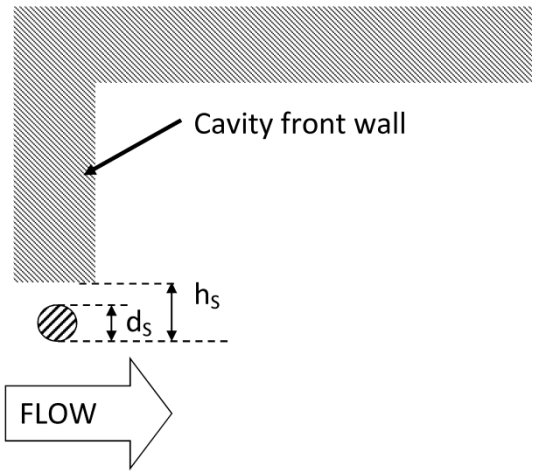

Figure 15 – Sketch a rod spoiler configuration upstream of the cavity front wall

To design a rod-type device which is installed horizontally across the span of the cavity just upstream of the leading edge (*Figure 15*), the following design rules and assumptions are typically made (Modified from reference [32]):

1. Von Karman vortex shedding key to attenuation.
2. The larger the diameter (d_s) of the rod, the larger the perturbation imposed upon the cavity shear layer, and the greater the potential suppression effect. $d_s/\delta=0.6$
3. The rod had to be positioned at a height (h_s) above the cavity such that there was sufficient gap to allow self sustained vortex shedding. $h_s/\delta=1.3$
4. The diameter (d_s) is chosen such that the shedding frequency is "high" relative to the Rossiter modal frequencies.
5. The rod diameter (d_s) should be less than one boundary layer thickness (δ).

High modal attenuation levels have been demonstrated for rod-type devices with peak attenuations of between 15dB and 20dB having been reported under both transonic and supersonic freestream conditions [2] [32] [45] [46]. High levels of OASPL attenuation, up to 15dB [32], accompany the peak reduction levels. Unlike with simple spoilers, there is a clear relationship between Mach number and attenuation across both the transonic and supersonic regimes, with increased attenuation levels under supersonic conditions. The size and location of the rod with respect to the oncoming boundary layer were shown to have the greatest effect on the attenuation performance of the devices. Under both transonic and supersonic conditions, the best attenuation results were for devices with $h_S/\delta=1.33$ and $d_s/\delta=0.66$, and for supersonic conditions the highest attenuation was for devices with $h_S/\delta=1.54$ and $d_s/\delta=0.77$ [6]. Both of these recommendations place a rod with $d_s/\delta<1$ close to the edge of the boundary layer, such that part of the rod is immersed in the boundary layer flow with the immersed depth referred to as $\Delta\delta$. For subsonic flow it was recommended that half the rod should be immersed ($\Delta\delta= d_s/2$) and for supersonic flows a third should be immersed ($\Delta\delta= d_s/3$) [6].

Due to the relationship between the attenuation characteristics of the rod in crossflow based devices and the approaching boundary layer properties (δ), rod based devices are not as versatile as other spoiler type palliatives. Rod in crossflow type devices suffer from a decrease in off design performance, which is partially caused by boundary layer properties. This reduction in the off-design performance is inherent to all passive devices, but the performance from rod devices are especially sensitive to the position of the rod within the boundary layer as below a critical h_S/δ no shedding will occur and the device will not function correctly. The diversion of the detached shear layer only plays a minor part in the attenuation offered by a rod in the crossflow based system and it is thought to be through this mechanism that off-design attenuation is provided.

2.3.2 Vortex generators

Vortex generators are installed upstream of the cavity front wall with the aim of introducing three-dimensional disturbances into the detached shear layer over the cavity

(*Figure 16*). These disturbances are introduced to improve the shear layer stability and also to inhibit growth of large scale vortical structures within the shear layer [2] [4]. These mechanisms are similar to those through which sawtoothed spoilers operate.

One of the first successful demonstrations of attenuation through the use of vortex generators deployed a pair of vertically mounted vanes upstream of the cavity. The vanes were twice as high as the approaching boundary layer and were angled at 45° to the cavity's longitudinal axis. These devices provided up to 20dB of peak attenuation from the dominant mode for Mach 0.9 and around 10dB at Mach 1.5 [4].

The majority of cavity tests are conducted at relatively small model scales, however occasionally full scale flight tests are undertaken. A full scale investigation into the attenuation of the fluctuating pressures within the weapon bay cavity of an F-111 at both Mach 0.85 and 1.15 was conducted [47]. For this test four vane type vortex generators with a height of 1δ were installed ahead of the cavity and again angled at 45° to the cavity's longitudinal axis. At both Mach 0.85 and 1.15, attenuations of the modal peaks of up to 7dB were demonstrated along with around 5dB of OASPL attenuation. The difference (3dB) in modal peak attenuation levels between the two test cases discussed here is attributed to the difference in the height of the devices, with larger attenuations for the larger 2δ configuration. In summary, the performance of vortex generators as cavity palliatives is promising with reasonable levels of attenuation demonstrated under both transonic and supersonic conditions. The main issue for full scale application is likely to be the large size of the devices that would be required to fulfil the 2δ condition (150mm) [2] [47].

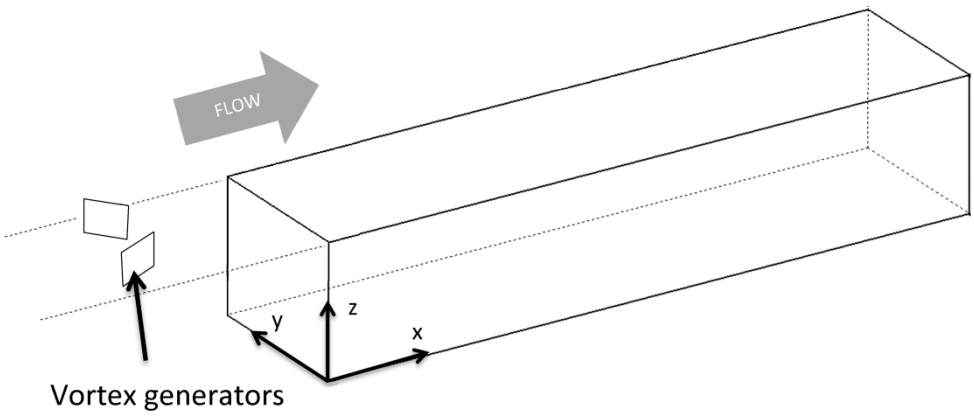

Figure 16 – Sketch of a pair of vortex generators installed upstream of a cavity. (vertically mounted vanes upstream of the cavity [4])

2.3.3 Geometric changes to the cavity planform shape

Full scale weapon bay cavities within operational aircraft are typically not rectangular in planform shape and often are filled with clutter over the internal surfaces. This is often due to structural constraints or aircraft systems such as engine intakes encroaching into

the cavity volume. It is therefore of interest to assess whether these or any other changes to the cavity geometry affect the cavity acoustic spectrum.

A number of options are available for cavity geometry changes and these include: front or rear wall sweep, a rearward facing step, and rear wall chamfer. Each of these alterations are designed to either affect the vortex shedding process at the front wall or the vortex impingement at the rear wall. Both of which are expected to interfere with the feedback process behind the generation of the modal peaks and therefore reduce the peak amplitudes.

2.3.3.1 Rear wall sweep

The rear wall of the cavity is widely regarded as the source of the modal pressure fluctuations within resonant cavities and it is therefore expected that any modification to the shape of this structure will affect the modal generation process and reduce the intensities of the modal peaks. Vortices shed from the cavity front wall will impinge upon a swept rear wall at different phases, which depend on the location of the vortices over the span of the cavity. The resultant pressure fluctuations would be out-of-phase with each other and this should prevent the successful generation of the feedback loop process within the cavity [4].

An example of the use of rear wall sweep investigated the palliative effect of swept rear walls at angles of θ=20° and θ=35° (*Figure 17*) under Mach 0.7 and 0.9 freestream conditions [34]. This study found that both cases of sweep were relatively ineffective as palliatives with up to 6dB of attenuation at Mach 0.7 and 3dB at Mach 0.9. This ineffectiveness of the oblique end wall configuration is in agreement with previous work that demonstrated no modal attenuation with both swept front and rear walls [4]. However, a study which swept both the front and rear walls simultaneously reported attenuation levels of around 8dB for Mach 0.85 flow [16].

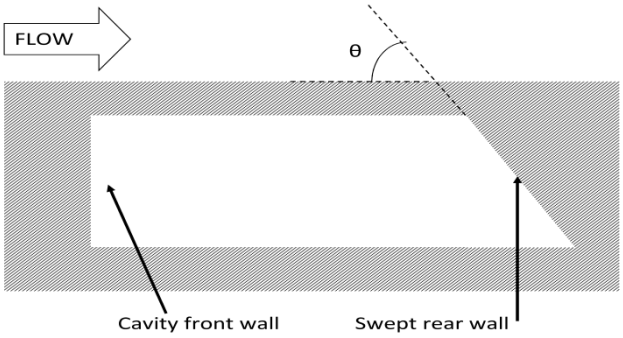

Figure 17 – Sketch of a cavity planform with a swept rear wall

2.3.3.2 Rearward facing step

A rearward facing step (*Figure 18*) is designed to disrupt the interactions between the internal cavity flow and shear layer at the detachment point on the edge of the front wall. This location at the edge of the cavity on the front wall is thought to complete the feedback loop between the internal pressure waves and the vortices within the shear layer [1] and is most receptive to interference at this point [48].

A study which examined the performance of steps used as cavity palliatives designed the step depth (h_S (*Figure 18*)) based on the reattachment length characteristics of flow over the corner of a rearward facing step [31] [49]. The configurations were designed so that the flow would either re-attach to the horizontal surface of the step or pass over the step with no re-attachment. This was controlled by the ratio h_S/h, where h is the cavity depth, and with a large h_S/h the flow is not expected to re-attach onto the step [31]. The performance of the steps was shown to be highly Mach number dependant with OASPL attenuation reducing to around 2dB for both Mach 0.70 and Mach 0.86 flow.

The steps with no re-attachment (largest h_S/h) provided the greatest levels of attenuation at Mach 0.9, with peak attenuations of up to 20dB and an OASPL reduction of around 6dB [31] [49]. This result was attributed to the presence of a large spanwise recirculation in the region between the step and the detached shear layer (h_S (*Figure 18*)) (*Figure 19*). This work [31] does propose a flow topology model based on oil flow visualisations of the flowfield (*Figure 19*) to account for how steps may attenuate the cavity modes. However, the evidence is insufficient to draw a firm conclusion on the attenuation mechanism.

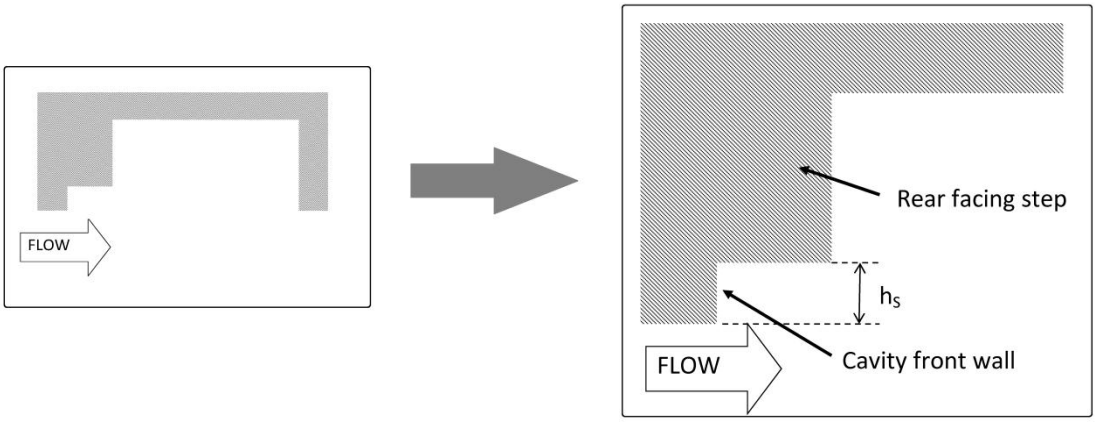

Figure 18 – Sketch of rear facing step

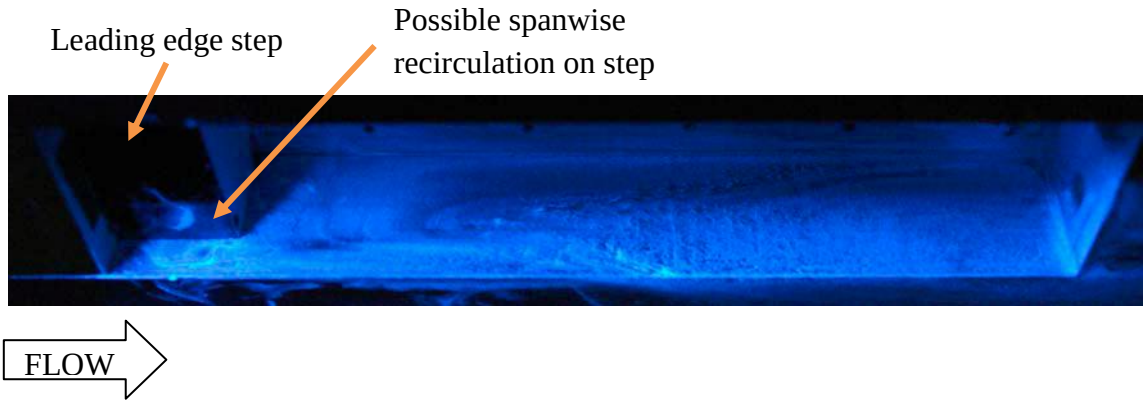

Figure 19 – Oil flow visualisation of the flow within a cavity with a leading edge step installed. (reproduced from reference [31])

2.3.3.3 Rear wall chamfer

The aim of altering the shape of the rear wall is to reduce the shear layer impingement interactions and reduce the intensity of the associated pressure waves which complete the feedback loop within the cavity. This should weaken the process within the cavity and reduce the modal pressure levels. Chamfering the rear wall so that it is inclined is one way to achieve this (*Figure 20*). Several studies have investigated the use of this simple modification with θ=45° as a palliative [34] [4] under both transonic and supersonic freestream conditions.

Both investigations demonstrated large attenuations of the modal peaks. Under transonic conditions 0.7<M<0.9 attenuation levels were typically between 5dB and 11dB with the highest attenuation at the lower Mach number conditions [34] [4] . For the supersonic case at Mach 1.2 significantly higher peak attenuation levels were shown, with up to 20dB of attenuation [4]. Significant reductions in the pressure coefficient levels in the aft of the cavities were also reported [34]. This was linked to an increase in flow exiting from the rear of the cavity and an external deflection of the detached shear layer in the region of the rear wall. This creates a region where a steady flow can be achieved [4]. The deflection of the shear layer at the rear wall stagnation point moves the

impingement point of the vortices shed from the front wall and therefore reduces their interaction with the cavity surfaces [34]. This breaks the feedback mechanism within the cavity and leads to the reduction of the modal pressure intensities. The acceleration of flow out of the cavity also causes a decrease in the local static pressure which reduces the mean pressure within the cavity and therefore reduces the pressure coefficient at the rear of the cavity. This creates a relatively benign pressure gradient in the cavity which may further improve the stores release characteristics of the open flow cavity.

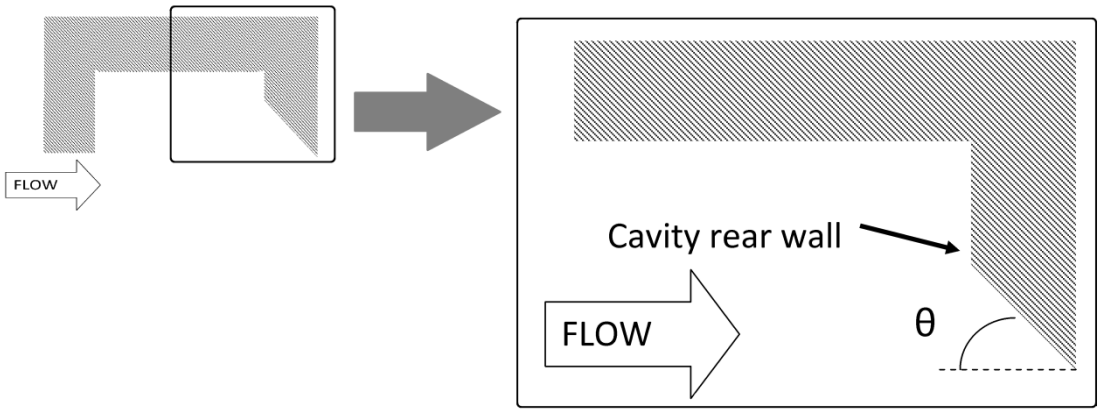

Figure 20 – Sketch of chamfered cavity rear wall

2.3.4 Absorptive material

Absorptive materials based on open celled foams are often used within the room acoustics field to attenuate both modal and broadband noise components. Sound propagation occurs within the open celled structure of the absorber and this causes both viscous and thermal losses which dissipates the acoustic energy [50]. This attenuation mechanism relies on large particle velocities caused by high acoustic pressures within the material. To ensure that the high particle velocities occur within the absorber it is usually placed a quarter wavelength (λ/4) distance from a reflective surface. For room acoustics applications this distance is of the order of 10mm, which for such installations is not usually an issue. However, one of the major issues with absorbent materials within aircraft cavities is the large volume which is required to meet the λ/4 condition. For a full scale weapon bay cavity (estimated at 4m long) this λ/4 condition could be as large as 1m for modal frequencies less than 100Hz. Within the weapon bay there would not be sufficient room to accommodate the absorptive material and it is therefore unlikely that devices based on this approach are suitable for full scale weapon bay applications.

Nevertheless, several investigations have been carried out which assessed the potential of absorptive material as a passive cavity palliative [2]. One such investigation used 12.5mm thick acoustic foam to attenuate broadband cavity noise about 1kHz within a

350mm long cavity (t/l=3.5%) [51]. At Mach 0.75 attenuation levels, for the modal peaks, of between 5dB and 12dB were demonstrated for single end and double end treatments respectively. This investigation did not use the foam to attenuate the dominant modal peaks as these occurred at a frequency which was lower than the foam optimum attenuation frequency [51] [2]. The issue of low frequency attenuation by absorptive materials poses the main obstacle for the use of these materials within full scale cavities. Whilst it is possible to demonstrate attenuation within small scale model cavities, which exhibit high frequency modes, this capability is not practical at full scale due to the large volume which would be required to accommodate the absorptive material with the appropriate characteristics for the much lower frequencies.

2.3.5 Resonant absorbers

Perhaps the most pertinent approach to review within the current body of work is that related to tuned resonant absorbers, or Helmholtz resonators. These devices typically provide attenuation through a tuned viscous loss approach, where the attenuation occurs over a relatively narrow band of frequencies. There is only one example, in the public domain, of resonant arrays being used experimentally as cavity palliatives and this investigation had mixed success under subsonic conditions [38]. A more recent numerical investigation tested the performance of the resonant absorber concept by adapting the properties of the internal surfaces to match the acoustic properties calculated for a series of arrays [37].

For the previous experimental investigation an open flow cavity was configured with an array of resonant absorbers connected to the cavity rear wall. The resonant absorbers were formed from individual hypodermic syringes, a design which enabled the volume of the syringe to be changed to vary the resonant frequency of the array. As each of the individual resonators was tuned separately there was difficulty in ensuring that all devices were set to the same frequency. The effectiveness of the arrays were investigated at Mach numbers of M=0.34, M=0.53, and M=0.90 with the arrays installed into either the rear wall or ceiling of the cavity. Whilst large peak attenuations, typically between 13dB and 22dB (*Figure 21*) were demonstrated for Mach 0.34 and 0.54 flows, only a small level (2dB) was demonstrated for the Mach 0.90 case with a rear wall array. The cases with arrays installed in the cavity ceiling were less successful at all Mach numbers investigated with attenuation levels typically no higher than 2dB being demonstrated. This investigation provided promising results for the use of Helmholtz type resonators as cavity palliatives for relatively low Mach number flows. However, under the higher subsonic Mach number (M=0.9) the low levels of attenuation were disappointing and perhaps explain why resonant arrays have been overlooked as potential future cavity palliatives. This does however provide an opportunity for the results from the current work to add to the current body of knowledge on the subject of passive palliatives for cavity flows.

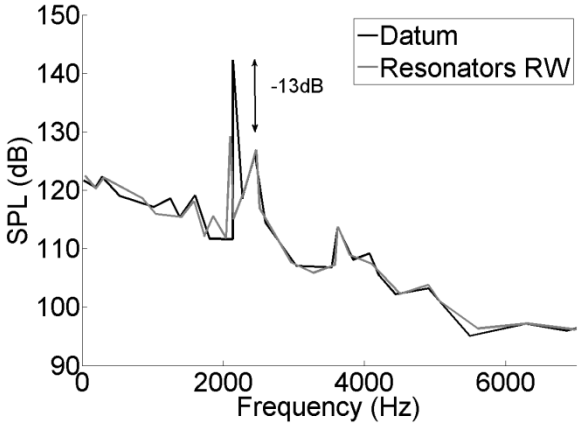

Figure 21 – Effect of rear wall (RW) mounted resonant arrays on the modal SPL spectrum at Mach 0.34 [38]

The numerical investigation was conducted for an open flow cavity with l/h=5 at Mach 0.85 [37]. The devices, which are described as porous media inserts, were modelled with a porosity of ε=11.2% and were imposed as zero-thickness conditions within the domain and as such no flow was calculated within the arrays. No indication is given about the tuning of the devices, however from the attenuation results the arrays provide a broadband attenuation with the main attenuation focussed on the dominant second mode. The study investigated the performance of the devices when installed at the rear wall, ceiling, and in a combination of the two locations. The largest modal attenuation of around 10dB was for the second modal peak when the devices were configured in both the rear wall and ceiling positions. This modal attenuation reduced to around 8dB for the rear wall alone case and further to 5dB for the ceiling alone case. This is an important result as it demonstrates that the cavity rear wall configuration provides a greater attenuation level compared with the ceiling, despite the larger surface area available to treat on the ceiling. Also, the results show that a combined configuration can improve the attenuation over a single configuration. This method of attenuation improvement, though combined installation, is directly applicable to the devices proposed within the current study and will be investigated in *section 5.6*.

2.4 Active approaches to cavity noise attenuation

Active palliative devices are categorised by the addition of energy into the cavity flow. Active systems can be further split into two subcategories referred to as quasi-static and dynamic [39] [52]. These two categories are related to the level of feedback and therefore complexity of the system. Typically, quasi-static systems are formed from an open loop system with either a slow response feedback loop or no feedback path and an example of such a system could be steady blowing at the front wall of the cavity [48]. A dynamic system requires a system of sensors to detect the cavity characteristics and a control system to tune the energy input to attenuate the characteristics. Examples of dynamic control methods include pulsed blowing or mass injection [53] and unsteady flap actuators [54]. The current study investigates the performance of a series of passive flow

control devices and therefore the performance of active devices is provided for comparative purposes. This section provides a brief overview of active concepts. Several review articles have been published which cover the wide range of the active approaches which have been undertaken to control cavity acoustics and the reader is directed to references [39], [52] and [55] for further information regarding active flow control techniques.

2.4.1 Mass injection

The first method of active flow to be discussed is mass injection, and this can be further split into both quasi-static or open-loop and dynamic or closed-loop techniques. Open-loop approaches include constant blowing or pulsed blowing at a pre-set frequency, which is different to the Rossiter frequencies. Open-loop type approaches are used to disrupt or de-tune the cavity resonance by forcing the cavity flow at frequencies other than those related to the Rossiter modes. A compromise has to be found between attenuation and finding a forcing frequency which is acceptable over the full range of flow conditions which may be encountered. Closed-loop systems remove the need for compromise as the system is able to adjust the forcing frequency based on feedback from a sensor located within the cavity. A closed-loop system will therefore provide the optimum energy input into the flow system for the given conditions.

One of the first examples of open-loop mass injection used steady blowing from sources located around the circumference of the cavity ceiling (*Figure 22*) [56]. The aim of this work was to reduce the oscillation of the shear layer at the rear wall of the cavity and therefore, to reduce the entrainment of mass from the freestream [57]. Attenuation levels at the modal peaks, for a freestream Mach number of M=0.23 with ceiling blowing, were reported at around 12dB for injection mass fluxes between 5% and 15% of the freestream mass flux per unit area ($\rho_\infty U_\infty$) [56].

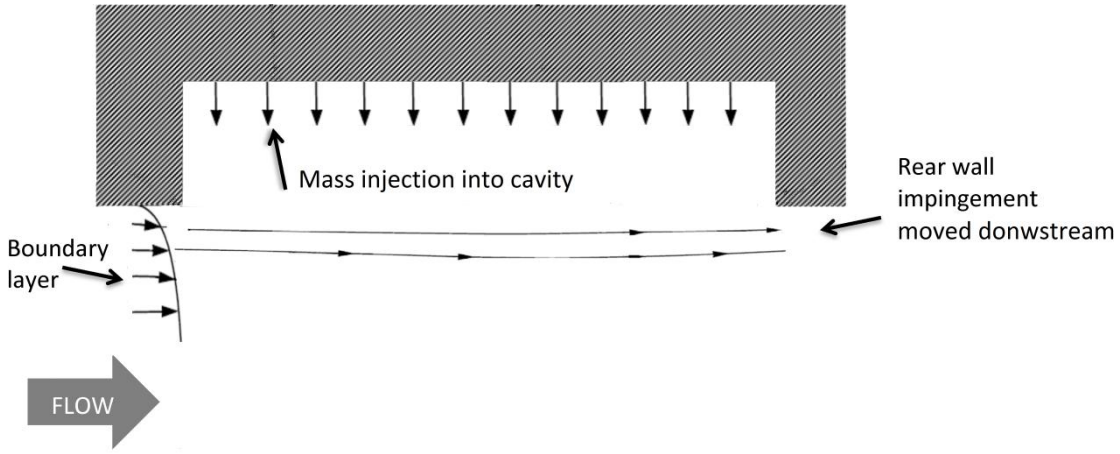

Figure 22 – Sketch of a cavity configured with mass injection around the circumference of the cavity ceiling. (Injection technique as of reference [56])

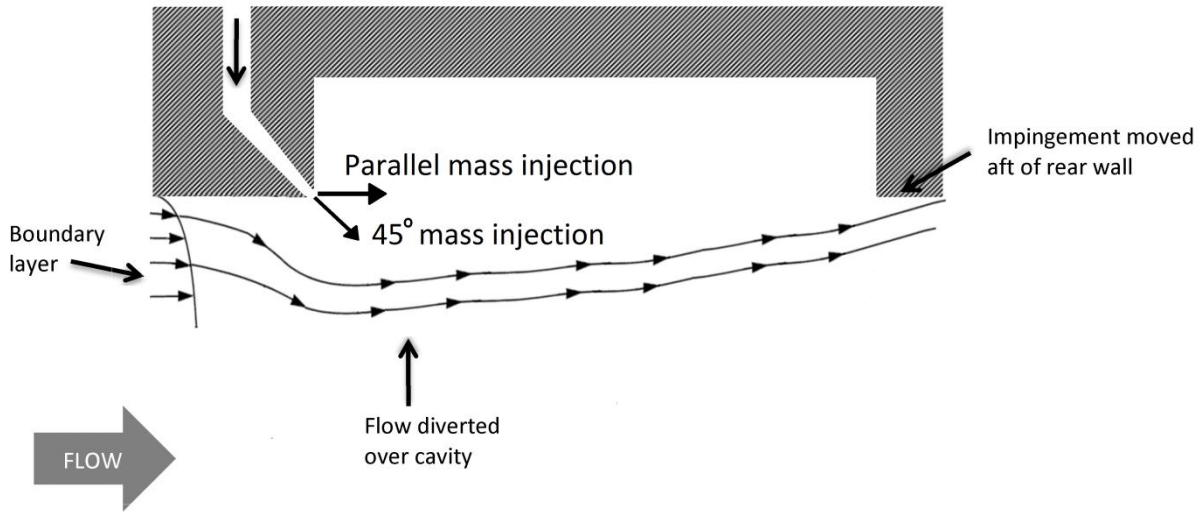

Figure 23 – Sketch of a cavity configured with mass injection at the front wall. Both injection parallel to the freestream direction and at 45° away from the freestream direction shown. (Injection technique as of reference [58])

Subsequent open-loop mass injection investigations tended to investigate the effectiveness of mass injection at the leading edge of the cavity in an attempt to both divert the shear layer over the cavity and to affect the vortex shedding properties of the cavity leading edge [52]. One such experiment investigated injection at the cavity front wall inclined at both 45° away from the freestream flow and parallel to the freestream direction (*Figure 23*) [58]. With steady injection, the 45° case provided the greatest levels of attenuation which were around 10dB compared to around 5dB for the parallel flow cases [58]. These attenuation levels were reported for Mach 1.28 flow with mass injection levels of around $0.07\rho_\infty U_\infty$ [52]. This study [58] also investigated the effect of low frequency pulsed blowing between the ranges $0Hz<f<80Hz$ for the 45° inclined case and this was found to be as effective as the steady mass injection for attenuation of the cavity modes.

The majority of mass injection investigations use an array of zero net-mass flux actuators (synthetic jets) [59], micro-jets [60] or similar devices [52] mounted within the front wall with the injection direction orthogonal to the freestream flow direction. Typically, for devices where the mass flow rate can be varied, the highest attenuation levels occur for the higher mass flow rates through the actuators [48] [59]. Open-loop pulsed blowing has demonstrated no improvement in attenuation over constant steady blowing alternatives with both cases achieving around 10dB of peak attenuation [39] [52] [59] [60].

Dynamic or closed-loop approaches to active control require an additional level of complexity over the more simple open-loop alternatives which have been mentioned previously. Typically, a dynamic device receives feedback from a sensor located within the cavity, which allows the actuator to tune its attenuation to a prescribed mode or

frequency. This targeted approach brings the advantages of a greater range of conditions over which attenuation can be achieved as the system is able to compensate for changes to the cavity acoustic signature, such as the changes in frequency which occur as the freestream Mach number is varied. Also, the power requirements of dynamic systems are often lower than open-loop approaches due to the targeted attenuation approach [52].

The most frequent device used for closed-loop cavity control is the zero-net-mass-flux actuator (synthetic jet) type device. These devices are located within the forebody of the cavity model upstream of the cavity front wall and are usually driven by piezoelectric actuators [52] [61]. Compression drivers have also been tested as the source of dynamic control [62] where both devices affect the flow through the same zero-net-mass-flux mechanism. Peak attenuation levels of the order 10dB (Mach 0.275 [61]) to 25dB (Mach 0.43 [62]) have been demonstrated for closed loop systems with actuators located at the front wall of the cavity. Numerical simulation of a 2-D cavity under Mach 0.6 conditions also demonstrate peak reductions of around 13dB [53].

2.4.2 Pulsed flap actuators

The second major type of actuator for active control of cavity acoustics is a pulsed flap located on or close to the front wall of the cavity. Again, both open-loop and closed-loop approaches are available to the designer. Typically, the open-loop techniques force the shear layer at low relatively low frequencies which can be close to the Rossiter modes, whereas the closed-loop techniques rely on disrupting the phase relationships related to the Rossiter modal generation process. When the frequency of the flap actuator is of the same order as the characteristic vortex shedding frequency from the cavity front wall, the pressure fluctuations associated with the convection of vortices from the device can be set asynchronously to the pressure waves within the cavity. This process breaks down the feedback loop which is associated with the modal generation process and reduces the net power transfer from the cavity flow to the shear layer as the two flow fields are out of phase [55].

The most frequent type of pulsed flap actuator for both open-loop and closed-loop investigations is a piezoelectric unimorph (*Figure 24*). This device deflects when an electric current is applied and is relatively simple to install upstream of a cavity. An example of open-loop excitation at relatively low Mach number (M<0.1) provided around 13dB attenuation by forcing the shear layer at a frequency close to the dominant Rossiter modal frequency [63]. This attenuation level was accompanied by around a 20dB increase in the SPL at the forcing frequency.

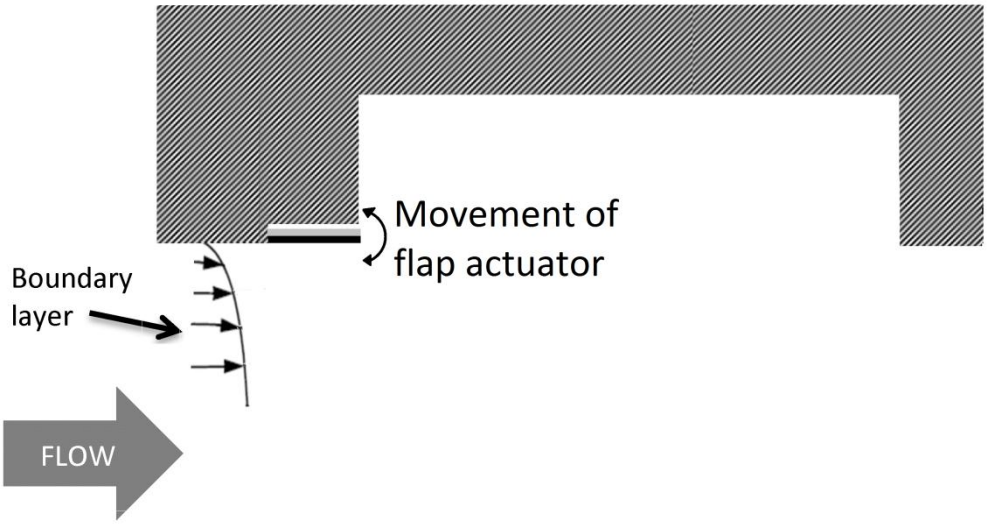

Figure 24 – Example of a piezo-electric actuator installed ahead of the cavity front wall

The amplification of the broadband noise at the forcing frequency is avoided for closed-loop control where the forcing frequency is related to the vortex shedding and not directly to the Rossiter frequencies. Peak attenuation levels of up to 20dB have been demonstrated for closed-loop systems at low Mach numbers (M<0.1) [63]. Experiments at the higher Mach number of Mach 0.6 have demonstrated peak attenuation levels of around 7dB at multiple modes simultaneously [54]. Above these Mach number ranges, stable operation of several of the control algorithms was not possible and therefore no attenuation could be achieved [64].

2.5 Summary of current cavity palliative technology

A brief review of active flow control concepts for the attenuation of cavity modes has been presented. This review provides background information for the current research to show how the levels of attenuation demonstrated within this body of work compare with other passive device, in-service devices, and the more complex active flow control techniques which have been investigated. For a full breakdown of the prior research into active flow control, both open loop and closed loop, the reader is directed to references [39], [52] and [55].

The most common and reliable device for both model-scale investigations and full-scale operation usage is a spoiler located upstream of the cavity front wall. Spoilers have typically provided the highest levels of peak attenuation under subsonic and transonic conditions, in the order of 20dB. However, spoilers may not be suited to supersonic operation where increases in modal amplitudes of up to 15dB for Mach 1.4 flows have been reported (*section 2.3.1*) [7].

2.6 Resonant absorbers in wider usage

This body of work aims to introduce a palliative into the cavity acoustic field which has previously received only limited attention. This palliative is to be an array of resonant absorbers. Resonant absorbers have been in use long before the concerns over cavity acoustics were known. This section provides a brief overview of the various other fields into which resonant absorbers have been adopted. Such devices are typically referred to as Helmholtz resonators after the German scientist and philosopher Hermann von Helmholtz who devised resonant devices to identify the tonal components of a complex sound [65].

The first recorded use of Helmholtz type absorbers dates back a further 2000 years and applies to ancient Greek and Roman amphitheatres [66] [67]. The Roman writer and architect Vitruvius, describes the placement of "εχεια" (echea) within theatres (*Figure 25*) [68] [69]. These devices or sounding vessels were made from pottery and took the form of tall vases known as amphorae. The tuning of the devices was achieved by filling the vessels with sand to effectively change their volume and therefore the resonant frequency. Attenuation could have been improved through the placement of liniment cloth or another porous material within the necks of the devices as this would increase the resistance of the device. The exact purpose of these devices has been the subject of much speculation [68], however, it is generally accepted that they were an attempt to control the echoes which occurred within the large stone built theatre structures of the time. The placement of the devices served to improve the intelligibility of the sound from the performers through the targeted attenuation of unwanted frequencies. It is interesting to note that the architects of the time realised that these devices were only required for the stone built structures which often created unwanted echoes, whilst the more flexible wooden structures did not exhibit such issues.

Returning to the modern era, resonant absorbers are still widely used to control noise and improve acoustic quality in public spaces and auditoria [50] [70]. Indeed, a wide variety of products are commercially available to treat wall and ceiling surfaces to improve speech intelligibility. Such devices can either be integral to the structure of a building, for example the Diffusor Blox ® concept [71] where a resonant device is formed out of masonry and built into a wall, or attached to the wall or ceiling as an aftermarket product [70]. Another major use of these devices is the broadcasting and recording industry [72], where it is important that reflections and echoes are controlled.

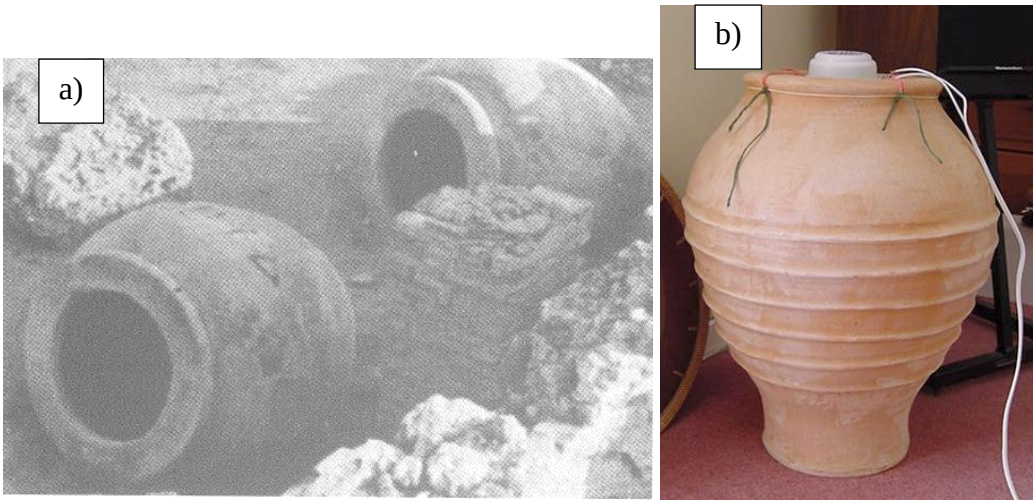

Figure 25 – a) Photograph of clay vessels found at an archaeological dig in a Sardinian theatre [68], b) Modern representation of an "echea" sounding vessel. [69]

The use of Helmholtz resonators for the control of unwanted pressure oscillations is not just restricted to the field of audio based acoustics. In modern gas turbine engines, high pressure pulsations may occur if the resonant frequencies of the system are excited [73]. These pressure fluctuations can lead to instabilities in the combustion process, which can reduce the operating range of some engines. If the combustion chamber is configured with an array of resonant absorbers the combustion instability conditions can be reduced [73] [74], the operating range can be extended. Interestingly the SPL of the instabilities reported are higher than those for room acoustics (SPL≈140dB for the gas turbine applications) and this level is close to that which is expected within the field of cavity acoustics. Therefore, this work with gas turbine combustors demonstrates that resonant absorbers are capable of providing attenuation under high SPL conditions similar to those within resonant cavity flows [74]. These contrasting applications for Helmholtz type absorbers demonstrate the versatility of their operation and provide preliminary support for their use within the high SPL environment of a resonant cavity.

The use of resonant type absorbers within gas turbine engines is not limited to the combustion chamber. Arrays are installed into the inside of the engine intake duct to absorb the discrete tones associated with the blade passing frequencies of the fan [75]. Such tones can reach intensities greater than 120dB [76]. Therefore, these liners also operate within a high SPL environment relative to room acoustic type applications. Typically, liners for aero-engines are formed from multiple layers of perforate separated by a backing volume. This backing volume is usually segregated by a honeycomb structure, which prevent higher frequency modes propagating within the device. The honeycomb structure also improves the attenuation of the modes which propagate in a direction orthogonal to the orifice axes. This grazing interaction of the modes with the liner is typical as the liners are installed around the circumference of the engine intake. The multiple layers of the device enable multiple frequencies to be attenuated from a

single installation. However a dual-layer device would require a greater depth to be available for its installation.

2.7 Modelling the generation of the high intensity unsteady pressure fluctuations

This section presents a summary of the underlying issues surrounding the use of open type cavities and two models which describe the modal generation process are presented. The first model, known as Rossiter's model, is the conventional approach used to describe the modal generation process and to predict the frequencies of the discrete modes within the acoustic spectrum. The second model, referred to as Delprat's approach, models the modal generation process as an amplitude modulation phenomenon. Crucially, Delprat's approach cannot be used to predict the modal frequencies independently of experimental work. Delprat's approach is supported under transonic conditions ($0.80<M<0.95$) for the first time by empirical data from the small scale ($1/40^{th}$) wind tunnel tests performed during this research. The same fundamental processes are behind both the Delprat approach and the more well-known Rossiter model. Each approach relies on vortices shed from the front wall of the cavity and upstream propagating pressure waves.

2.7.1 Summary of the acoustic spectrum within an open type cavity

Open-type cavity flows are a cause for concern to both aircraft and stores designers because of the high intensity modal characteristics which can occur. An example of a modal spectrum from an open type cavity is shown in *Figure 26* and the peak SPL values within an operational cavity can reach levels up to 160dB [88]. Despite the possible damage caused by the vibrations imparted to the cavity structures by the high intensity modes, open flow cavities remain in use because of their favourable pressure gradient conditions [2] over alternative closed flow cavities. Therefore, the alleviation of these undesirable unsteady flow characteristics is of paramount importance to improve stores lifespan.

The following sections discuss two approaches which can be used to explain the frequencies at which the modal peaks occur within an open flow cavity. The first approach to be discussed is perhaps the most well known and widely used approach and is attributed to Rossiter [1]. The second approach, attributed to Delprat [89], is less well known and uses signal processing techniques to link the frequencies within the cavity spectrum. This study provides the first experimental evidence in support of the second approach.

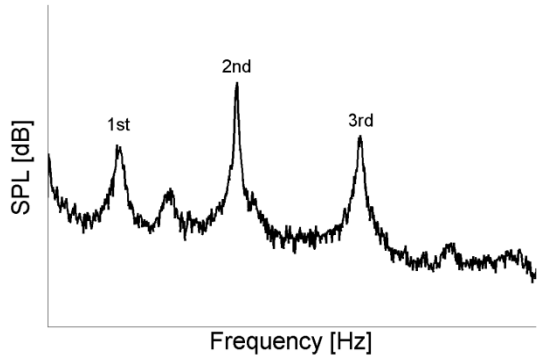

Figure 26 – Example of a typical modal spectrum for an open flow cavity

2.7.2 Rossiter's semi empirical model

Perhaps the most well known work related to cavity flows is the work carried out in 1966 by Rossiter [1]. This work (*Equation 3* to *Equation* 8) is best known for the introduction of the so called Rossiter equation which is used to predict the frequencies of the discrete modal peaks within the spectrum of an open flow cavity. This equation (*Equation 8*) still forms the basis for many predictive methods related to the frequencies of the modes within cavities to this day.

Rossiter's work is based on a series of experiments carried out using a resonant open flow cavity. The experiments comprised unsteady pressure measurements and shadowgraph imaging. From the unsteady pressure data, Rossiter noticed that the spectra contained discrete periodic components where the frequencies exhibited a series of the form m-α (where m=1, 2, 3… and α<1). In this instance Rossiter describes α as the phase lag between the impingement of a vortex and the propagation of pressure wave within the cavity. The frequencies of the discrete modal peaks, which this process creates, are inversely proportional to the cavity length and directly proportional to the freestream velocity. Dimensional analysis suggests that the frequency of the modes follows the relationship set out in *Equation 3*.

From the shadowgraph imagery Rossiter was able to determine that the underlying cause of the modal spectra was related to a feedback loop. This loop consists of the downstream convection of large scale vortical structures which are shed from the front wall of the cavity and the upstream propagation of pressure waves within the cavity (*Figure 27*). Rossiter proposed that the interaction of the vortices with the rear wall of the cavity produced the pressure waves and that the interaction of the pressure waves with the front wall of the cavity caused further vortices to be shed from the front wall. This therefore assumes that the frequency (f) of each event is equal (*Equation 4*), where the constants are: $U\infty$ = freestream velocity, k = ratio of vortex convection speed to freestream speed, λ_v = vortex spacing, V_p = pressure wave speed, and λ_p = pressure wave spacing (shown schematically in *Figure 28*).

Equation 5 relates the phase difference (α) between the arrival of a vortex at the rear wall and the upstream propagation of a pressure wave. *Equation 6* represents the distance that the pressure wave inside the cavity has travelled within the time between vortices (t' represents an arbitrary time). If t' is eliminated from *Equation 5* and *Equation 6* then the vortices, pressure waves and cavity modal frequencies are related by *Equation 7*. To produce the final formula (*Equation 8*) two main assumptions are required. The first assumption is that the cavity mode number (m) is the sum of the vortical and pressure wave mode numbers (i.e. $m=m_v+m_p$). The second assumption is that the pressure wave velocity equals the speed of sound (i.e. $V_p=a$). The second assumption was required as no information about the temperature difference between the freestream and the cavity was available and this assumption is further investigated in *section 2.7.3* which discusses modification made to the original Rossiter model.

Equation 8 provides a simple means for predicting the modal frequencies within a resonant cavity with only basic information about the cavity required (namely; cavity length (l), cavity depth (h), freestream velocity (U∞), and freestream Mach number (M)). Rossiter proposed a value of k=0.57 to provide the best agreement with experimental data and subsequent experimental investigations agree with this value provide a value of α=0.062l/h for the phase lag constant [17]. The following section (*section 5.1.1*) uses correlation analysis to measure the characteristic speeds of the vortices and pressure waves within the cavity flow. For cases at Mach 0.9 and 0.95 the measured values for the convection speed of the vortices over the freestream speed (k) compares favourably with the assumed value of 0.57 (*Table 18*).

$$\frac{\omega}{2\pi}\frac{l}{U_\infty} = f\left(M, \mathrm{Re}\right) \qquad \textbf{Equation 3}$$

$$f = \frac{kU_\infty}{\lambda_v} = \frac{V_p}{\lambda_p} \qquad \textbf{Equation 4}$$

$$m_v\lambda_v = l + \alpha\ \lambda_v + kU_\infty t' \qquad \textbf{Equation 5}$$

$$l = m_p\lambda_p + V_p t' \qquad \textbf{Equation 6}$$

$$\frac{kU_\infty}{U_p} m_p\lambda_p + \lambda_v\left(m_v - \alpha\ \right) = kl\left(M\frac{a}{V_p} + \frac{1}{k}\right) \qquad \textbf{Equation 7}$$

$$f = \frac{U_\infty}{l} \frac{(m-\alpha)}{\left(M + \frac{1}{k}\right)}$$

Equation 8

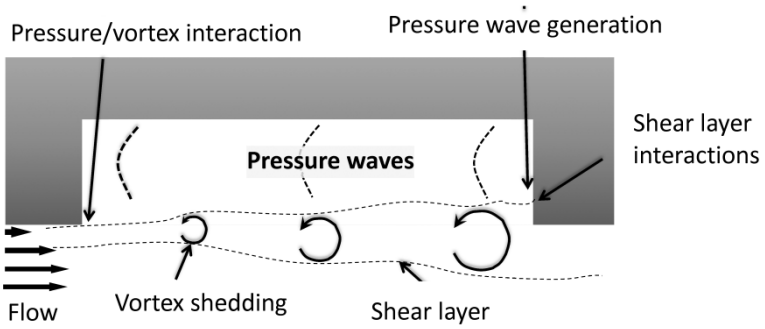

Figure 27 – Sketch of the underlying flow features contained within the feedback loop of a resonant cavity as described by Rossiter [1]

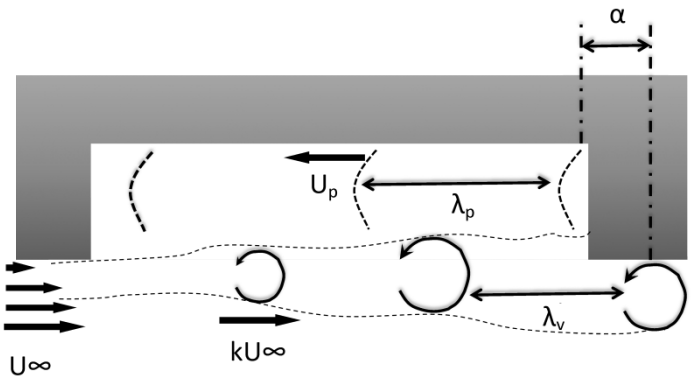

Figure 28 – Sketch demonstrating the significance of the constants used in the Rossiter equation. (N.B. α represents a temporal spacing)

2.7.3 Modified Rossiter equation

This section discusses modifications which have been proposed for the Rossiter equation (*Equation 8*) to improve the reliability at higher Mach numbers. The modified Rossiter equation (*Equation 9*) addresses the assumption that the speed of sound within the cavity equals the free stream sound speed, through the assumption that the cavity static temperature (T_c) is equal to the freestream stagnation temperature (T_0) [20]. This assumption can be made because the Mach number within the cavity is much lower than the freestream conditions and therefore the cavity static temperature is greater than the freestream static temperature, but not as a high as the freestream total temperature.

Under isentropic conditions the freestream stagnation temperature is equal to the freestream total temperature and can be related to the sound speed and Mach number through the relations set out in *Equation 10* and *Equation 11*. *Equation 12* demonstrates how the stagnation temperature relationship can be used to calculate the Mach number (M_0) based on the cavity static temperature (T_c), where $T_c = T_0$. This Mach number (M_0) is calculated based on the ratio of the sound speed within the cavity (a_0) and in the freestream (a). The final form of the modified Rossiter equation is shown in *Equation 9* and relates the modal frequencies to the freestream Mach number (M). The reliability of this modified form is discussed in conjunction with the results from the small scale transonic wind tunnel tests in *section 5.1*.

$$f = \frac{U_\infty}{l}\frac{(m-\alpha)}{M_0+\frac{1}{k}} = \frac{U_\infty}{l}\frac{m-\alpha}{\frac{M}{\left(1+\left(\frac{\gamma-1}{2}M^2\right)\right)^{\frac{1}{2}}}+\frac{1}{k}} \qquad \textbf{Equation 9}$$

$$\frac{T_0}{T} = \left(\frac{a_0}{a}\right)^2 = 1+\left(\frac{\gamma-1}{2}M^2\right) \qquad \textbf{Equation 10}$$

$$\left(\frac{T_0}{T}\right)^{\frac{1}{2}} = \frac{a_0}{a} = \left(1+\left(\frac{\gamma-1}{2}M^2\right)\right)^{\frac{1}{2}} \qquad \textbf{Equation 11}$$

$$M_0 = \frac{U_\infty}{a_0} = \frac{\frac{U_\infty}{a}a}{a_0} = \frac{Ma}{a_0} = \frac{M}{\left(1+\left(\frac{\gamma-1}{2}M^2\right)\right)^{\frac{1}{2}}} \qquad \textbf{Equation 12}$$

2.7.4 Delprat's amplitude modulation approach

Recent studies have investigated the Rossiter equation (*Equation 9*) as well as the modal generation process within resonant cavities based on a detailed analysis of the unsteady pressure field. The aim was to establish a link between the underlying flow features and the Rossiter frequencies for different flow conditions to those investigated within this work [89] [90] [91]. These works considered a modal generation process based on the principle of amplitude modulation and it was proposed that within the cavity flow there are two discrete frequency components [89].

The first is a high-frequency fundamental aero-acoustic loop frequency (f_a) [89] and the second is a low-frequency modulating signal (f_b). The loop frequency, f_a is related to the sum of the time for the shed vortices to convect from the front to the rear wall of the cavity (T_v) and the time for the instigated pressure wave to travel from the rear wall to the front wall of the cavity (T_p). In this work, the characteristic time lags associated with the disturbances within the cavity are presented in non-dimensional form ($T^*=T/t_{ref}$). The non-dimensionalising factor (t_{ref}) was calculated as the freestream travel time over one cavity length (l (*Fig. 1*)) ($t_{ref}=U_\infty/l$). Overall, the loop frequency is defined in terms of the combined time for both vortex convection and pressure propagation i.e. $f_a=1/T_a$, where $T_a=T_v+T_p$. This loop frequency (f_a) can also be calculated by *Equation 9* with the constants m=1 and α=0.

However, the source of the modulating frequency f_b is yet to be confirmed although it was proposed that it is a sub-harmonic of f_a with the relation $f_b \approx 0.5 f_a$ [89] [90]. The amplitude modulation process can produce the Rossiter frequencies (f_n, n=1,2,3…) using the relations set out in *Equation 13* to *15*.

$$f_1 = f_a - f_b \qquad \textbf{Equation 13}$$

$$f_2 = 2f_a - f_b \qquad \textbf{Equation 14}$$

$$f_3 = 3f_a - f_b \qquad \textbf{Equation 15}$$

Previous work has demonstrated that the modal peaks within an unsteady cavity spectrum can be related through this amplitude modulation method [89] and this approach has also been used to identify the source of peaks within a spectrum [91].

However, this current study aims to provide fundamental empirical evidence of the process behind the modal generation. This study strives to confirm the process behind the creation of f_a and to provide evidence that both f_a and f_b are present within the cavity flow field. Neither of these factors have previously been demonstrated experimentally under high transonic conditions (0.80<M<0.95). The modal characteristics of the datum small scale (1/40th) Build 1 cavity under transonic conditions are investigated using

correlation analysis to provide experimental values for the fundamental loop frequency (f_a) and to demonstrate supporting evidence for the amplitude modulation process.

2.7.5 Analytical modelling of the waveforms within the cavity

Within the cavity a wave form similar to that exhibited by standing waves is exhibited [117]. Whereby, the modal amplitudes vary with position within the cavity (x/l). This is due to both constructive and destructive interference which cause pressure nodes and anti-nodes. Pressure is at its maximum at an anti-node. Simple semi-empirical models exist which can calculate this pressure profile based on the SPL at the rear wall (SPL_{RW}). The semi-empirical model which is used to calculate the modal pressure profiles within the current body of work is given in *Equation 16*. Where a_n is a mode dependant constant with the values of 3.5, 6.3, and 10 for the first, second and third modes respectively [117].

Equation 16

$$SPL(\frac{x}{l}) = SPL_{RW} - 10\left(2 - \frac{x}{l} - \left|\cos\left(a_n \frac{x}{l}\right)\right|\right)$$

2.8 Innovation to the previous body of knowledge

The current body of work aims to improve the current state of the art in four specific areas, which are discussed below. These innovations are not limited to the use of palliatives for the control of the cavity modes, but also include more fundamental aspects of the cavity flowfield, such as the modal generation process and modal intermittency.

- This study provides experimental evidence in support of the use of resonant arrays as cavity palliative devices under both transonic and supersonic regimes. Attenuation from resonant arrays has not previously been demonstrated under either of these flow conditions. The cases of attenuation under supersonic conditions represent an improvement to the current state of the art as typically passive palliatives do not provide large attenuation under supersonic conditions and in some cases can exacerbate the problematic acoustic modal peaks.

- Typically, resonant array type palliatives are used for attenuation in low to medium SPL environments and not the high SPL environment within a cavity. Therefore, an assessment of how the high SPL (SPL>150dB) operating environment within a cavity is conducted to provide a semi-empirical update to the analytical model used for the design of the proposed palliative devices.

- A link between the cavity modal frequencies and the fundamental characteristics of the cavity flow environment is presented. This section of the research contributes to a better understanding of the underlying flow physics within open cavity flows.

There is little work on this in the current published literature and therefore, it was important to investigate this relationship.

- Previous studies of the performance of active control systems have linked the amplification of non-targeted modes with the intermittency of the modal system with respect to time. The current research aims to provide evidence in support of this link through the use of short time Fourier analysis.

3 Experimental methods

This section will describe all of the experimental facilities and operating procedures used within this study. The facilities can be categorised into two types, the first are the wind tunnels and the second are the impedance tubes. The wind tunnel facilities were used to directly measure the palliative performance within a cavity environment and also to investigate the underlying process behind the modal generation. The impedance tube facilities were used to measure the acoustic properties of the palliative devices and also to provide feedback about the reliability of the analytical model used for the palliative design.

3.1 Cranfield University 2.5" transonic wind tunnel

The majority of the wind tunnel investigations were conducted using the Cranfield University 2.5" tri-sonic wind tunnel. This facility provided a useful small scale cavity model and enabled many test configurations to be investigated within a short time scale.

The tunnel is an open circuit, intermittent facility with the test section connected to a $40m^3$ vacuum tank through a diffuser. The flow Mach number is controlled through the use of contoured liners combined with a downstream throttle (*Figure 30*). This throttle controls the mass flow rate through the working section and provides a simple means of Mach number setting. The tunnel is able to achieve Mach numbers across the range 0.4 to 3.0 which covers the transonic region of interest (Mach 0.8 to Mach 0.95). Within the working section the static pressure along the upper liner has been measured and the ratio of these static pressures to the total pressure measured in the upstream settling chamber can be used to calculate the Mach number at the tap locations within the working section. A typical Mach number profile within the working section for Mach 0.80, 0.90, and 0.95 cases are shown in *Figure 29*, where the cavity location is marked by the vertical dashed lines. Over the working section the maximum deviation of the Mach number from the required level is less than ±0.02, which means this tunnel is suitable for the proposed cavity tests.

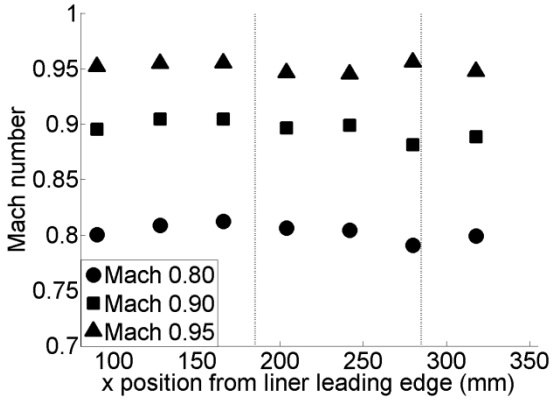

Figure 29 – Mach number profiles over the upper liner of the Cranfield University 2.5" wind tunnel

However, due to the profile of the supersonic liners they are unsuitable for use with either cavity build and therefore no supersonic testing can be conducted within the Cranfield facility. To run the tunnel atmospheric air is passed through an alumina drying bed to avoid condensation before entering the tunnel settling chamber. The continuous stable run time for the tunnel at Mach 0.9 was approximately 30s. After an initial settling time of approximately 3s the unsteady pressure data were acquired over a typical sample period of 3s.

The test section is formed by both an upper and contoured lower liner which are bound on either side by optical windows. The lower liner is inclined to alleviate the growth of the boundary layer in the working section and the surface is also perforated with 13% porosity leading to a ventilated plenum cavity [77]. For the reference working section, without the cavity installed, the pressure gradient over the region of interest was 13 Pa/mm at Mach 0.9.

The model cavity has a length (l) of 100 mm and a depth (h) of 20 mm which provides a longitudinal aspect ratio (l/h) of 5 (Figure 34.). At the Mach numbers of interest (Mach 0.8, 0.9 and 0.95) this places the cavity within the open cavity classification. The cavity width is 25 mm which gives a width to depth aspect ratio (w/h) of 1.25. The cavity is estimated to be a $1/40^{th}$ scale model of a full sized cavity (based on an estimated full size weapon bay length of 4m (see *section 5.10*).

3.1.1 Cavity builds description

Two cavity builds were available for experimental investigations. Both cavity builds share the same overall dimensions and transducer locations (*Figure 34*). However, the position of the cavity within the tunnel working section is different for the two builds (*Figure 30*).

Build 1 was previously designed to house the cavity within the upper liner of the wind tunnel working section (*Figure 30* and *Figure 31*) [34]. *Build 1* allowed for the performance of arrays to be assessed for both front and rear wall cases only.

Build 2 was designed to investigate the effectiveness of resonant arrays in the sidewalls and ceiling of a cavity as well as the front and rear walls. The space surrounding the *Build 1* cavity was insufficient to house resonant array installations in the sidewall and ceiling. Therefore, to support these investigations the cavity was re-located to the sidewall of the wind tunnel working section in *Build 2* (*Figure 32*, and *Figure 33*). To ensure similar spectral conditions between both cavity builds it was important that both cavities were located at the same axial position within the tunnel working section. This ensured that the approaching boundary layer for each build had the same distance over which to grow and also ensured that both cavities experienced the same pressure gradient over the cavity length. A general assembly diagram and description of Build 2 are provided in *Appendix A* and the validation analysis of the Build 2 cavity is included in *Appendix B.*

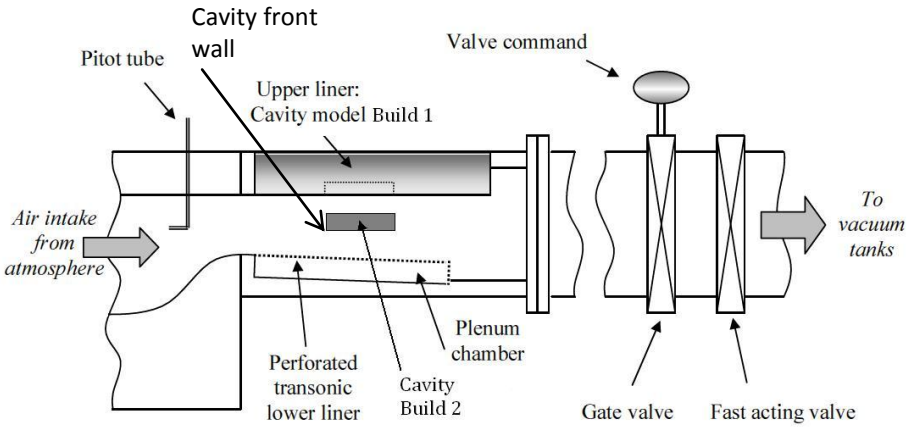

Figure 30 – Schematic of the Cranfield University 2.5" wind tunnel showing the locations of cavity *Builds 1* and *2*.

Figure 31 – Build 1 cavity in upper liner of wind tunnel working section (with 1δ spoiler installed at front wall)

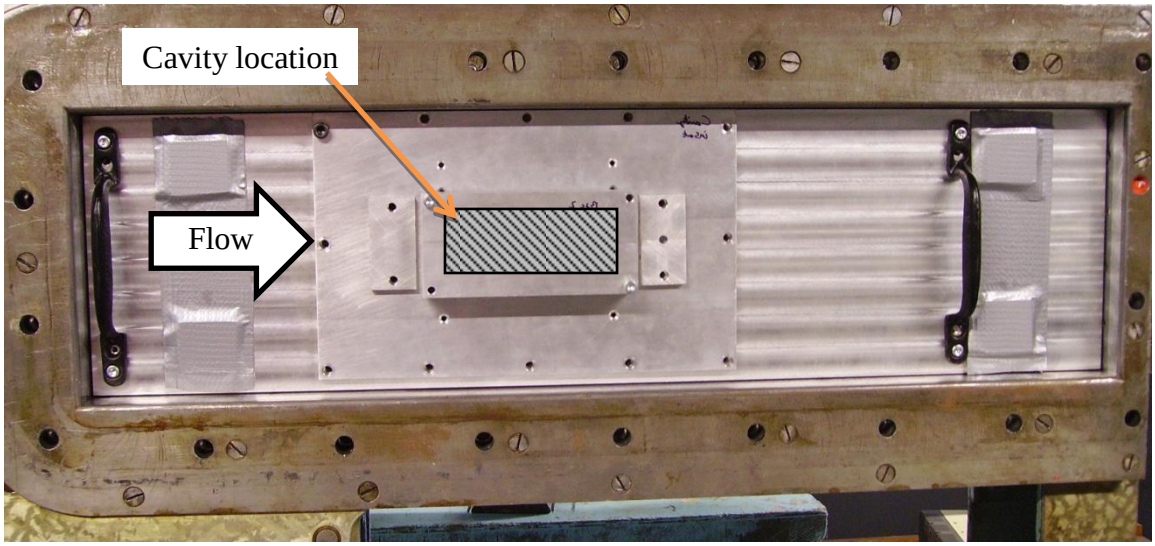

Figure 32 – Build 2 installed into cavity working section side wall

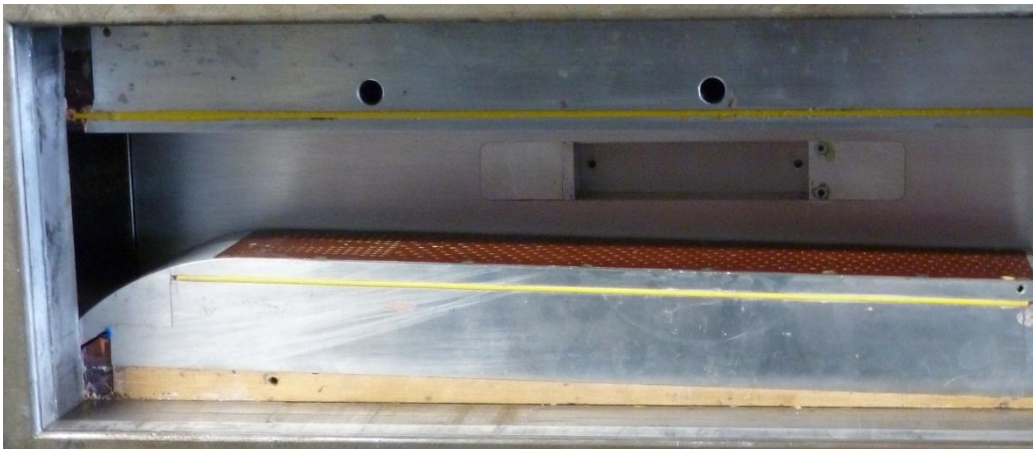

Figure 33 – View of the Build 2 cavity installed into cavity working section side wall

3.1.2 Instrumentation and measurement techniques

The settling chamber total pressure (P_0) was measured using a Setra 239 0.5 psi differential transducer and the working section static pressure (P_{stat}) was measured using a Druck PDCR22 15 psi differential transducer. The operating Mach number was calculated from the total pressure (P_0) in the upstream settling chamber and the static pressure (P_{stat}) in the test section. The loss in total pressure from the settling chamber to the working section has been shown to be negligible (below measurable levels) for flows at Mach 0.8 and Mach 0.9 [31].

The unsteady pressure measurements within the cavity were taken using Kulite XCS-190-15A absolute pressure transducers. The locations of the transducers within the cavity are shown in *Figure 34*. When a resonator array was positioned either in the cavity front wall (FW) or rear wall (RW) it was not possible to locate a transducer at that location and a transducer was placed at the opposite wall. However, the transducers on the cavity ceiling (numbers 2,3) were always present, where transducer number 3

was used as the reference location (*Figure 34*). Further unsteady pressure measurements were taken in the absence of the cavity at a position equivalent to a cavity location of x/l=0.64. This was achieved using an unsteady transducer (Kulite XCS-190-15A) mounted flush to the upper liner of the wind tunnel working section. The aim of this measurement was to demonstrate that all of the characteristics within the cavity spectra were due to the modal generation process and not the result of spurious noise within the tunnel working section.

The transducer output was amplified using a gain of 20 and filtered at 40 kHz using a Fylde 251UA filter module. The unsteady pressure transducers were sampled through a 16-bit NI PCI-6225 DAQ card at 80 KHz to obtain 2^{18} (262144) samples. The data were then split into 31 blocks of 2^{14} (16384) samples with a 50% overlap and a resultant frequency resolution of 4.8 Hz. Each block was windowed using the Hanning function and then analysed using a fast Fourier transform. An ensemble average of the 31 blocks was then calculated to produce the spectral data.

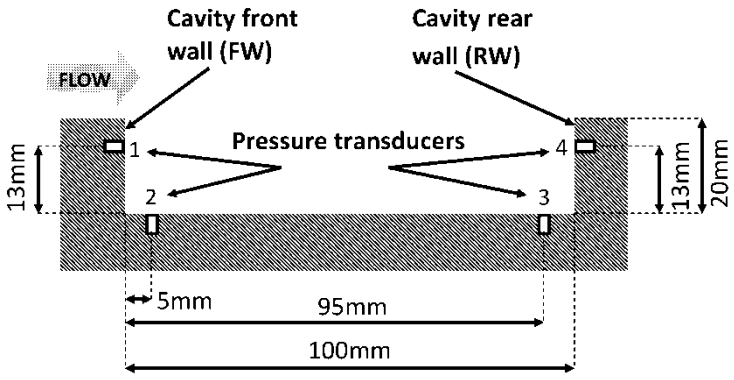

Figure 34 – Sketch of unsteady pressure instrumentation positions within Cranfield cavity (not to scale).

3.1.3 Boundary layer analysis

3.1.3.1 Cavity Build 1

The boundary layer over the top liner of the test section was measured by traversing a flat headed Pitot probe (*Figure 35*) in the absence of the cavity at a location $\Delta x/l=0.36$ behind the nominal cavity front wall position. Total pressure measurements were taken with a resolution of 0.3mm. The measured non-dimensionalised boundary layer profiles are shown in *Figure 36* and the characteristics are presented in *Table 1*. Density variations over the boundary layer thickness were accounted for. To estimate the density at each location the static temperature for each location was calculated from the isentropic relationship between the calculated Mach number (M) and the static temperature (T) (*Equation* 17), where it was assumed that T_0 was equal to the ambient total temperature. It was assumed that the ratio of local static temperature (T) to the freestream static temperature (T_∞) was equal to the ratio of the local density (ρ) and the freestream density (ρ_∞) (*Equation* 18). Therefore, the local density could be estimated as a ratio of the freestream value and this ratio was used directly to calculate the integral parameters. The integral parameters of displacement thickness (δ^*) and momentum thickness (θ) were calculated numerically using *Equation* 19 and *Equation* 20. The velocity was derived from the relationship shown in *Equation 21* which required the Mach number and static temperature at each probe location.

$$\frac{T_0}{T} = 1 + \frac{\gamma - 1}{2} M^2 \qquad \textbf{Equation 17}$$

$$\left(\frac{T}{T_\infty}\right)^{\frac{\gamma}{\gamma-1}} = \left(\frac{\rho}{\rho_\infty}\right)^{\gamma} \qquad \textbf{Equation 18}$$

$$\delta^* = \int_0^\infty \left(1 - \frac{\rho U}{\rho_\infty U_\infty}\right) dy \qquad \textbf{Equation 19}$$

$$\theta = \int_0^\infty \frac{\rho U}{\rho_\infty U_\infty}\left(1 - \frac{U}{U_\infty}\right) dy \qquad \textbf{Equation 20}$$

$$U = M\left(\gamma R T\right)^{\frac{1}{2}} \qquad \textbf{Equation 21}$$

It was assumed from the shape factor ($H=\delta^*/\theta$) and approaching Reynolds number per metre ($Re_m=\rho Ul/\mu$, where l=1m) that the boundary layer was naturally turbulent during this entire test. The Reynolds numbers (Re_m) are also consistent with previous work carried out on rectangular cavities [9] although Reynolds number has been shown not to affect the acoustic characteristics of the flow field [78]. The ratio of the cavity depth to the approaching boundary layer thickness (h/δ) lies in the middle of the range for previous studies with the length to boundary layer thickness ratio satisfying the condition $l/\delta > 6$ for a resonant cavity [79]. A thick turbulent boundary layer can effectively damp out the pressure oscillations within a cavity. However, the current test cavity has been shown to exhibit modal characteristics at the calculated Rossiter frequencies [49]. The modal characteristics of the Build 1 cavity are discussed in *Section 5.1*.

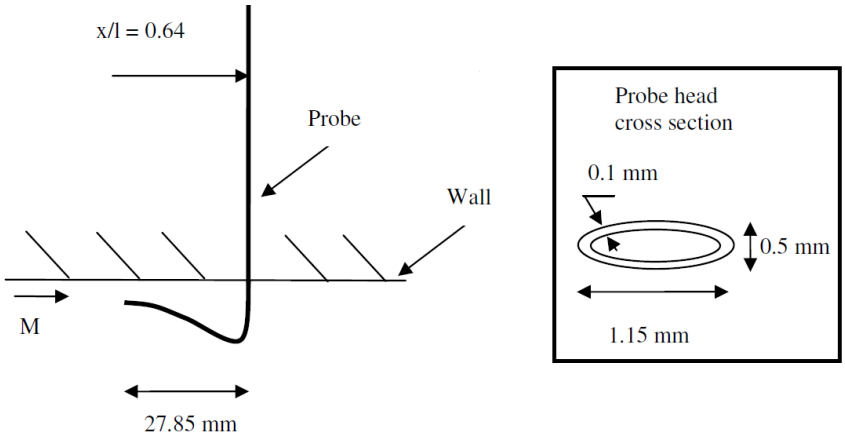

Figure 35 – Characteristic dimensions of the flat headed Pitot probe used for the boundary layer measurements.

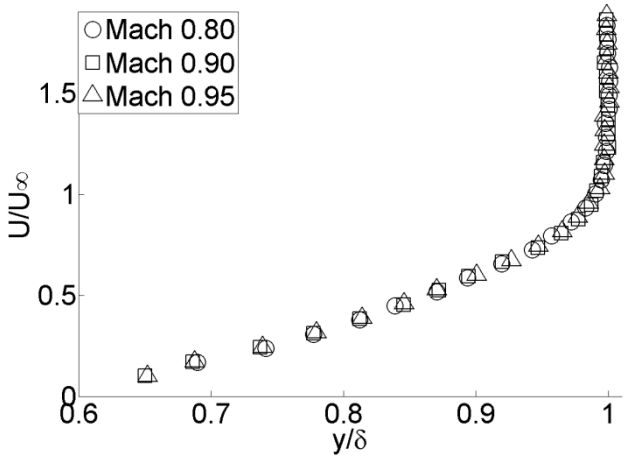

Figure 36 – Non-dimensional boundary layer profiles over the upper liner within the Build 1 working section at Mach 0.80, 0.90, and 0.95.

Mach number	δ_{99} (mm)	δ^* (mm)	θ (mm)	H	h/δ	l/δ	Re_l
0.80	3.55	0.495	0.339	1.46	5.63	28.2	$1.9x10^7$
0.90	3.54	0.492	0.330	1.48	5.65	28.2	$2.1x10^7$
0.95	3.53	0.490	0.328	1.49	5.67	28.3	$2.2x10^7$

Table 1 – Cranfield University 2.5" transonic wind tunnel working section properties for Build 1

3.1.3.2 Cavity Build 2

The boundary layer over the side wall of the tunnel working section was also measured by traversing a flat headed Pitot probe in the absence of the cavity. For the side wall the measurement was taken at a position 95mm behind the nominal cavity front wall location. The measured boundary layer characteristics are given in *Table 2* and it was again assumed from the shape factor (H<1.8 [80]) and approaching Reynolds number (Re_l) that the boundary layer over the tunnel side wall was attached and naturally turbulent during the entire test. In similarity to Build 1 the ratio of the cavity depth to the approaching boundary layer thickness (h/δ) lies in the middle of the range for previous studies with the length to boundary layer thickness ratio satisfying the condition $l/\delta > 6$ for a resonant cavity [79]. The modal characteristics of the Build 2 cavity are discussed in *Appendix B.*

Mach number	δ_{99} (mm)	δ^* (mm)	θ (mm)	H	h/δ	l/δ	Re_l
0.80	4.98	0.761	0.515	1.47	4.02	20.1	$1.9x10^6$
0.90	4.67	0.739	0.492	1.50	4.28	21.4	$2.1x10^6$
0.95	4.63	0.741	0.487	1.52	4.32	21.6	$2.2x10^6$

Table 2 – Cranfield University 2.5" transonic wind tunnel working section properties for Build 2

3.1.4 Uncertainty analysis

The wind tunnel Mach number was calculated from the ratio of the total pressure in the settling chamber (P_0) to the local static pressure in the working section (P_{stat}). The uncertainty of the Mach number comprised systematic and random components such as the calibration uncertainty, resolution of the sampling system, number of samples, and transducer accuracy which were combined following the approach of quadrature [81]. Overall, the total uncertainty on the working section Mach number is evaluated to be ±0.01. The uncertainty of the unsteady pressure measurements also depends on both systematic and random components. The data were sampled through a 16-bit DAQ card which discretized the voltage inputs over the 10 V sampling range into 2^{16} samples.

The overall uncertainty for the OASPL readings including calibration uncertainty, resolution of the sampling system, number of samples, transducer accuracy, and repeatability was found to be ±0.4dB. The uncertainty in the SPL distributions took into account the effect of the ensemble averaging using the standard deviation of the mean

over the 31 blocks used in the ensemble. For a typical modal peak (around 2 kHz) the uncertainty of the SPL magnitude was estimated to be ±2.6dB. This is coupled with a frequency resolution of 4.8Hz from the post processing procedure. The analysis of the uncertainty is shown in *Appendix C* along with a worked numerical example.

The measurement of the boundary layer thickness was estimated to have an uncertainty of ±0.1mm taking into account systemic uncertainties from the micrometer and callipers used.

3.2 AFRL Tri-sonic Gas dynamics Facility

As part of the investigation into passive flow control devices a small amount of wind tunnel testing was also completed using the ADDICT cavity model installed into the Tri-sonic Gas Dynamics Facility (TGF) at Wright Patterson Air Force Base in the USA. This facility provided a larger scale cavity model ($1/20^{th}$ scale) and also the ability to test at supersonic Mach numbers (Mach 1.5) [30] [82].

3.2.1.1 Medium scale wind tunnel description

The TGF is a closed circuit wind tunnel (*Figure 37c*) and is capable of Mach numbers between Mach 0.23 and 3.0 through the use of contoured nozzle blocks. The tunnel operating pressure ranges from 0.5 to 2.0 atmospheres, but is limited by the operational Mach number and the tunnel stagnation temperature is typically held between 297K and 311K. The test section is 0.61m high and 0.61m wide with a length of 1.22m and has optical access to both sides (*Figure 37b*).

The model cavity has a length (l) of 216 mm and a depth (h) of 38 mm (*Figure 38*) which provides a longitudinal aspect ratio (l/h) of 5.68. At the Mach numbers of interest (Mach 0.7 and 1.5) this places the cavity within the open cavity classification. The cavity width is 64 mm which gives a width to depth aspect ratio (w/h) of 1.7. The cavity is estimated to be a $1/20^{th}$ scale representation of a full sized cavity (based on an estimated cavity length (l) of 4m for a full scale cavity). The cavity is housed in a separate model which is supported by a crescent mounted sting and model pitch can be varied from -1° to +18.5° and roll can be varied between -90° to +180° [30] (*Figure 37*). The model has a 178mm forebody in front of the cavity onto which a row of 1mm diameter trip dots was placed at a distance of 25mm from the model leading edge. These dots were to ensure that the approaching boundary layer was both attached and turbulent in nature.

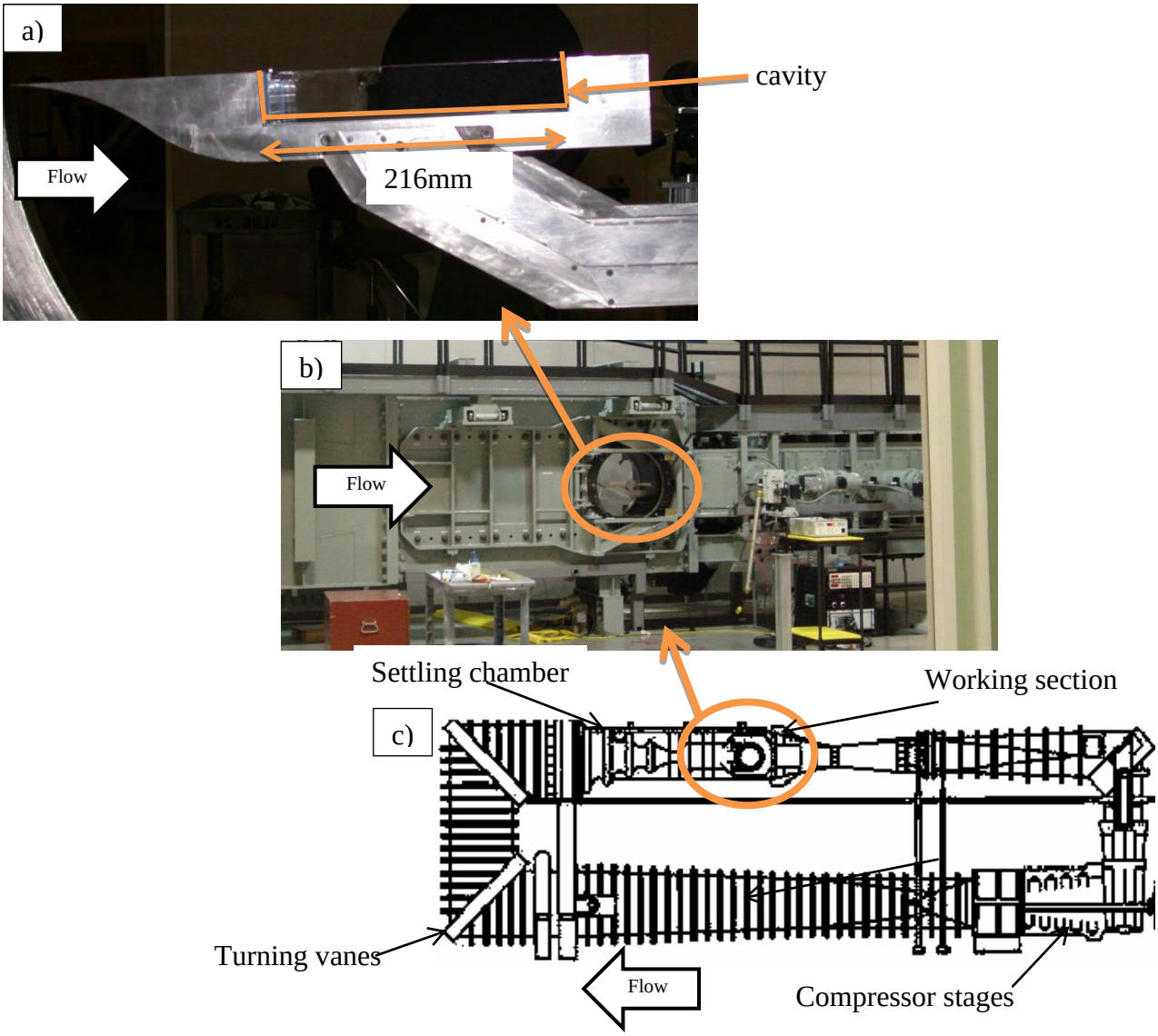

Figure 37 – a) ADDICT cavity model installed into TGF, b) TGF working section, a) Schematic diagram of TGF [83]

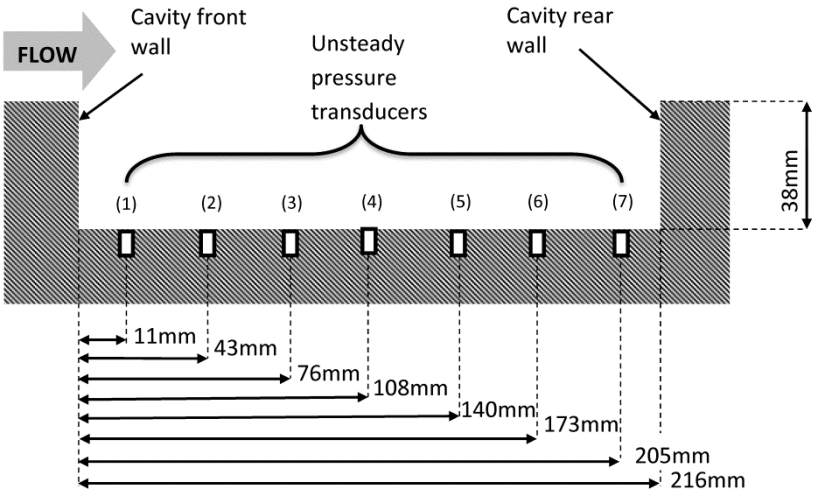

Figure 38 – Sketch of unsteady pressure instrumentation positions within ADDICT cavity model (not to scale).

3.2.1.2 Instrumentation and measurement techniques

The cavity ceiling housed 7 Endevco 8507c-2 differential dynamic pressure sensors with a range of 13.79kPa (2psig) and their locations within the cavity are shown in *Figure 38* and given in *Table 3*. The cavity ceiling also housed 3 static pressure ports and two thermocouples. The locations of these measurement positions are given in *Table 4*.

Dynamic pressure data are acquired through a proprietary 16-bit high speed data system known as Whisper. This system can provide simultaneous sample and hold acquisition at a rate of 75kHz for data records of 2s in length. The dynamic pressure sensors are also calibrated in situ and have a manufacturer stated uncertainty of 1.0% FS.

Temperature data were sampled at 1kHz and the mean was recorded at 5Hz through a National Instruments DAQ card. Static pressure was acquired through a Pressure Systems Model 8400 Scanner at 100Hz and the mean was recorded at 5 Hz. Both the static pressure and temperature sensors are calibrated in situ and have an uncertainty of 0.1% FS.

The TGF also allows for digital images to be acquired simultaneously to the pressure data. A Photron FASTCAM SA1 was used to capture the images and the process is coordinated by a trigger signal sent from the dynamic pressure acquisition system [82]. This camera setup is coupled with a two colour schlieren system that can record disturbances within the internal cavity flow.

Transducer	x/l	y/h	z/w
1	0.05	-1.00	0.00
2	0.20	-1.00	0.00
3	0.35	-1.00	0.00
4	0.50	-1.00	0.06
5	0.65	-1.00	0.00
6	0.80	-1.00	0.00
7	0.95	-1.00	0.00

Table 3 – Locations of the dynamic pressure transducers within the generic 1.20th scale cavity model

Transducer	x/l	y/h	z/w
Static 1	0.25	-1.00	0.00
Static 2	0.50	-1.00	0.06
Static 3	0.75	-1.00	0.00
Thermocouple 1	0.15	-1.00	0.00
Thermocouple 2	0.90	-1.00	0.00

Table 4 – Locations of the static pressure and temperature measurement locations within the generic 1.20th scale cavity model

3.2.1.3 TGF uncertainty analysis

The uncertainty of the Mach number comprised systematic and random components such as the resolution of the sampling system, number of samples, and transducer accuracy which were combined following the approach of quadrature [81]. Overall, the total uncertainty on the working section Mach number is evaluated to be ±0.004, which is around 0.6% at Mach 0.70. The uncertainty of the unsteady pressure measurements also depends on both systematic and random components.

The overall uncertainty for the OASPL readings including the resolution of the sampling system, number of samples, transducer accuracy was found to be ±0.16dB. The uncertainty in the SPL distributions took into account the effect of the ensemble averaging using the standard deviation of the mean over the blocks used in the ensemble. For a typical modal peak the uncertainty of the SPL magnitude was estimated to be ±3.7dB. This is coupled with a frequency resolution of 19Hz from the post processing procedure. As only one repeat run was conducted for the main cases there is insufficient data to comment on the repeatability of the facility. This analysis is presented in full in *Appendix C*.

3.3 Impedance tube testing

Impedance tubes allow the absorption coefficient of an acoustic absorber to be measured experimentally. This is beneficial for two reasons. Firstly, the wind tunnel results do not provide any feedback into the analytical models used for the array tuning (see *section 4.2*) as a peak SPL reduction in the wind tunnel results is not equivalent to an absorption coefficient. Thus having an experimental value for the absorption coefficient enables the reliability of the analytical model to be investigated. Secondly, using an impedance tube enables resonator arrays to be tested at frequencies that do not have to be related to the modal frequencies experienced in the wind tunnel. For example, the effectiveness of an absorber at the much lower frequencies expected in full sized weapons bays can therefore be obtained.

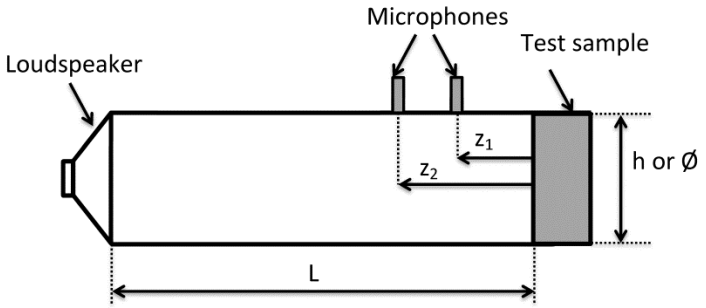

Figure 39 – Schematic of a typical impedance tube using the two microphone technique

3.3.1 Large scale, medium SPL impedance tube

The large scale impedance tube is 6.1 m long and has a cross section of h=0.5 m (*Figure 39* and *Table 5*). The walls are constructed of thick concrete to prevent absorption caused by the vibration of the structure (*Figure 40*). The sound was input into the tube through a FANE Colossus 18B 600 W loudspeaker installed at one end of the tube. The test sample was secured to the opposite end of the tube to the loudspeaker. White noise was generated by a Brüel and Kjær Type 1405 noise generator and then amplified with a Marantz PM711 AV sound amplifier before being output by the speaker.

The data was sampled through two Brüel and Kjær 4190 microphones which were mounted flush to the upper tube wall. These were connected to a Brüel and Kjær Type 2609 amplifier before being connected to a PC through an NI PCI-5124 data acquisition card. The sampling rate was 20 kHz and 10000 samples were recorded. The average of 20 readings was taken and after 10 readings the microphone positions and channels were swapped to eliminate any instrumentation bias as per BS EN ISO 10534-2 [84]. The distance between the microphones was set for each frequency to give to the best definition of the data. Lower frequencies required a larger distance between the microphones to account for the longer wavelength. Typically z_2 was increased from 707mm to 907mm (*Table 5*).

Figure 40 – End cap containing resonant array for large scale impedance tube

Dimensions	
L (mm)	6100
h (mm)	500
z_1 (mm)	507
z_2 (mm)	707

Table 5 – Dimensions for the large scale impedance tube (refer to *Figure 39*)

3.3.2 Medium scale, medium SPL impedance tube

The impedance tube is formed from a section of steel tubing with flanged ends (*Figure 41*). The heavy construction is necessary to prevent absorption of sound from the vibration of the structure and the flanges are required to secure the test samples to the end of the tube (*Figure 41*). The tube has a 70x70mm square cross section and allows measurement using the two-microphone technique [85]. The defining dimensions are given in *Figure 39* and *Table 6*.

To generate the absorption coefficient profiles the two-microphone or transfer function method of data processing was used [85]. This method calculates the fast Fourier transform of the data set to analyse the frequency content and then uses the ratio of the sampled voltages from the microphones to yield the absorption coefficient and the impedance. All of the experimental work will be carried out following the recommendations from BS EN ISO 10534-2 [85] and should result in a maximum uncertainty of the magnitude of the measured absorption coefficient of ± 1%.

Firstly, the transfer function for the incident (H_I) (*Equation 22*) and reflected (H_R) (*Equation 23*) waves are calculated where s=z1-z2 (microphone separation distance) and k_0 is the wavenumber. The transfer function for the total sound field (H_{12}) is calculated from the complex pressures at the two microphone positions (*Equation 24*). From *Equation 24* the reflection factor (r) can be calculated using *Equation 25* and this can be converted to the absorption coefficient (α) using *Equation 26*.

$$H_I = \frac{P_{2I}}{P_{1I}} = e^{-ik_0(z_1 - z_2)} = e^{-ik_0 s}$$ **Equation 22**

$$H_R = \frac{P_{2R}}{P_{1R}} = e^{ik_0(z_1 - z_2)} = e^{ik_0 s}$$ **Equation 23**

$$H_{12} = \frac{P_2}{P_1} = \frac{e^{ik_0 z_2} + re^{-ik_0 z_2}}{e^{ik_0 z_1} + re^{-ik_0 z_1}}$$ **Equation 24**

$$r = \frac{H_{12} - H_I}{H_R - H_{12}} e^{2ik_0 z_1}$$ **Equation 25**

$$\alpha = 1 - |r|^2$$ **Equation 26**

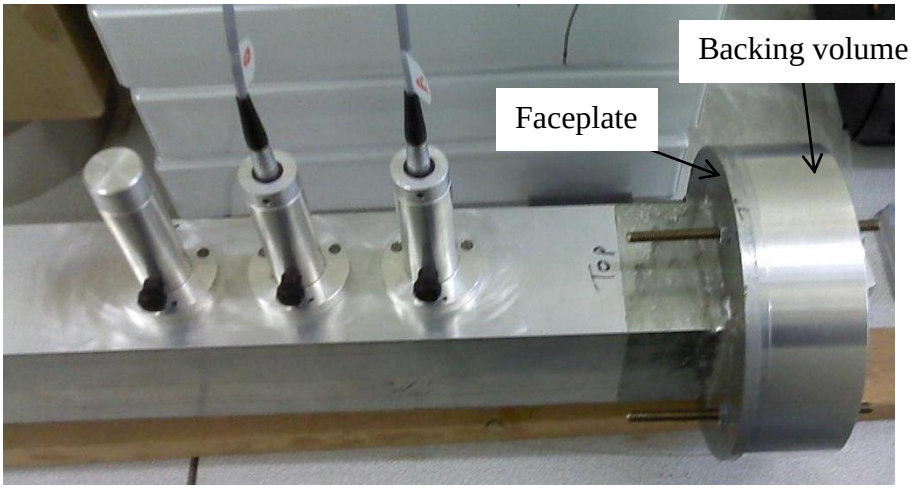

Figure 41 – Microphone positions and test sample for medium scale impedance tube

Dimensions	
L (mm)	2300
h (mm)	70
z_1 (mm)	150
z_2 (mm)	215

Table 6 – Dimensions for the medium scale impedance tube (refer to *Figure 39*)

3.3.3 Small scale, high SPL impedance meter

The high SPL impedance tube testing was carried out using a Brüel & Kjær Type 9737 portable impedance meter (*Figure 42*). This device combines the typical attributes of an impedance tube into a small portable form and the defining dimensions for the small scale impedance meter are given in *Figure 39* and *Table 7*. Unlike the larger scale devices the main tube has a circular cross section and the samples are not secured to the open end. Instead the device was rested on top of the sample and the inbuilt flexible flange sealed the components for the tests. This device allowed for the performance of an array to be tested at an SPL of up to 155dB. The data contained 29520 samples, recorded at a rate of 16.4kHz and was post processed using the supplied proprietary software which followed the ASTM E 1050-08 [86] standard and should result in an 8Hz frequency resolution. The samples were constructed in a similar manner to the medium scale tests with a spate faceplate and a backing volume (*Figure 43*).

Figure 42 – Small scale high SPL impedance meter [87]

Dimensions	
L (mm)	208
Ø (mm)	29
z_1 (mm)	29
z_2 (mm)	49

Table 7 – Dimensions for the medium scale impedance tube (refer to *Figure 39*)

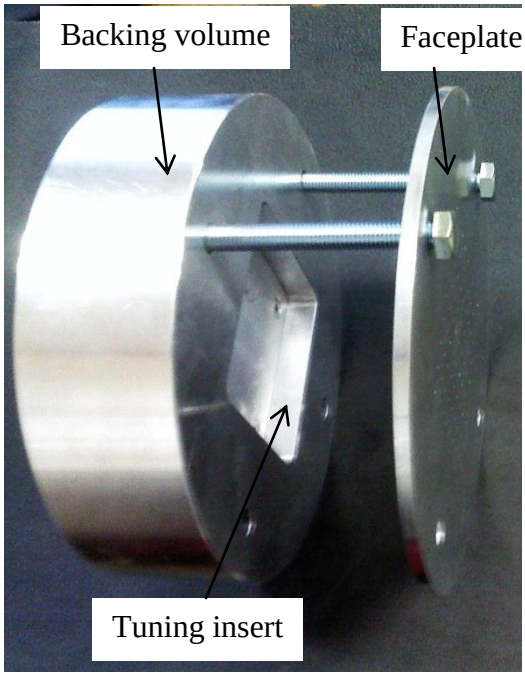

Figure 43 – Test sample for small scale high SPL impedance tube testing

4 Palliative device design

This section discusses the fundamental properties of the various analytical models used within this body of work to calculate the attenuation performance of the various resonant array palliative devices. An initial introductory section is provided which describes the proposed palliative devices and demonstrates the provenance of such devices in the wider literature. The following sections introduce the initial stages of an analytical model for the performance prediction and sets out additional updates which can be made to improve the reliability of the analytical calculations when the arrays are exposed to the expected conditions within an open cavity flow. For example the effects of high SPL and grazing flow on the attenuation performance are discussed for resonant arrays. A section which introduces a variety of alternative palliative devices is also included. These devices are currently used in other fields, such as room acoustics, to attenuate noise and it was therefore of interest to investigate whether they could also demonstrate a potential for attenuation of the modal peaks within an open cavity spectrum.

4.1 Introduction to the concept of acoustic resonant absorbers

Acoustic liners based on Helmholtz resonators have been successfully used to reduce acoustic signatures in a diverse range of applications, from recording studios [72] to gas turbine engines [95]. Whilst the overall field of open cavity acoustics has been extensively studied, along with a wide range of control techniques [39], the idea of using resonators as palliatives within this field has received comparatively little attention for this application [38] [37].

The principle of this technology is based on the characteristics of a resonating column of air and a Helmholtz type resonator is formed from an enclosed backing volume with an elongated neck to enclose the resonating air column. The neck is open at both ends and when excited, the air within the neck vibrates. When the resonant frequency condition is met a maximum displacement of the air column, and therefore attenuation, is reached. Typically, the attenuation from a Helmholtz type resonator is achieved through frictional losses, vortex shedding and the effective spring action of the air within the backing cavity. Viscous losses also occur in the neck region. The technology is designed to attenuate longitudinal waves and therefore lends itself to the cavity configuration where the waves within the cavity are thought to be longitudinal in nature [96] [15]. The resonant arrays can be installed with only minor geometric changes to the internal surfaces of a cavity and are fully passive so they have no requirement for actuation or energy input.

It has been previously demonstrated that this general type of device can be an effective attenuation device for the cavity modal amplitudes, and reductions in peak SPL values of up to 20 dB have been reported for flows at Mach 0.53 [38]. This case of experimental work used an array of individual Helmholtz resonators with separate backing volumes, and thus the frequency of each resonator could be individually manually adjusted [38]. However, no experimental work has exhibited such high levels of attenuation at higher transonic or supersonic Mach numbers. A computational study, which used a porous wall model for the acoustic liners, calculated a reduction in peak SPL of around 10 dB for Mach 0.85 flow [37]. Both of these studies demonstrate the potential of resonators as acoustic treatments for cavity flows.

The resonant arrays used in the current study comprise multiple orifices coupled with a common backing volume which can also be adjusted. Each orifice unit is based upon the principle behind Helmholtz resonators. A sketch of two resonators within an array is shown in *Figure 44* along with the design variables used for tuning the resonators in the current study. It is known that this arrangement behaves in a similar way to individual Helmholtz resonators and can provide a similar tuned attenuation approach [97]. The device is tuned to the required resonant frequency by selecting the porosity (ε) of the faceplate and the volume of the backing cavity. In this work the word resonator is synonymous with a resonator array or could also be considered as a perforated plate with a simple common backing volume (*Figure 44*).

Whilst the method of attenuation tested within this study is passive, the concept behind the attenuation can be modified to create an active or adaptive array. Such devices comprise of an array of resonators in which the resonant frequency of each device can be actively changed by a control system. Such devices have been demonstrated for use with gas turbine combustors and duct flows where the change in resonant frequency can be effected by changing the backing volume of an array [98] or the diameter of the orifice [74]. Both cases reported a reduction in SPL of over 25dB. However, active devices are beyond the scope of the current study.

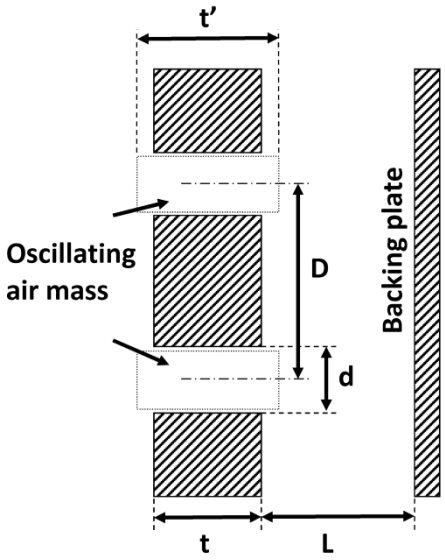

Figure 44 – Schematic arrangement of perforated plate with common backing volume

4.2 Analytical modelling of palliative performance under medium SPL conditions

To design the resonant arrays to target the modal frequencies within a cavity an analytical model was required. Due to the widespread use of resonant absorbers within the field of room acoustics an initial analytical model was adopted from this field. Typically, the SPL at which these devices operate is much less than 100dB and certainly not as high as the 160dB exhibited within resonant cavities. It is expected that when an array is exposed to a high SPL environment only the absorption coefficient levels would be affected [99] and the resonant frequency would remain unaffected. Therefore, the array should remain tuned to its prescribed modal frequency irrespective of the pressure intensity, however the absorption levels may not correlate with expectations [99].

This initial analytical model also assumes the absence of any grazing flow and that the sound wave impinges normally upon the resonator orifice. However, within the cavity flow field there is a low speed grazing flow which is expected to be around Mach 0.2 [100]. Previous experimental investigations have demonstrated that a grazing flow of this order improves the absorption coefficient of an array [101] and therefore should result in a greater attenuation compared to a case with no grazing flow. It is also generally accepted that the pressure waves within the cavity travel in a direction orthogonal to the front and rear walls. Therefore, the pressure waves are expected to impinge normally upon the end walls and it is postulated that the best attenuation will occur for arrays placed at these cavity end walls.

The analytical model enables the resonator design to be tuned to the modal frequencies through modifications to the four main geometric properties (*Figure 44*) perforation diameter (d), pitch spacing (D), neck length (t) and backing volume length (L). A

profile of absorption coefficient as a function of frequency can then be calculated through *Equation 27* to *Equation* 32 which identify the frequency at which attenuation would be expected.

4.2.1 Introduction to initial medium SPL analytical model

To design the resonant arrays for the cavity application, an initial analytical model was proposed based on an absorption coefficient metric (α) (*Equation 27*) [97]. The absorption coefficient of an acoustic absorber is defined as the ratio of the absorbed to the incident energy and is frequently used for medium SPL applications to predict the performance of resonant absorbers. Typically, a resonator requires a large absorption coefficient ($\alpha \approx 1$) to provide a high attenuation performance. The relative performance of an array can be calculated for an ideal case, with no grazing flow and under medium SPL conditions, but it was previously unknown how this relates to the performance of an array within an open-flow cavity. Previous research which used resonant arrays in cavities only took the array resonant frequency into account and did not discuss the expected attenuation level [38].

The absorption coefficient (α) is related to the normalised impedance of the arrays (Z*) through the reflection coefficient (R (*Equation 28*)). The acoustic impedance (Z) is estimated for a single unit resonator and is normalised by the characteristic impedance ($Z_0=\rho_\infty a_\infty$) where the density (ρ_∞) and speed of sound (a_∞) are taken as the freestream values. The non-dimensional absorption coefficient for an individual unit resonator is assumed to be equal to that of the entire array as each resonator is expected to behave identically with little influence upon the neighbouring resonators. Additionally, the number of resonators contained within an array is expected to affect only the amount of attenuation and not the tuning of the device.

The acoustic impedance of an array (Z*) is complex and comprises of the real part known as resistance (Re(Z)*) and the imaginary part known as reactance (Im(Z)*) (*Equation 29 to* Equation 31). The reactance of an array takes into account the effects of inertia and elasticity of the air within the system. The reactance is formed from two components, where the first term on the right hand side is the mass reactance and the second term is the stiffness reactance (Equation 31). These components act in opposition and are equal when an array operates at resonant frequency and therefore, the resonant condition of an array is defined by the frequency at which Im(Z)*=0. The mass (m) in the reactance equation (*Equation 31*) is defined in *Equation 32* and is related to the mass of the air contained within the neck of the devices plus end corrections.

At resonance the normalised resistance (Re(Z)*) of the array is the only contributor to the impedance of the array. The resistance term of an array calculated from the initial analytical model (*Equation 30*) represents the linear viscous loss mechanisms within an array and this resistance is linked to the resonant frequency, the porosity of the array (ε) and the orifice aspect ratio (t/d). To design an array with a high α, the normalised

resistance should be close to unity (*Figure 45*) and this assumption generally holds true for applications up to an SPL of around 100dB. However, above this SPL the resistance of an array is subjected to non-linear effects, which affect the resistance characteristics of the array and may impede the attenuation performance if Re(Z)* is increased beyond unity (*Figure 45*). *Section 4.3* discusses how the high SPL environment within a weapon bay cavity could affect the attenuation from a resonant array.

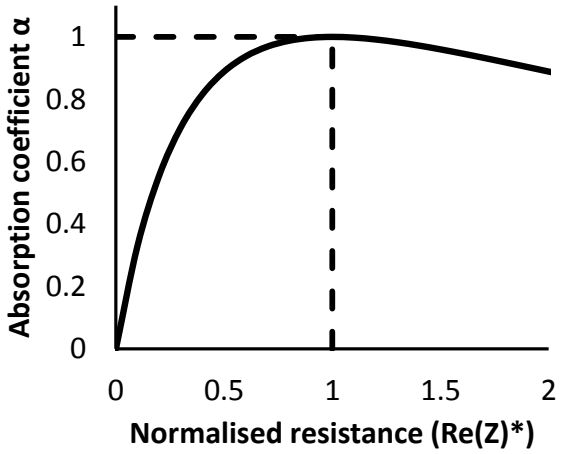

Figure 45 – Theoretical absorption coefficient against normalised resistance (for a fixed frequency)

$$\alpha = 1 - |R|^2 \qquad \textbf{Equation 27}$$

$$R = \frac{Z^* - 1}{Z^* + 1} \qquad \textbf{Equation 28}$$

$$Z^* = \mathrm{Re}(Z)^* + \mathrm{Im}(Z)^* \qquad \textbf{Equation 29}$$

$$\mathrm{Re}(Z)^* = \frac{\sqrt{8\upsilon\omega}}{\varepsilon a}\left(1 + \frac{t}{d}\right) \qquad \textbf{Equation 30}$$

$$\mathrm{Im}(Z)^* = \frac{\omega m}{\rho a} - \left(\frac{1}{\tan(kL)}\right) \qquad \textbf{Equation 31}$$

$$m = \rho D^2 \frac{t + 1.7\frac{d}{2}\left(1 + \left(1 - 1.25\frac{d}{D}\right)\right)}{\pi\left(\frac{d}{2}\right)^2}$$ **Equation 32**

4.2.2 Accuracy of the initial analytical model under medium SPL conditions

It was important to establish the reliability of the initial analytical model that was used to design the arrays as a discrepancy between the expected tuned frequency and the measured frequency would result in a reduction of the peak attenuation provided. An impedance tube was used to measure experimental values for the both the impedance and absorption coefficient properties of various sample devices. These measured profiles were then compared to calculated value and the differences between the two would demonstrate the reliability of the analytical model. The small scale medium SPL impedance tube used for this investigation placed an upper limit of 2kHz on the measureable frequency for the devices (see *section 3.3.2*).

The absorption coefficient profile for a representative array with a resonant frequency of around 1400Hz is shown in *Figure 46a*, and the impedance results are shown in *Figure 46b* and *c*. This representative array is the same scale as the small ($1/40^{th}$) scale wind tunnel cavity test arrays and shares the same faceplate properties (d=1mm, D=3mm, t=5mm) as *ARRAY 2-1* (*Table 10*), and should therefore exhibit similar resistance (Re(Z)*) properties. The backing length of the example array used for the impedance tube investigation was L=20mm, which is twice that of ARRAY 2-1, however this is not expected to affect the resistance properties of the device.

*Figure 46*a shows the measured absorption profile compared to the analytical absorption profile produced by the analytical model and there is a reasonable agreement between the measured and calculated absorption profiles for the profile peak (*Figure 46*a). However, the analytical model slightly under predicts the peak absorption coefficient by around 0.05 (*Figure 46*a). This is due to the model under predicting the resistance of the array by around 3% which results in a slightly lower (-2%) resonant frequency prediction (*Figure 46*b). The model does however yield a good prediction for the imaginary impedance of the array, where the maximum difference from the measured absorption coefficient level is around 0.1 and the resonant frequency is calculated to be within ±30Hz (±2%) of the measured value.

This result demonstrates the two-fold capability of the analytical model to predict both the resonant frequency and absorption coefficient of an array under the ideal low SPL conditions for which it was designed. Within the cavity the SPL is higher than the level within the impedance tube and also the aerodynamics and noise mechanisms are

different. Within the cavity the arrays will be exposed to a low Mach number grazing flow and may experience vortex impingement upon their surfaces. These factors are not thought to affect the tuning of the arrays, but may impact the level of attenuation that the array can provide. The following section investigates how the high SPL within a resonant cavity may affect the performance of the arrays. Comment is also provided on how the grazing flow and pressure wave directionality may also affect the performance of the device.

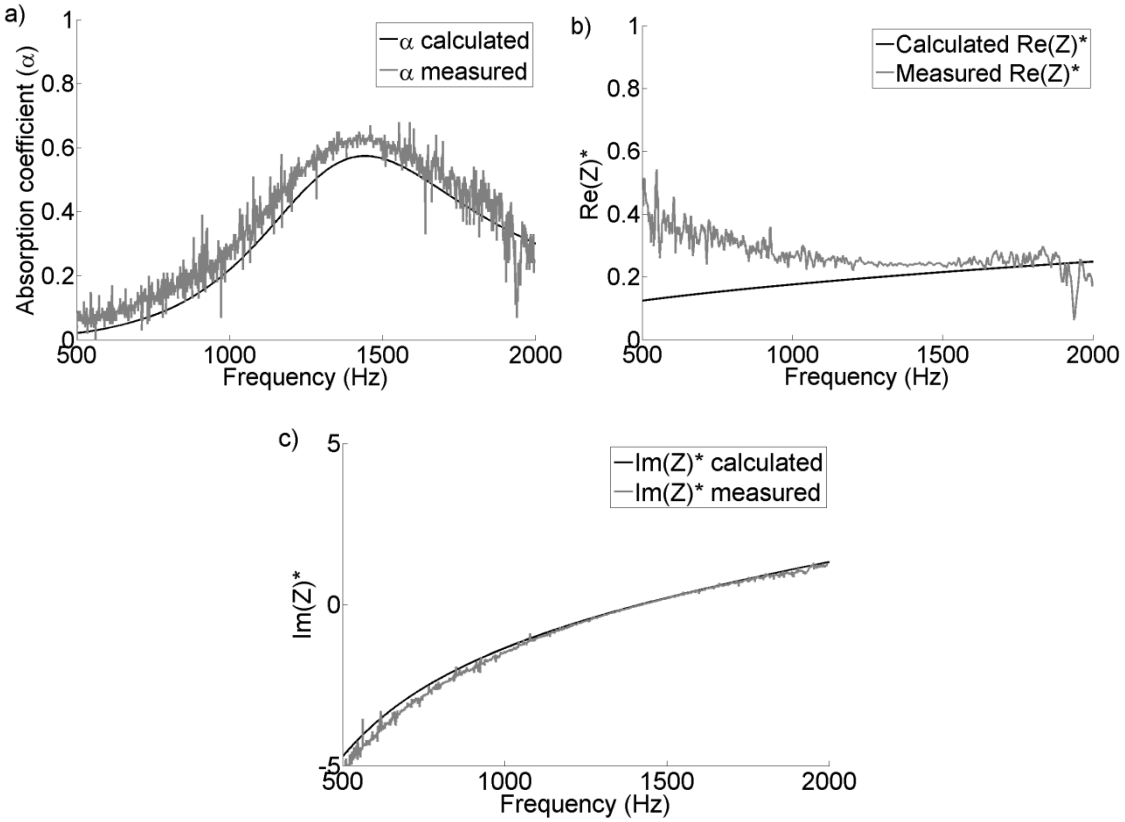

Figure 46 – Comparison between a) calculated and measured absorption coefficient profiles, b) calculated and measured resistance profiles, c) calculated and measured reactance profiles for a representative resonator case.

4.3 Effect of the environment within an open cavity on the performance of resonant arrays

The analytical model used in the design process for the resonant arrays is based on an approach used for room acoustics [50]. Resonant arrays are widely used in the room acoustics field as they offer a simple and robust approach when attenuating over a narrow band of frequencies. Arrays which operate within the room acoustics field typically experience low to medium SPL levels with a maximum intensity of around 100dB. In the low intensity environment the arrays performance can be accurately calculated by the analytical model (*Figure 46*). However, the environment within an open flow cavity exhibits significantly higher SPL intensities with levels typically around 160dB. It was therefore important to assess how the high SPL within a cavity may affect the performance of the resonant arrays. The high SPL investigation will also provide an indication of how reliable the analytical model is for the prediction of both the array's resonant frequency and attenuation properties when exposed to high SPLs.

A family of three resonant arrays was designed to be compatible with a Type 9737 impedance meter (*Table 8*). Each of these arrays consisted of a confined backing volume and a perforated faceplate (*Figure 47*). All of the arrays share the same faceplate and to change the tuning a series of inserts were also designed. The geometric and acoustic properties of the three resonant arrays tested are given in *Table 8*. HSPL ARRAY #1 shares the same properties as ARRAY 2-1 from the small ($1/40^{th}$) scale wind tunnel tests and targets a frequency around 2kHz with a relatively high absorption coefficient (α) and narrow bandwidth (β). HSPL_ARRAY #2 targets the third modal frequency from the small scale cavity and HSPL ARRAY #3 was designed to target a frequency based on the characteristics of the impedance meter. HSPL_ARRAY #2 and #3 do not replicate the properties of arrays used within the wind tunnel tests and are used to investigate whether the frequency of operation has any influence on the effects of high SPL. The following sections will discuss the effects of the high SPL environment on both the absorption coefficient and the impedance properties of the arrays.

Array name	$1/40^{th}$ scale target mode	f (Hz)	d (mm)	D (mm)	t (mm)	L (mm)	ε (%)	α_{max}	β (%)	Re(Z)*
HSPL_ARRAY #1	2^{nd}	1942	1	3	5	10	8.7	0.63	46	0.25
HSPL_ARRAY #2	3^{rd}	3116	1	3	5	4	8.7	0.72	31	0.31
HSPL_ARRAY #3	N/A	1377	1	3	5	20	8.7	0.57	62	0.21

Table 8 – Geometric and acoustic properties of the resonant arrays used for high SPL impedance tube tests

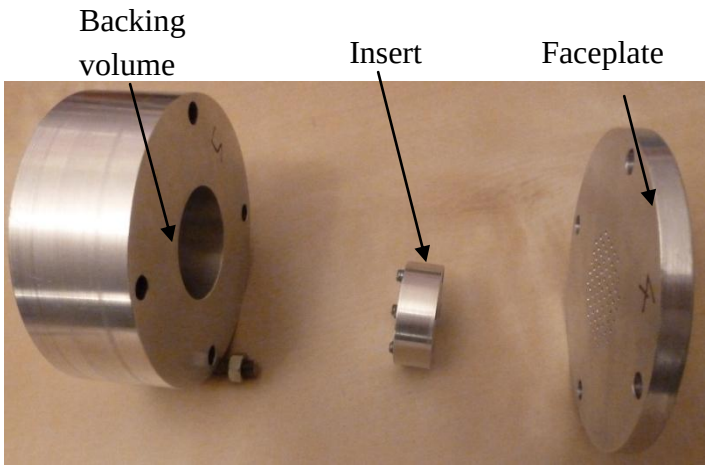

Figure 47 – Resonant array used for high SPL impedance tube testing

4.3.1 Effect of the high SPL environment on array absorption coefficient

The absorption properties of a series of three arrays were investigated over a range of SPLs from 126dB to 155dB using a portable SPL meter. HSPL_ARRAY #1 shares the geometric properties of ARRAY 2-1 and is designed to target the frequency of the second Rossiter mode from the small scale wind tunnel modal. HSPL_ARRAY #2 was designed to target the third mode at $1/40^{th}$ scale and HSPL_ARRAY #3 was designed to target a frequency within the range of frequencies suitable for the impedance meter. All three arrays shared the same perforated faceplate and their tuning was changed by varying the backing length (L).

For all three arrays the increase in SPL from 126dB to 155dB caused a corresponding increase of the absorption coefficient (α) by around 30%. The resonant frequency was also affected and exhibited a 3% increase at 155dB compared with 126dB (*Figure 48*). The initial medium SPL analytical model calculated the resonant frequency of the three arrays to within ±4%, which is acceptable for tuning the arrays to the modal frequencies of a resonant cavity. However, the model was far less accurate for predicting the absorption levels for all three arrays because the analytical model does not currently have an input to correct for the effect of the high SPL environment and therefore cannot be assumed to be reliable for the performance prediction of arrays within a cavity. The effect of high SPL is an aspect which needs to be addressed and *section 4.3.3* discusses a variety of analytical models which can be used to calculate the acoustic properties of arrays which operate within a high SPL environment. The next section discusses the effect of the high SPLs on the impedance properties for the high SPL arrays.

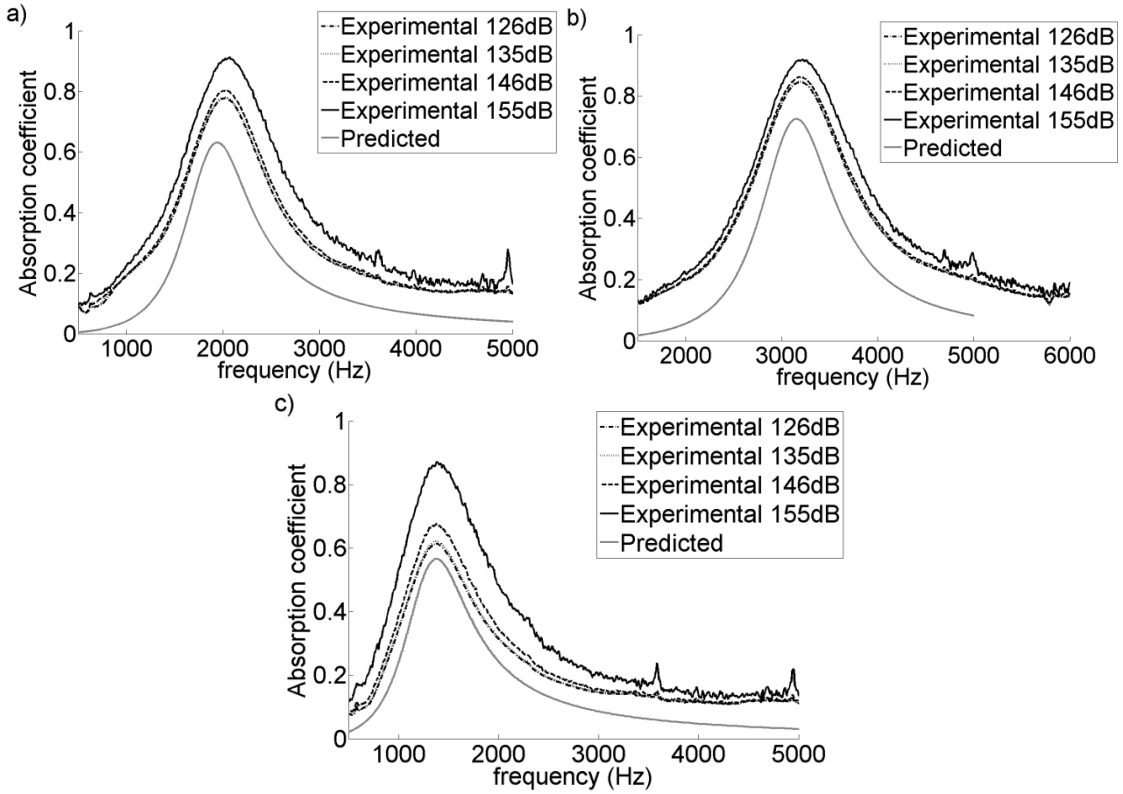

Figure 48 – Measured and calculated absorption coefficient over the SPL range 126dB to 155dB for a) HSPL_ARRAY #1, b) HSPL_ARRAY #2, c) HSPL_ARRAY #3

4.3.2 Effect of the high SPL environment on the impedance characteristics of resonant arrays

The impedance of the three sample arrays were investigated under high SPL conditions using an impedance tube (*section 3.3.3*). The impedance tube investigations provide an empirical measure of both the array's absorption coefficient (α) and impedance values (Z*). This allows for the effect of increased SPL on the acoustic properties of the devices to be investigated. *Figure 49a* shows that the maximum absorption coefficient of HSPL_ARRAY_1 increases from around 0.75 to 0.90 when the SPL is raised from 126dB to 155dB. This pressure intensity (155dB) is similar to the SPL which is typically expected within resonant weapon bay cavities. However, despite the large change in the absorption coefficient level, the resonant frequency of HSPL_ARRAY_1 remains within ±1% of the mean value over the SPL range 126dB to 155dB.

These factors can be explained by further examination of the impedance (Z*) characteristics of the array. The resonant condition of an array is determined by the frequency for which the reactance (Im(Z)*) is equal to zero. Over the SPL range 126dB to 155dB the reactance (Im(Z)*) profiles only vary within ±1% of one and other (*Figure 49b*). Therefore, the resonant frequency would be expected to remain relatively constant for all SPL values, which is what is shown in *Figure 49b*. The increase in the absorption coefficient, with SPL level, for HSPL_ARRAY_1 (*Figure 49a*) is caused by the increase in the resistance (Re(Z)*) of the array (*Figure 49c*). For SPLs of 126dB,

135dB, and 146dB the resistance remains fairly constant at around Re(Z)*≈0.45. However, at resonance, the resistance undergoes an increase up to around Re(Z)*≈0.54 when the SPL reaches 155dB (*Figure 49c*). Similar effects were exhibited for HSPL_ARRAY_2 and HSPL_ARRAY_3. Overall, the high SPL did not affect the resonant frequency and at the maximum SPL of 155dB, resonance occurred within ±3% of the frequency at 125dB. All three of the HSPL arrays exhibited a significant change in α and Re(Z)* at 155dB compared to 125dB, with around a 30% increase in α at 155dB (*Table 9*). As with HSPL_ARRAY_1, and given the common faceplate geometry, the main changes in the acoustic characteristics are seen in the resistance (Re(Z)*) terms. Overall, these changes in the array characteristics which arise under high SPL conditions are attributed to a non-linear behaviour of the flow within the orifice of the arrays.

There are various parameters which can be used to define the non-linear behaviour of an array. A typical rule of thumb is to treat any SPL above 100dB as causing some degree of non-linear behaviour [102]. Also non-linear resistance characteristics are expected when the displacement of the oscillation within the orifice is of the same order as the orifice diameter [103]. Typically, at higher SPLs the Reynolds number (Re_d) of the flow through the orifice increases beyond the laminar flow threshold (Re_d>2000 (*Equation 33*) which contributes to the increase in the array resistance through skin friction increases within the orifice. The orifice velocity is calculated from the acoustic particle velocity which is linked to the SPL (*Equation 34* and *Equation 35*), where P_{ref} is the standard reference pressure for SPL ($2x10^{-5}$Pa), u_n is the particle velocity in front of the orifice, and u_o is the velocity through the orifice.

An increase in the Reynolds number (Re_d (*Equation 33*)) with a corresponding rise in SPL is expected as previous work has also demonstrated this trend along with a link between larger energy losses through an orifice with the greater convective flow terms [104]. The relationship between orifice velocity (u_o) used in *Equation 33* and SPL is given in *Equation 34* and *Equation 35*. Previous work [104] provides the parameters set out in *Equation 36* and *Equation 37* to assess whether an array will be operating in the linear or non-linear regime. These equations are related to the ratio of momentum convection to shear (*Equation 36*) and inertia (*Equation 37*), where the momentum convection is linked to the particle velocity through the orifice (u_o) and ω is the frequency of the flow calculated from the resonant frequency of the array.

$$\mathrm{Re}_d = \frac{\rho u_o d}{\mu} \quad \textbf{Equation 33}$$

$$u_o = \frac{u_n}{\varepsilon} \quad \textbf{Equation 34}$$

$$u_n = \frac{P_{ref}\left(10^{\frac{SPL}{20}}\right)}{\rho a} \quad \textbf{Equation 35}$$

$$\frac{u_o}{\sqrt{\nu\omega}} > 1 \quad \textbf{Equation 36}$$

$$\frac{u_o}{\omega d} > 1 \quad \textbf{Equation 37}$$

$$\mathrm{Re}_\omega = \frac{\rho u_n u_o}{\mu\omega} \quad \textbf{Equation 38}$$

The resultant parameters have been calculated for the high SPL sample arrays (*Table 9*) and the results are also pertinent to the small scale tests. It is expected that if only one of the parameters is greater than unity that the array will exhibit slight non-linear properties, but the resistance will remain predominantly linear. This was seen for all of the 126dB to 146dB cases. However, when both parameters are greater than one, the array will exhibit highly non-linear characteristics. This highly non-linear behaviour was exhibited by all of the HSPL_ARRAYs for the measured resistance case at 155dB (*Figure 50*). At this SPL there was a step increase in the array resistance compared with the lower SPL cases below 146dB. This increase in the resistance only for the 155dB case agrees with the parameters in *Table 9* as they are both only greater than 1 for the 155dB case. Therefore, it is postulated that the behaviour of the resistance term (Re(Z)*) at high SPL is due to non-linear effects within the orifice of the array.

The following section discusses how the effects of high SPL can be incorporated into an analytical model, which will provide a more reliable calculation of the acoustic properties of the arrays during the design process. Whilst, the high SPL within the cavity environment is not expected to affect the resonant frequency and therefore the attenuation frequency of the proposed devices, it is expected to affect the relative levels of attenuation through changes to the absorption coefficient. If reliable relationships are to be found between acoustic properties, such as α and Re(Z)*, these must be accurately calculated for the devices prior to any subsequent investigation. Accurate links between attenuation levels and acoustic properties allow for design rules to be established which

provide recommendations for future designs. The resistance for the three HSPL arrays over the SPL range 125dB to 155dB is shown in *Figure 50* and this demonstrates that each array exhibits different levels of non-linear resistance. Despite the three arrays sharing a single faceplate, the resistance which is typically attributed to the faceplate properties [50], is different for each array. This indicates a dependency between the non-linear resistance and frequency which has not previously been established. To capture not only the SPL dependence, but also the frequency dependence the unsteady Reynolds number (Re_ω)

Equation 38 [105]) was introduced and the values for each array are given in *Table 9*. This term (Re_ω) has been included to capture the frequency dependence of the resistance values of the HSPL arrays under the high SPL conditions (*Figure 51*). The unsteady Reynolds number (Re_ω) is used within this study to provide a link between array resistance, cavity SPL and operational frequency (see *section 4.3.3.5*).

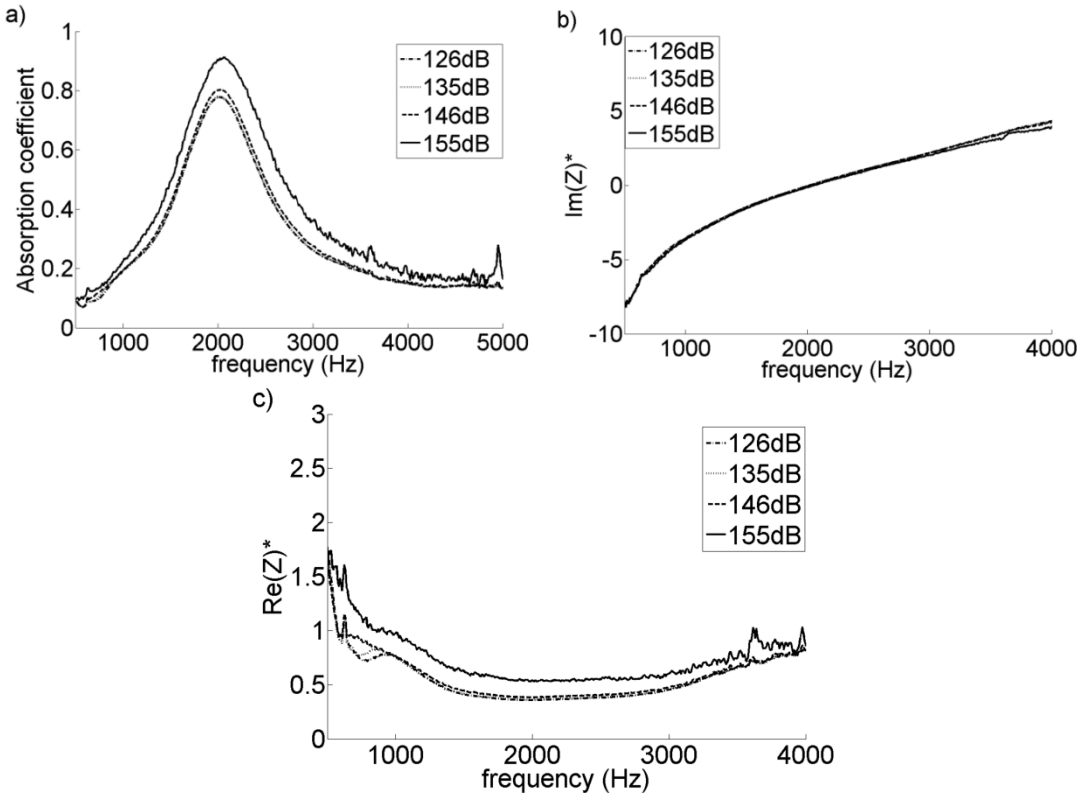

Figure 49 – The effect of increased SPL on the measured acoustic properties of resonant array HSPL_ARRAY_1. a) Absorption coefficient, b) Normalized Reactance (Im(Z)*), c) Normalized Resistance (Re(Z)*).

HSPL_ARRAY (f (HZ))	SPL (dB)	$\frac{u_o}{\sqrt{\nu\omega}} > 1$ (*Equation 36*)	$\frac{u_o}{\omega d} > 1$ (*Equation 37*)	Peak $\alpha_{measured}$	$Re(Z)^*_{measured}$	Re_ω
1 (2000Hz)	126	2.29	0.08	0.78	0.36	0.45
	135	7.23	0.25	0.78	0.36	4.56
	146	22.8	0.77	0.80	0.38	45.4
	155	71.6	2.40	0.90	0.54	447
2 (3200Hz)	126	2.78	0.11	0.84	0.43	0.29
	135	8.78	0.36	0.84	0.44	2.87
	146	27.7	1.14	0.84	0.46	28.7
	155	86.6	3.52	0.91	0.55	285
3 (1400Hz)	126	1.81	0.05	0.61	0.23	0.67
	135	5.74	0.15	0.62	0.23	6.72
	146	18.1	0.49	0.67	0.27	66.9
	155	57.2	1.54	0.86	0.46	654

Table 9 – Calculated non-linearity parameters at the resonant frequency for the HSPL_ARRAY series over the SPL range of 126dB to 155dB

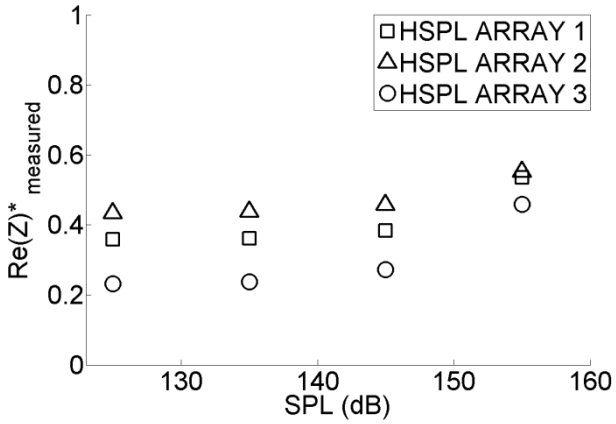

Figure 50 -- Measured resistance Re(Z)* as a function of SPL at the resonant condition for all HSPL_ARRAYs.

4.3.3 Analytical models for high SPL resistance prediction

Within resonant cavities the SPL can reach an intensity of around 160dB [7] and this level is dramatically different to the low SPL (<100dB) environments in which resonant arrays are typically used. Therefore, it was important to assess how the operation of the resonant arrays may change when used within such a high SPL environment. Initially, this section reintroduces the fundamental aspects of the analytical model used to predict the acoustic properties of the resonant arrays under linear low SPL conditions. Secondly, several analytical approaches are introduced, and these models can be used to estimate the non-linear resistance characteristics of an array.

4.3.3.1 Analytical model to link impedance properties to absorption coefficient (low SPL conditions)

Typically the analytical model is used to provide an estimate of the absorption coefficient (α) for resonant array designs. The absorption coefficient is the ratio of absorbed to incident energy upon an array's faceplate (*Equation 27*) and, under ideal conditions, a good absorber will usually exhibit an α of unity. The absorption coefficient is related to the pressure reflection coefficient ((R) *Equation 27*), which can be calculated from the normalized impedance of the array (Z*) (*Equation 28*).

The impedance of an array is a complex number, where the imaginary part (Im(Z)*) is the reactance and the real part (Re(Z)*) is the resistance. Whilst the resistance was shown to be greatly affected by the SPL of the operating environment (*Figure 50*), the reactance is not affected and can be calculated reliably through the relationship set out in *Equation 31* [50]. The reactance of an array is concerned with the effects of inertia and elasticity of the air within the system and is formed from both a mass and stiffness component (*Equation 31*). The components act in opposition and are equal in magnitude when an array operates at resonant frequency. Therefore, the resonant condition of an array is defined by the frequency at which Im(Z)*=0, where the first term on the right hand side is the mass reactance and the second term is the stiffness reactance (*Equation 31*). *Equation 30* is used to calculate the linear component of the array resistance [50]. This term is widely used for low SPL applications and does not take into account the increase in resistance at higher SPLs. The following section introduces several analytical models, which are designed to calculate the increase in resistance due to the high SPL conditions within a resonant cavity.

4.3.3.2 The work of Guess [106]

The first model to be introduced is the work of Guess [106]. The aim of this work was to produce a design method for single degree of freedom acoustic liners to be used within a high SPL environment. The focus was to design an array with prescribed reactance and resistance values. The resistance term (Re(Z)*) is split into three constituent parts (*Equation* 39). The first term on the right hand side of *Equation* 39 is the viscous element and corresponds to the linear resistance term used for a variety of low SPL analytical models ($Re(Z)_{linear}$ (*Equation 30*)) [50]. The two additional terms account for the increased resistance caused by the radiation of energy close to the orifice and the resistance due to non-linear interactions within the orifice. The radiation term is negligibly small (0.01% of the viscous term for HSPL_ARRAY_1) and is not expected to affect the final resistance value. However, the non-linear term is expected to be much greater than the viscous term under high SPL conditions (around 20 times greater than the viscous term) and this will provide the expected increase in the resistance at higher SPLs. The non-linear term is related to the particle velocity within the orifices (u_o) and also to the Mach number of the flow through the orifices. The orifice velocity is calculated from the velocity normal to the faceplate u_n (Equation 35). The orifice velocity u_o (Equation 34) is expected to increase rapidly at high SPL intensities and this will greatly increase the resistance of the array when exposed to the high SPL environment. The K term in *Equation* 39 is an empirical factor (taken as K=0.3 [106]) which is related to the thickness of the boundary layer over the surface of the perforated faceplate and M is the grazing flow Mach number within the cavity flow. An increase in the boundary layer thickness over the plate would be expected to increase the K value. The quiescent conditions of the impedance tube where there is no grazing flow over the device is not expected to cause this discrepancy as with a value of K=0.3 the grazing flow interaction term is expected to only add a normalized resistance of around $2x10^{-4}$ compared with values of the order 0.1 from the linear viscous term (*Figure 46*).

$$\mathrm{Re}(Z)^*_{model} = \frac{1}{\rho a}\left[\mathrm{Re}(Z)_{linear} + \frac{\pi^2}{2\varepsilon}\left(\frac{d}{\lambda}\right)^2 + \frac{\left(1-\varepsilon^2\right)}{\varepsilon}\left(\frac{|u_o|}{a} + KM\right)\right] \qquad \textbf{Equation 39}$$

4.3.3.3 The work of Maa [107]

The second model to be assessed is the work of Maa [107]. The focus of this work was to produce an analytical model capable of capturing the non-linear behaviour of micro-perforated arrays under high SPL conditions. Typically, micro-perforated arrays have a low porosity (ε) and an orifice diameter (d) of the order of 1mm or less. Therefore, with a value of d=1mm and a relatively low ε it was expected that this model would provide a good representation of the resistance properties of HSPL arrays. To capture the non-linear behaviour of the array an extra term ($\rho|u_o|/\varepsilon$) was added to the linear resistance ($Re(Z)_{linear}$) in *Equation 40*. The non-linear term relates the particle velocity (u_o) within the orifice to the pressure drop over the orifice. The non-linear term is then summed with the standard viscous resistance term to produce the total non-linear plate resistance. Again the non-linear resistance term is independent of the frequency of operation.

$$Re(Z)^*_{model} = \frac{1}{\rho a}\left[Re(Z)_{linear} + \frac{\rho|u_o|}{\varepsilon} \right] \qquad \textbf{Equation 40}$$

4.3.3.4 The work of Tayong and Leclaire [108]

The third approach to be investigated is the work of Tayong and Leclaire [108]. The main aim of this work is to assess to what extent any interaction between the oscillating mass within one orifice interacts with the mass of an adjacent orifice. However, a semi-empirical expression for the non-linear component of the resistance is also provided. This study links the increase in the resistance to the steady Reynolds number of the flow through the orifice Re_d (*Equation 33*) using *Equation 41*. In *Equation 41* C_1 and C_2 are empirically determined constants, which relate to the specific arrays investigated in reference [108]. Therefore, the values of C_1=0.049 and C_2=0.98 [108] were chosen as these correspond to the array which best compares with the HSPL series of arrays within the current body of work. As these constants are prescribed for a specific array it is unlikely that they will be acceptable for arrays where the design is different to the HSPL series tested in the current work. For instance changes in the array porosity (ε) or faceplate thickness (t) may invalidate these constants. The constants are used to fit a curve to the measured non-linear resistance of a model scale resonant array, which is representative of the transonic arrays tested within this study and in previous work [109].

$$Re(Z)^*_{model} = \frac{1}{\rho a}\left[Re(Z)_{linear} + C_1\, Re_d^{C_2} \right] \qquad \textbf{Equation 41}$$

4.3.3.5 A new empirical approach for high SPL array resistance estimation

The previous sections introduced three analytical models which have been previously used to calculate the increase in resistance which is exhibited by resonant arrays under high SPL conditions. For HSPL_ARRAY_1 at 125dB and 135dB the measured resistance values are within ±1% of one another (*Figure 49b*), which indicates that the SPL of 125dB represents the linear resistance ($Re(Z)^*_{linear}$) of the array. At SPLs above this, the resistance values are expected to exhibit non-linear increases with values at 155dB higher than those at 125dB. This trend was also exhibited for the other HSPL arrays and the resistance values at 125dB were taken as the linear resistance component (*Table 9* and *Figure 50*) ($Re(Z)^*_{linear}$ (*Equation 43*). Therefore, the increase in resistance due to the non-linear component ($Re(Z)^*_{NL\text{-}measured}$) is the difference between the measured resistance and the measured resistance at 125dB (*Equation 42*).

The non-linear resistance ($Re(Z)^*_{NL\text{-}model}$) for each of the three previous analytical approaches are plotted against the unsteady Reynolds number (Re_ω) in base ten logarithm form (*Figure 51*). The previous models do not include a frequency dependent term in their calculation of the non-linear resistance and this is highlighted by the horizontal groupings which are displayed for these previous models (*Figure 51*). The vertical spacing for the previous model cases is solely due to the variation in SPL. The measured resistance values ($Re(Z)^*_{NL\text{-}measured}$) for all three HSPL arrays are also shown. *Figure 51* demonstrates that the previous analytical approaches were unable to accurately model the increases in $Re(Z)^*_{NL}$ at the various high SPLs and the different frequencies at which the three HSPL arrays operate. Therefore, an empirical relationship was developed between $Re(Z)^*_{NL}$ and Re_ω and this is given in *Equation 42*. To calculate the overall resistance of an array this non-linear term is summed with the linear term (*Equation 43*). This model is used to calculate the acoustic properties of the resonant arrays designed within this study and is discussed in *section 4.2.1*. This new approach represents an improved method to account for the increases in resistance due to the high SPL environment compared to previous analytical approaches.

$$Re(Z)^*_{NL-model} = Re(Z)^*_{measured} - Re(Z)^*_{measured}\big|_{125dB} = 1.26\times10^{-3}\,Re_\omega^{0.81} \qquad \textbf{Equation 42}$$

$$Re(Z)^*_{model} = Re(Z)^*_{linear} + Re(Z)^*_{NL-model} \qquad \textbf{Equation 43}$$

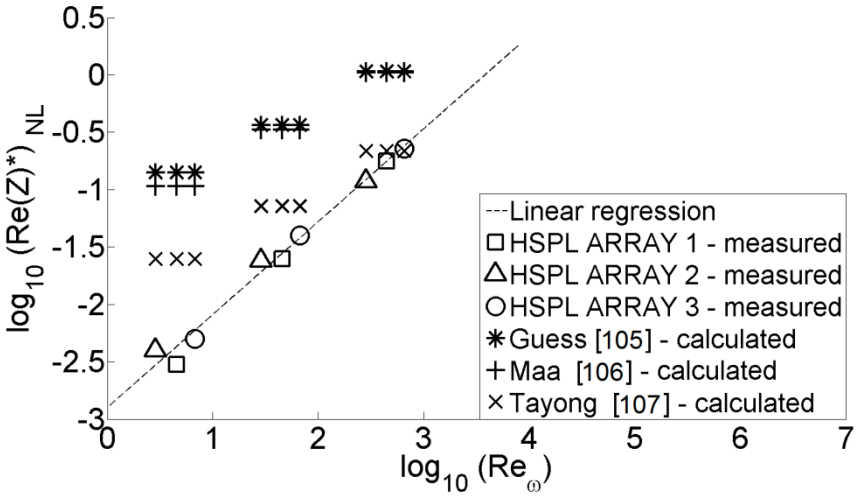

Figure 51 – Base ten logarithm of the measured and calculated non-linear resistance ($Re(Z)^*_{NL}$) against the base ten logarithm of the calculated unsteady Reynolds number (Re_ω). Linear regression carried out to provide linear line for measured data.

4.3.3.6 Effect of the grazing flow within a cavity on the attenuation performance of a resonant array

It was not possible to experimentally assess the effect of grazing flow across the resonant array faceplate due to the limitation of the impedance measuring equipment. However, as all of the possible array positions within a cavity experience a grazing flow it is important to comment on the possible effects grazing flow may have on the attenuation performance characteristics. Previous investigations into the effect of grazing flow on the attenuation performance of resonant arrays have shown that a grazing velocity will provide a small increase in the resistance of an array [103]. Several studies have concluded that the increase in array resistance due to grazing flow ($Re(Z)^*_{GF}$) can be accounted for using the term in *Equation 44*, where K is a constant (K=0.3 [110] or K=0.53 [111]) and M is the grazing flow Mach number. For a typical array as used in this study with a porosity of ε=8.7% and with a grazing Mach number of M=0.3 the effect of grazing flow is expected to be negligible with a value of between 0.0025 and 0.0043. As the effect of grazing flow is expected to be negligible and no experimental data are available to confirm the values calculated, this term will not be used within the analytical model used for the prediction of the performance of the resonant arrays used within this study.

$$\mathrm{Re}(Z)^*_{GF} = \frac{KM}{\rho a \varepsilon} \qquad \textbf{Equation 44}$$

4.4 Description of resonant arrays used for the experimental investigations

This section discusses the resonant array designs used with each of the separate pieces of apparatus within the experimental investigations of this body of work. Firstly the wind tunnel devices for the small scale ($1/40^{th}$) and medium scale ($1/20^{th}$) tests are discussed and example devices are shown. Secondly, the resonant array designs used for the assessment of the analytical models through impedance tube tests are discussed. This includes the small scale high SPL arrays, the medium scale medium SPL arrays and the full scale, medium SPL arrays. The design spaces available for the arrays within each piece of apparatus are described in Appendix A. The acoustic properties for all of the arrays have been calculated using the linear analytical model set out in *section 4.2* [50] as this model has greater provenance than the updated model suggested within this body of work and this provides consistency throughout this thesis. The use of the various acoustic models and their constituent elements as performance metrics is discussed later in this thesis (see *section 5.8*).

4.4.1 Small ($1/40^{th}$) scale wind tunnel arrays

A total of sixteen individual resonant arrays were designed for the tests within the small ($1/40^{th}$) scale wind tunnel. These included 10 arrays to attenuate the second mode at around 2kHz and 6 arrays to attenuate the third mode at around 3.2kHz. A summary of the geometric and acoustic properties are provided for all the arrays in *Table 10* and an example of a typical second and third mode array are shown in *Figure 52a* and *b*. The absorption coefficient profiles for the second mode arrays are presented against frequency which has been non-dimensionalised by the array resonant frequency in *Figure 53* and similarly for the third-mode arrays in *Figure 54*. Arrays which target the second mode are named with a prefix of "2-" and similarly arrays which target the third mode are named with the prefix "3-".

The majority of the second mode arrays were designed with relatively low porosity (ε) and high absorption coefficient (α). Typically, the third-mode arrays were designed with a different philosophy where the arrays exhibit high ε and low α. For all arrays there is a trade-off between a high α and large β, because of this second-mode arrays typically exhibit low β and third-mode arrays exhibit a high β. However, as the modal peaks within a resonant cavity spectrum typically exhibit relatively low bandwidths (β) this trade-off is not expected to pose an issued for the design of the arrays for this study. The wide variety of designs reflects the advances in the understanding of how attenuation can be achieved through the use of resonant arrays. Trends demonstrated from initial tests were used to drive further designs and these performance related design trends are discussed in *section 5.8*.

Array 2-1 was designed with a conservative value of absorption coefficient (α=0.63 (*Table 10*)) because in the initial stages of the investigation it was unknown as to whether tuned arrays could provide a high level of attenuation. Arrays 2-2 and 2-3 were designed with slightly lower α values of 0.43 and 0.39 respectively (*Table 10*),

compared with Array 2-1. These arrays (2-2 and 2-3) were designed to assess the effect of absorption coefficient on the level of attenuation which could be provided. Arrays 2-4 and 2-5 were designed with high porosity (ε) and low absorption coefficients to assess whether a high attenuation of the second mode within the small scale cavity could be achieved by low α arrays with a large faceplate porosity. Arrays 2-4 and 2-5 are calculated to have absorption coefficients of 0.24 and 0.15 respectively (*Table 10*).

To investigate if the attenuation from resonant arrays could be improved through an increase to the absorption coefficient arrays 2-6 and 2-8 were designed with high absorption coefficient values of around α=1 (*Table 10*). The final arrays (2-9 and 2-10) were designed based on their calculated resistance terms (Re(Z)*). These arrays were used to investigate whether attenuation levels could be improved by selecting an optimum resistance (Re(Z)*) value based on the trends demonstrated by the previously tested small scale arrays. This method of design is different to the initial arrays as instead of following the approach used for medium SPL applications, the high SPL nature of the cavity environment is taken into account within the design process to provide a more reliable calculation of the array performance.

Arrays which target the third mode were in general designed with a different philosophy to those which target the second mode. Arrays 3-1 and 3-2 were designed with low absorption coefficient values at the third mode, which follows an example design from previous work [34] (*Table 10*). Array 3-3 was designed with a high absorption coefficient value of α=0.93 (*Table 10*) to assess whether attenuation at the third mode could be improved through the use of a high α array, as would be expected for general attenuation of acoustic noise under medium SPL conditions. Arrays 3-4 to 3-6 were designed with low resistance characteristics (Re(Z)*) to assess whether attenuation at the third mode could be better achieved by low α, low Re(Z)* arrays.

Array	Mode	Build	d (mm)	D (mm)	t (mm)	L (mm)	ε (%)	Calculated peak α	Calculated β (%)	Calculated Re(Z)*
2-1	2nd	1+2	1	3	5	10	8.7	0.63	46	0.25
2-2	2nd	1+2	1	3	2	13	8.7	0.42	65	0.13
2-3	2nd	1+2	1	3	2	18	8.7	0.39	74	0.12
2-4	2nd	1+2	2	4	5	15	19.6	0.24	65	0.07
2-5	2nd	1+2	2	4	2	18	19.6	0.15	86	0.04
2-6	2nd	1	1	6	4	3	2.2	0.99	20	0.82
2-7	2nd	1	1	4	8	4	4.9	0.96	24	0.65
2-8	2nd	1	1	4	6	5	4.9	0.89	27	0.51
2-9	2nd	1	1	4	2	11	4.9	0.58	48	0.22
2-10	2nd	1	1	3	7	8	8.7	0.74	38	0.33
3-1	3rd	1+2	3	5	4	11	28.3	0.14	66	0.04
3-2	3rd	1+2	2	3	2	13	34.9	0.11	94	0.03
3-3	3rd	1	1	5	3	2	3.1	0.93	19	0.58
3-4	3rd	1	4	6	2	13	34.9	0.08	82	0.02
3-5	3rd	1	3	6	4	7	19.6	0.20	45	0.05
3-6	3rd	1	5	7	4	11	40.1	0.08	69	0.02

Table 10 – Summary of the geometric and calculated acoustic properties of the resonant arrays designed for the 1/40th scale cavity model

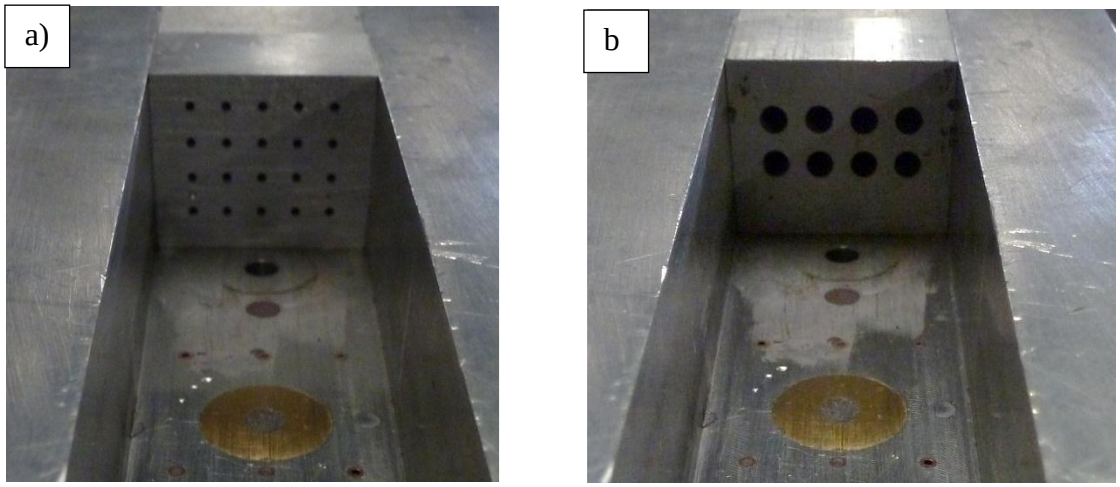

Figure 52 – a) ARRAY 2-10 installed into the Build 1 cavity, b) ARRAY 3-1 installed into the Build 1 cavity rear wall

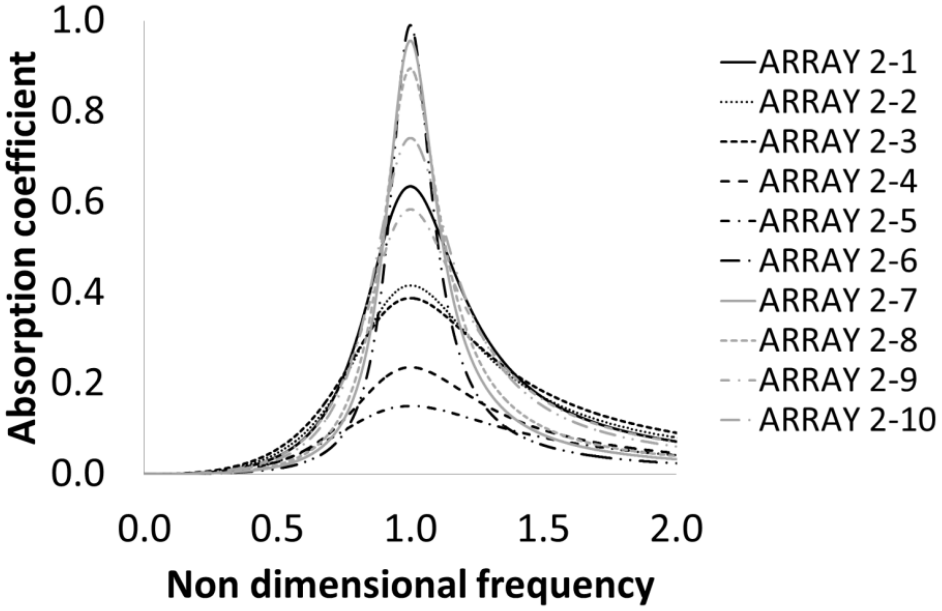

Figure 53 – Calculated absorption coefficient profiles for small (1/40th) scale arrays which target the second mode (2kHz).

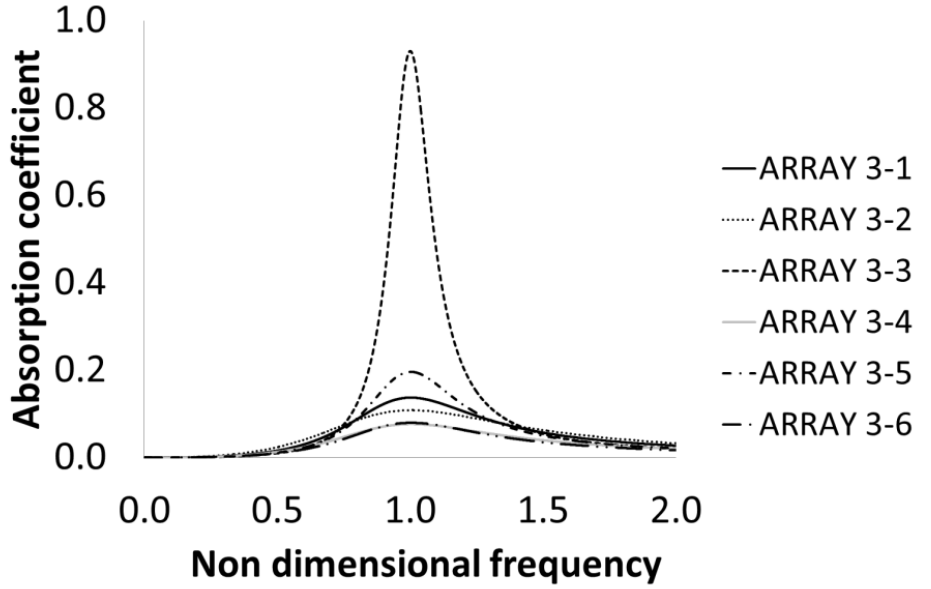

Figure 54 – Calculated Absorption coefficient profiles for small (1/40th) scale arrays which target the third mode a(3.2kHz).

4.4.2 Medium (1/20th) scale wind tunnel arrays

To investigate the attenuation performance of resonant arrays within a medium scale cavity a second separate series of resonant arrays was designed. Investigations using the medium ($1/20^{th}$) cavity were conducted subsonically and supersonically at both Mach 0.7 and 1.5. However, at each Mach number the acoustic signature was different and the frequencies of the respective modes varied by up to 40%. These changes in modal frequency, due to the large change in Mach number, required a different set of arrays to attenuate the modal peaks at each condition as the frequency variation was much larger than the expected bandwidth of a single resonant array. The geometric and acoustic properties of the arrays for both Mach 0.7 and Mach 1.5 are given in *Table 11* and *Table 12*. An example of two arrays installed into the $1/20^{th}$ scale cavity are shown in *Figure 55a* and *b*. The arrays for the medium scale facility are identified by the "TGF" prefix and follow the same name convention as for the small scale cases were "2-" indicates a second mode array and "3-" indicates a third mode array. The arrays for the supersonic test cases are identified by the "S" in their name.

For the subsonic tests (Mach 0.7) five arrays were designed to target the second mode and following the work at small scale these typically exhibit low porosity (ε) and high (α). The small scale tests and subsequent high SPL impedance tube tests indicated that the faceplate resistance (Re(Z)*) is an important design variable to obtain high attenuation levels (see *section 4.3*). To investigate the effect that the faceplate resistance (Re(Z)*) has on the attenuation level the second mode arrays exhibit Re(Z)* values within the range $0.22 < Re(Z)^* < 0.57$ (*Table 11*). Two arrays were designed to target the third mode at Mach 0.7 (*Table 11*). TGF_3-1 was designed with low (Re(Z)*) and TGF_3-2 was designed with high (Re(Z)*) to investigate whether the resistance of the faceplate affects the attenuation of third mode. Non-dimensional absorption coefficient profiles for the second mode are arrays are shown in *Figure 56* and for the third mode arrays the profiles are shown in *Figure 57*. The absorption coefficient profiles clearly show the different peak α values and how changes to the resistance (Re(Z)*) affect the bandwidth (β) of the devices. The different design approached for the attenuation of the second and third modes are also apparent, as the second mode arrays typically exhibit a higher absorption coefficient.

For the supersonic second mode four arrays were designed with various Re(Z)* values between $0.05 < Re(Z)^* < 0.51$ (*Table 12*). These arrays exhibit relatively low porosity (ε) and high absorption coefficients (α). The variation of the resistance (Re(Z)*) was introduced to assess the effect of faceplate resistance on the attenuation performance of resonant arrays under supersonic freestream conditions. Non-dimensional absorption coefficient profiles for the second mode are arrays are shown in *Figure 58*. This figure (*Figure 58*) clearly demonstrates the differences in α and β caused by the variations in the Re(Z)* of the arrays. Two arrays were designed to attenuate the third mode at Mach 1.5 (*Table 12*). TGF_S_3-1 was designed with a low resistance of $Re(Z)^*=0.03$ and TGF_S_3-2 was designed with a higher resistance of $Re(Z)^*=0.23$. It was expected that

for the third mode the array with the lower resistance would provide the higher attenuation level (see *section 5.2.2*). Non-dimensional absorption coefficient profiles for the third mode arrays are shown in Figure 59 and this clearly demonstrates the different design philosophies behind the two third mode arrays.

Array	Mode	d (mm)	D (mm)	t (mm)	L (mm)	ε (%)	α	β (%)	Re(Z)*
TGF_2-1	2nd	1.7	7.1	8.7	17.3	4.7	0.73	35	0.31
TGF_2-2	2nd	2	10	4	19	3.1	0.6	35	0.22
TGF_2-3	2nd	2	9	11	12	3.9	0.8	25	0.38
TGF_2-4	2nd	2	10	12	9	3.1	0.9	21	0.52
TGF_2-5	2nd	1	7	3	15	1.6	0.93	36	0.57
TGF_3-1	3rd	5.2	11.9	6.9	19.1	14.9	0.17	48	0.05
TGF_3-2	3rd	2	8	8	8	4.9	0.7	24	0.30

Table 11 – Summary of the geometric and calculated acoustic properties of resonant arrays designed for the 1/20th scale cavity model at Mach 0.7

Array	Mode	d (mm)	D (mm)	t (mm)	L (mm)	ε (%)	α	β (%)	Re(Z)*
TGF_S_2-1	2nd	1.7	4.8	8.7	17.3	10.2	0.51	46	0.17
TGF_S_2-2	2nd	1	6	3	10	2.2	0.89	33	0.51
TGF_S_2-3	2nd	5.2	11.9	6.9	19.1	14.9	0.17	48	0.05
TGF_S_2-4	2nd	2	8	8	8	4.9	0.7	24	0.3
TGF_S_3-1	3rd	5.2	8	6.9	19.1	33	0.10	70	0.03
TGF_S_3-2	3rd	2	10	2	5	3.1	0.60	22	0.23

Table 12 – Summary of the geometric and calculated acoustic properties of resonant arrays designed for the 1/20th scale cavity model at Mach 1.5

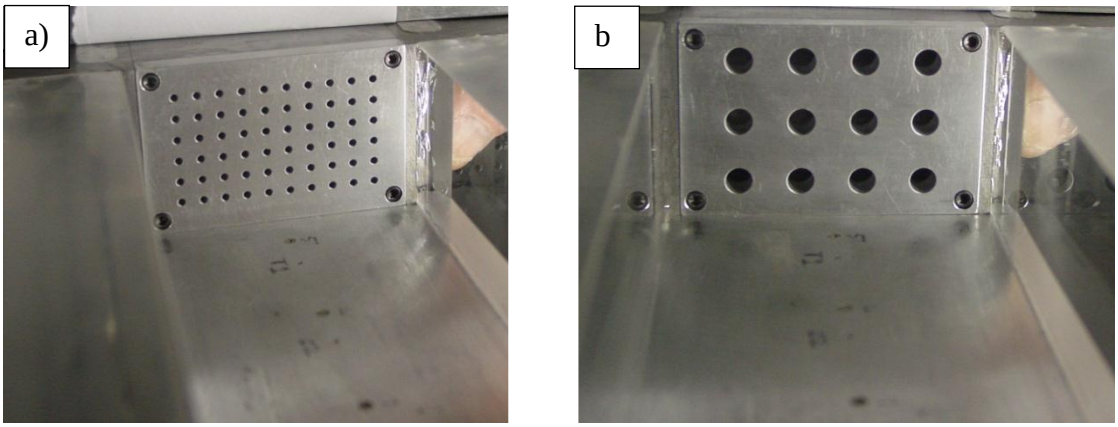

Figure 55 – a) TGF_S_2-1 installed in the 1/40th scale cavity front wall, b) TGF_S_3-1 installed in the 1/40th scale cavity front wall

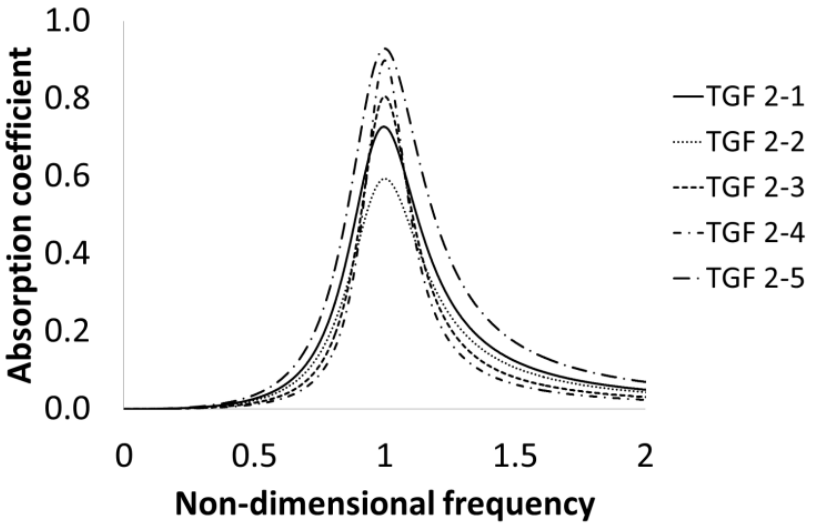

Figure 56 – Calculated absorption coefficient profiles for medium (1/20th) scale arrays which target the second mode at Mach 0.7 (825Hz).

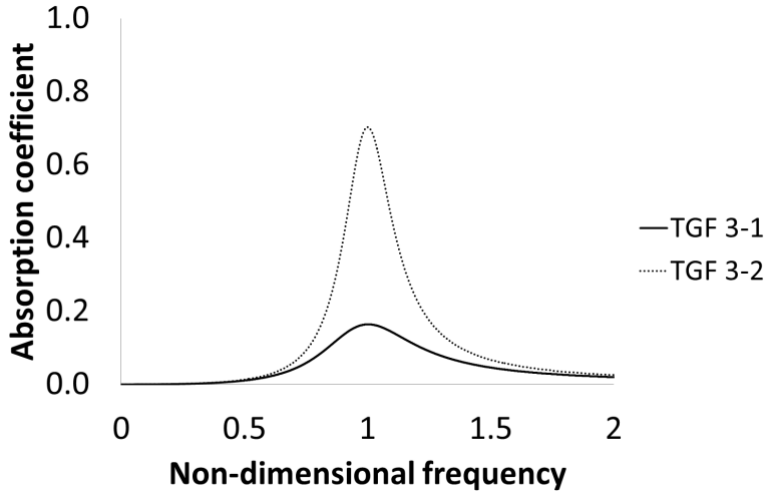

Figure 57 – Calculated absorption coefficient profiles for medium (1/20th) scale arrays which target the third mode at Mach 0.7 (1.2kHz).

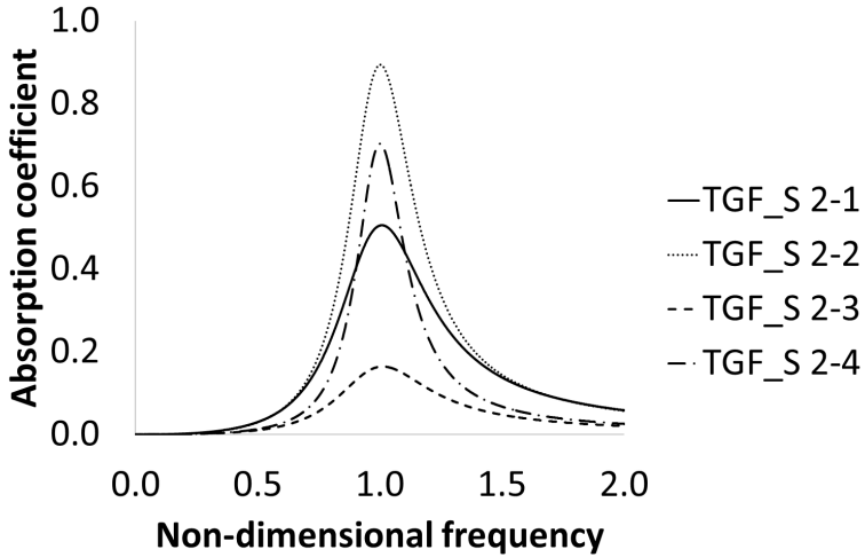

Figure 58 – Calculated absorption coefficient profiles for medium (1/20th) scale arrays which target the second mode at Mach 1.5 (1.2kHz).

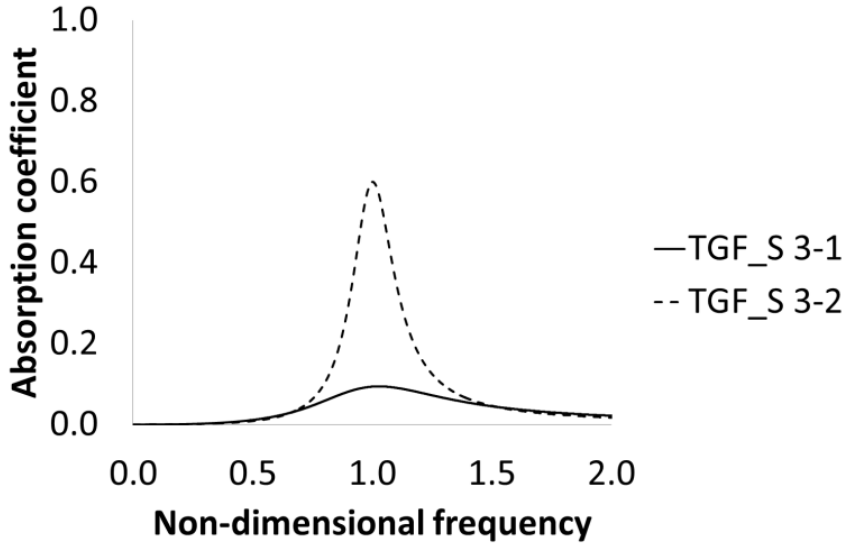

Figure 59 – Calculated absorption coefficient profiles for medium (1/20th) scale arrays which target the second mode at Mach 1.5 (1.9kHz).

4.4.3 Small scale, high SPL impedance tube arrays

A family of resonant arrays was designed to be compatible with testing using a Type 9737 impedance meter (see *section 3.3.3).* Each of these arrays consisted of a confined backing volume and a perforated faceplate, much like the model cavity arrays. The design space for this device is described in *Appendix A.* A series of inserts was also designed, which when inserted into the backing volume component changed the frequency characteristics of the arrays. The properties of the three resonant arrays, referred to as HSPL or high SPL arrays, are given in *Table 8* (*section 4.3*). HSPL ARRAY #1 and #2 target modal frequencies from the 1/40th scale cavity, which are around 2.0kHz and 3.2kHz respectively. The third array in this series, HSPL ARRAY #3, was designed to target a frequency based on the characteristics of the impedance meter.

4.4.4 Medium scale, medium SPL impedance tube arrays

A series of resonator arrays was designed to investigate the reliability of the analytical model used for the initial design of the palliatives proposed by this study (*section 4.2.1*). The arrays consist of separate faceplates combined with a backing volume (Appendix A and *Figure 60*) and their geometric properties are given in *Table 13*. Arrays LSPL_ARRAY #1 and LSPL_ARRAY #2 target the second modal frequency within the small (1/40th) scale cavity. The aim of testing these arrays was to assess how accurately they had been tuned to their target frequencies and how reliable the initial analytical model is for the design of resonant arrays.

Name	Scale/mode	d (mm)	D (mm)	t (mm)	L (mm)	f (Hz)
LSPL_ARRAY #1	1/40th 2nd mode	1	3	5	10	1942
LSPL_ARRAY #2	1/40th 2nd mode (20° swept holes)	1	3	5	10	1978

Table 13 – Geometric properties of resonant arrays used for the low SPL impedance tube tests

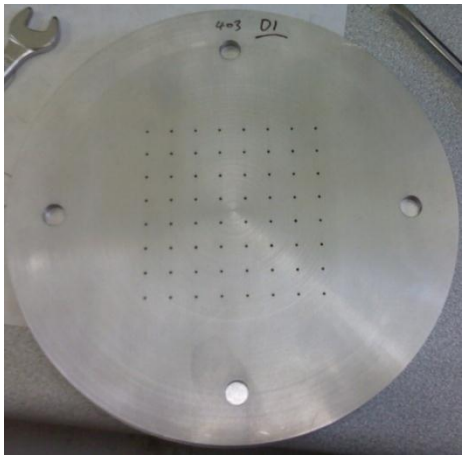

Figure 60 – Example of a faceplate used for the low SPL impedance tubes

4.4.5 Large scale, medium SPL impedance tube arrays

To investigate the effectiveness and feasibility of resonant arrays as sound absorption devices for use within a full scale cavity a series of arrays were designed to be used in conjunction with a large scale, low frequency impedance tube. This device (see *section 3.3.1*) was used to determine the absorption properties of resonant arrays at the low frequencies expected within a full scale weapon bay cavity. The geometric properties of the arrays and their target frequencies are shown in *Table 14*. LS_ARRAY_1 was designed to target the second mode within a 4m long weapon bay cavity (50Hz) and LS_ARRAY_2 was designed to target the third mode also within a 4m long cavity (80Hz). A third array (LS_ARRAY_3) was designed to target a higher frequency of 150Hz to investigate whether the target frequency itself had any effect on the absorption properties of the arrays. It should be noted that due to the constraints placed on the array sizes by the apparatus, a series of devices with low porosities (ε) have been designed.

Name	Frequency (Hz)	d (mm)	D (mm)	t (mm)	L (mm)	ε (%)
LS_ARRAY_1	50	1	57	2	68	0.024
LS_ARRAY_2	80	1	37	2	68	0.057
LS_ARRAY_3	150	1	20	2	68	0.196

Table 14 – Geometric design properties for resonant arrays used with the large scale impedance tube

4.5 Alternative palliative devices

A series of alternative palliative device which could be considered as alternatives to the proposed resonant arrays are investigated within this study. These approaches are assessed to investigate whether other devices which are typically used in other fields, such as room acoustics, can yield attenuation within an open cavity flow. The first type of alternative palliative device to be discussed is formed from a porous wire mesh coupled with a sealed backing volume. The defining dimensions are shown in schematic (*Figure 61*). Typically, this device is used to provide wideband attenuation where the resistance of the flow passing through the porous mesh provides the attenuation through viscous losses only. These devices can be tuned to improve attenuation at specific frequency by setting the backing length ((L) *Figure 61*) to a quarter of the target wavelength (λ/4). However, this is likely to be impractical for cavity applications as this would require a large fraction of the cavity length to install the device. These resistance based devices have been investigated at both small ($1/40^{th}$) and medium ($1/20^{th}$) scale under both subsonic and supersonic freestream conditions. The following two sections describe the geometric and acoustic properties of the test devices.

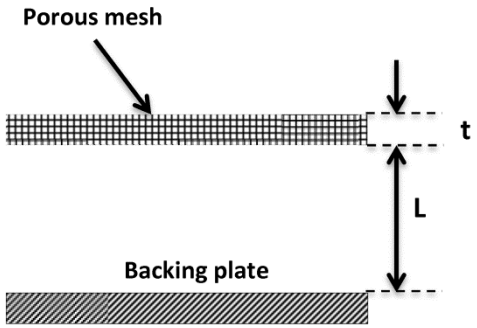

Figure 61 – Schematic arrangement of a porous wire mesh device

4.5.1 Small (1/40th) scale porous-mesh, resistance-based devices

Three porous wire mesh based devices were designed for the 1/40th scale tests. Each device shares a common porous faceplate, but the ventilation properties of the backing volume (*Figure 62*) differ to assess the impact of ventilation on the attenuation performance of the porous mesh devices. The geometric and acoustic properties of the arrays are given in *Table 15*. *MESH A* has been designed with the same dimensions as the array which was tested using an impedance tube to assess its acoustic properties and is formed from a porous faceplate coupled with a non-ventilated backing volume (*Figure 62a*). The absorption coefficient profile for MESH A under an SPL of 155dB is shown in *Figure 63* and demonstrates that MESH A is expected to provide high levels of attenuation for both the second and third mode (2.0kHZ and 3.2kHz respectively) with α typically greater than 0.6 at the modal frequencies. *MESH B* and *MESH C* are formed from the same porous faceplate as MESH A coupled with a backing volume which has a ventilated surface open to the freestream flow (*Figure 62b*). All three mesh devices are expected to provide broadband attenuation with the greatest attenuation at higher frequencies, especially above 3kHz where α increases to around 0.8 for MESH A (*Figure 63*).

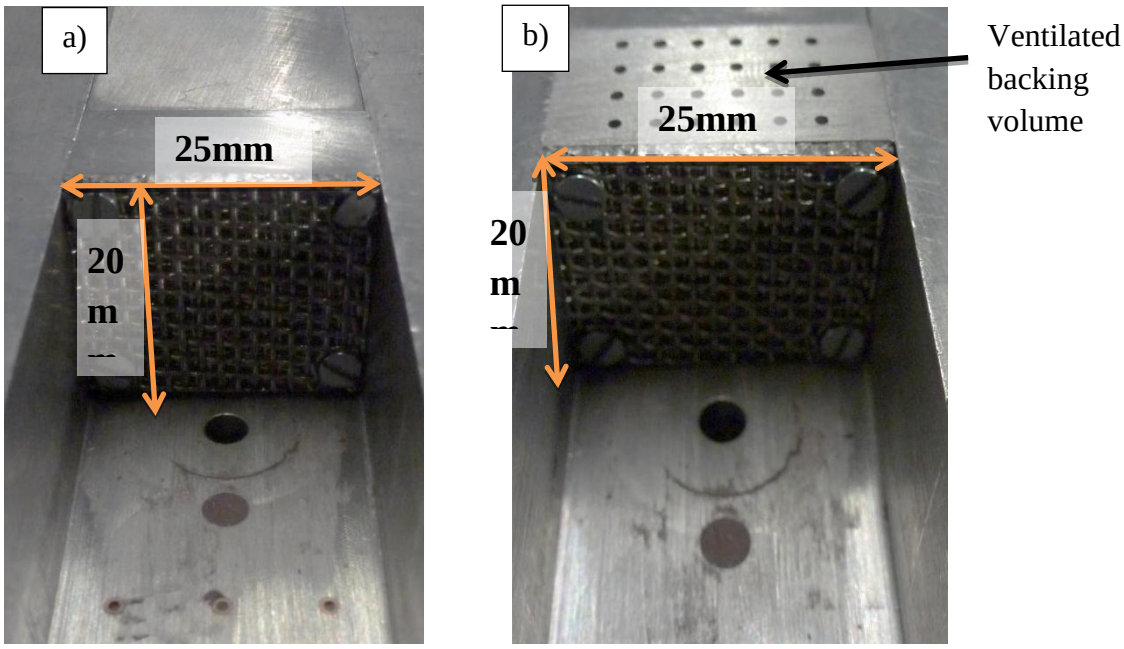

Figure 62 – a) Porous mesh device with non-ventilated backing volume (*MESH A*) installed into cavity model, b) Porous mesh device with 8.7% porosity ventilated backing volume (*MESH B*) installed into cavity model.

	Mesh ε (%)	L (mm)	Ventilation ε (%)	Measured absorption coefficient (α) at 2kHz	Empirical faceplate Re(z)* at 2kHz
MESH A	53	13.2	0	0.6	0.3
MESH B	53	13.2	8.7	N/A	0.3
MESH C	53	13.2	29	N/A	0.3

Table 15 – Geometric and acoustic properties of the small scale MESH devices

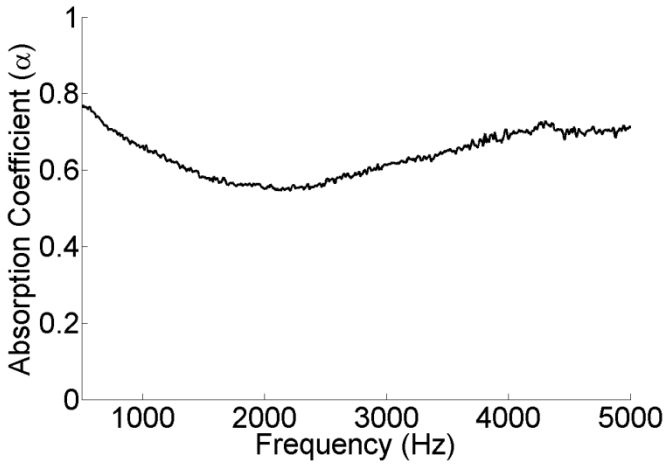

Figure 63 – Absorption coefficient profile for an unvented porous mesh device (MESH A) at 155dB

4.5.1.1 Small (1/40th) scale porous-mesh device with bias flow

A subset of the porous mesh devices uses a bias flow through the device, which is expected to improve the attenuation performance of the devices (*Figure 64*). The cavity configuration used for the mass injection/removal tests is described in *section 3.1.3.2*. For these tests the bias flow is driven by the pressure difference which exists between the tunnel working section static pressure and the ambient atmospheric pressure. It is expected that the static pressure within the model cavity (p_{stat}) is in the ratio of $p_{stat}/p_{atm}=0.6$ with the atmospheric static pressure (p_{atm}) during a run at Mach 0.90 and this difference is great enough to drive the bias flow through the mesh.

The *build 2* cavity was used as this provided the best access to the backing volume of the devices, which was required to connect the inlet/outlet tube. A needle valve was used to control the flow rate and a rotameter was used to measure the flow rates (*Figure 65*). Bias flow has been previously demonstrated as a successful method of improving the attenuation characteristics of acoustic devices [112] [101] and therefore it was of interest to see if this was the case for a simple wire mesh based device within the small scale cavity.

For the bias flow tests a single porous mesh device was designed. This was comprised of a large backing volume, which acted as a plenum chamber for the flow inlet, and the separate mesh faceplate (*Figure 64*). The mesh faceplate has the same properties as that used for the previous MESH arrays (*Table 15*) however, the backing length was larger at L=30mm. The larger backing length compared with MESH A is expected to reduce the frequencies at which attenuation occurs. This is acceptable as the absorption coefficient profile for MESH A (*Figure 63*) indicates that attenuation is expected at the third mode (3.2kHz) and higher frequencies.

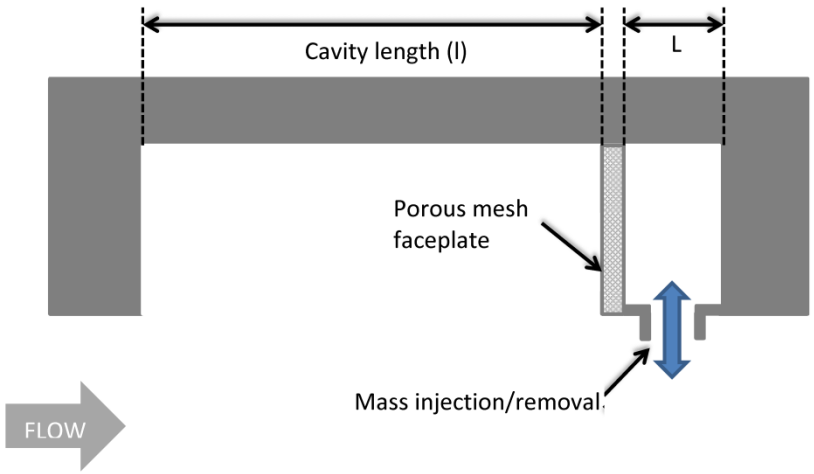

Figure 64 – Schematic arrange to show mass injection/removal from a rear wall mounted porous mesh device

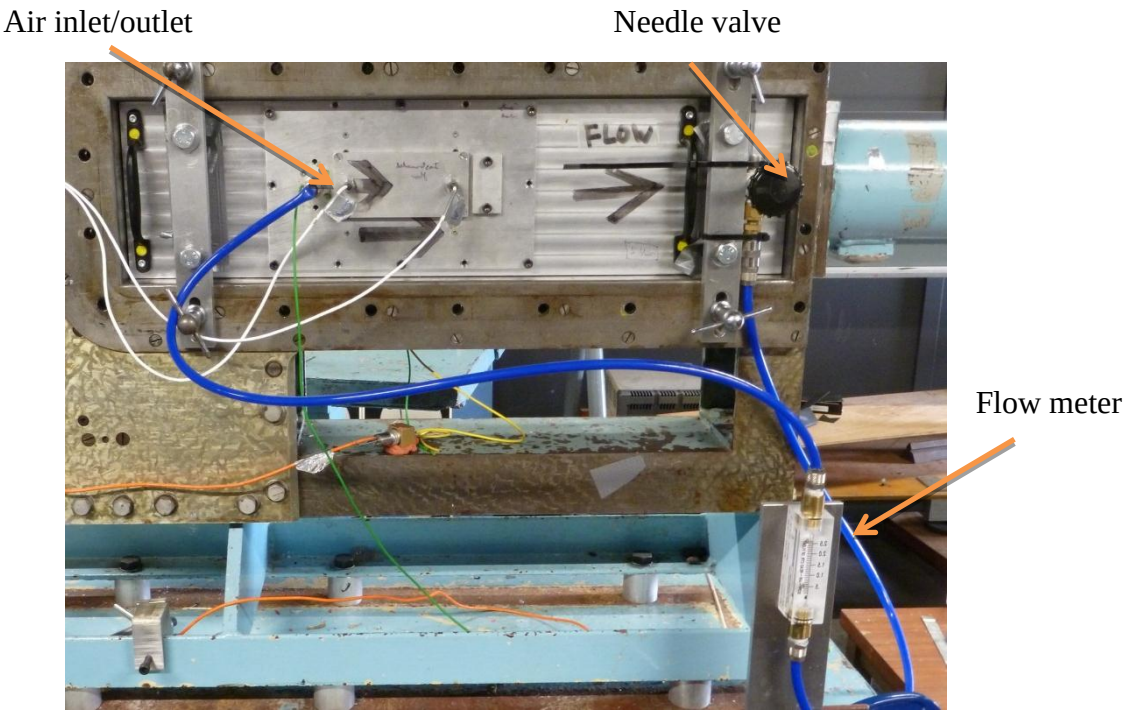

Figure 65 – Build 2 configured with bias flow device in the cavity front wall

4.5.2 Medium (1/20th) scale porous-mesh, resistance-based devices

A set of three porous mesh type devices were tested within the 1/20th scale cavity. These devices are formed in a similar way to the 1/40th scale mesh devices where a porous faceplate is coupled with a confined backing volume. A summary of the mesh devices is given in *Table 16*. Two mesh faceplates will be used for the arrays, one exhibits a low resistance (Re(Z)*=0.3) and the second exhibits a higher resistance (Re(Z)*=1.5).

The attenuation from the porous mesh devices was investigated at Mach 1.5. This investigation included the effect of mesh location on the attenuation performance by installing the devices either at the front or rear wall of the model cavity. *Figure 66b* demonstrates TGF_m3 installed in the rear wall of the ADDICT cavity model. In the rear wall configuration the device was expected to relieve the region of high static pressure which exists in the rear of the cavity and also to provide an acoustically soft boundary from which no reflections would occur. When combined these two actions were expected to reduce the intensity of the modal peaks within the cavity spectrum. In the front wall configuration the purpose of this ventilation was to divert the flow over the cavity. It was expected that the expulsion of mass caused by the upstream propagation of acoustic waves would create an air spoiler upstream of the cavity and cause a similar lofting effect to a solid spoiler. The aim of this was to reduce the intensity of the interactions of the shear layer and the rear wall of the cavity.

The expulsion of mass into the supersonic freestream was also expected to create a shock wave ahead of the cavity front wall. It was expected that this shock wave would reduce the flow velocity over the cavity and therefore alter the modal acoustic properties. A slower velocity over the cavity is expected to reduce the vortex convection speed over the cavity and therefore affect the modal generation feedback loop.

Mesh device	Steady flow resistance Re(Z)*	Ventilation ε (%)
TGF_m1	1.5	0
TGF_m2	0.3	0
TGF_m3	0.3	50

Table 16 – Summary of the porous mesh devices designed for the 1/20th scale cavity model

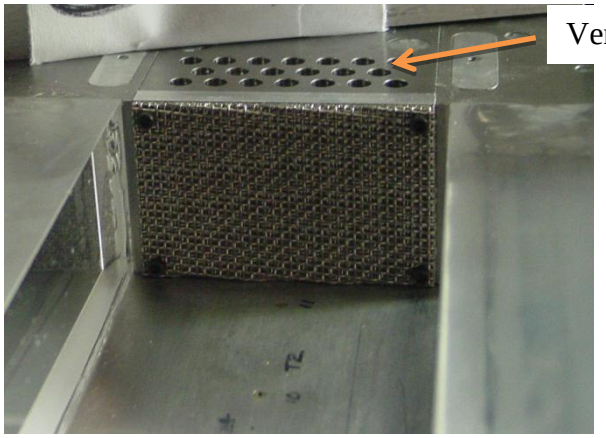

Figure 66 – a) TGF_m3 installed in the ADDICT cavity rear wall

4.5.3 Acoustic foam linings

Acoustic foam liners are used for a wide variety of medium SPL room acoustic applications, such as in recording studios and auditoria. The mechanism through which acoustic foam achieves attenuation is primarily based on the resistance properties of the foam. The foam itself is made up from an open-celled formation which allows the passage of acoustic waves through its structure. The additional viscous resistance created by the passage of the waves through the foam structure absorbs energy from the waves and this attenuation is typically broadband in nature. This resistance is increased for higher modal pressures as the associated particle velocities through the structures are also increased. Therefore, these devices are typically located to coincide with regions of high modal pressure. The attenuation can also be targeted to specific frequency ranges based on the thickness of the absorbent layer. If the thickness of the absorbent layer (L) coincides with the quarter wavelength condition ($L= \lambda/4$) for an incident wave then a higher attenuation will occur at that specific frequency as the point for which the particle velocity, associated with the pressure wave, is greatest will occur within the absorber. A similar effect can also be created by an offset between the absorbent layer and a solid backing plate.

Commercially available acoustic foam was chosen for use within the small scale model cavity based on the reported absorption coefficient profile (*Figure 67*). From this profile it was expected that a large attenuation would be expected at both the second and third cavity modes (2kHz and 3.2kHz respectively) as the absorption coefficient is at least 0.9 (*Figure 67*). However, a subsequent investigation of the acoustic properties of the foam through the use of an impedance tube revealed a measured absorption coefficient with a much lower value ($\alpha<0.2$ (*Figure 67*)). This places a great uncertainty on the expected performance of the foam devices. Nevertheless, a series of foam inserts was designed for the *build 2* cavity model (*Figure 68*). These inserts (*Figure 68*) enabled the attenuation performance of the foam to be investigated when installed into the cavity end walls, side walls, and ceiling.

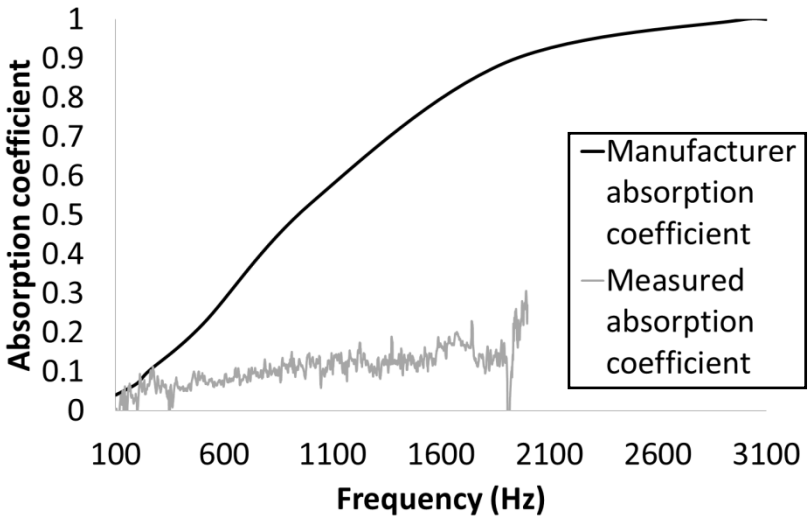

Figure 67 – Comparison between the absorption coefficient profile provided by the acoustic foam manufacturer and the profile measured using the medium scale, medium SPL impedance tube.

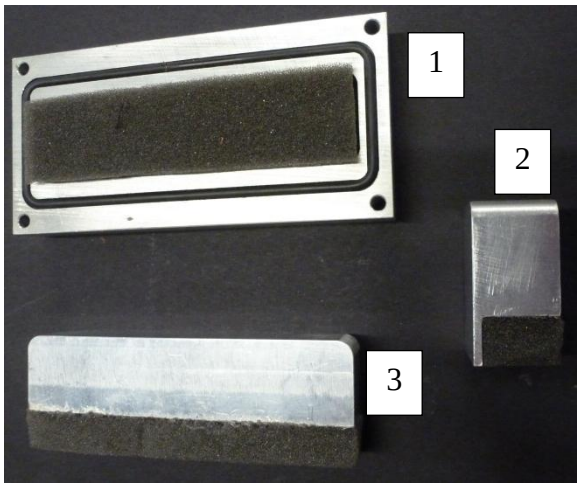

Figure 68 – Foam liner parts for small scale cavity. 1) ceiling lining, 2) end wall lining, 3) side wall lining.

5 Results and discussion of main findings

This section discusses the main findings from the small ($1/40^{th}$) and medium ($1/20^{th}$) scale wind tunnel tests which have been carried out during this study. The discussion starts with the small scale datum cavity and background characteristics and then moves onto the targeted attenuation of the individual modes. Next, the effects of the cavity configuration and environment on the attenuation are discussed. A section is included which discusses the medium-scale supersonic test results which also details the datum characteristics for the medium-scale facility. The final part of this section provides a recommendation for the best approach for the designer to take when designing resonant arrays as cavity palliatives.

5.1 Small ($1/40^{th}$) scale tunnel background noise and datum cavity characteristics

The tunnel background noise was measured for Mach 0.8, 0.9, and 0.95 flow in the absence of either the Build 1 or Build 2 cavities (see *section 3.1.2*) and the resultant spectrum for the Mach 0.9 case is shown in *Figure 69*. The spectrum shows that the background noise across the frequency range of 1 kHz to 5 kHz is between the levels of 108 dB and 120 dB for Mach 0.9 flow. No modal SPL peaks are present between 1kHz and 5kHz. There are small peaks in SPL between 6kHz and 8kHz, which are attributed to higher order duct modes within the wind tunnel working section.

As expected when the Build 1 cavity was installed the broadband SPL increased by around 20dB (*Figure 69*) and the modal peaks typical of open cavity flows become prominent. There is good agreement between the calculated Rossiter frequencies and the measured values (*Figure 69*). The modal frequencies typically occurred within ±4% of the calculated values for Mach 0.9 and 0.95 flows and within ±2% for the Mach 0.8 case. For the Mach 0.95 case the modal peak SPLs were around 5dB higher than for Mach 0.9. For the Mach 0.8 case the modal peak SPLs were typically around 8dB lower than the Mach 0.9 case.

As expected the Build 2 cavity exhibits similar spectral characteristics when compared with the Build 1 configuration. The frequencies of the first and third modes (850Hz and 3.2kHz respectively) for the Build 2 case are within ±1% of those from the Build 1 case. However, the frequency of the second mode (1.9kHz) is around 100Hz (5%) lower for the Build 2 case compared with the Build 1 configuration. This reduced frequency is within ±8% of the calculated value. The broadband noise levels and number of modes exhibited are the same for both cavity Builds. The differences in the modal characteristics are caused by the different approaching boundary layer characteristics experienced by the two cavity Builds (*Table 1* and *Table 2*). For all Mach numbers the

boundary layer thickness (δ) over Build 2 was around 30% greater than for the Build 1 case. Previous studies have demonstrated that a thicker approaching boundary layer can increase the SPL of the dominant second mode, whilst reducing or even eliminating the presence of the first and third modal peaks [17].

Whilst the datum spectra for Builds 1 and 2 are not an exact match the discrepancies between the two are within acceptable bounds. The discrepancies in the spectra can be explained by the differing boundary layer thicknesses over the two cavity Builds. Therefore, both Build 1 and Build 2 exhibit an acceptable spectrum for an investigation into open cavity flows and their control. The following section discusses the correlation investigations which were undertaken to better understand the modal generation process within the cavity flow system. The aim of these investigations was to link the frequencies of the Rossiter modes to underlying processes and events within the cavity flowfield.

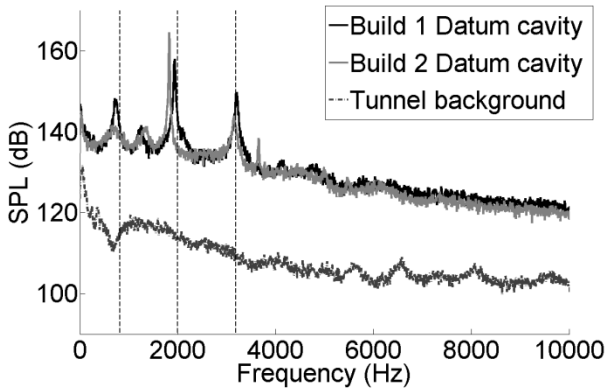

Figure 69 – Build 1 and 2 datum cavity spectra compared to tunnel background noise spectrum (Mach 0.9). (Vertical dashed lines correspond to calculated frequency for the first three Rossiter modes)

5.1.1 Cross-correlation investigation of datum cavity

The cross-correlation of the signals from two transducers identifies the key time differences (*T*) which can be used to infer a relationship between flow events. As the distance between the two ceiling transducers (2 and 3) is known (*Figure 34*) this can be used to derive a mean speed of the disturbance. The cross-correlation profiles between the ceiling transducers for Mach 0.85, 0.90, and 0.95 are shown in *Figure 70*. In each case the peaks are labelled sequentially from zero lag where peaks with a positive time lag (*cp*) are from upstream travelling disturbances and peaks with a negative time lag (*cn*) are from downstream travelling disturbances. For consistency over the Mach number range investigated the peak numbers correspond to local maxima and minima within the correlation profiles.

The peaks relating to the vortex convection and pressure waves were identified by their characteristic speeds, where V_V is the vortex convection speed and V_P is the pressure wave propagation speed. Typically the vortices shed from the front wall of the cavity

convect at around V_V=0.57U_∞ [1] (V_V=186ms^{-1} at Mach 0.95) and the pressure waves are assumed to travel at roughly the local speed of sound (V_p=344ms^{-1}). Therefore for all the cases, peak *cp2* has been identified as being related to the pressure wave (T_p*=0.9, for Mach 0.95 (*Table 17*)) and peak *cn2* has been related to the shed vortices (T_v*=1.58, for Mach 0.95 (*Table 17*)). These peaks also exhibit the largest cross-correlation coefficients and therefore have the greatest significance within the signal.

Peak *cn1* is considered to be caused by the downstream travelling reflection of the pressure waves within the cavity, as the time lag for peak *cn1* is roughly the same as that of peak *cp2*. Similarly, it is proposed that peak *cp3* is related to the upstream reflection of the pressure waves which accompany the vortices within the shear layer as the magnitude of the time lag for peak *cp3* is roughly equal to that for *cn2*. The overall loop frequency (f_a) depends on both the vortical and pressure disturbances and has a time period of $T_a=T_v+T_p$. This characteristic time period can be seen in the cross-correlation profiles where the peak *cp4* has a time lag which corresponds to that expected for T_a (*Figure 70*).

The characteristic mean speeds obtained from the cross-correlation profiles are given in *Table 17* and these values are close to those demonstrated in previous works [1] [92]. The mean speed of the disturbances is used to estimate the travel times of the vortices and pressure waves (T_v and T_p) over the cavity length. The fundamental loop frequency at Mach 0.95 (f_a=1178Hz) was determined from these time periods (T_v*=1.74 and T_p*=1.00 (*Table 18*)) and the values are within 10% of the frequencies calculated from *Equation 1* with the constants of m=1 and α=0. The discrepancy between the calculated and measured f_a values may be caused by the use of the mean velocities provided by the cross-correlation analysis. In *Equation 1* a mean convection speed ($V_V=kU_\infty$) is assumed for the travelling vortices and this may also affect the reliability of the frequency predictions from this model. The speed of the vortex convection is not constant over the length of the cavity [93] [94] and this will have a bearing on the travel time used to set up the fundamental loop process. It is also expected that the speed of the pressure wave propagation within the cavity will vary over the cavity length. Uncertainty also arises from the travel distance for each of the disturbances as typical numerical or schlieren data cannot identify the vortices in the regions close to the cavity end walls [94] due to the high levels of unsteadiness at these locations. The use of the cavity's geometric length provides an upper estimate for the travel distance. Based on examinations of both schlieren and numerical unsteady flow visualisations a better estimate for the effective vortical travel distance (l_e) is l_e=0.9l [94]. If this value for travel distance is used the loop frequency at Mach 0.90 becomes 1288Hz and the difference between the measured and calculated values for f_a reduces to within ±2%. This value also lies within ±2% of the peak shown at 1.2kHz within the SPL spectrum for Mach 0.90 flow (*Figure 69*) and a similar level of agreement is also found for Mach 0.95 and at Mach 0.85.

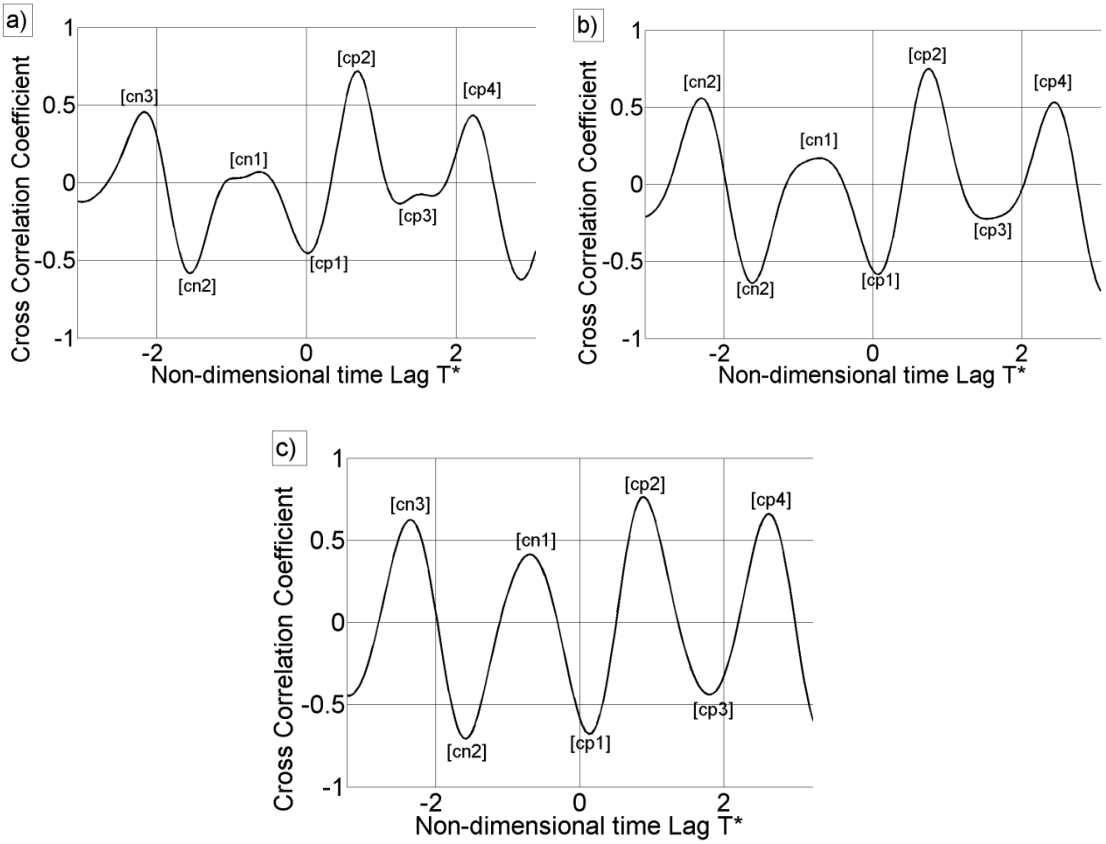

Figure 70 – Measured cross correlation profiles between transducers 2 and 3 on the cavity ceiling for a) Mach 0.85, b) Mach 0.90, and c) Mach 0.95.

Mach number	Characteristic	Peak *cn2*	Peak *cp2*
0.85	T*	1.55	0.69
	V (ms^{-1})	168	377
	V/U∞	0.58	1.3
0.90	T*	1.62	0.77
	V (ms^{-1})	171	360
	V/U∞	0.56	1.2
0.95	T*	1.58	0.90
	V (ms^{-1})	184	327
	V/U∞	0.57	1.0

Table 17 – Measured characteristic velocities obtained from the cross correlation profiles (*Figure 70*).

Mach number	Characteristic	
0.85	T_V*	1.72
	T_P*	0.77
	f_a (Hz)	1162
0.90	T_V*	1.77
	T_P*	0.86
	f_a (Hz)	1160
0.95	T_V*	1.74
	T_P*	1.00
	f_a (Hz)	1178

Table 18 – Measured disturbance travel times over cavity length and estimated fundamental cavity loop frequencies

5.1.2 Auto-correlation investigation of datum cavity

An auto-correlation of a time history is expected to reveal characteristic time scales within a signal and it is expected that this process will show that both T_a and T_b are present in the current cavity flow and that these can then be related to both f_a and f_b. The experimentally obtained values for f_a and f_b are used to derive the Rossiter frequencies through the amplitude modulation approach [89] (*Equation 13* to *Equation 15*). The auto-correlation profiles for transducer 3 located on the cavity ceiling (*Figure 34*) are given in *Figure 71* and the characteristic frequencies obtained are presented in *Table 19*. Corresponding profiles for transducer 2 near the cavity front wall (*Figure 34*) were also analysed and demonstrated both similar correlation coefficients and time lag magnitudes. Therefore, the characteristics obtained are considered to be global throughout the cavity. The plots in *Figure 71* show typical auto correlation profiles where there is a maximum correlation coefficient of 1 at zero time lag with a quasi-sinusoidal profile as time increases. The profiles are symmetrical about the y-axis and therefore only the positive portions are shown.

Peaks *ap3* and *ap6* have the largest auto-correlation coefficients for all Mach numbers ($0.85<M<0.95$) and therefore are considered to be important within the cavity flow (*Figure 71*). The case at Mach 0.90 will be used as an example of the calculation process, where Peak *ap3* has been identified as being related to f_a because its frequency (1290Hz (*Table 19*)) is close to that obtained from the cross correlation profiles (1160Hz (*Table 18*)) and from *Equation 1* (1.2kHz). It is proposed that f_b with a value of around 600Hz is a sub harmonic of f_a and therefore the frequency of f_b would be half that of f_a (around 1.2kHz). It is therefore proposed that peak *ap6* relates to f_b.

To confirm the relationship between f_b and f_a, the values inferred from the auto-correlation profiles (*Table 19*) are compared with values estimated from both the experimentally measured f_a value and the measured spectral data following the graphical approach set out by Delprat [90]. The spectral approach proposed by Delprat [90] also allows for f_a to be found from the cavity spectrum, as the frequency difference between the Rossiter modes ($f_a=f_{n+1}-f_n$). This frequency difference is within ±5% of the f_a values calculated from the auto-correlation profiles and provides evidence in support

of this analysis approach. The lower modulating frequency f_b can be found from the difference between a harmonic of f_a and the corresponding Rossiter mode through the relationship $f_b=nf_a-f_n$ and the values for this at the three Mach numbers investigated are given in *Table 20*. These data in *Table 20* confirms that for all Mach numbers, the modulation ratio is $\zeta\approx0.5$ as demonstrated by the auto-correlation data in *Table 19.*

Peak *ap1* has a delay which corresponds to the time period of the pressure waves within the cavity (T_p*=0.77 (*Figure 71* and *Table 17*)) and peak *ap2* corresponds to the frequency of the second Rossiter mode. The characteristic frequency of peak *ap5* broadly agrees with the frequency of the Second Rossiter mode (2kHz (*Table 21*)). All the peaks within the auto-correlation spectrum are approximately spaced by an equal amount (Δt*=0.84) which corresponds to a signal with a frequency around 4kHz. A signal with this frequency is expected from the pressure wave travel time (T_p*=0.77) within the cavity. This difference relationship between the individual correlation peaks may be the cause of peak *ap4* placing it Δt*=0.84 between *ap3* and *ap5* respectively.

From the values for f_a and f_b obtained from the correlation analyses, the frequencies of the first three Rossiter modes have been calculated through the amplitude modulation approach presented in *Equations 13* to *15*. These frequencies are given alongside the predictions from *Equation 1* and the measured values in *Table 21*. For the second and third Rossiter modes the frequencies obtained through the amplitude modulation method, (*Equation 13* to *15*) are in better agreement with the measurements than those calculated through Rossiter's method (*Equation 1*). This is observed for all Mach numbers and the difference between the amplitude modulation frequency and the measured value was as low as 0.05% (*Table 21*). However, both the amplitude modulation method and the Rossiter equation are less accurate when calculating the frequency of the first mode, where both calculated values are typically more than 10% different to measured frequencies (*Table 21*). Similar characteristics regarding the large uncertainty placed on the prediction of the first mode frequency through the Rossiter equation (*Equation 1*) have been reported previously [89] [91].

To address this large uncertainty placed on the estimates of the first modal frequency, instead of taking f_b as the average of all of the nf_a-f_n values as proposed by Delprat [90], if the modulation ratio (ζ) is calculated for each Rossiter mode (f_n) an improved estimate can be obtained. For all the Mach numbers under consideration the first Rossiter mode (f_1) demonstrates a lower ζ ratio compared with the second and third modes. This accounts for the larger discrepancy when the averaged f_b value is used to calculate the first mode and also explains why f_1 does not equal f_b for any of the cases. For all the first Rossiter modes under all Mach numbers investigated in this current work the value of ζ was lower, in the range $0.4<\zeta<0.46$, than the proposed 0.5 value used for the successful calculation of the other cavity modes. Nevertheless, overall this is strong evidence for the link between the measured modal frequencies and those obtained through the combined use of correlation analysis and the amplitude modulation

approach [89] [90] and this supports the amplitude modulation model proposed by Delprat [89] for transonic flow cases (Mach 0.85 to 0.95).

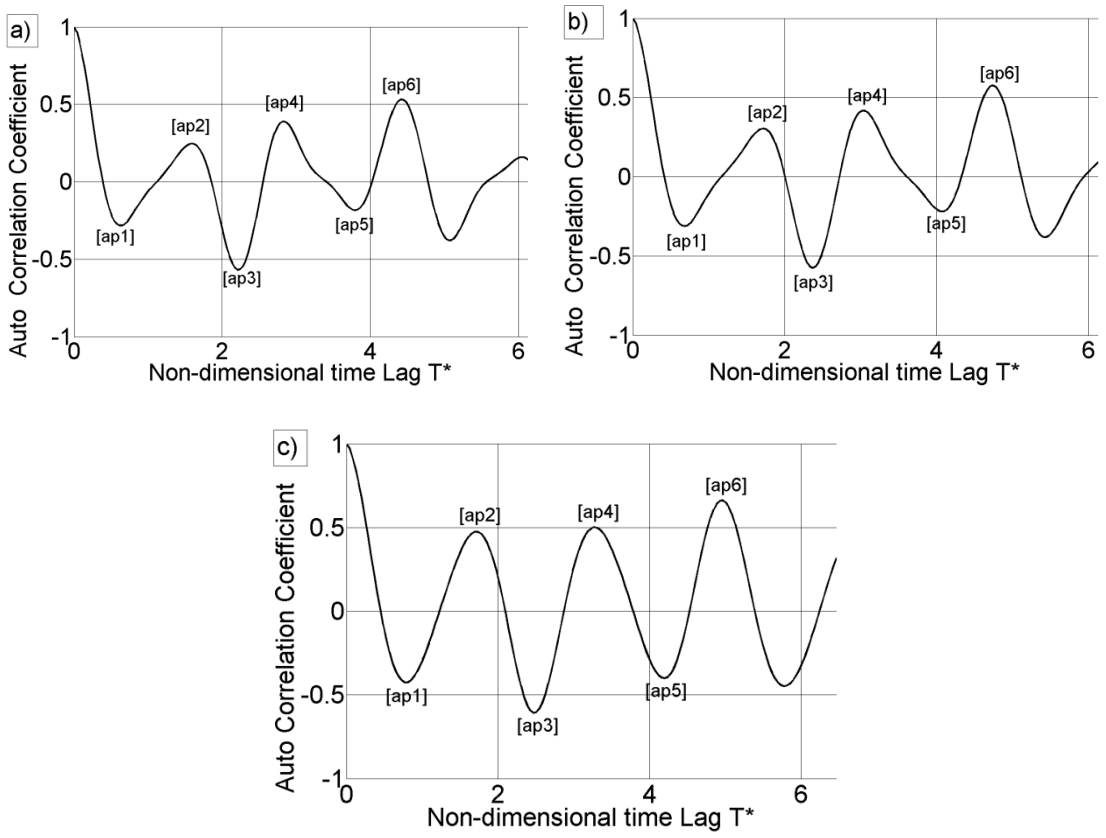

Figure 71 – Measured auto correlation profiles for transducer 3 on the cavity ceiling for a) Mach 0.85, b) Mach 0.90, c) Mach 0.95.

Mach number	Characteristic	Peak ap3 (f_a)	Peak ap6 (f_b)	$\zeta=f_b/f_a$
0.85	T*	2.20	4.41	
	Frequency (Hz)	1314	655	0.50
0.90	T*	2.39	4.74	
	Frequency (Hz)	1290	645	0.50
0.95	T*	2.45	4.97	
	Frequency (Hz)	1311	650	0.50

Table 19 – Measured characteristic time periods and associated frequencies for f_a and f_b obtained from the auto correlation profiles (*Figure 71*)

Mach no	f_a (Hz)	Difference between fundamental frequency harmonics and Rossiter modes $(nf_a-f_n)\approx f_b$			Average f_b	$\zeta=f_b/f_a$
		n=1	n=2	n=3		
0.85	1314	572	655	710	646	0.49
0.90	1290	548	637	667	617	0.48
0.95	1311	599	674	647	640	0.49

Table 20 – Estimated f_b values from measured spectral data [90] to confirm $\zeta= f_b/f_a$ ratio from autocorrelation analysis (Table 3).

Mach number	Mode number	Modal frequency (Hz)			Difference relative to SPL spectral frequency (%)	
		Amplitude modulation approach	Rossiter's equation (*Equation* 1)	From SPL spectra	amplitude modulation approach	Rossiter's equation (*Equation* 1)
0.85	1	659	791	742	11	6.6
	2	1973	1943	1973	0.0	1.5
	3	3287	3095	3232	1.7	4.2
0.90	1	645	813	742	13	10
	2	1938	1998	1943	0.4	3.0
	3	3226	3182	3203	0.7	0.7
0.95	1	661	845	712	7.0	19
	2	1973	2077	1948	1.0	7.0
	3	3284	3308	3286	0.05	0.7

Table 21 – Frequencies derived from the amplitude modulation approach compared with the Rossiter frequency estimate and measured frequency values for Mach 0.85 to 0.95. (Rossiter constants: k=0.57, α=0.062l/h)

The spectral characteristics of a small-scale model of a cavity were investigated over the Mach number range 0.85<M<0.95. This study has provided evidence in support of a link between an amplitude modulation process and the generation of discrete modes within transonic cavity flows. The fundamental aeroacoustic loop frequency within the cavity has been calculated from cross-correlation, auto-correlation and spectral investigations. This revealed the characteristic speeds of the shed vortices and pressure waves which are thought to contribute to the generation of the cavity acoustic modes. The characteristic time delays for the discrete frequencies required to generate the modal peaks were also present in the auto-correlation profiles recorded within the cavity. This demonstrates that the frequencies required for the amplitude modulation process were present within the cavity environment and supports the model of the cavity unsteady flow field previously proposed by Delprat. From the observed characteristics, the second and third Rossiter modal frequencies, for the three Mach numbers considered, were calculated using the amplitude modulation approach on average to within 0.64% of the measured value. This compares favourably to the predictions from the Rossiter equation which was typically accurate to within 2.85%. Therefore these

results provide experimental evidence in support of the amplitude modulation approach proposed by Delprat [89] for open cavities exposed to transonic freestream flow conditions.

5.2 Effect of targeted modal attenuation on the cavity SPL spectrum

The attenuation from a resonant array is expected to occur over a narrow bandwidth and this narrowband attenuation is designed to coincide with the Rossiter modal frequencies within the cavity. Therefore, it is anticipated that a single resonant array will only attenuate one Rossiter mode. The following sections will discuss the findings from arrays which target the second and third modes independently.

5.2.1 Attenuation of the second mode

The primary role of resonant arrays is to attenuate at a particular frequency which coincides with a problem cavity mode. It was therefore of interest to investigate whether the attenuation provided from resonant arrays could be successfully targeted at the different modal frequencies within the small scale model cavity. *Figure 72* demonstrates the attenuation level which can be achieved for a front wall configuration tested at Mach 0.95. In this case ARRAY 2-10 provides an attenuation of 16dB at the second mode (2kHz) which reduces the modal intensity from 163dB to 147dB (*Figure 72*). This level of peak attenuation is of the same order as other passive devices such as spoilers [6] which is an important result as it demonstrates that resonant arrays could provide an alternative approach for peak attenuation. As expected there is no attenuation of the broadband noise within the spectrum as attenuation is only evident between around 1.7kHz and 2kHz. This corresponds to around ±7% of the modal frequency and is much lower than the calculated bandwidth of the device (*Table 10*). Because of this, the OASPL within the cavity was reduced by around 3dB which is much lower than other passive devices, but is in line with expectations for the narrowband attenuation devices.

One consequence of the second mode attenuation at Mach 0.95 is the small increase in the amplitude of the third mode (*Figure 72*). This phenomenon is known as "peaking" and involves the redistribution of energy between the cavity modes from one mode to another receptive mode. At lower Mach numbers no peaking was evident when the second mode was attenuated (see *Section 5.2.4*). A discussion of the proposed mechanism behind the peaking phenomenon is included in *Section 5.2.3*.

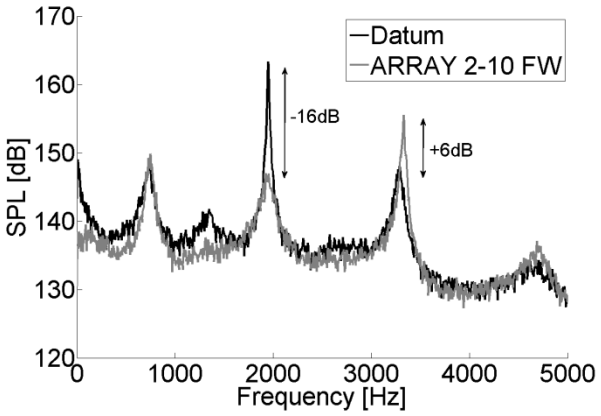

Figure 72 – Targeted attenuation of the second mode from ARRAY 2-10 installed into the cavity front wall (FW) at Mach 0.95

5.2.2 Attenuation of the third mode

The third mode (3.2kHz) can also be attenuated by the targeted approach of resonant arrays. *Figure 73* demonstrates that an attenuation of 16dB can be achieved from a rear wall configuration using ARRAY 3-6. This reduced the modal intensity of the third mode from 148dB to 132dB. As expected there is little effect on the broadband noise within the spectrum and attenuation is observed between 2.8kHz and 3.7kHz. This corresponds to around ±15% of the modal frequency which is lower than the calculated bandwidth (β) of the device. In fact the OASPL increased by around 3dB due to the peaking observed at the second mode (*Figure 73*). Peaking was observed at the second mode for all cases of third mode attenuation.

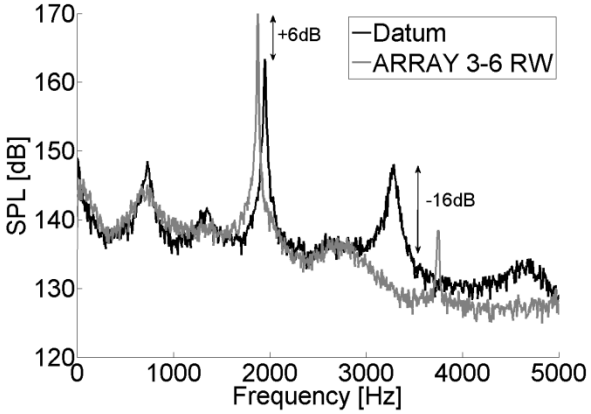

Figure 73 – Targeted attenuation of the third mode from ARRAY 3-6 installed into the cavity rear wall (RW) at Mach 0.95

It has been demonstrated that resonant arrays can provide a useful amount of targeted modal attenuation. The typical levels of peak attenuation (16dB) at Mach 0.95 are around the same order of other passive devices such as spoilers. However, as expected the arrays were only effective over a narrow range of frequencies which span the tuned target mode and as such did not greatly affect the OASPL within the cavity.

5.2.3 Mode switching and spectral peaking

To investigate the underlying cause of the spectral peaking effect, where the attenuation of one mode coincides with the simultaneous amplification of another mode, the time histories for several test cases were analysed using a short term Fourier transform (STFT). A STFT differs from the Fourier transform routine which is used throughout this study in that it performs a Fourier transform routine on a small portion of a data set. By splitting the data in this way the frequency content of the data can be analysed at discrete time steps and the evolution of the dynamic phenomena can be captured in both the frequency and time domains. The STFT method requires a trade-off between the temporal and frequency resolutions. This trade-off is controlled by the values of the sample/window size and the window overlap. The sample/window size was set at 2^{10} and the overlap was set at 2^{9}. These values resulted in resolutions of 0.0064s for the temporal case and 78.13Hz for the frequency case. Whilst, this frequency resolution is around 20 times less than that used for the spectral analysis it is equivalent to 6.5% of the frequency separation of the individual modes. This enables the individual modes to still be identified by their frequency. However, due to the larger frequency resolution the peak values for the modal SPL will differ between the spectrogram and the typical spectral plots. The data from this process are plotted as a carpet plot with time on the x-axis, frequency on the y-axis, and contours coloured by SPL.

The phenomenon of peaking has been discussed in previous studies relating to other cavity palliatives [113]. Peaking involves the redistribution of energy between the cavity modes from one mode to another receptive mode. This mode switching behaviour has been demonstrated within open cavity flows at low (<Mach 0.1) and medium (Mach 0.4) flows [114] [115]. *Figure 75a* shows the spectrogram from the STFT analysis of the small scale datum cavity flow at Mach 0.95. The three prominent Rossiter modes are seen as the dark horizontal bands at frequencies of around 750Hz, 2kHz, and 3.2kHz where the darker colour corresponds to a higher SPL intensity. In this case the mode switching phenomenon is present for the second and third modes. Periods of high intensity of the third mode coincide with periods of low intensity for the second mode and periods of high intensity for the second mode coincide with periods of low intensity at the third mode. This is denoted by the solid vertical lines enclosed by arrows. To highlight this effect the same data is re-plotted with defined cut on levels for the individual modes (*Figure 75b*). This creates a plot where a point is only made when the modal intensity increases over a defined level. *Figure 75b* provides a clearer indication of the mode switching behaviour between the second and third modes. The intermittency of the first mode does not appear to be related to the occurrence of either the second or third Rossiter modes.

When a large attenuation was demonstrated at either the second or third Rossiter mode the intensity of another mode within the cavity spectrum was seen to increase. It is proposed that this increase in the modal intensity is related to the switching of energy between the modes. *Figure 76* shows the STFT spectrograms for the cases of targeting

the second (*Figure 76a*) and third (*Figure 76b*) Rossiter modes which resulted in peaking. These plots show that for a cavity with an array configuration the intermittency of the modes is removed and the mode which undergoes the peaking effect becomes dominant for all time steps within the sample. The targeted attenuation of a mode appears to impede the modal receptivity to the switching energy within the cavity and instead of the energy being spread between several modes it is limited to a single frequency. This limiting of the energy dispersal manifests as the increase in modal amplitude seen in *Figure 72* and *Figure 73*.

When the second mode was targeted peaking only occurred at Mach 0.95 and not lower Mach numbers as can be seen for the Mach 0.90 case in Figure 74. In this Mach 0.90 case (Figure 74) only the second mode is affected by the array with around 14dB of peak attenuation. However, when the third mode was targeted peaking occurred at all subsonic Mach numbers tested. Within the small scale cavity datum spectrum the second mode is dominant with an SPL of around 164dB. The third mode has the second largest intensity with an SPL of around 150dB. Therefore, the receptivity of a mode is thought to be related to the intensity level of a mode. If a mode has an SPL below a certain threshold that mode will no longer receive the shared energy and peaking will occur. For instance, a small attenuation at the third mode will reduce the modal SPL to a relatively low level and the mode may no longer be receptive to the shared energy. However, the same attenuation level at the second mode may result in the modal intensity remaining above the critical threshold value and so the mode is still receptive to the shared energy. In this example case the attenuation of the third mode would result in peaking as the energy cannot be accepted by the third mode. However, the attenuation of the second mode will not stop the mode accepting the shared energy and would not be expected to cause peaking within the spectrum.

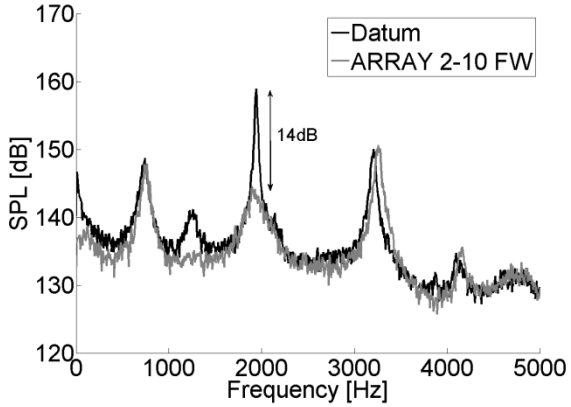

Figure 74 – Attenuation from ARRAY 2-10 installed in the cavity front wall at Mach 0.90 to show no peaking at the third mode for Mach number below M=0.95.

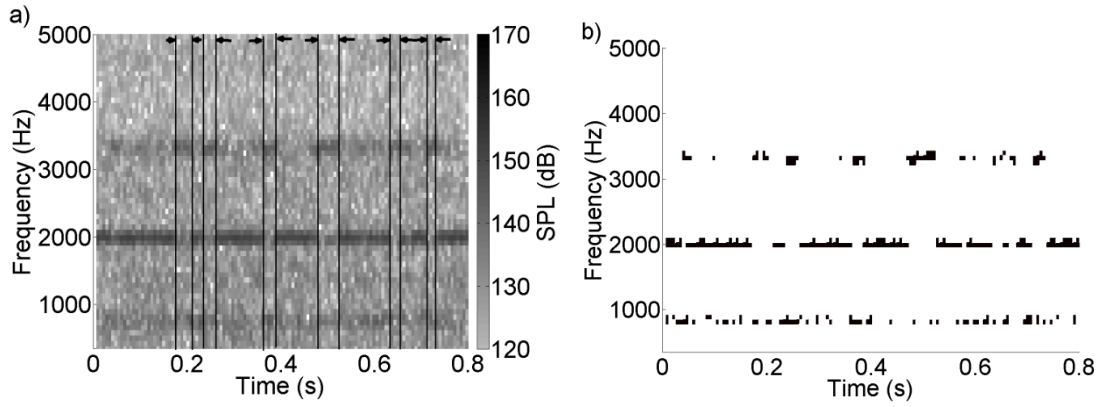

Figure 75 – a) Datum spectrogram for Mach 0.95 freestream flow (vertical lines enclosed by arrows indicate mode switching periods), b) Datum spectrogram for Mach 0.95 freestream flow with cut on levels defined for individual modes to highlight mode switching (1st= 137dB, 2nd=145dB, 3rd=140dB).

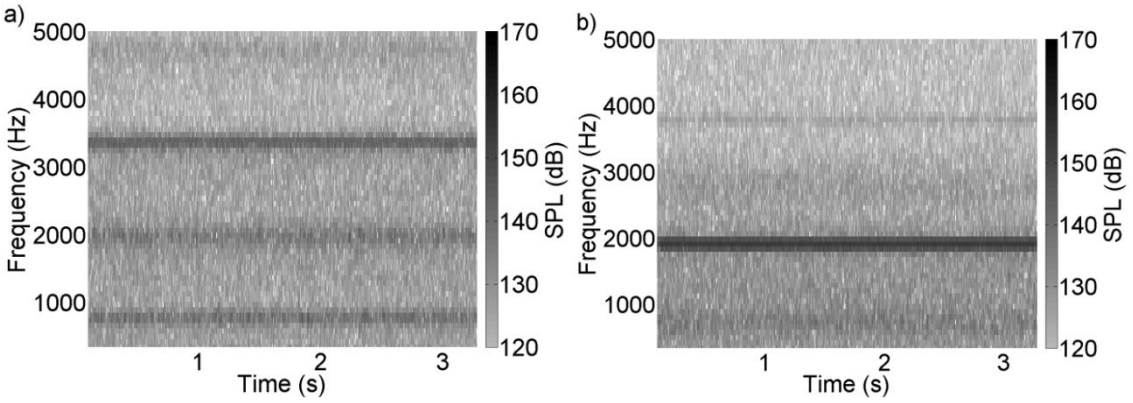

Figure 76 – Spectrogram for cavity configuration at Mach 0.95 with a) ARRAY 2-10 FW, b) ARRAY 3-6 RW

5.3 Effect of Mach number on attenuation under subsonic conditions

The effect of Mach number on the attenuation provided by resonant arrays was investigated using the small ($1/40^{th}$) scale cavity model. The attenuation performance of arrays for the second and third modes was assessed over the range Mach 0.8 to 0.95.

When the second mode was targeted using ARRAY 2-10 the attenuation increased from 9dB at Mach 0.8 up to 16dB at Mach 0.95 (*Figure 77*). For the datum cavity case the increase in Mach number from 0.8 to 0.95 resulted in a 12dB increase in the SPL at the second mode (*Figure 77*). This increase in SPL corresponds to around a 4 fold increase in the acoustic pressure (p') at the second mode. Therefore, the resonant array is expected to provide a larger attenuation at higher Mach numbers, which is in agreement with the measurements (*Figure 77*). The attenuation achieved by ARRAY 2-1 at these high subsonic Mach numbers (Mach 0.8 to Mach 0.95) is a notable improvement over previous work which did not show attenuation of the modal peaks at Mach numbers above 0.53 [38]. It should also be noted that for the Mach 0.95 test case peaking of the third mode at around 3.2kHz was observed (*Figure 77c*). As discussed in *Section 5.2.3* this is due to the large attenuation of the second mode which prevented it receiving shared energy from the cavity flow mechanism. Peaking was not demonstrated for any second mode attenuation case at Mach numbers below Mach 0.95.

Attenuation of the third mode also followed the trend of increased attenuation for the higher Mach numbers with attenuation increasing from 10dB at Mach 0.8 to 16dB for Mach 0.95 (*Figure 78*). Again it is thought that this increase in attenuation is related to the increase in acoustic pressure associated with the greater SPL for higher Mach number cavities. For all Mach numbers (Mach 0.8 to 0.95) peaking was evident when the third mode was attenuated. In opposition to the attenuation levels the amount of peaking reduced from 14dB at Mach 0.8 to 6dB for Mach 0.95. The proposed mechanism for this peaking was discussed in *Section 5.2.3*. The reduction in peaking with increased Mach number is related to the SPL of the cavity modes. Despite the greater attenuation at the higher Mach numbers the modal SPL is larger. Therefore, the mode requires a greater level of attenuation relative to the cavity SPL to reduce it below the expected peaking threshold value.

In general, the performance of resonant arrays increases with increasing subsonic Mach number. This relationship was demonstrated at the second mode using ARRAY 2-1 and at the third mode using ARRAY 3-1 over the Mach number range Mach 0.8 to 0.95 (*Figure 79*). A useful amount of attenuation can be achieved between Mach 0.8 and Mach 0.95 at both the second and third cavity modes. Attenuation at the second mode increases from 8dB at Mach 0.8 up to a plateau of around 15dB above Mach 0.9 (*Figure 79b*). This increase in attenuation of the second mode follows the increase in SPL of the second mode from around 148dB at Mach 0.8 up to 161dB at Mach 0.95. The SPL of the second mode after attenuation remains relatively constant over the Mach number range Mach 0.8 to Mach 0.95, which indicates that attenuation beyond this level may

not be possible as broadband noise sources may be present which will not be affected by the resonant array.

The attenuation of the third mode increases from around 3dB at Mach 0.8 up to around 15dB at Mach 0.95 (*Figure 79b*). A peak in attenuation is reached at around Mach 0.86 and at Mach number above this the level of attenuation follows the SPL of the datum modal peak. As with the second mode a drop in datum modal SPL results in a drop in modal attenuation. The SPL of the attenuated third modes across the Mach number range 0.8 to 0.95 are also relatively constant at a level which corresponds to the broadband level. As the resonant arrays are narrowband devices it was not expected that they would attenuate noise from broadband noise sources. Importantly attenuation of the modal peaks does not decrease at the higher subsonic Mach number as is often observed for other passive palliatives [7].

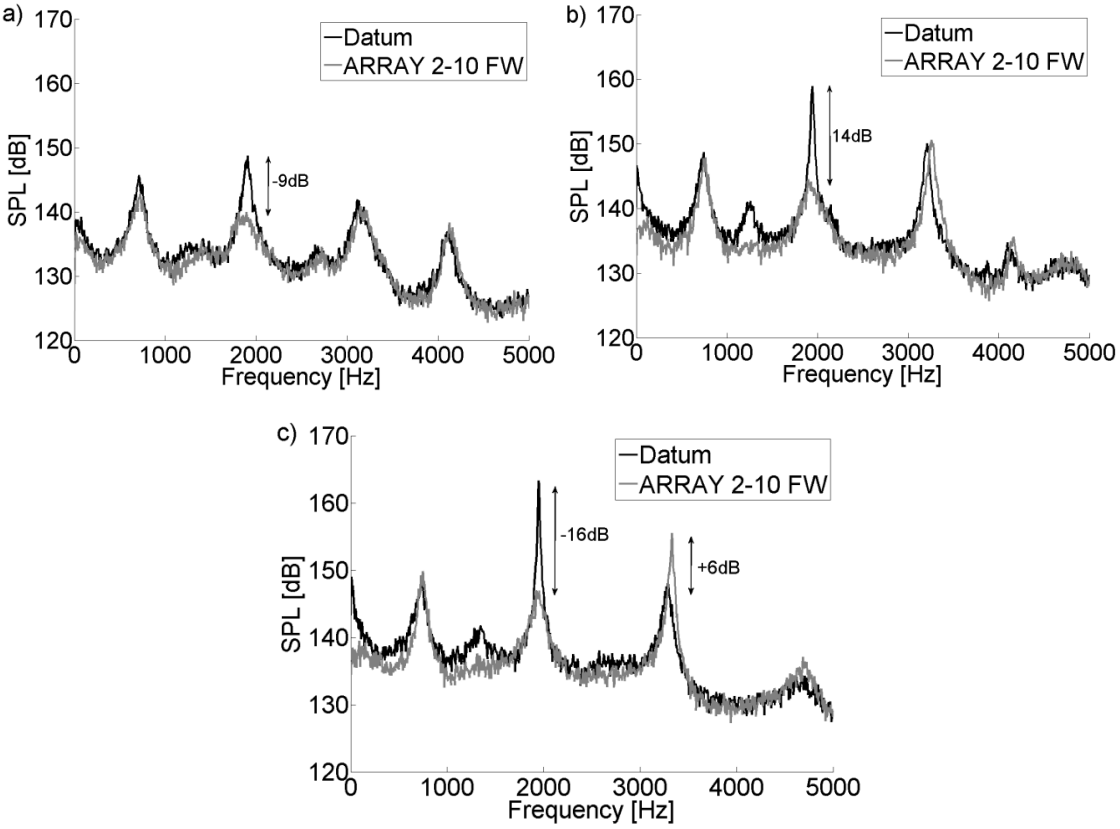

Figure 77 – Attenuation from ARRAY 2-10 installed in the cavity front wall for a) Mach 0.8, b) Mach 0.9, and c) Mach 0.95

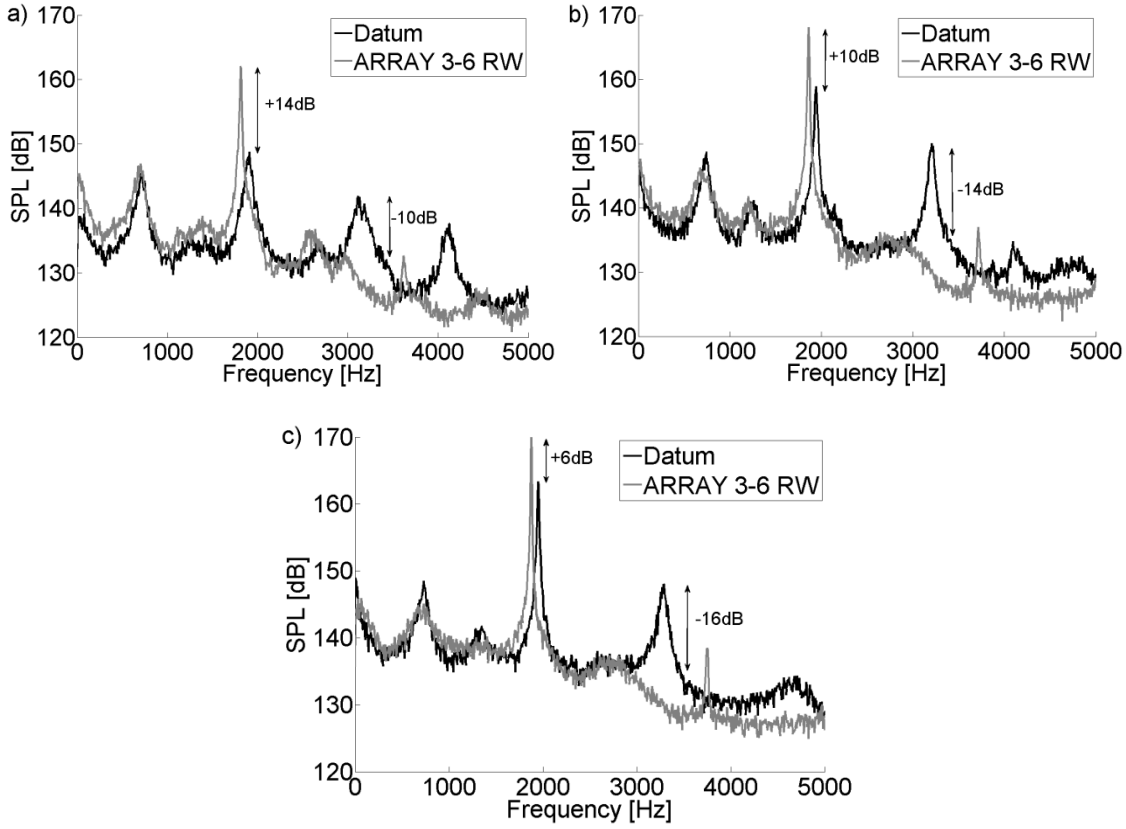

Figure 78 – Attenuation from ARRAY 3-6 installed in the cavity front wall for a) Mach 0.8, b) Mach 0.9, and c) Mach 0.95

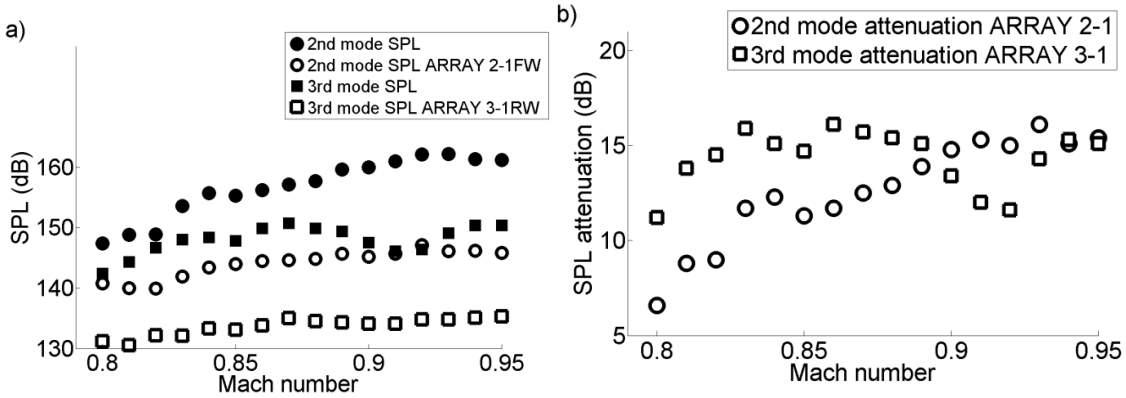

Figure 79 – a) SPL for modal peaks with and without resonant arrays against varying Mach number, b) SPL attenuation from ARRAY 2-1 and ARRAY 3-1 over the range Mach 0.8 to 0.95.

5.4 Targeted attenuation at 1/20th scale

An opportunity arose to carry out an investigation of palliative performance in a 1/20th scale model cavity. Whilst the main focus of this investigation was to assess the performance of resonant arrays under supersonic freestream conditions the facility also had the ability to operate up to Mach 0.7 subsonically. It was therefore of interest to investigate whether resonant arrays designed using the same approach as used for the small (1/40th) scale tests would attenuate the modal peaks within a medium 1/20th scale cavity and in a different facility.

5.4.1 Datum modal characteristics for the medium 1/20th scale cavity model

As the 1/20th scale testing took place in a different facility the modal characteristics within the cavity differ somewhat from the 1/40th scale case. The SPL spectra over the cavity ceiling for the 1/20th scale cavity at Mach 0.7 are shown in *Figure 80a*. The spectrum displays two clear modal peaks with the peaks at 800Hz and 1250Hz corresponding to the second and third Rossiter modes respectively. The spectra cropped to these modes are shown in *Figure 80b* and *Figure 80c* respectively. No modes are present at higher frequencies than the third mode and the broadband noise level decreases rapidly from 135dB at 2kHz to around 125dB at 5kHz. Unlike with the 1/40th scale case, the third mode is dominant within the 1/20th scale cavity (*Figure 80*). At 1/20th scale the third mode exhibits a narrow peak with a width of around 200Hz. However, the second mode exhibits a wider peak with a width of around 400Hz. The second mode also consists of multiple split peaks. It is expected that the narrow third mode can be successfully attenuated using resonant arrays. However, the wider second mode may not be suitable for attenuation from the targeted approach offered by resonant arrays. The following sections will discuss the results from the resonator tests at Mach 0.7. The SPL of both modes typically increases by around 15dB from the front of the cavity to the rear. The modal shapes correspond well to the calculated shapes (*Figure 81*). It is expected that little or no attenuation will be exhibited at the transducer locations which correspond to the modal pressure nodes as the reduced pressure at this point will not improve the resistance characteristics of the arrays. For the second mode these positions are at x/l of 0.20 and 0.65 and for the third mode the nodes are at an x/l of 0.2, 0.5, and 0.8.

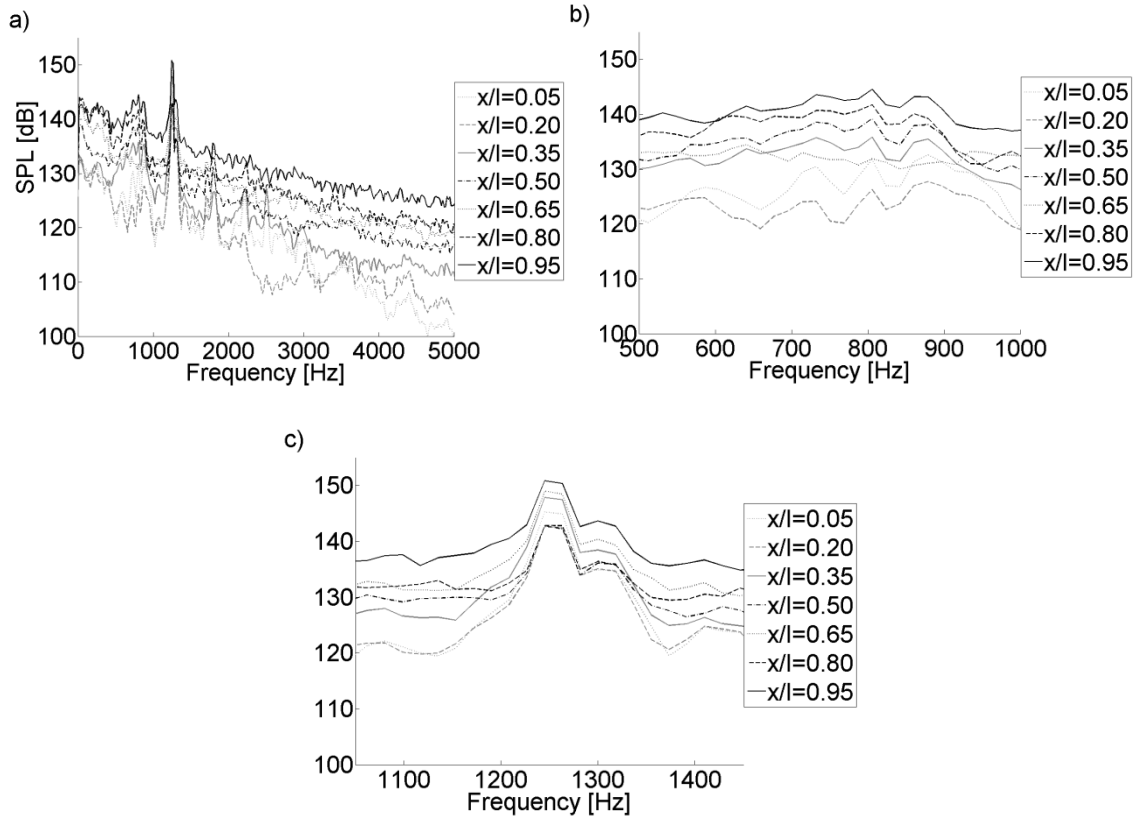

Figure 80 – a) Datum cavity spectrum for the ADDICT cavity model at Mach 0.7 at each transducer location, b) Datum cavity spectrum for the ADDICT cavity model at Mach 0.7 cropped to the second mode only, c) Datum cavity spectrum for the ADDICT cavity model at Mach 0.7 cropped to the third mode only.

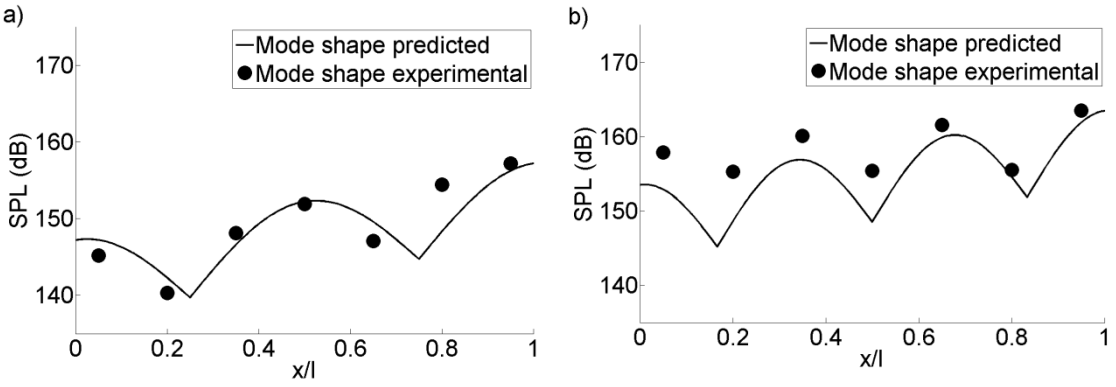

Figure 81 – a) Calculated and measured mode shape for the second mode within the ADDICT cavity model at Mach 0.7, b) Calculated and measured mode shape for the third mode within the ADDICT cavity model at Mach 0.7

5.4.2 Targeted attenuation of the second mode

Following the successful attenuation of the second mode within the small ($1/40^{th}$) scale tests an array (TGF 2-1) was designed to target the second mode within the medium scale ($1/20^{th}$) cavity. TGF 2-1 was designed following the same principles as ARRAY 2-1 (*section 4.4.1*). However, due to the lower Mach number (Mach 0.7 compared to Mach 0.8-0.95 for the $1/40^{th}$ scale cases) and the different modal characteristics it was unknown if a resonant array would be a suitable palliative for the second mode within the $1/20^{th}$ scale case. *Figure 82* shows that TGF 2-1 has no effect on the cavity SPL for the front wall configuration. The same disappointing result was also exhibited for the rear wall configuration. Across the cavity ceiling there was no attenuation exhibited for either the front or rear wall configurations. Therefore, this test case demonstrates that the modal characteristics of the ADDICT cavity at Mach 0.7 causes difficulties for successful attenuation using a resonant arrays. Due to the low Mach number (Mach 0.7) the SPL of the targeted modal peak is relatively low which is also expected to have a detrimental effect on the resistance properties of the array and therefore reduce the ability to attenuate. The wideband and split nature of the second mode are also not ideal for targeting with resonant arrays as the devices only offer narrowband attenuation.

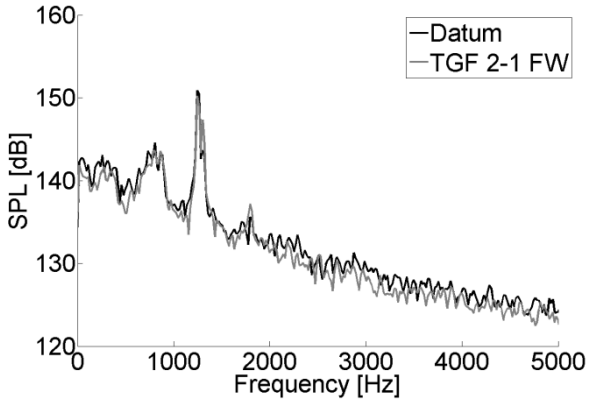

Figure 82 – Spectrum comparison with TGF 2-1 in front wall (FW) at Mach 0.7. (Transducer x/l=0.95)

5.4.3 Targeted attenuation of the third mode

A high level of attenuation has been demonstrated at the third mode within the small ($1/40^{th}$) scale cavity (*Figure 73*). TGF 3-1 was designed following a similar design principle to the small scale test cases (notably ARRAY 3-1). However, due to the different spectral characteristics of the medium scale cavity it was unknown if an array designed based on the small scale finding would provide a comparable high level of attenuation.

Figure 83a shows that TGF 3-1 achieved an attenuation of around 4dB at the third mode within the medium ($1/20^{th}$) scale cavity. This attenuation is much lower than that exhibited for the small scale test cases, where attenuation levels were up to 15dB for a similar device at Mach 0.9. However, it was expected that testing at a lower Mach number would result in lower attenuation levels due to the lower acoustic pressure

within the cavity at the lower Mach numbers. An attenuation of around 4dB was typical across the cavity ceiling for the rear wall configuration (*Figure 83b*). For the front wall configuration attenuation levels on the ceiling near to the front wall (x/l=0.05 and x/l=0.2) improved to around 10dB. However, attenuation across the remaining cavity ceiling was of a level similar to the rear wall case. For both front and rear wall configurations there was around 3dB of broadband attenuation exhibited at frequencies at and above the third mode (*Figure 83a*). In a similar manner to the small scale tests when the third mode was targeted the second mode exhibited peaking (*Figure 83a*). The cause of this peaking effect was discussed in *section 5.2.3*.

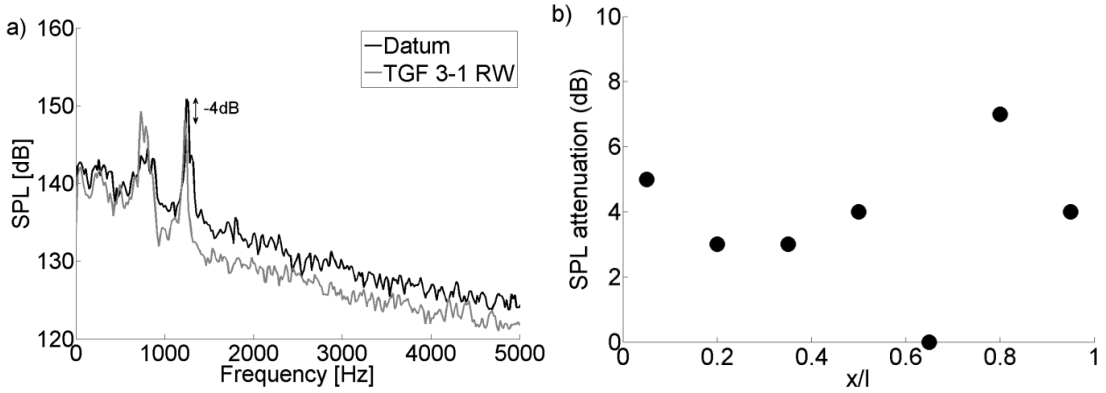

Figure 83 – a) Attenuation from TGF 3-1 in the rear wall (RW) at Mach 0.7. (Transducer x/l=0.95), b) Attenuation from TGF 3-1 over the cavity ceiling for Mach 0.7.

5.4.4 Can the poor attenuation at low Mach number (Mach 0.7) be improved by combined installation?

No attenuation of the second cavity mode at 800Hz was exhibited when the second mode was targeted with a single resonant array configuration (*Figure 82*). Therefore it was decided to investigate the attenuation that was exhibited at the third mode through a combined configuration using an array which did exhibit some useful attenuation. This combined configuration placed TGF 3-1 at both the front and rear wall of the cavity. This combined approach improved the attenuation on the ceiling at x/l=0.95 from 4dB up to 9dB (*Figure 84a*) and also improved the attenuation near the front wall (x/l=0.05) up to around 15dB (*Figure 84b*). However, the improved attenuation of the third mode led to significant peaking at the second mode (*Figure 84a*), which was typically amplified by around 12dB. This combined installation produced an average OASPL attenuation of around 2dB over the cavity ceiling. A wider investigation of the effect of combined arrays is conducted for the small scale cavity in *section 5.6.1*.

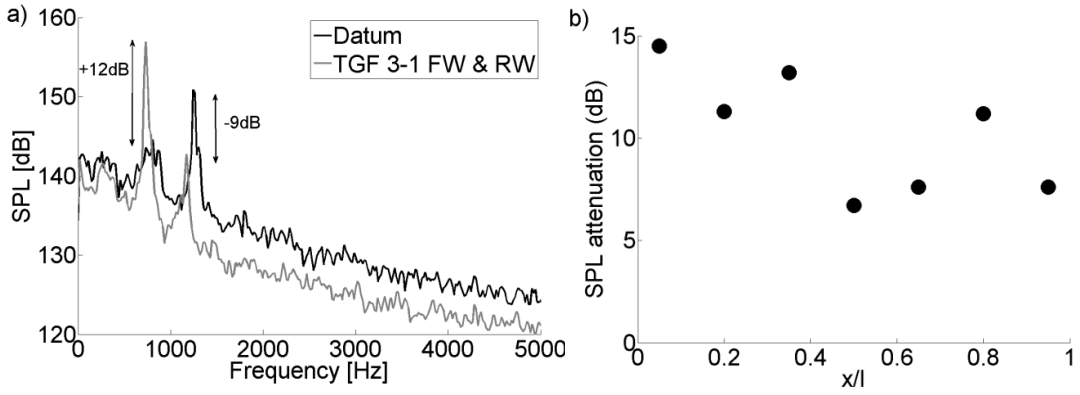

Figure 84 – a) Attenuation from the combined installation of TGF 3-1 in the front and rear cavity walls at Mach 0.7 (transducer x/l=0.95), b) Attenuation of the third mode from TGF 3-1 across the cavity ceiling at Mach 0.7.

5.5 The impact of array location within cavity upon attenuation performance

Within a cavity there are five prospective surfaces which could be treated with resonant arrays. These are the front wall, rear wall, ceiling, and two side walls. The small scale ($1/40^{th}$) *Build 1* cavity model enabled the performance of resonant arrays to be investigated at both the front and rear wall of the cavity. The *Build 2* cavity model was used to assess the performance of arrays installed into the cavity ceiling and side walls.

Previous studies [38] [35] placed the resonator at the rear wall as this is closest to the source of the pressure instability within the cavity and a Helmholtz type resonator is expected to achieve a greater attenuation when placed in a region of high modal pressure. Therefore, it was expected that placing a resonator at the cavity rear wall would result in a higher attenuation than when placed at the front wall. This study will investigate the performance of arrays installed into each of the five internal surfaces within a cavity.

5.5.1 Cavity front and rear end walls

The assumption that a rear wall array configuration will provide a greater level of attenuation than the front wall arrays was examined experimentally. *Figure 85* demonstrates that for an array which targets the second mode (ARRAY 2-1) a greater attenuation is achieved for a front wall installation. In this case the front wall configuration provides 14dB attenuation (*Figure 85a*) compared to 8dB for a rear wall configuration (*Figure 85b*). However, when the third mode was targeted with ARRAY 3-1 an attenuation of 9dB was achieved for the front wall configuration (*Figure 86a*) and an attenuation of 14dB was achieved for the rear wall configuration (*Figure 86b*).

The higher attenuation achieved by placing the *ARRAY 2-1* resonator at the front wall rather than the rear wall could be explained by the characteristics of the pressure waves. The source of the pressure instability is widely regarded as being the impingement of the shear layer upon the freestream edge of the cavity rear wall [96]. The pressure waves therefore do not impinge normally upon the upstream facing surface of the rear

wall. However, as the pressure propagates upstream within the cavity the waves are thought to propagate parallel to the ceiling. This will result in the wave impinging at an angle close to normal when the wave reaches the cavity front wall. From the analytical model it was expected that the maximum attenuation is achieved when the pressure wave impinges normally upon the resonator faceplate. The attenuation is expected to drop to zero for the case where the resonator orifice is orthogonal to the pressure wave propagation direction. This effect of orthogonality may be more noticeable for the *ARRAY 2-1* resonator as it has an orifice aspect ratio of d/t = 0.2 and this is compared to d/t = 0.75 for *ARRAY 3-1*. A larger orifice diameter may be less susceptible to the orthogonality of the pressure wave because of the greater range of angles for which there is a clear path through the neck. Certainly *ARRAY 3-1* was capable of a greater attenuation when installed at the rear wall compared to *ARRAY 2-1* which has a lower porosity (ε) and d/t ratio.

The effect of the aspect ratio of the orifices may be further complicated by the different number of perforations in *ARRAY 2-1* and *ARRAY 3-1*. *ARRAY 2-1* has 35 resonators compared to 8 in *ARRAY 3-1* due to the difference in pitch spacing and the fixed size of the arrays faceplate. It has been previously shown that the total amount of attenuation is directly proportional to the number of resonators [38]. Although this previous case looked at individually installed resonators it is expected that *ARRAY 2-1* would achieve a greater attenuation than *ARRAY 3-1* when placed in ideal conditions with orthogonal pressure wave impingement. This is evident for the front wall installation however it does not hold for the rear wall where the pressure wave may not impinge normally to the resonator orifice. Therefore, the location of the array is thought to be more important than the number of resonators installed. It is thought that as part of the modal generation process a pressure wave travels upstream within the cavity and impinges normally on the front wall this wave then undergoes a reflection before reaching the rear wall. Therefore, the pressure waves will have different characteristics at the various locations within a cavity.

In general, arrays which target the second mode achieve a higher level of attenuation when installed into the front wall of the cavity (*Figure 87a*). Typically, a front wall configuration will provide around 8dB more attenuation at the second mode compared to a rear wall case. For arrays which target the third mode the attenuation is less sensitive to the array location, but typically a rear wall configuration will provide around 4dB more attenuation compared with a front wall case (*Figure 87b*).

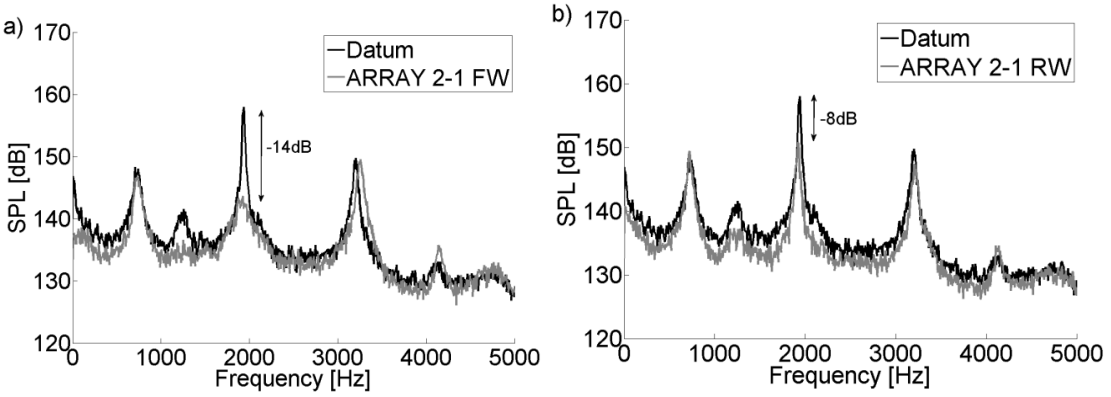

Figure 85 – Attenuation from ARRAY 2-1 installed in the cavity end walls for Mach 0.9 flow

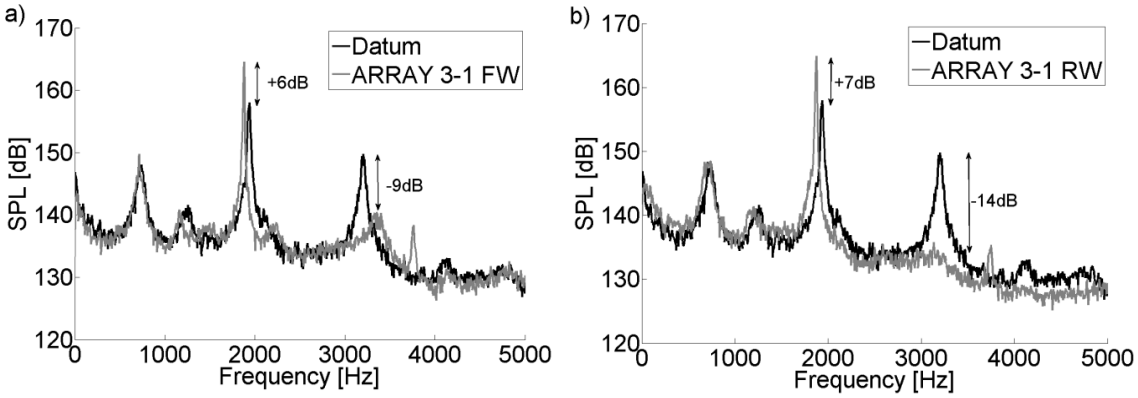

Figure 86 – Attenuation from ARRAY 3-1 installed in the cavity end walls for Mach 0.9 flow

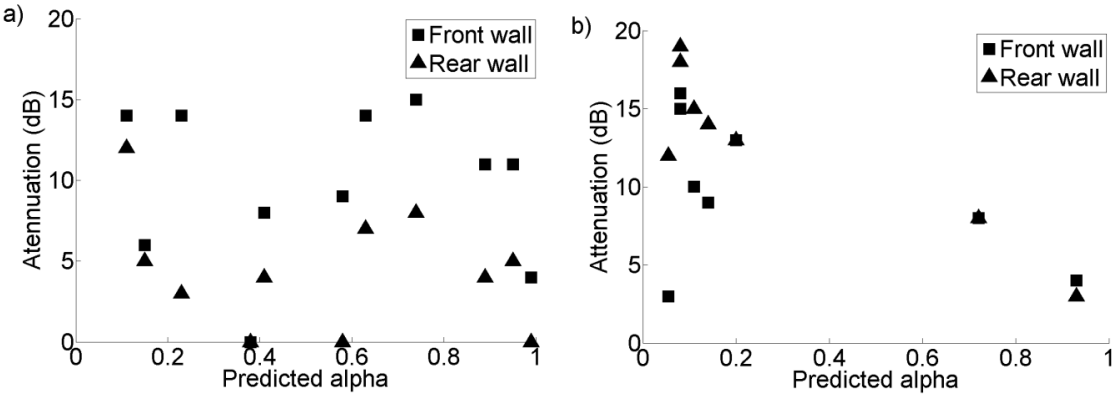

Figure 87 – Attenuation comparisons for front and rear wall configurations a) second mode arrays, b) third mode arrays. (Mach 0.9).

5.5.2 Do the other surfaces within the cavity matter?

Whilst the front and rear cavity walls offer good levels of attenuation for various resonator configurations it was also of interest to investigate whether a reasonable level of attenuation could be achieved from treating the side walls and ceiling of the cavity. As both the side wall and cavity ceiling have a greater surface area a larger number of resonant orifices could be installed into the surface. Therefore, an attenuation performance benefit was expected for these surfaces when treated with resonant arrays.

The cavity spectra for ARRAY 2-1 installed into the cavity side wall and ceiling are shown in *Figure 88*. It was expected that this array would attenuate at the second mode, however no attenuation was present in the spectra for either the side wall or ceiling case. The poor performance levels were also exhibited for arrays which targeted the third mode (ARRAY 3-1 and ARRAY 3-2).

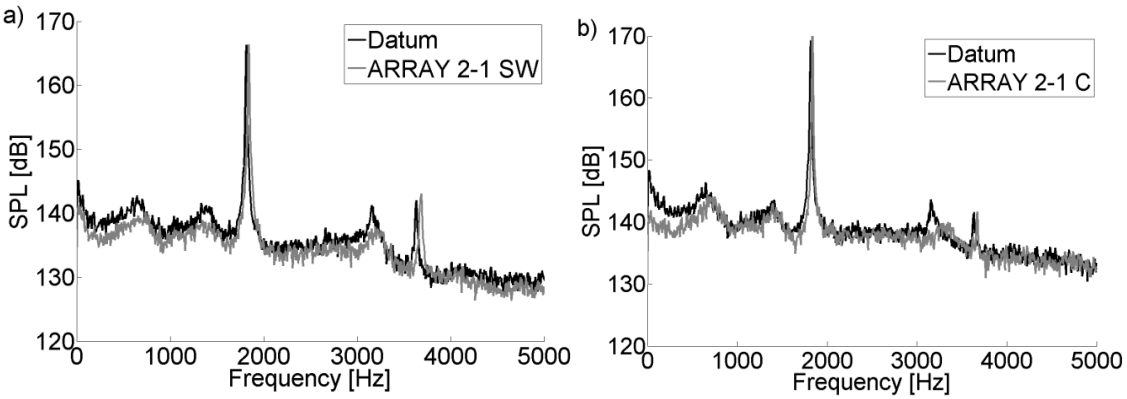

Figure 88 – Attenuation from ARRAY 2-1 installed in the cavity a) Side wall (SW), b) Ceiling (C) (N.B. position of transducer for ceiling case moved from x/l=0.95 to x/l=1 on rear wall). (Mach 0.9)

5.6 Effect of combined palliatives on attenuation performance

To improve upon the attenuation performance from a single palliative the performance of multiple combinations were investigated. This section firstly discusses the performance of multiple resonant array cavity configurations and secondly a combination of a spoiler with resonant arrays.

5.6.1 Attenuation performance of multiple resonant arrays

This study has demonstrated that resonant arrays can successfully attenuate a single modal peak within a typical open cavity spectrum. However, the performance from resonant arrays could be improved upon. Firstly the ability to improve upon the attenuation of a single mode is investigated using multiple arrays tuned to a single frequency within the cavity. Secondly, as each array can only attenuate one mode the attenuation performance from a combination of two differently tuned arrays is investigated. The combined installations are expected to improve upon single mode attenuation and allow for the simultaneous attenuation of multiple modes within the cavity spectra. The differently tuned arrays are also expected to ameliorate the peaking

effects demonstrated for typical third mode attenuations and higher Mach number second mode attenuations.

5.6.1.1 Multiple arrays to target a single modal frequency

It has been demonstrated that ARRAY 2-1 can successfully attenuate the second mode within the small scale cavity spectrum (*Figure 77*) and that the greatest levels of attenuation were achieved for a front wall array configuration (*Figure 87*). To improve upon the single mode attenuation from an individual configuration a cavity was configured with multiple resonant arrays. This placed ARRAY 2-1 at both the front and rear wall of the cavity.

As expected, the attenuation from the multiple arrays was greater than the attenuation from a single device. At all Mach numbers the combined configuration provided up to 5dB more peak attenuation when compared with the single device configuration (*Figure 89* and *Figure 85*). The increase in peak attenuation was also coupled with an increase in the broadband attenuation, with around 2dB more attenuation for the combined case compared with the individual case. For both Mach 0.8 and 0.9 a slight (4dB) attenuation of the third mode is also present within the spectrum (*Figure 89*). The attenuation of the third mode is not present for the Mach 0.95 case as this is where the peaking phenomenon exhibited by the individual configuration would be expected to amplify the third mode. The addition of the extra resonant array has absorbed part of the extra energy that would be associated with the peaking phenomena. In a similar manner to the individual cases the attenuation from this combination increased from 11dB at Mach 0.8 to 20dB at Mach 0.95.

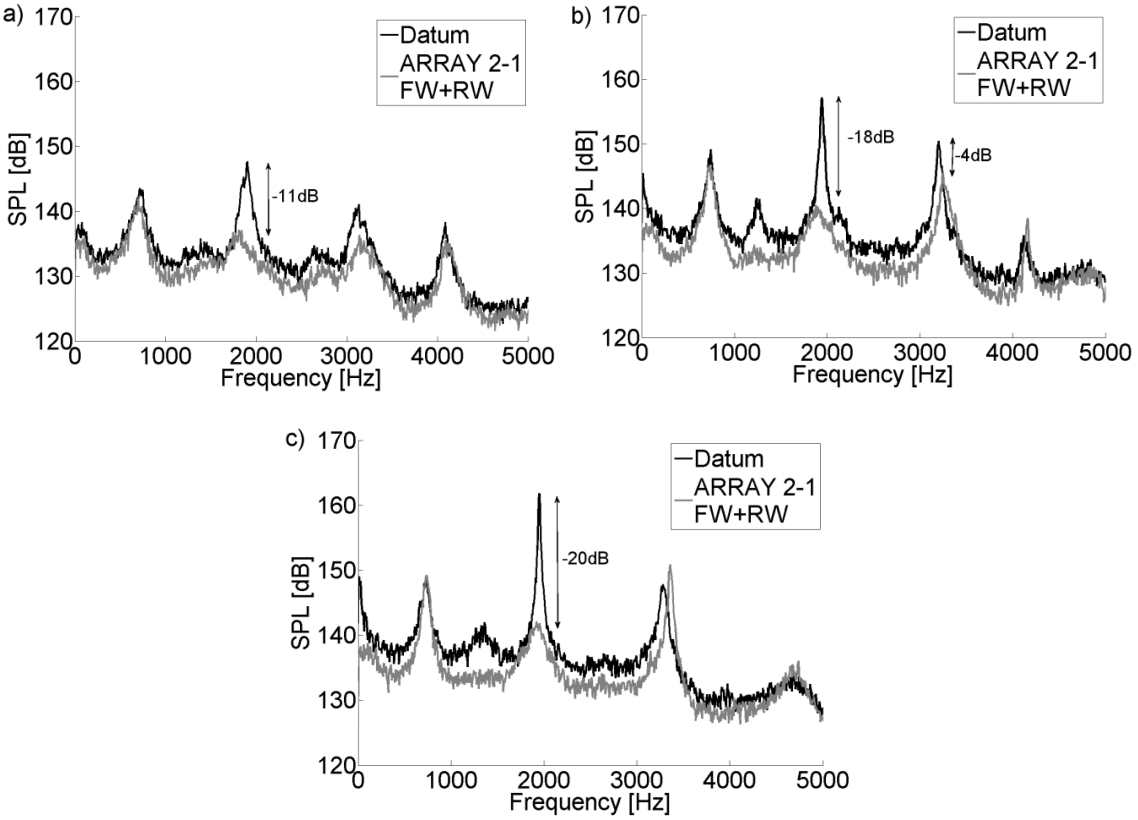

Figure 89 – Attenuation from combined configuration with ARRAY 2-1 resonator in both the cavity front and rear wall for a) Mach 0.8, b) Mach 0.9, and c) Mach 0.95

5.6.1.2 Multiple arrays to target different modal frequencies

A different approach to improve the attenuation of a single resonant array was to use multiple resonators with different tuning. It was expected that if a cavity was configured with two differently tuned arrays that attenuation would occur at multiple modal peaks simultaneously.

The first case examines the attenuation from ARRAY 2-1 installed into the front wall and ARRAY 2-2 in the rear wall. The front wall was chosen for ARRAY 2-1 as this was the location where the greatest attenuation was achieved. ARRAY 2-2 was chosen as it is expected to provide attenuation at a frequency in between the second and third mode. For this combined configuration attenuations of 18dB was achieved at the second mode and 8dB at third mode for Mach 0.9. Again as with the multiple ARRAY 2-1 configuration this attenuation level is an improvement over the single array cases. The configuration with ARRAY 2-1 and ARRAY 2-2 demonstrates that a combined installation can attenuate multiple modes simultaneously. Notably, the broadband noise is also attenuated by around 5dB compared to no attenuation for a single array case. The underlying cause of this is discussed at the end of this section.

The final configuration investigates the combined performance of arrays for attenuation of the second mode (ARRAY 2-1) and the third mode (ARRAY 3-1). The aim of this configuration was to attenuate at the second and third modes simultaneously and also to

ameliorate the effects of peaking caused by the attenuation of third mode. ARRAY 2-1 was installed into the cavity front wall and ARRAY 3-1 was installed into the rear wall as these were the positions where the greatest attenuation was achieved. With this configuration attenuations of 11dB were evident at both the second and third modes simultaneously (*Figure 91a*). Whilst, this configuration did not improve upon the individual peak attenuation levels attenuation was effected at multiple modes and again the broadband noise was reduced by around 5dB. The attenuation of the second mode was not improved due to the peaking effect caused by the attenuation of third mode. *Figure 91b* examines the effect of switching the positions of ARRAY 2-1 and ARRAY 3-1 within the cavity. With ARRAY 2-1 and ARRAY 3-1 in their non-optimal positions the attenuation from the configuration was reduced. There was little or no attenuation of the second mode and 8dB of attenuation at the third mode (*Figure 91b*). This test demonstrates the importance of positional effects when using combined resonant arrays to attenuate multiple cavity modes simultaneously.

In all cases of combined resonant arrays, the arrays are effective beyond the relatively narrow bandwidth they exhibit for their individual test cases. Attenuation occurred over a broad range of frequencies and not just at specific modal peaks. The generation of the broadband noise within a cavity flow is typically attributed to the weakly coherent small scale structures within the shear layer across the cavity and also the low energy noise contained in the freestream [116]. An attenuation of the broadband noise therefore indicates a modification to the interaction between the mean flow of the cavity system and the pressure waves [39]. The relatively large reduction in the amplitudes of the dominant cavity modes shown in *Figure 90* and *Figure 91* is expected to cause such a modification to the interactions between the small scale structures and the pressure waves energy is absorbed directly from the cavity flowfield. With combined installations the cavity spectra remain modal (*Figure 90*) and therefore the arrays do not disrupt the overall modal generation process related to the large scale vortical structures within the shear layer.

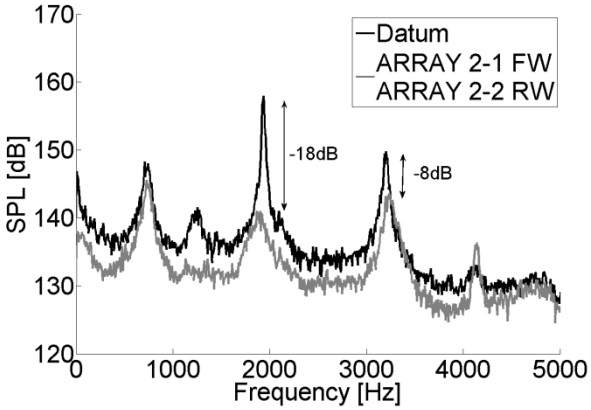

Figure 90 – Attenuation from combined configuration with ARRAY 2-1 resonator in the front wall (FW) and ARRAY 2-2 in the rear wall (RW) at Mach 0.9

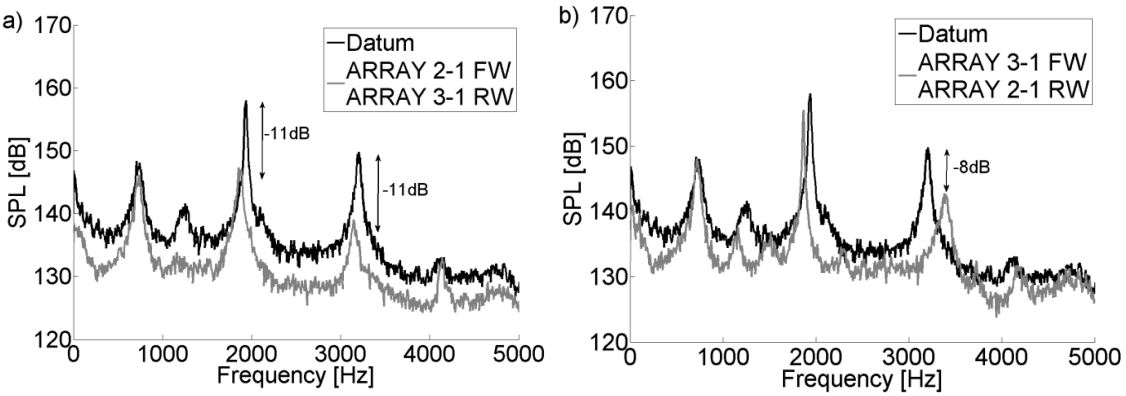

Figure 91 – Attenuation from combined configuration with a) ARRAY 2-1 front wall (FW) and ARRAY 3-1 rear wall (RW), b) ARRAY 3-1 front wall (FW) and ARRAY 2-1 rear wall (RW). (Mach 0.9).

5.6.2 Attenuation performance of a spoiler and resonant array

Previous investigations conducted at Cranfield into cavity palliatives have used a spoiler mounted upstream of the cavity to attenuate the modal peaks [35]. Whilst the spoilers used typically provided around 15dB of peak attenuation at all of the modal peaks combined with around 7dB of broadband attenuation the cavity spectra remained modal. The residual modal peaks in the cavity with spoiler configuration spectrum were around 15dB above the broadband noise and therefore could still cause damage within the cavity. Therefore, the attenuation from cavity configurations which used an upstream spoiler in conjunction with a rear wall resonant array were investigated. Due to the spoiler installation method resonant arrays could not be installed into the front wall when combined with a spoiler.

Figure 92a demonstrates that the combination of a δ/2 spoiler with ARRAY 2-1 at the rear wall can provide up to 5dB more peak attenuation when compared with the spoiler alone case. Peak attenuation of the second mode increased from 13dB for the spoiler case to 18dB for the case with ARRAY 2-1 and a similar increase was also evident at the third mode. No change was made to the broadband noise. *Figure 92b* demonstrates that the third mode can be completely removed within a cavity configured with a δ/2 spoiler with ARRAY 3-1 in the rear wall. This is an attenuation at the third mode of 23dB compared to 11dB for the spoiler alone case. As has been seen for the resonant array cases the large attenuation of the third mode was accompanied by the amplification of the second mode. The attenuation of the second mode from the combined spoiler and resonant array case with ARRAY 3-1 was 8dB compared to 14dB for the spoiler alone case.

Both cases of combined resonator and spoiler configurations have demonstrated that the residual modes that remain present within a spoiler/cavity configuration can be attenuated by the addition of a resonant array at the cavity rear wall. As with the individual resonant array cases the extra attenuation from the resonant arrays can be targeted at whichever residual mode required the further attenuation. It is expected that

if arrays could be installed into the cavity front wall in combination with a spoiler the attenuation levels could be improved upon.

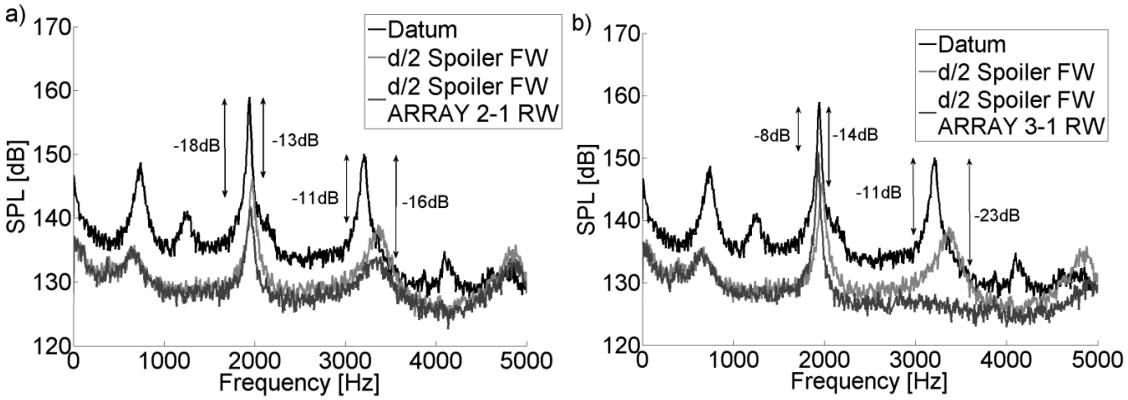

Figure 92 – Attenuation from combined spoiler and resonant array configuration with a) δ/2 spoiler at the front wall with ARRAY 2-1 in the rear wall (RW), b) δ/2 spoiler at the front wall with ARRAY 3-1 in the rear wall. (Mach 0.9).

5.7 Do resonant arrays attenuate under supersonic conditions?

The typical passive control choice for operational cavities is a full width spoiler installed upstream of the cavity. Indeed, previous investigations have shown attenuations of around 20dB for solid spoilers at high subsonic Mach numbers [7]. However, while the attenuation performance of a spoiler may increase with increasing Mach number within the subsonic regime the attenuation performance from spoilers decreases with increasing supersonic Mach numbers and in some cases can lead to a significant increase in the modal intensities [7] [17]. Above Mach 1.3 increases in modal intensities of around 15dB have been demonstrated by previous experiments [7] which could cause additional damage to the stores and aircraft. Therefore, an alternative attenuation approach is required for supersonic flight conditions. It was therefore of great interest to assess whether resonant arrays could provide useful attenuation levels under supersonic conditions.

The following supersonic cavity tests were conducted using the TGF at Wright Patterson Air Force Base (*section 3.2*) as the Cranfield University 2.5" wind tunnel is not capable of achieving supersonic conditions with the cavity liners installed. These tests were conducted using the ADDICT cavity model which is roughly 1/20th scale and exhibits open flow characteristics [30] [82] (*section 3.2*). Firstly the acoustic characteristics of the datum cavity are discussed to identify the features which were targeted for attenuation from the resonant arrays. Secondly, the attenuation of the second and third modes are discussed. This is followed by the attenuation results from a combined configuration which was designed to target multiple modes simultaneously.

5.7.1 Datum modal characteristics for the medium scale cavity at Mach 1.5

The datum acoustic spectrum for the medium ($1/20^{th}$) scale ADDICT cavity model under supersonic (Mach 1.5) conditions is shown in Figure 93. The spectrum is typical of open flow type cavities and clearly exhibits at least six modal peaks. The first three modes exhibit the highest SPL with the second mode (1.2kHz) as the dominant mode (153dB) compared with 144dB for the first and third modes (700Hz and 1.9kHz respectively (Figure 93)). No modal peaks were exhibited above 5kHz and this frequency range will not be considered. The modal spectrum is similar to the spectrum from the small scale transonic tests (s*ection 5.4.1*), and therefore it is expected that resonant arrays will provide a high level of attenuation. Because of the characteristics of the second and third modes they were selected for the targeted attenuation from the resonant arrays. Both of these modes (1.2kHz and 1.9kHz (Figure 93)) exhibit peaks with a narrow bandwidth (β=6%), and therefore these are compatible with attenuation from resonant arrays as the resonator bandwidth is greater than the measured modal bandwidth.

The medium scale cavity was configured with an instrumented ceiling, so that unsteady pressure measurements could be made at seven locations over the surface (*Figure 38*). This enabled the shape of the cavity modes to be investigated and an assessment was carried out to determine if the measured mode shapes corresponded to the expected profiles. For both the second and third modes the SPL typically increases by around 15dB as x/l is increased from 0.05 to 0.95 (Figure 94*a* and *b*). From the spectra the peak SPL relating to each mode can be plotted against x/l position on the ceiling to produce the plots showing the shape of the modes within the cavity (Figure 94*a* and *b*). The analytical mode shapes were calculated using a semi empirical model, which requires the SPL at the rear wall of the cavity and the cavity l/h aspect ratio (see *section 2.7.5*) [117]. The second mode exhibited two pressure nodes around positions of x/l of 0.2 and 0.8 (Figure 94*a*). The third mode exhibits three pressure nodes at positions of x/l around 0.2, 0.5, and 0.8 (Figure 94*b*). Low levels of attenuation are expected at the pressure nodes as these are related to destructive interference between incident and reflected pressure waves within the cavity.

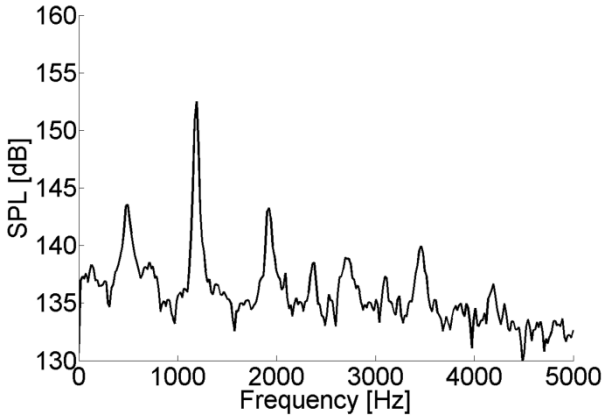

Figure 93 – Datum cavity spectra for the medium (1/20th) scale cavity at Mach 1.5 (measured at x/l=0.95).

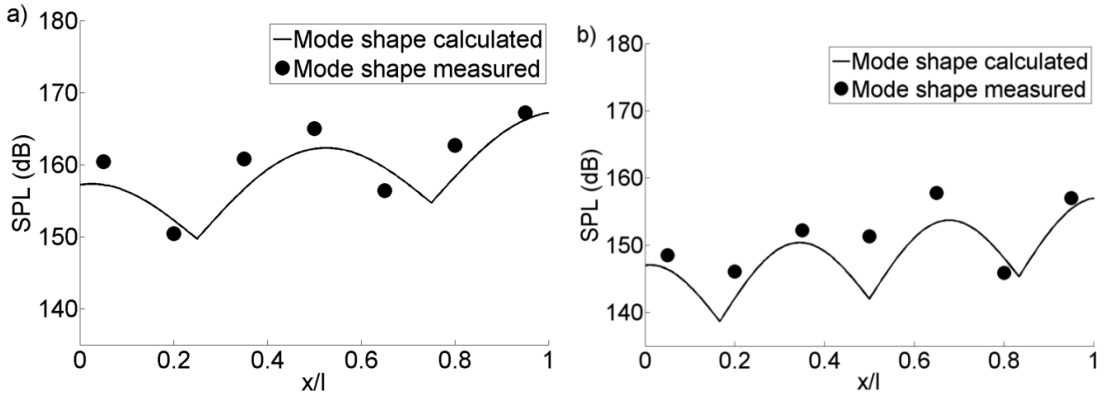

Figure 94 – Calculated and measured mode shapes over the medium scale cavity ceiling. a) second mode, b) third mode for Mach 1.5 flow.

5.7.2 Targeted attenuation of the second cavity mode

The second mode exhibited the highest SPL peak within the spectrum for the medium scale ADDICT cavity, under supersonic (Mach 1.5) conditions, (153dB (Figure 93)) and was therefore the primary target for attenuation. The initial attenuation results for the medium scale second mode are for TGF_S 2-1, which was designed based on the findings from the transonic investigations (*section* 5). These small scale transonic results indicated that an array designed with a resistance (Re(Z)*) of around 0.3 would provide a high level of attenuation and TGF_S 2-1 was designed accordingly. Figure 95*a* shows that TGF_S 2-1 provided around 9dB of attenuation at the second mode, when installed into the cavity front wall. This front wall configuration reduced the second mode from 153dB to around 144dB and there is no effect on the surrounding modes or the broadband noise (Figure 95*a*). The small scale transonic results indicated that a front wall configuration would provide the greatest attenuation level for the second mode (*section 5.2.1*). However, this does not appear to be the case for the supersonic tests as for a rear wall configuration TGF_S 2-1 provided around 8dB of attenuation, which reduced the second mode to around 155dB. Whilst this attenuation

level is lower than for the front wall case, the amount lies within the ±3.7dB of uncertainty placed on the measurements (*section 3.2.1.3*) and therefore cannot be considered to be significant. Nevertheless, these results represent a significant improvement in the attenuation levels which can otherwise be achieved under supersonic conditions. Next the attenuation performance from a different array, which was also used to attenuate the second mode, is discussed.

TGF_3-1 was primarily designed to target the third mode within the medium scale cavity at Mach 0.7. However, the frequency of the transonic third mode and the supersonic second mode are similar, both at around 1.2kHz (*Figure 93*). TGF_3-1 was designed to target this frequency with a low resistance (Re(Z)*) value compared with TGF_S 2-1 (*section 4.4.2).* This test was designed to assess whether the design rules based on the transonic test results were suitable for use under supersonic conditions or whether a low Re(Z)* array could attenuate the supersonic second mode. From the small scale test results and previous work [109], it was expected that TGF_3-1 would provide a lower level of attenuation at the second mode compared with TGF_S 2-1 due to the lower resistance of the array faceplate. However, this was not the case and for a front wall configuration TGF_3-1 provided around 11dB of attenuation at the second mode (*Figure 96*). Whilst this 2dB increase in attenuation from TGF_3-1 over TGF_S 2-1 is within the ±3.7dB uncertainty it does not represent the expected decrease in attenuation level due to the lower array Re(Z)*. This result is important as it indicates that the attenuation provided by TGF_3-1 may be due to a different mechanism compared with TGF_S 2-1. An investigation of the fundamental behaviour of the palliative devices was conducted in *section* 4 and discussed the possible attenuation mechanism through which TGF_3-1 provides a large attenuation.

The attenuation from a resonant array is expected to vary with the SPL within the cavity as the absorption of modal energy results in less energy propagation within the cavity. As the spectra remained modal even with the attenuation from the arrays the standing wave structures which set up the mode shapes within the cavity were expected to remain. Therefore, over the cavity ceiling the attenuation levels were expected to follow the mode shapes (Figure 94) and in general this was the case for the attenuation provided by TGF_S 2-1 (Figure 97*a*). For this array the peaks in attenuation coincided with the positions of the highest modal intensity within the cavity. However, this was not the case for the attenuation levels from TGF_3-1 where the attenuation levels were fairly constant over the cavity ceiling (Figure 97*b*). For TGF_3-1 the attenuation levels varied between around 11dB and 13.5dB over the cavity ceiling, which indicates that the attenuation from TGF_3-1 is achieved through a different mechanism compared with TGF_S 2-1. This mechanism will be discussed in *section 5.8*.

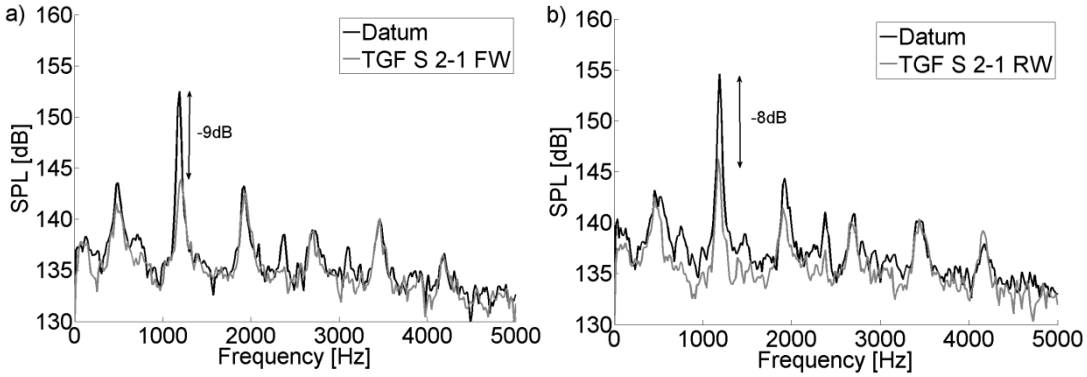

Figure 95 – a) Attenuation from TGF_S 2-1 installed in the cavity front wall (FW) for Mach 1.5 flow, b) Attenuation from TGF_S 2-1 installed in the cavity rear wall (RW) for Mach 1.5 flow. (measured at x/l=0.95).

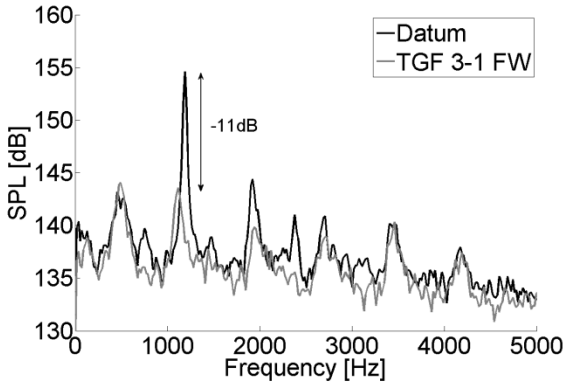

Figure 96 – Attenuation from TGF_3-1 installed in the cavity front wall (FW) for Mach 1.5 flow for Mach 1.5 flow. (measured at x/l=0.95).

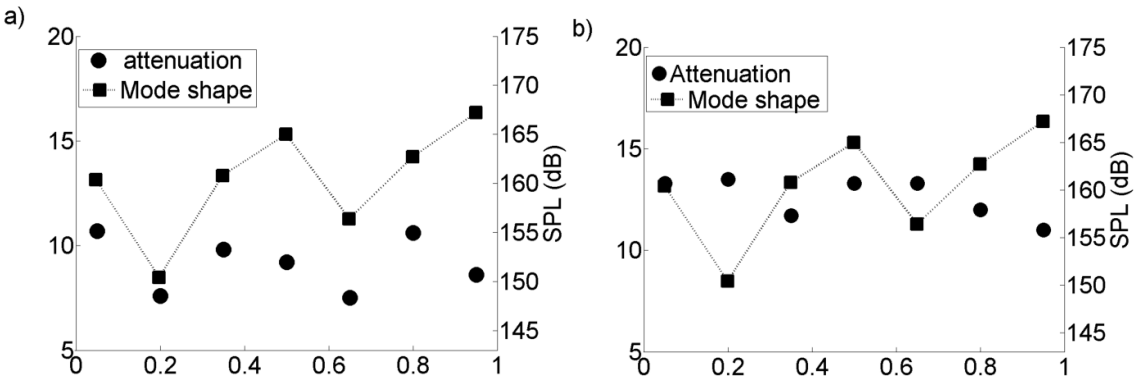

Figure 97 – Measured attenuation of the second mode at varying positions over the cavity ceiling alongside the measured mode shape for. a) TGF_S 2-1 FW, b) TGF_3-1 FW at Mach 1.5.

5.7.3 Targeted attenuation of the third cavity mode

The third mode of the medium scale cavity was primarily targeted for attenuation with TGF_S 3-1 (*section 4.4.2*), which was designed based on the results from the preliminary investigation conducted at small scale under transonic conditions (*section 5.2*). These transonic results indicated that a high attenuation for the third cavity mode could be achieved from an array with a relatively low faceplate resistance (Re(Z)*) and TGF_S 3-1 was designed accordingly to exhibit Re(Z)*<0.1.

Therefore, from the transonic results, it was expected that the highest attenuation of the third cavity mode would be achieved for an array installed into the rear wall of the cavity. For the front wall configuration TGF_S 3-1 achieved around 10dB of attenuation at third mode (Figure 98*a*), which reduced the modal intensity from around 144dB to 134dB. For the rear wall configuration the attenuation from TGF_S 3-1 increased to 12dB which reduced the modal intensity to around 132dB (Figure 98*b*). This 2dB increase in attenuation, due to the position of the array, is within the ±3.7dB uncertainty, but it does indicate that third mode attenuation is not sensitive to the array location within the cavity as both front and rear wall configurations provide similar results. Notably, for the rear wall configuration there is around a 2dB attenuation of the broadband noise (Figure 98*b*) compared with the front wall case where only the modal peak is affected (Figure 98*a*). This increase in attenuation of the broadband noise is likely to be caused by the ingress of the oscillating shear layer into the array at the rear of the cavity. This process effectively reduces the interactions between the cavity flow and the small scale structures within the shear layer which are related to the generation of the broadband noise.

For the high resistance second mode array (TGF_S 2-1) the attenuation levels followed the SPL intensities over the cavity ceiling (Figure 97*a*), however the attenuation from the low resistance array (TGF_3-1) did not vary to the same extent (Figure 97*b*). Therefore, the attenuation level from TGF_S 3-1 was expected to remain at a constant level over the cavity ceiling as this array was designed with low resistance. The attenuation levels were constant at around 17dB over the centre of the cavity ceiling ($0.2<x/l<0.65$) (Figure 99). At the position of $x/l=0.8$ the attenuation level drops to around 2dB which coincides with the modal pressure node (Figure 99). However, the highest attenuation level (around 27dB) from TGF_S 3-1 is exhibited at the front of the cavity ($x/l=0.05$) (Figure 99). The attenuation levels from TGF_S 3-1 do not strictly follow the modal intensities, as was the case for TGF_S 2-1 (Figure 97*a*). It is therefore likely that the attenuation from TGF_S 3-1 is provided through a different mechanism, which will be discussed in *section 5.8* and supported by the results from the other TGF_S arrays.

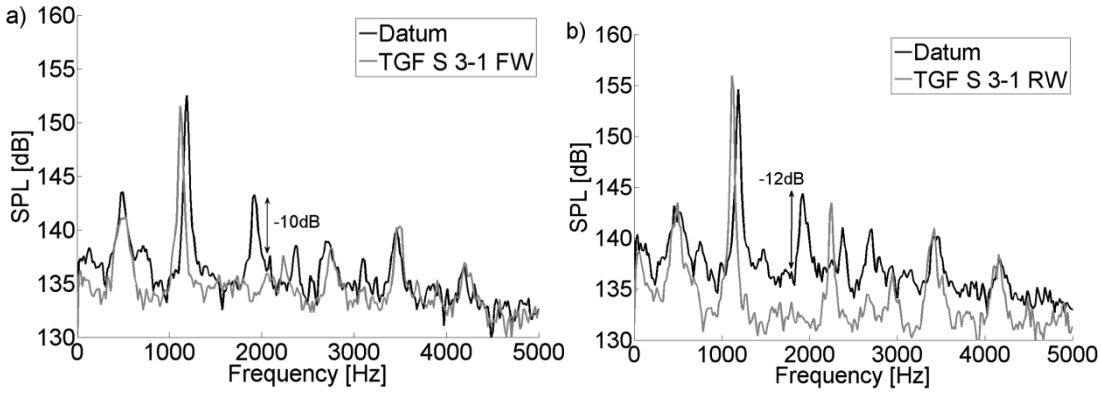

Figure 98 – a) Attenuation from TGF_S 3-1 installed in the cavity front wall (FW) for Mach 1.5 flow, b) Attenuation from TGF_S 3-1 installed in the cavity rear wall (RW) for Mach 1.5 flow. (measured at x/l=0.95).

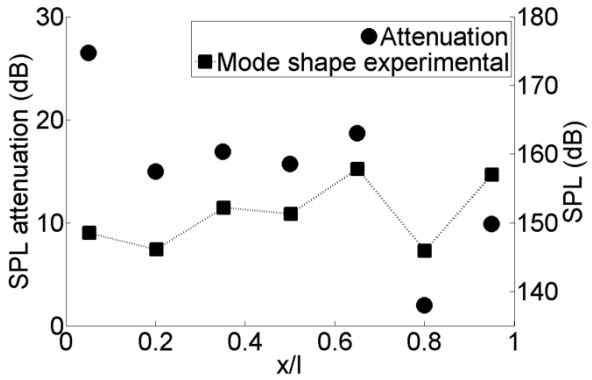

Figure 99 – Attenuation of the third mode at varying positions over the cavity ceiling for TGF_S 3-1 RW for Mach 1.5 flow.

5.7.4 Can attenuation be improved through combined array configurations?

A high level of attenuation, under supersonic conditions, has been demonstrated at both the second and third modes from resonant arrays tuned to the separate modal frequencies (*Figure 95, Figure 96* and *Figure 98*). It was therefore of interest to investigate whether a combined resonator configuration would both improve the overall performance and provide attenuation at multiple modes simultaneously.

The medium scale cavity was configured with TGF_S 2-1 in the front wall and TGF_S 3-1 in the rear wall. This placed the second mode array in the expected favourable front wall position and the third mode array in the rear wall (*section 5.6)* and exhibited the expected high levels of attenuation with around 9dB of attenuation at the second mode and 15dB of attenuation at the third mode simultaneously (Figure 100*a*). This reduced the second mode from around 151dB to 141dB and the third mode SPL from 145dB to 130dB. These peak attenuation levels were coupled with a broadband attenuation of around 6dB which contributed to an average OASPL reduction over the cavity ceiling of 7dB. These results represent an important improvement in the performance of resonant arrays as a notable level of attenuation was achieved at multiple modes with a

significant effect on the broadband noise. Attenuation levels across the cavity ceiling were more constant than for the individual cases, both the attenuation level at the second and third modes were around 10dB throughout the cavity with the largest attenuation levels coinciding with the higher modal SPLs at the rear end of the cavity (Figure 100*b*). As with the individual third mode case the attenuation of the third mode is reduced at the position x/l=0.8 as this coincides with a pressure node for the third mode.

In summary, resonant arrays have demonstrated a potential for use as cavity palliatives under supersonic flow conditions. Peak attenuation levels within the cavity of up to 26dB have been shown at single modes for both single and combined array configuration. The typical attenuation provided from a single array is around 10dB at one peak and for combined configuration this increases to around 15dB for multiple modes simultaneously. Therefore, the combined configurations represent an improved attenuation performance over the single cases. These are important results, as alternative palliative devices such as spoilers do not typically provide high attenuation levels under supersonic conditions. In addition to the attenuation results, it is important to gain an understanding of the mechanisms through which the resonant arrays provide the attenuation. The following section will investigate the trends between the attenuation levels and the resistance (Re(Z)*) of the arrays and two attenuation mechanisms for the resonant arrays are discussed.

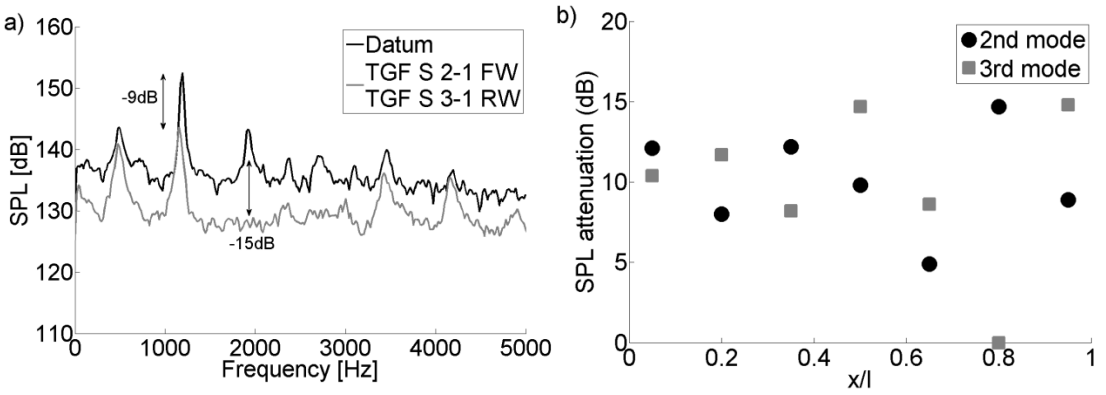

Figure 100 – a) Attenuation from TGF_S 2-1 installed in the cavity front wall (FW) and TGF_S 3-1 installed in the rear wall (RW) for Mach 1.5 flow (measured at x/l=0.95), b) Attenuation of the cavity modes at varying positions over the cavity ceiling with TGF_S 2-1 and TGF_S 3-1 installed into the cavity FW and RW respectively for Mach 1.5 flow.

5.8 Choosing the best performance metric for resonant arrays

To design a palliative based on resonant arrays the designer needs to know which parameters are important to ensure that the device provides an effective attenuation level at a frequency where it is required. The tuning aspect of the array design is especially important as resonance based palliatives typically provide a narrowband attenuation, where little or no attenuation is expected to occur for off design conditions.

It is expected that if a resonant array based palliative were to be installed within a full scale cavity it would be used to attenuate the modal peaks which exhibited the highest peak SPL values. This section examines the various metrics which can be used to characterise the performance of the various resonant arrays used throughout this body of work. Throughout this section the values for the performance metrics are calculated through the initial linear, medium SPL analytical model (*section 4.2.1*). This model is acceptable for drawing overall conclusions as any effect of high SPL is thought to be proportional to the linear levels (*section 4.3*).

5.8.1 Attenuation performance as a function of absorption coefficient

For conventional acoustic applications, when a resonant array is designed the performance is calculated in terms of an absorption coefficient. The absorption coefficient is defined as the proportion of the incident energy that is absorbed or dissipated by the device (see *section 4.2.1*). A good design will typically exhibit a large absorption coefficient at the target frequency. Therefore, it was expected that the attenuation provided by the resonant arrays installed into the cavities would be proportional to the absorption coefficient. This assumption is examined for both the small and medium scale tests, under both transonic and supersonic conditions, in the following subsections.

5.8.1.1 Small (1/40th) scale transonic conditions (Mach 0.90)

The attenuation performance from a large series of resonant arrays was investigated under transonic conditions within the small (1/40th) scale cavity model. These investigations provided a large database of attenuation values, which are used to provide conclusions about which performance metric best showed the respective attenuation levels. The attenuation results for all of the small scale, transonic arrays against the calculated linear absorption coefficients (see *section 4.2.1*), for both second and third mode cases, are shown in *Figure 101*. It was expected that a high attenuation would coincide with an absorption coefficient values of around unity.

*Figure 101*a shows that there is little trend between high attenuation levels at the second mode and a high absorption coefficient. This feature of the results is true for both front and rear wall configurations. The highest attenuations were achieved for arrays which exhibit absorption coefficient (α) values of both α=0.2 and around α=0.7 (*Figure 101*a). The high attenuation levels achieved by arrays with an α=0.7 can be explained by the under prediction of the absorption coefficient by the linear analytical model (*section 4.2.1*). High SPL impedance tube tests demonstrated that the α of an array could increase by around 30% when installed into the cavity due to the high SPL (*see section 4.3.1)*. For the arrays with an α of around 0.7 this would be equivalent to an arrays with an α of around one and these arrays would therefore provide a large attenuation.

However, the high attenuation from the array which exhibits a low α of around 0.2 is harder to explain. If this result, of high attenuation for a low Re(Z)* array, for the

second mode (*Figure 101*a) is taken in context with the results for the third mode (*Figure 101b*) it appears that high levels of attenuation can also be achieved by arrays which exhibit low α values. *Figure 101b* shows that there is clear trend for high attenuation of the third mode and a low absorption coefficient (α). The attenuation provided by these low α arrays must be due to a different mechanism than for the high α arrays. An array with a low α would not be expected to absorb much, if any, of the energy incident upon its faceplate and therefore would not provide these high levels of attenuation.

Therefore, it is suspected that instead of the absorption of the incident energy these devices are linked to the modal propagation within the cavity. All of the arrays used within this study provide a change in the acoustic impedance at their boundary with the cavity and when a wave reaches a change in impedance a reflection is created [118]. If, as in the case of the resonant arrays, this boundary impedance is less than the characteristic impedance (Z_0) of the air within the cavity the pressure of the reflected waves will be 180° out of phase with the incident pressure wave. This out of phase reflection will have a destructive effect on the incident wave due to superposition of the pressure amplitudes. It has previously been discussed (see *section 4.2*) that at the resonant frequency of an array, i.e. a modal frequency of the cavity, the array impedance (Z) is comprised of the resistance (Re(Z)) only and it is this resistance term which affects the peak value of α. A low Re(Z) will result in an array with a low α. Therefore, as a low α array exhibits a low resistance and is expected not to attenuate the incident wave, the out of phase reflection will have a pressure amplitude comparable with the incident wave. This out of phase reflection will therefore have a greater destructive effect on the incident pressure waves compared with the reflection from an array which exhibits a high α, where the amplitude of the reflected wave will be greatly reduced when compared with the incident wave due to the absorption effect of the arrays resistance.

This phase related attenuation mechanism is similar to the fundamental operation of non-resonant devices such as quarter wave tubes, where an out-of-phase reflection is used to have a destructive effect on an incident wave. For the arrays used within this study this approach still offers a targeted attenuation approach as the relative attenuation levels exhibited on the reflective wave are related to the frequency of the incident wave. An incident wave with a frequency not equal to the array resonant frequency will not experience the same impedance levels as a wave with matching frequency and will therefore, not experience a phase shift of the same order. A phase shift with a magnitude less than 180° will not provide the high levels of destructive interference and will therefore not affect the acoustic spectrum within the cavity to the same extent.

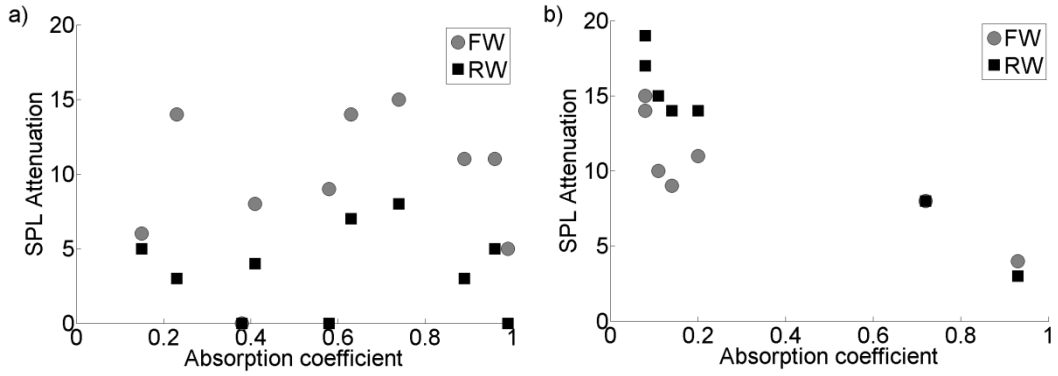

Figure 101 – Comparison between attenuation for front wall (FW) and rear wall (RW) installations which target a) the second mode, b) the third mode against the calculated linear absorption coefficient (see *section 4.2.1*) (Mach 0.9).

5.8.1.2 Medium (1/20th) scale, supersonic conditions (Mach 1.5)

A smaller database of attenuation results is available for the medium (1/20th) scale cavity cases. Insufficient data were taken at Mach 0.7 to draw any conclusions about which arrays provide the best levels of attenuation, however, there are sufficient data to generate trends for the cases investigated at Mach 1.5.

The attenuation provided by the arrays plotted against the calculated absorption coefficient for both second and third mode arrays are shown in *Figure 102*. Unlike for the small scale transonic cases, the relationships between attenuation and resistance are the same for both the second and third modes. In these cases, the largest attenuation levels coincide with arrays that have a low calculated α. This is an unexpected result as it was expected that the second mode devices, which were designed based on the best performing small scale transonic arrays, would demonstrate a similar relationship between attenuation and α as the small scale transonic second mode devices. This would demonstrate a cluster of high attenuation results around arrays which exhibit an α of around 0.7 (*Figure 101a*). In fact, the highest attenuation of the supersonic second mode was achieved using an array with α=0.2 (*Figure 101a*).

The high attenuation of both the second and third cavity modes by arrays which exhibit low calculated α values is again attributed to the destructive interference created by the high intensity out-of-phase reflections caused by the low attenuation at the array faceplate as discussed in the previous section.

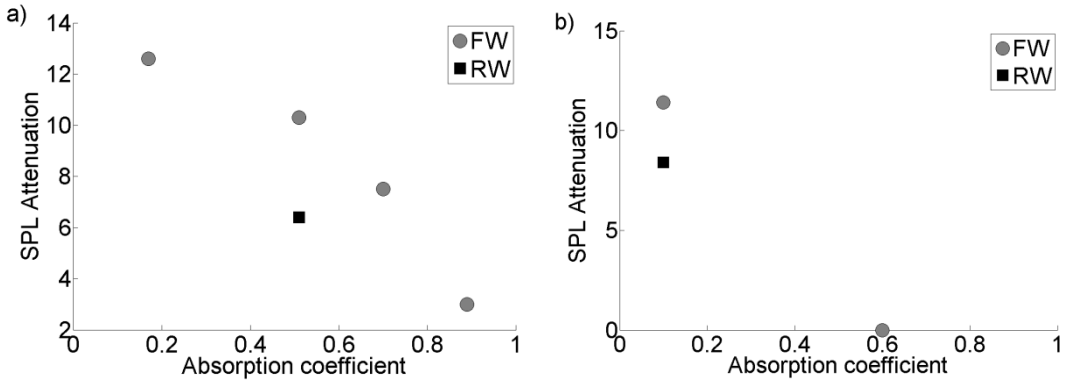

Figure 102 – Comparison between the average attenuation over the cavity ceiling for front wall (FW) and rear wall (RW) installations which target a) the second mode, b) the third mode against the calculated linear absorption coefficient (see *section 4.2.1*) (Mach 1.5).

5.8.2 Attenuation performance as a function of linear viscous resistance (Re(Z)*)

The absorption coefficient metric is comprised of fundamental properties of the devices, which are known as impedances, and impedances have been shown to be important when devices are to be used within the high SPL environment of a resonant cavity (*section 4.3.3*). The complex impedance term (Z*) (Equation 29) is formed from the real part known as the resistance (Re(Z)*) and the imaginary part known as reactance (Im(Z)*). The resistance has been shown to be the important term, which is related to the level of attenuation exhibited by an array (*section 4.3.3*) and therefore it was of interest to assess whether or not there was a relationship between attenuation levels and the resistance (Re(Z)*) of the small and medium scale arrays under both transonic and supersonic conditions.

For continuity and to aid comparison only the linear resistance (Re(Z)*) term has been used for the investigation into the relationship between performance of resistance (*section 4.2.1*). Whilst it is recognised that the high SPL environment within the cavity will affect the resistance value, this effect is proportional to the linear resistance value and therefore would not affect the overall relationship between attenuation and resistance. The non-linear model presented earlier in this body of work has only been tested on a small set of sample cases and therefore only limited comments on reliability can be made. As the current section is primarily interested in the relationships that are displayed by the array properties, the absolute values of the resistance are of secondary importance and are provided for design guidance purposes.

5.8.2.1 Small (1/40th) scale transonic conditions (Mach 0.90)

It was demonstrated in the previous section that attenuation at the second and third modes were achieved through different mechanisms (*Figure 101*). Therefore, due to the link between absorption coefficient and resistance a similar result was expected for attenuation in terms of the array resistance (Re(Z)*). The variation in modal SPL attenuation is plotted against the calculated liner resistance, for both the second and third modes of the small scale transonic cavity model, in *Figure 103*.

There is no clear relationship between attenuation and resistance for the second mode results (*Figure 103a*). High levels of second mode attenuation have been achieved by arrays which demonstrate resistance within the range 0.05<Re(Z)*<0.4. This large range over which high levels of attenuation have been exhibited is again further evidence that arrays within this regime operate under two separate attenuation mechanisms. Arrays which exhibit the higher resistance values follow the typical viscous attenuation mechanism for resonant arrays and the attenuation from the arrays which exhibit low resistance values are attributed to an out-of-phase reflection mechanism, where the slightly attenuated reflection from a low Re(Z)* array is expected to create destructive interference between the incident and reflected waves. Therefore, two design approaches are possible, one which designs arrays with Re(Z)*>0.4 and one which designs arrays with Re(Z)*<0.1. Both of these design approaches were evaluated for the medium scale supersonic tests and these results are discussed in *section 5.7*.

For the third mode, there is a clear relationship between high levels of attenuation and arrays with low resistance. The highest attenuation was demonstrated from arrays which exhibit Re(Z)*<0.1 (*Figure 103b*). As was discussed in the previous section, where large attenuations of the third mode were achieved by arrays with low absorption coefficient (α) values, it is thought that this relationship is explained by the third mode being most susceptible to the out-of-phase reflection mechanism, where attenuation is effected through destructive interference and not viscous losses within the resonant arrays.

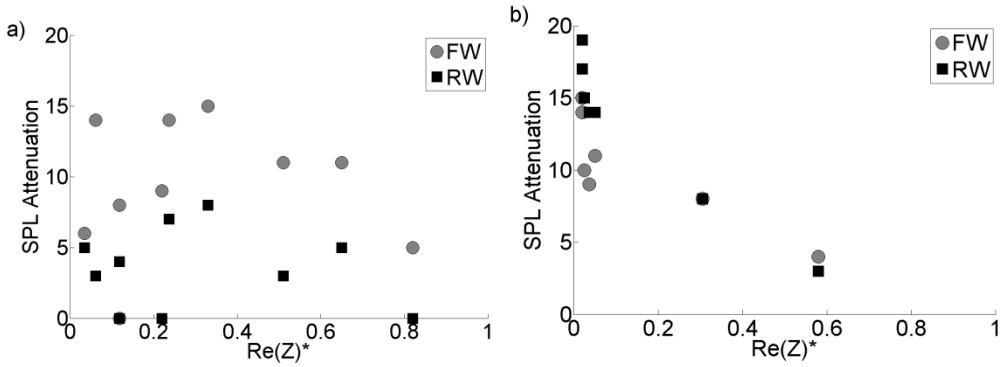

Figure 103 – Comparison between attenuation for front wall (FW) and rear wall (RW) installations which target a) the second mode, b) the third mode against the calculated linear normalised resistance (Re(Z)*) (see *section 4.2.1*) (Mach 0.9).

5.8.2.2 Medium (1/20th) scale Supersonic cases (Mach 1.5)

As expected from the absorption coefficient results (*Figure 102*) there is a clear relationship between a high attenuation level and a low resistance for both the medium scale supersonic second and third modes (*Figure 104*). For the second mode these supersonic results are contrary to those from the transonic tests, where under transonic conditions a high attenuation could be achieved by either a low resistance or high resistance array. These supersonic results are further evidence that the characteristics between the small scale transonic and medium scale supersonic cavities may be different and therefore, different attenuation techniques are suitable for each case. Overall, for both the transonic and supersonic second and third mode a high attenuation could be achieved by arrays which have a low resistance (Re(Z)*<0.1) value. This is an important result as it is perhaps contrary to what would be expected based on the knowledge from the medium SPL room acoustics field where the resonant array device was developed.

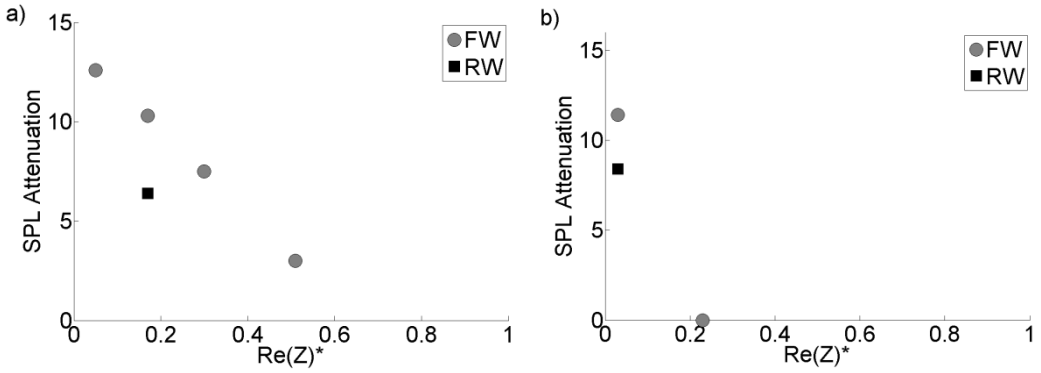

Figure 104 – Comparison between the average attenuation over the cavity ceiling for front wall (FW) and rear wall (RW) installations which target a) the second mode, b) the third mode against the calculated linear normalised resistance (Re(Z)*) (see *section 4.2.1)*(Mach 1.5).

5.8.3 Summary of the performance metrics and attenuation mechanisms within resonant cavities

Typically, when resonant arrays are designed the resistance (Re(Z)*) properties of the array are important as this is directly linked to the absorption coefficient of the array (*section 4.2.1*). The small scale investigation, under transonic conditions, indicated that a high level of attenuation at the second mode could be achieved by an array which exhibited a resistance of around 0.3<Re(Z)*<0.4 (*Figure 103a*) and it was expected that the attenuation level would be proportional to this resistance value. However, large attenuations of the second modal peak were also demonstrated for an array with a relatively low resistance value (Re(Z)*<0.2 (*Figure 103a*)). The case of a large attenuation from a low Re(Z)* array was also shown at the third mode for the transonic tests. Where a high attenuation was achieved from an array with a low resistance value of around Re(Z)*=0.05 (*Figure 103b*). These results where attenuation can be achieved

by two greatly different resistance values indicate that two attenuation mechanisms may be present within the cavity.

For the medium scale, supersonic devices the relationship between attenuation and the array resistance show there is a clear trend between high attenuation and lower resistance levels, for both the second and third modes (*Figure 104*). Typically, for both the second and third modes the highest attenuation was achieved with arrays that exhibit resistance levels of around Re(Z)*=0.05. If these results are taken alongside the results from the transonic investigation it indicates that attenuation of the second and third modes may be better achieved through an alternative to the classic resonant array attenuation mechanism.

Typically, attenuation from the classic resonant absorber approach is achieved through viscous frictional losses within the array perforations and the associated vortex shedding at the ends of the orifices. This type of viscous attenuation is linked to the absorption coefficient of an array and would be expected to increase with an increased resistance value. Therefore, arrays which exhibit high resistance (Re(Z)*) values would be expected to achieve high levels of attenuation. However, arrays with low levels of resistance have demonstrated attenuation levels which are in some cases significantly greater than arrays designed with a high resistance (*Figure 103* and *Figure 104*). Therefore, these low resistance arrays must attenuate the cavity modes through a different mechanism which is not dependent on the viscous loss mechanism of typical absorbers.

Within the cavity, mode shapes (*section 5.7.1*) indicate that a series of standing waves are present which are related to each of the cavity modes. These modes are a result of the superposition of the reflected pressure waves from the cavity end walls. It is expected that the installation of a resonant array into the cavity end walls will affect the reflections within the cavity. The phase of the reflected pressure wave from a resonant array is linked to the resonant frequency of that device. A pressure oscillation at the resonant frequency of the array will be reflected 180° out-of-phase when compared with the incident wave. This 180° out-of-phase reflection will have a destructive interference effect within the cavity and will affect the buildup of the standing waves. An oscillation with a frequency not equal to the resonant frequency of the array will not be reflected with such a large phase change and will experience the end wall of the cavity as an effectively solid surface. This is why the cavity remains modal with the same modal frequencies as the datum cases even with resonant arrays installed (*section 5.2*).

This destructive interference mechanism is expected to be more effective for arrays which exhibit low resistance (Re(Z)*) values as these arrays will absorb less of the incident wave and therefore provide a reflection with a greater intensity. An out-of-phase reflection with a greater intensity will remove a greater proportion of an incident wave compared to a lower intensity reflection. Whilst this mechanism does not require

the arrays to provide an attenuation themselves, they are still required to be tuned to the modal frequencies. The destructive reflections will only occur when the frequency of the incident wave equals the resonant frequency of the array. This is an important consequence as typically this type of attenuation is typically achieved from quarter wave tubes. These tubes, which can be found in exhaust and air-conditioning systems, create 180° out-of-phase reflections which cancel out incident waves. However, this type of device would be unsuitable for both small model scale and full scale cavity applications, due to the large size required to match the quarter wavelength condition.

From the tests conducted within this study two attenuation mechanisms have been identified as viable techniques for the reduction of the unsteady noise associated with open flow cavities. The first technique is based on the viscous losses associated with the resonance of an air mass constrained within the orifices of the arrays. The second attenuation mechanism is related to the destructive interference created by the out-of-phase reflections from lightly damped arrays. For the second case, little or no attenuation is achieved within the array which at first appears contrary to the purpose of the devices. However, if attenuation were present this would reduce the effectiveness of this mechanism as the reflected wave would have a lower intensity compared with the incident wave and the destructive interference would not cancel out such a large proportion incident wave.

Therefore, whilst all the devices presented can be considered as resonant arrays they provide attenuation in different manners and a designer would have to take this into account when deciding on the best approach for any given cavity. To create the most versatile arrays, which could operate over the greatest range of freestream Mach numbers and at different modes, the low resistance approach appears to offer the better performance levels compared with the typical higher resistance devices.

5.9 Alternative approaches for modal attenuation

In addition to the resonant array palliatives the performance of a series of alternative approaches has also been investigated experimentally. These alternative devices have also been adopted from other fields, such as room acoustics and gas turbines, much like the resonant arrays. It was of interest to assess whether these other devices demonstrated the same level of versatility compared with the resonant arrays and whether they could be used to provide a useful level of modal attenuation within an open cavity flow.

The first of these alternative approaches is a device based on the resistive properties of a porous wire mesh. These porous wire mesh devices have been tested subsonically (Mach 0.8 to 0.95) at small ($1/40^{th}$) scale and supersonically (Mach 1.5) at medium scale. The second type of alternative device tested was an acoustic foam liner installed into the cavity wall surfaces. This type of device was tested at small scale where the modal frequencies coincide with frequencies which are often targeted by acoustic foam liners in the room acoustic field [97]. Finally, the effect of bias flow through a porous

wire mesh faceplate on the attenuation performance was also investigated. It was expected that the addition of a bias flow through the faceplate would improve the resistance characteristics of the wire mesh. Also, the injection or removal of mass from the cavity flow system is expected to interrupt the modal generation process and result in a cavity with lower SPL intensities.

5.9.1 Wire mesh, resistance based devices

It was expected that attenuation could be achieved by placing a porous wire mesh, backed by a confined backing volume, into one of the cavity end walls. The attenuation from such devices is due to the viscous resistance to flow passing through the porous mesh structure. This resistance is expected to increase with particle velocity and therefore these devices are expected to be effective within a high SPL environment where the particle velocities are known to be high (see *section 4.3*). These devices are expected to provide attenuation with a large bandwidth. This is because the porous mesh exhibits a similar level of resistance over a wide range of frequencies when compared with the perforated faceplates of a resonant array.

To improve the attenuation, through an increase in the effective resistance, the particle velocity through the device can also be increased by pairing the mesh with a backing length which is equal to one quarter of the target wavelength ($L=\lambda/4$). This quarter backing length relation is a well-known phenomenon and uses the reflection properties of waves from solid surfaces to superimpose the pressure and velocity of the acoustic waves and particles [97]. However, due to the size restriction in the model cavities, this condition could not be satisfied and it is unlikely that this could be satisfied for the frequencies expected within a full scale cavity. However, despite this, it is expected that porous mesh devices can provide a significant amount of wideband attenuation at off design conditions as they offer resistance to all flow which passed through the mesh structure. Wire mesh based devices were investigated at both small and medium scale and at Mach numbers of 0.7, 0.8, 0.9, 0.95, and 1.5. The attenuation results from the wind tunnel tests are discussed in the following sections.

5.9.1.1 Small (1/40th) scale wire mesh cases (subsonic (Mach 0.8 to 0.95))

A series of three mesh palliative designs were tested within the small scale cavity (Table 15). The three devices all shared a common porous mesh faceplate, but each array had a varying level of ventilation (from 0% to 29% open area) between the enclosed backing volume and the freestream flow (*Figure 105*). It was expected that the backing volume porosity would improve attenuation as it would allow for the pressure waves to pass through the device and vent any excess pressure to the freestream. This effect would then disrupt the modal generation process as the amplitude of any reflected pressure waves would be reduced.

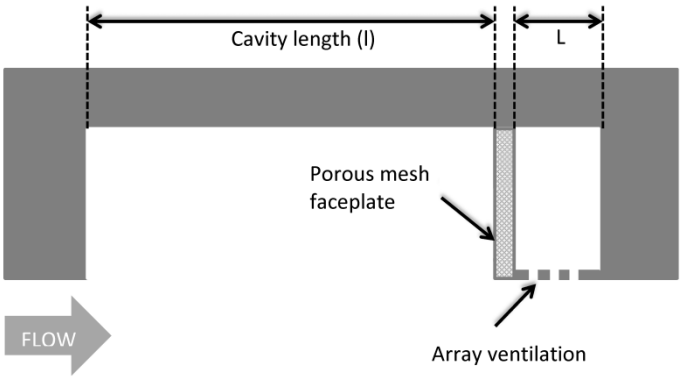

Figure 105 – Sketch of a porous mesh device with ventilation installed into the rear wall of a cavity.

Firstly, the effect of Mach number on the attenuation performance of Mesh A (Table 15) are investigated. *Figure 106* shows that the attenuation from Mesh A only affects the third cavity mode with a slight peaking effect on the second mode also evident. Based on the impedance tube measurements (see *section 4.5*) it was expected that the attenuation would be greatest at higher frequencies as this is where the porous mesh exhibited its highest resistance (Re(Z)*) values (Figure 63). Attenuation also increases with an increase in the freestream Mach number. The attenuation level rose from 5dB at the third mode for the Mach 0.8 case (*Figure 106a*) up to 12dB for the Mach 0.95 case (*Figure 106c*). This effect was expected as an increase in particle velocity within the cavity is associated with an increase in SPL and an increase in velocity typically provides a higher level of resistance to the flow.

Figure 107 shows the effect of backing volume ventilation on the attenuation provided by a porous mesh device. As the open area of the backing volume ventilation was increased from 0% (the enclosed case (*Figure 106*)) to 8.7% (*Figure 107b*), and 29% (*Figure 107a*) the level of attenuation reduced from around 12dB at the third mode to 5dB. This result is thought to be due to the ventilation of the backing volume, which reduces the unsteady pressure levels within the device backing volume. A reduced unsteady pressure will cause a lower time averaged particle velocity through the porous mesh faceplate. The peak pressures within the backing volume can be vented to the freestream flow, and this would reduce the effect of superposition due to the reflection of the pressure waves off the rear wall of the backing volume. The attenuation due to viscous resistance would be reduced to a lower level with the lower time-averaged particle velocities caused by the ventilation. A similar effect would be expected due to lower SPL within the cavity, where the peak pressures are initially lower than those at higher Mach numbers.

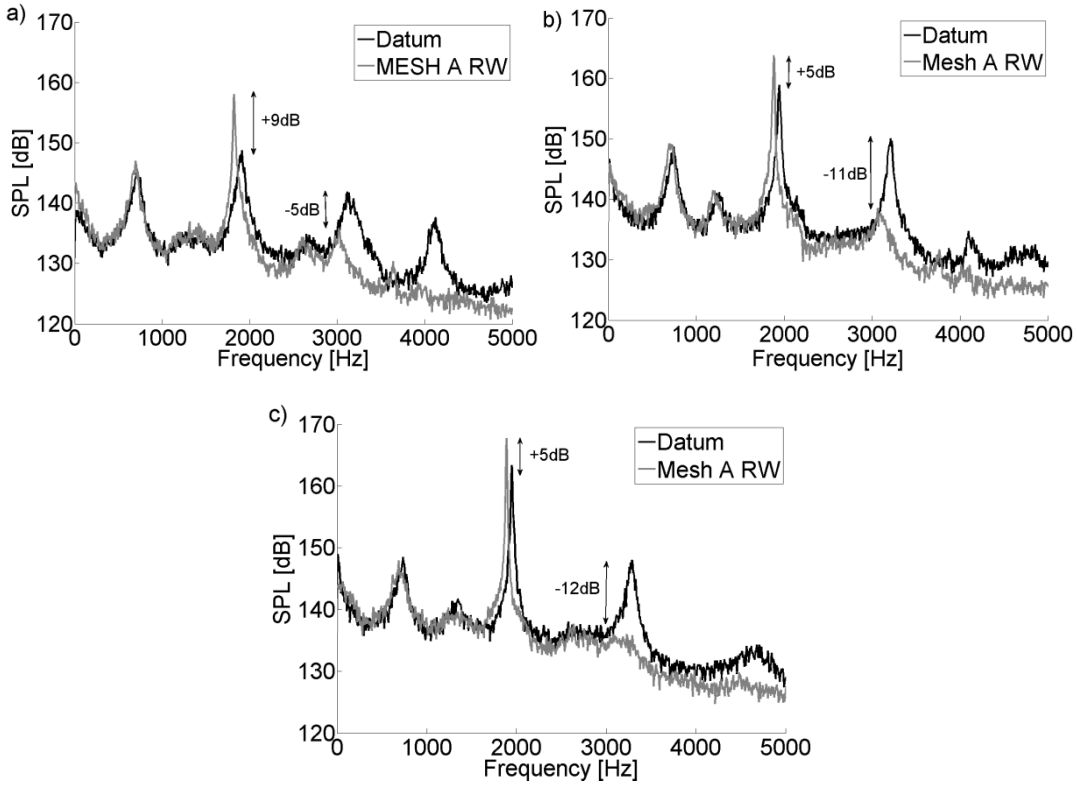

Figure 106 – Effect of Mach number on the attenuation performance of a porous wire mesh based palliative device a) Mach 0.8, b) Mach 0.9, c) Mach 0.95

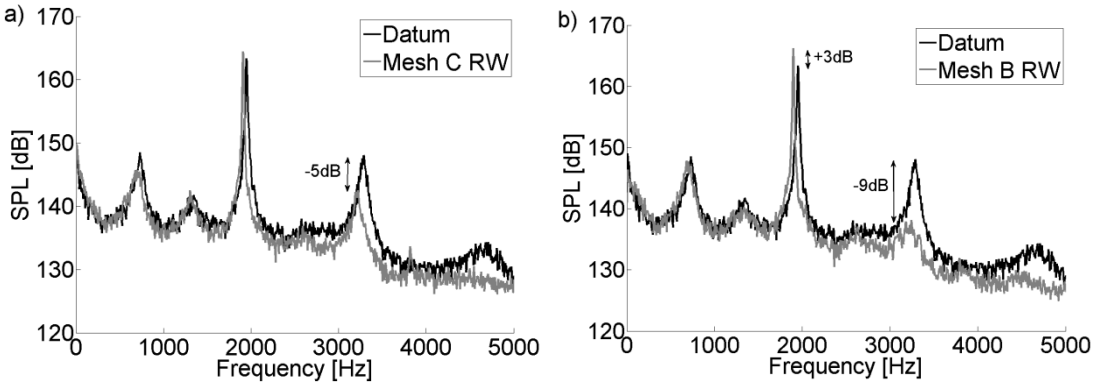

Figure 107 – Effect of backing volume ventilation porosity on the attenuation performance of a porous wire mesh based palliative a) Mesh C with a backing volume porosity of 29% , b) Mesh B with a backing volume porosity of 8.7%. (Mach 0.95)

5.9.1.2 Medium (1/20th) scale wire mesh cases

The small scale test results demonstrate that porous wire mesh devices can provide a significant level of attenuation at higher frequency modes within a subsonic cavity spectrum (*Figure 106*). The attenuation performance from a series of mesh devices was assessed at Mach 0.7 in the medium scale cavity. For this subsonic condition (Mach 0.7), the mesh type devices with an enclosed backing volume (*TGF m1* and *TGF m2* (*Table 16*) did not demonstrate any attenuation of the cavity modes, however *TGF m3* (*Table 16*), with the ventilated backing volume, provided an average attenuation of 2dB over the cavity ceiling. This level is within the uncertainty for this facility and cannot be considered as a significant result.

As *TGF m1* and *TGF m2* did not provide any attenuation under subsonic condition they were disregarded for the supersonic tests due to time constraints. However, the performance of *TGF m3* was investigated, because it was of interest to investigate whether *TGF m3* would affect the modal generation process when installed in the front wall of the cavity for the supersonic cases. As this device has a 50% porous backing volume it was expected that the flow which passes through this ventilation will cause shock waves ahead of the cavity and therefore reduce the velocity of the shear layer over the cavity. A reduction of the shear layer velocity would be expected to reduce the modal frequencies and disrupt the interactions between the shed vortices constrained within the detached shear layer and the pressure waves within the cavity.

A schlieren image which clearly shows the shock waves created by the passage of air from the cavity through the ventilated backing volume of a porous mesh devices is shown in *Figure 108*. This image supports the assumption that the ventilations would cause shock waves to form upstream of the cavity. The shear layer over the cavity is also clearly visible within this figure, which shows that the cavity modal generation process is not completely disrupted by the presence of the shock waves. However, as the freestream flow velocity will decrease across the shock waves, the convection speed of the vortices ($V_V=kU_\infty$) within the shear layer would be expected to decrease accordingly. A reduction in the vortex convection speed would manifest as a decrease in the modal frequencies within the acoustic spectra. This is due to the associated increase in travel time over the cavity length which effectively increases the time period of the fundamental loop frequency (f_a). Such a decrease in the modal frequencies is demonstrated within the acoustic spectrum (*Figure 109*) where the peak modal frequencies are reduced by around 3% with the *TGF m3* configuration at the front wall.

The *TGF m3* case provided an attenuation of around 7dB for the third cavity mode for the Mach 1.5 case (*Figure 109*). This level of attenuation was typical of the levels exhibited across the ceiling of the medium scale cavity model. This result (*Figure 109*), where the attenuation is limited to only the third cavity mode and higher frequencies (f>1.9kHz) is similar to the results shown for the subsonic small scale tests (*section 5.9*) and is thought to be due to the resistance properties of the mesh. The mesh used for

these devices was tested using a high SPL impedance meter and it was demonstrated that the resistance and the attenuation levels were greater for frequencies higher than 2.0kHz (*section 5.9*).

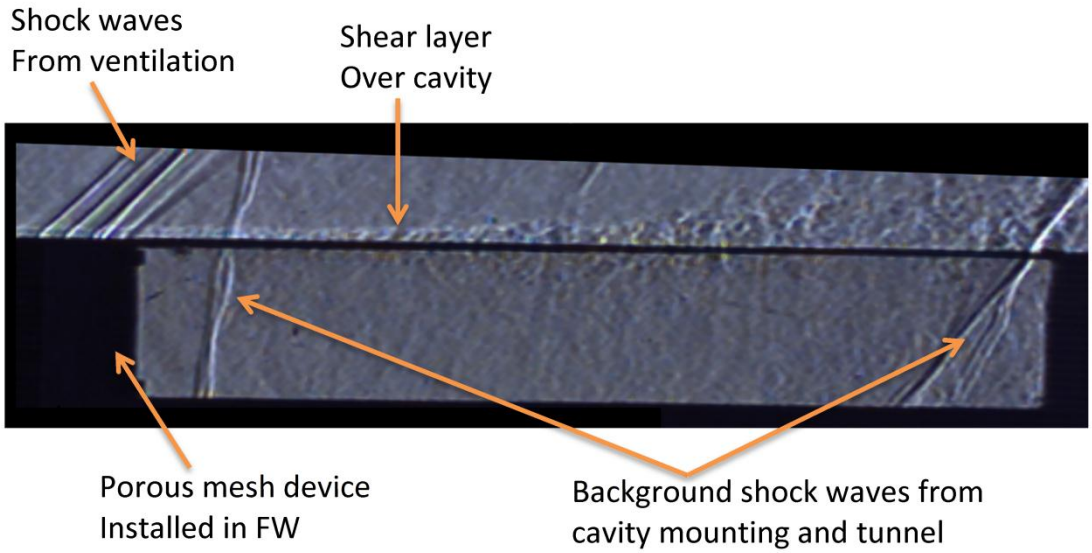

Figure 108 – Schlieren image of shock waves caused by the ventilated backing volume of a mesh device installed at the front wall. Taken under Mach 1.5 conditions within the TGF tunnel.

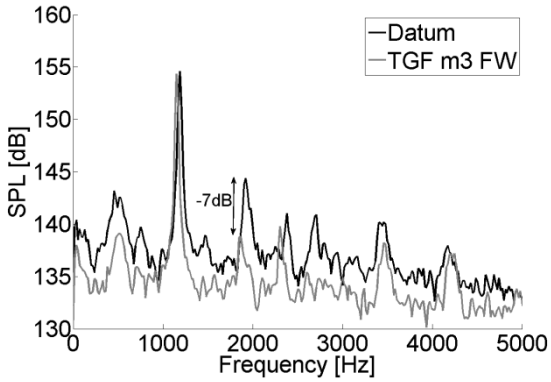

Figure 109 – Attenuation performance of a wire mesh based palliative device under supersonic freestream conditions (Mach 1.5).

5.9.2 Acoustic foam under subsonic conditions (Mach 0.9)

The attenuation provided by acoustic foam is generated in a similar way to porous mesh devices in that it solely relies on the resistance properties of the foam material. Also, in similarity to mesh devices the attenuation from foam is expected to be broadband in nature with the highest levels of attenuation at frequencies which correspond to the condition where the disturbance quarter wavelength is equal to the thickness of the foam. This is again to ensure that the maximum bulk particle velocity of the disruption is encountered by the foam and therefore the maximum resistance and attenuation can be provided to the system. The foam used for the current investigation has been designed for use within a low SPL room environment and its properties are discussed in *section 4.5.3*.

The attenuation results from the tests conducted with the acoustic foam installed within the cavity are shown in *Figure 110*. The foam provided the greatest attenuation (13dB (*Figure 110d*)) when installed into the rear wall of the cavity and not only was the modal attenuation higher there is also a 5dB increase in the attenuation of higher frequency broadband noise (f>3.2kHz (*Figure 110d*)) compared with the front wall, sidewall and ceiling positions. The attenuation levels from the foam installed in the front wall (*Figure 110a*), side wall (*Figure 110b*), and ceiling (*Figure 110c*) are all of a similar 10dB level at the third mode with little or no effect at any other mode or frequency.

This increase in the attenuation for the rear wall configuration is due to higher SPL in the rear of the cavity compared to the other cavity locations. Much like for porous meshes the attenuation provided by acoustic foam is due to the resistance properties of the material and it is known that the resistance of porous materials increase with increased SPL [50]. The increased SPL creates higher bulk particle velocities through the open celled structure of the foam which increase the viscous losses within the foam. The higher SPL at the rear wall improves the attenuation performance of the foam and enables higher frequencies to be attenuated as well as the third modal peak.

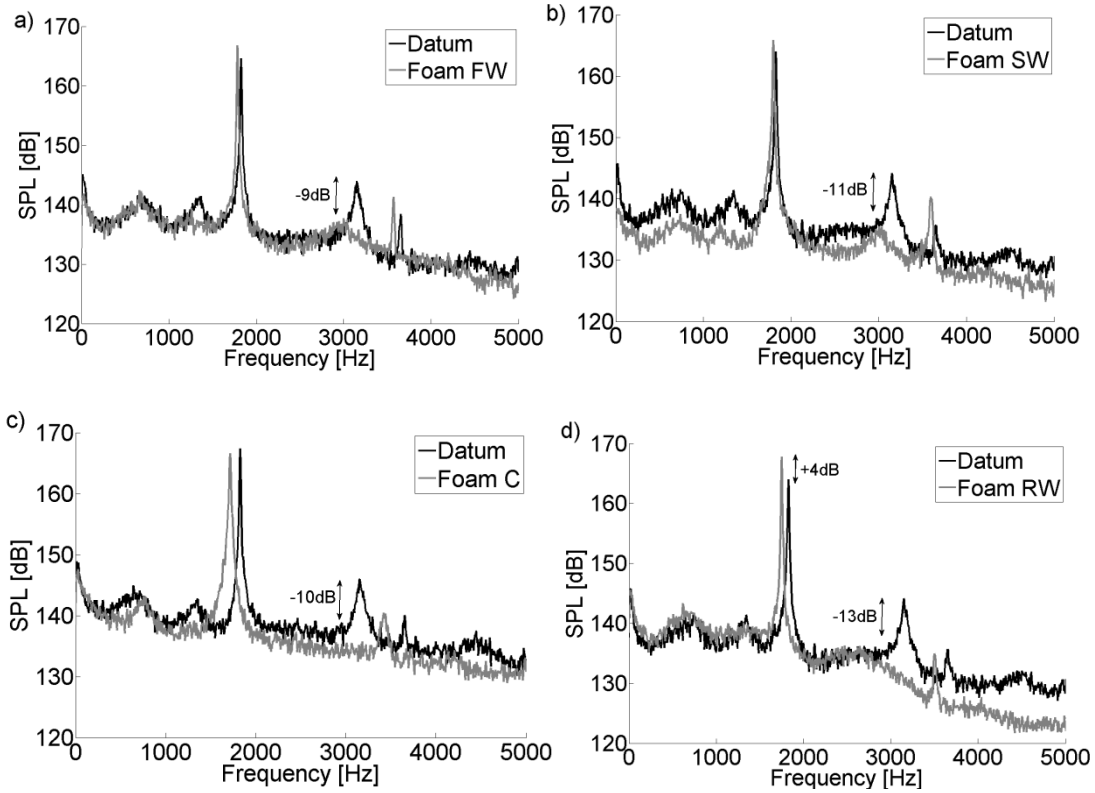

Figure 110 – Attenuation performance from acoustic foam liners installed into the various cavity surfaces a) Front wall (FW), b) Side wall (SW), c) Ceiling (C), d) Rear wall (RW). (Mach 0.9)

5.9.3 Mass injection and removal under subsonic (Mach 0.9) conditions

To improve the attenuation from the wire mesh cases within the small ($1/40^{th}$) scale facility the cavity was configured to allow mass injection into and removal from the cavity through a porous mesh device (see *section 5.9.1*). The purpose of this process, known as bias flow, was to both improve the mesh resistance characteristics and also to affect the modal generation process. The *build 2* cavity was used as this provided the best access to the backing volume of the devices, which was required to connect the inlet/outlet tube.

Bias flow, in both the injection and removal sense, has been previously demonstrated as a successful method of improving the attenuation characteristics of acoustic devices [112] [101] and therefore it was of interest to see if this was the case for a simple wire mesh based device within the small scale cavity. The addition or removal of mass from the cavity flow system is also expected to affect the modal generation process and result in a cavity with altered modal characteristics. Mass removal at the rear wall was expected to provide the greatest attenuation as this is where the vortices within the shear layer interact with the cavity surface to produce the pressure waves within the cavity. If the additional mass, which is entrained by this process, could be removed it was expected that the intensity of the pressure waves generated would be reduced. This should interrupt the modal generation process and reduce the intensity of the modal spectrum.

Two levels of mass injection were assessed. Firstly, the inlet port of the device was left open to the atmosphere and this provided a mass flux per unit area of greater than $5kgs^{-1}m^{-2}$, where $5kgs^{-1}m^{-2}$ was the largest mass flux that could be measured by the flow meters. Therefore, for this case the mass flux was at least 1.3% of the freestream value ($\rho_\infty U_\infty$). Secondly, the flow was restricted through the use of a needle valve, which reduced the flow rate to around $1kgs^{-1}m^{-2}$ (0.3% of $\rho_\infty U_\infty$). For the rear wall case both of these flow levels resulted in a similar level of attenuation at the third mode ((12dB) *Figure 111a*). There is also around 5dB attenuation of the broadband noise at frequencies higher than the second mode (2kHz).

For the mass removal cases, again two flow levels were used. Firstly the outlet port was connected directly to a vacuum and this provided a flux per unit area greater than $5kgs^{-1}m^{-2}$ (1.3% of $\rho_\infty U_\infty$). Secondly, the outlet flow was restricted through the use of a needle valve, which again reduced the flux to $1kgs^{-1}m^{-2}$ (0.3% of $\rho_\infty U_\infty$). The rear wall cases for these two mass removal configurations both provided around 12dB of attenuation at the third mode (3.2kHz) and around 5dB of broadband attenuation (*Figure 111b*). These results do not demonstrate the expected benefits from mass removal at the rear wall and the modal generation process appears to be relatively unaffected as the cavity still exhibits high intensity modal peaks.

Both of the bias flow configurations, mass injection and removal, did not provide a greater level of attenuation when compared with the no flow case (*Figure 111c*). When the device was installed into the cavity with no flow it returned an attenuation of around 13dB at the third mode and around 5dB of broadband attenuation (*Figure 111c*). For all front wall configurations the attenuation levels were significantly lower with maximum peak attenuation levels of around 5dB. These devices provided a mass flux per unit area which was at least 1.3% of the freestream mass flux ($\rho_\infty U_\infty$). However, due to the ineffectiveness the actual mass flux must have been less than the levels of 5% and 15% recommended by previous work [56]. Therefore, as these bias flow devices have relatively low mass fluxes, and they do not represent an improvement in the attenuation over the zero flow case they are not recommended as potential cavity palliatives.

In all cases where a porous wire mesh type devices was used the cavity modes exhibit a shift to a lower frequency of around 6% (*Figure 106* and *Figure 111*). This is of the same order as the frequency shift that would be expected if the cavity length were extended by an additional amount equal to the length of the backing for the mesh devices. Unlike for the resonator cases the resistance based porous mesh devices are not expected to interact differently between modes of different frequencies. This factor means that the pressure waves from all modes, and importantly from the modal generation process, can pass through the mesh faceplate as they all experience it as an acoustically soft boundary. This effectively increases the cavity length and results in the lower frequency modes exhibited in the results (*Figure 106* and *Figure 111*).

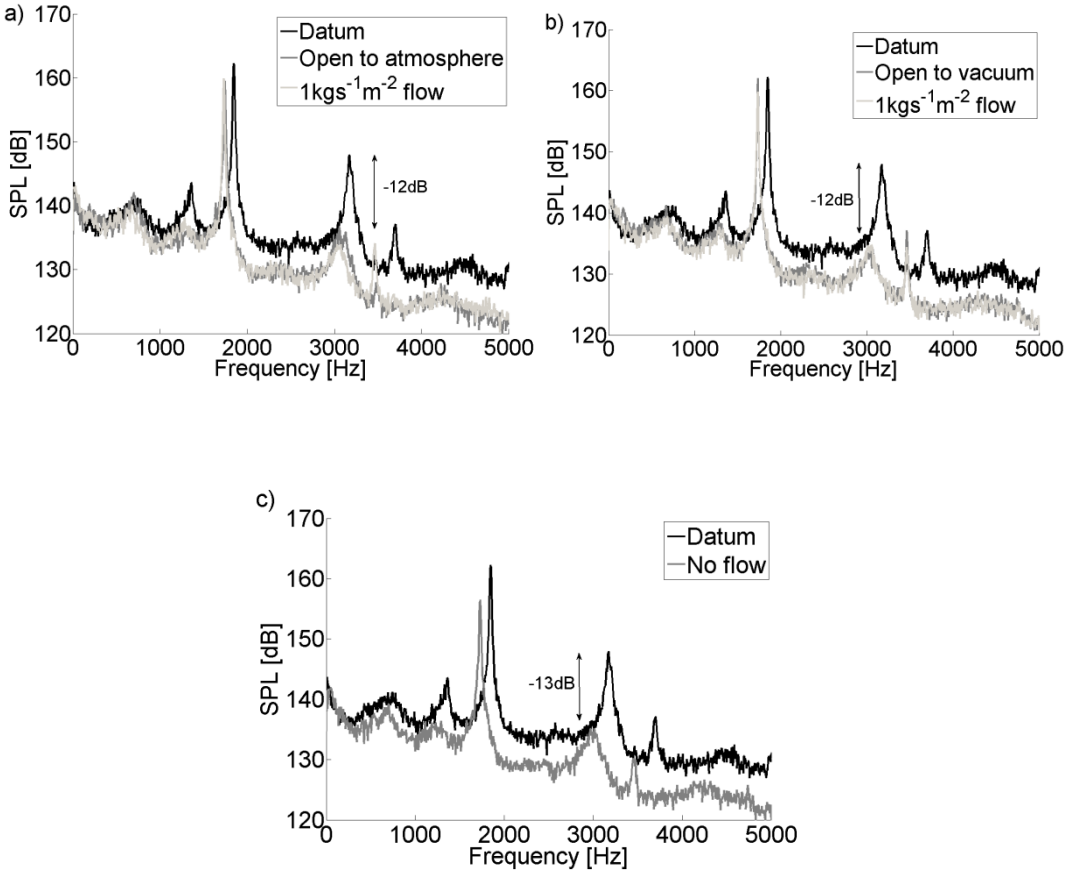

Figure 111 – Attenuation from a porous mesh configuration with bias flow through the perforation. a) Mass injection into cavity through rear wall device, b) Mass removal from cavity through rear wall device, c) No flow through the porous mesh device used for the bias flow tests (RW configuration). (Tested at Mach 0.9)

5.10 Preliminary assessment of resonant devices for a full scale weapon bay cavity

This section investigates the effects of the aircrafts operational flight envelope (Mach number and altitude) on the Rossiter modes and the consequences that any changes may have on the attenuation performance of resonant arrays is assessed. Whilst these are factors which cannot be tested the discussions focussed on an analytical assessment. However, an impedance tube can be used to investigate the attenuation properties of a series of arrays which target the calculated modal frequencies of a full scale cavity. Since the function of a weapons bay cavity is to carry stores, the effect these stores may have on the acoustic signature is also considered and an assessment of the resonator size as an installation penalty within the bay is also carried out.

5.10.1 Effect of the flight envelope on the Rossiter frequencies

The altitude at which an aircraft opens its weapon bay is expected to affect the frequencies at which the Rossiter modes occur. This effect is caused primarily by the changes in the air temperature and density which affect the speed of sound at different altitudes. An analytical investigation into how these effects may affect the performance

of arrays is discussed. The two extreme cases for the effect of altitude are sea level and an expected service ceiling of 20 km. The estimated Rossiter mode frequencies at these two cases show that the maximum possible deviation in modal frequency is expected to be around 11 Hz (*Figure 112*). This is of comparable level to the deviation caused from changes in Mach number over the transonic regime (*Figure 113*) and is also expected to be within the tolerance of the resonator bandwidth. The altitude at which stores are released is therefore not expected to greatly affect the attenuation performance of the arrays.

The effect of Mach number on the cavity acoustic signature has already been discussed for the model cavity case (*section 5.3*). The peaks in absorption coefficients occurred at approximately the same frequency for cases at Mach 0.8, 0.9, and 0.95. The frequencies for the first 3 Rossiter modes of a 4m long cavity are calculated to remain within a range of 10 Hz for Mach numbers from 0.8 to 0.95 (*Figure 113*). It is expected that the bandwidth over which attenuation occurs for a resonant absorber will cover this range. Therefore no deterioration of attenuation performance should be seen from the frequency change alone within this small subsonic range. However, at higher supersonic Mach numbers (Mach 1.5) the modal frequencies increase by up to 50% compared with the Mach 0.8 frequencies (*Figure 113*). This variation in modal frequency is too large to be covered by a single array. Therefore, much like the medium scale test cases (*section 4.4.2*) a separate array will be required for attenuation at subsonic and supersonic Mach numbers.

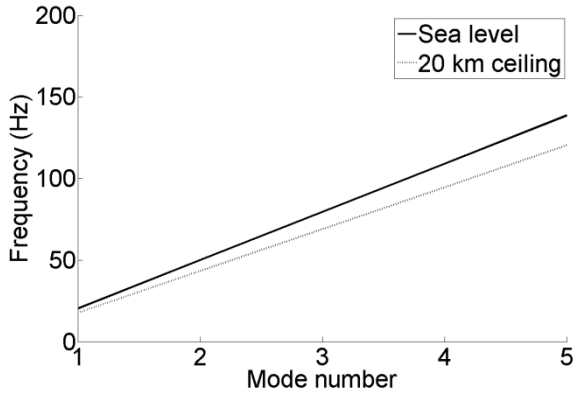

Figure 112 – Effect of altitude on the calculated Rossiter frequencies within a 4m long open flow cavity (l/h=5)

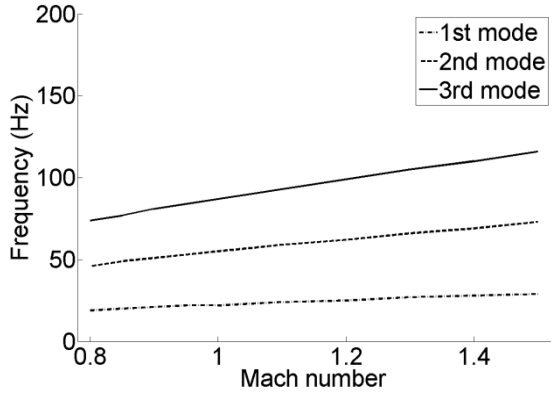

Figure 113 – Effect of Mach number on the calculated Rossiter frequencies within a 4m long open flow cavity (l/h=5)

5.10.2 Effect of clutter on the cavity acoustic environment

Whilst the majority of exploratory tests concerning cavity flows are conducted in the absence of stores within the bay, aircraft will not primarily operate with an open empty weapon bay. Therefore, when designing a new palliative device for weapon bay cavities it is important for the designer to take the effects of stores or clutter within the weapon bay on the spectral characteristics into account. For instance, a full stores load may be expected to displace around half of the air volume within a cavity [119] (*Figure 114*). Also, the walls of a typical weapons bay cavity are not smooth as cables and pipes often ingress into the bay creating a roughened wall surface. It is important then that a palliative device can retain the integrity of the weapon bay and the aircraft and also improve the store separation characteristics through a reduction in the unsteadiness within the cavity flow.

Whilst the presence of stores within a cavity would partially block the feedback mechanism between the shear layer and the pressure waves, this is shown not to reduce the modal signature (*Figure 115*). However, the presence of stores within the bay is expected to increase the travel time of the acoustic waves within the cavity, due to the obstruction creating a larger travel distance, and therefore the frequency of the Rossiter modes is expected to reduce [119]. Also, the stores and clutter associated with the non-smooth cavity walls (*Figure 114*) scatter and absorb the pressure fluctuations within the bay and a reduction in modal amplitudes is expected for all Rossiter modes. Indeed, the effects of stores are confirmed in *Figure 115* where both the modal amplitude and frequencies are reduced for the cavity carrying stores. *Figure 115* demonstrates that stores reduce the modal frequency by around 10% and reduce the peak SPL by around 5% [119].

It is important to note that even with stores within the cavity the acoustic spectrum remained modal with high peak SPLs. This demonstrates that the feedback mechanism is not blocked and that damage would still be expected to occur within the bay. The change in modal frequencies due to the stores does however need to be taken into account as this effect would not be captured by predicting the modal frequencies using

the modified Rossiter equation (Equation 9). If the modal frequencies are required for the design of a palliative device (see section 4) then the change in frequency due to the presence of stores could reduce the effectiveness of the device and cause potentially damaging conditions to remain within the bay environment.

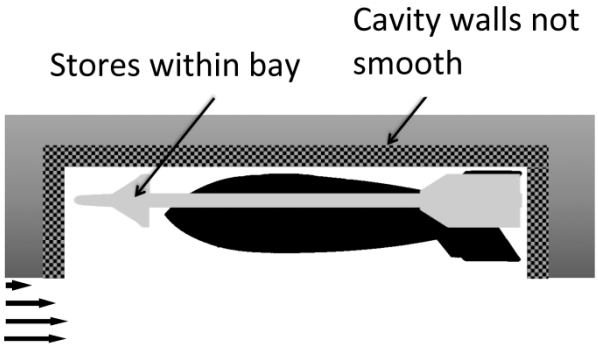

Figure 114 – Sketch of typical stores arrangement within a weapon bay cavity

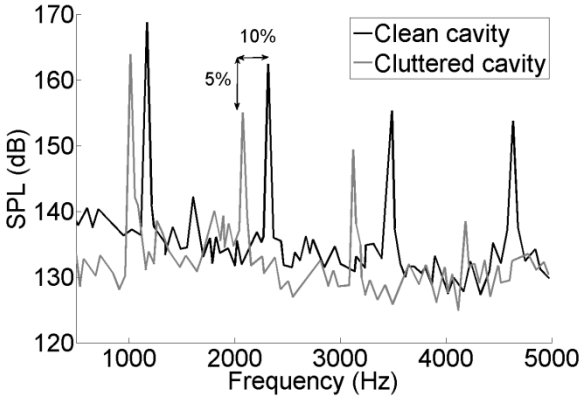

Figure 115 – Effect of stores/clutter on the acoustic environment of an open flow cavity (reproduced from [119])

5.10.3 Assessment of cavity size effects on the Rossiter frequencies

All of the wind tunnel tests carried out within this body of work have been conducted at relatively small scales (1/40th and 1/20th). The results from these tests are representative of the fundamental cavity noise mechanisms and provide modal spectra on which palliatives can be tested. However, the modal frequencies are expected to orders of magnitude different between the small scale and full scale cases. The typical munitions carried within a full scale weapon bay can be represented by the AMRAAM AIM-120C-7. The full sized length of this missile is 3.65m [120] and it is estimated that a space margin of 5% of the missile length is required at either end of the weapon bay. This results in a full scale cavity with a length of around 4m and it is estimated that the cavity will have an l/h ratio equal to 5. At this scale and for this configuration, the

calculated modal frequencies for the second and third modes at Mach 0.9 are around 50Hz and 80Hz respectively (*Figure 116*). These frequencies are several orders of magnitude lower than the small scale tests and it was unknown as to whether resonant absorbers would be able to achieve high levels of absorption at the low frequencies expected for full scale cavities.

To investigate whether resonant arrays could be used to attenuate at these low frequencies a large scale, low frequency impedance tube facility was used (*section 3.3.1*). This facility enabled the absorption properties of arrays which were designed to target the lower full scale modal frequencies to be experimentally measured. Two arrays were designed to target these full scale modal frequencies (LS_ARRAY1 and LS_ARRAY2 respectively) and a third array (LS_ARRAY3) was designed to target an upper frequency limit of 150Hz. The design space available for these array designs is discussed in Appendix A and whilst these arrays are not accurate representations of possible devices which could be used at full scale they represent a measured example of whether or not high levels of attenuation could be provided at the low frequencies estimated within a full scale weapon bay. The limits on the design space necessitated that the arrays designed would have low porosities (ε) and this in turn created arrays with very high resistance Re(Z)* values (*Table 22*). It was demonstrated in *section 5.2* that arrays which exhibit high Re(Z)* properties do not provide favourable attenuation characteristics within a cavity. The link between Re(Z)* and attenuation is discussed in *section 5.8* where the best performance prediction metric is selected.

Both of the arrays (LS_ARRAY1 and LS_ARRAY2) exhibited promising absorption properties. There are clear peaks in absorption coefficient close to the frequencies calculated by the analytical model (*Figure 117a* and *b*). LS_ARRAY1 was designed to target 50 Hz with an absorption coefficient (α) of around 0.4, however the peak in its absorption was at 70 Hz with a higher absorption coefficient of α = 0.7 (*Figure 117a).* LS_ARRAY2 was tuned to target 80 Hz and was expected to achieve an absorption coefficient of around 0.66. The calculated level of absorption coefficient for LS_ARRAY2 matches that obtained in the impedance tube, however the experimental results show that LS_ARRAY2 was tuned to a frequency of 90 Hz (*Figure 117b*). The results for the third array (LS_ARRAY3) are more encouraging as the modal frequency of the array is correctly calculated and the peak absorption coefficient level is calculated to within 15% of the measured level (*Figure 117c*).

The relatively accurate prediction of the peak absorption coefficient levels for LS_ARRAY2 and LS_ARRAY3 is due to the accurate representation of the resistance by the analytical model, where Re(Z)* is calculated to be within around 30% of the measured value (*Table 23*). However, for LS_ARRAY1 the analytical model over calculated Re(Z)* by around a factor of two which resulted in the lower calculated α levels (*Table 23*). The frequency component of the arrays performance is governed by the reactance (Im(Z)*) of the arrays. Whilst, the analytical model accurately calculated

Im(Z)* for LS_ARRAY3 to within ±1% it was less accurate for LS_ARRAY1 and LS_ARRAY 2 where Im(Z)* was over predicted by around a factor of 20 (*Table 23*).

These impedance tube tests were conducted to assess whether an array could provide a useful α at the relatively low frequencies expected within the weapon bay of a full aircraft and the arrays used do not represent the ideal cases due to the limitations of the impedance measurement apparatus. Both LS_ARRAY1 and LS_ARRAY2 exhibit a peak in absorption coefficient within 20Hz of the target frequency (*Figure 117a* and *b*) and the discrepancies between the calculated and measured resonant frequencies are caused by the low porosity (ε) of the arrays. It is expected that realistic full scale arrays would have a higher ε than these arrays and would be designed to take into account the effects of high SPL on the resistance of the faceplate. Nevertheless, these preliminary tests indicate that resonant arrays could be used as a potential palliative device for a full scale weapon bay cavity.

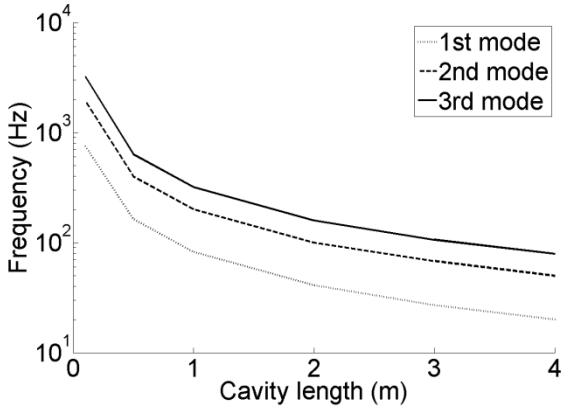

Figure 116 – Effect of cavity length on the calculated Rossiter frequencies within am open flow cavity (l/h=5)

Name	f (Hz)	d (mm)	D (mm)	t (mm)	L (mm)	ε (%)	α	β (%)	Re(Z)*
LS_ARRAY_1	52	1	57	2	68	0.02	0.4	56	7.2
LS_ARRAY_2	81	1	37	2	68	0.06	0.65	51	3.8
LS_ARRAY_3	151	1	20	2	68	0.2	0.96	48	1.5

Table 22 – Geometric and acoustic properties for the preliminary arrays to target the calculated Rossiter frequencies at full scale (l=4m).

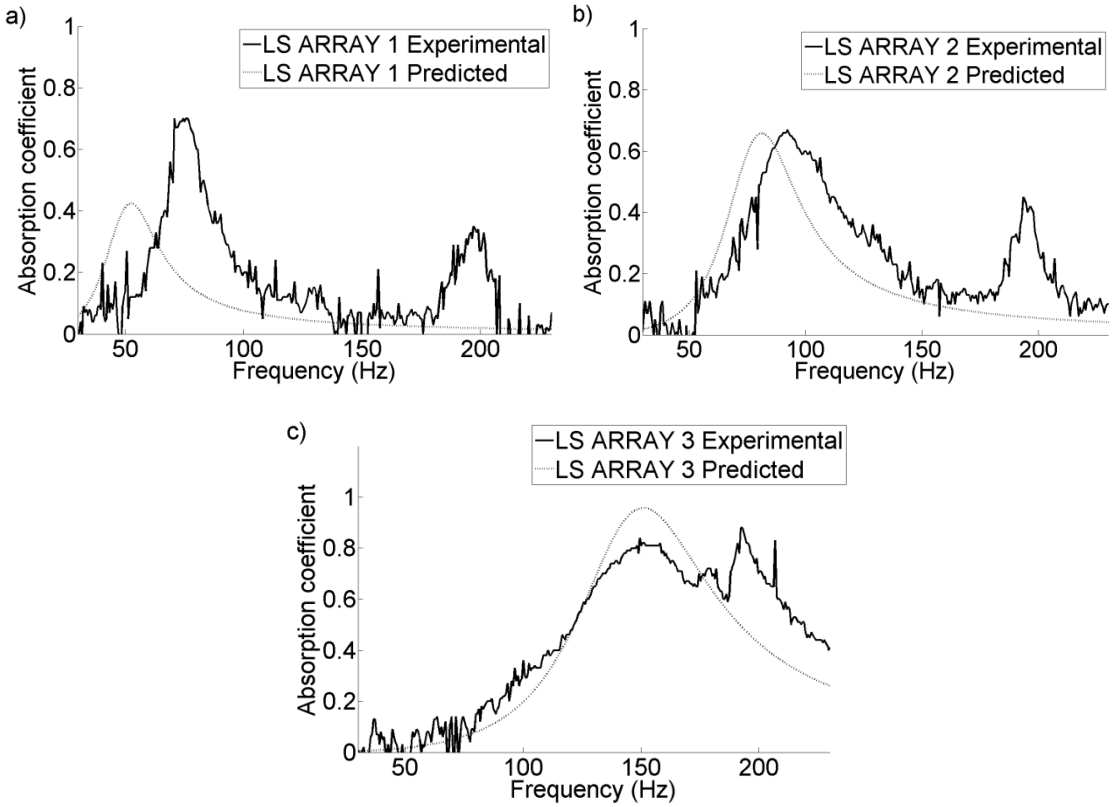

Figure 117 – Comparison between experimental and calculated absorption coefficient profiles for resonant arrays targeting full scale frequencies at a) 50 Hz, b) 80 Hz and c) 150 Hz.

	Resistance (Re(Z)*)		Reactance (Im(Z)*)	
ARRAY	calculated	measured	calculated	measured
LS_ARRAY1	7.0	4.0	20	0
LS_ARRAY2	3.6	3.7	2.6	0
LS_ARRAY3	1.5	2.4	0	0

Table 23 – Calculated and measured impedance characteristics for the low frequency arrays tuned to the calculated frequencies for a full scale weapon bay. (values quoted for measured resonant frequency of array)

6 Conclusions and consequences

This study has investigated the attenuation performance characteristics of a variety of passive palliative devices designed to alleviate the problems associated with the unsteady flow conditions within cavity flows. An experimental investigation of the underlying flow physics behind the unsteady cavity acoustics was also conducted. The problems associated with unsteady cavity aero-acoustics have been widely reported previously and the field is currently undergoing renewed interest. Historically, the focus of previous investigations was on fundamental analysis of the flowfield and simple palliative techniques. With the advent of high-speed data acquisition and improved data processing techniques, much of the previous research focused on complex active control methods and gaining a better understanding of the underlying flow physics. Despite this shift in focus, and increases in palliative complexity, large areas of understanding have received a relatively small amount of interest and palliative performance levels have plateaued. Under certain conditions, especially supersonic freestream conditions, palliatives can be ineffective and the attenuation levels can be insufficient.

This body of work has addressed some of the areas which require a greater understanding through the investigation of the modal generation process and a new palliative concept. Correlation analyses of the pressure measurements for a small scale model cavity were used to provide experimental evidence which underpins a previously proposed mechanism through which the modal peaks, associated with cavity flows, were generated. To investigate the performance of the proposed palliative device, an analytical tool was developed, a range of design philosophies were tested under both transonic and supersonic freestream conditions, and guidelines for the use and performance of such philosophies have been provided. The following sections discuss the conclusions and consequences from the current body of work. This discussion includes the findings surrounding the modal generation process and the attenuation from the newly proposed palliative devices. Design recommendations and the viability for full scale use are provided as well as a set of recommendations for further work.

6.1 Modal generation process

- To investigate the characteristics of the fundamental cavity flow and the attenuation performance from a range of palliatives, a small scale ($1/40^{th}$) cavity model was designed and commissioned. The model was shown to have modal characteristics in line with the established database, which were within ±4% of the measured values under transonic conditions ($0.80<M<0.95$). The more fundamental characteristic of the vortex convection speed over the cavity was measured using correlation analysis. Cross-correlations for transonic flows (M=0.9 and M=0.95) revealed that the measured k values are within ±2% of the k=0.57 assumption recommended by Rossiter (k (Equation 12). Therefore, the experimental facility is suitable for the investigation of the both the fundamental flow field as well as the performance of palliative devices.

- An alternative, more fundamental, understanding of the modal generation process, based on an amplitude modulation mechanism [15], was also investigated using correlation analysis. For the first time, this study has shown experimental data, within the transonic flow regime ($0.80<M<0.95$), that supports this alternative view of the modal generation process. This mechanism provided the modal frequencies to within ±1% for the second and third modes and around ±10% for the first mode. This correlation analysis can be used to analyse numerical data and provide information about whether the numerical approach can capture the fundamental flow features within the cavity flowfield.

- Short term Fourier analyses have revealed the intermittency of the dominant cavity modes with respect to time. Under both transonic and supersonic conditions the modal peaks demonstrated intermittency, where no peak has a constant SPL over the sample period. This intermittency developed into clear mode switching, where the presence of one mode precludes the presence of another, under transonic ($0.80<M<0.95$) conditions. In this case the two dominant modes alternated for the highest SPL within the spectrum. This indicates that the individual modes may require different flow conditions, such as the number of vortices which span the cavity. All mode switching and intermittency was removed when a modal peak was attenuated by a resonant array, which indicates that the modes are related through a central process within the cavity.

6.2 Modal attenuations

This work has primarily investigated the modal attenuation from resonant arrays under both transonic and supersonic conditions. However, alternative approaches for attenuation have also been considered and the conclusions from both investigations are discussed.

6.2.1 Attenuation from resonant arrays

- Resonant arrays have demonstrated large peak attenuation levels for single modes of up to 26dB under supersonic (Mach 1.5) freestream conditions and up to 17dB for high transonic (Mach 0.95) conditions. These peak attenuations have been specifically targeted at the dominant cavity modes within a typical "open flow" type spectrum. This is a notable result as, typically, passive palliatives are unsuccessful under supersonic freestream conditions. Therefore, resonant arrays represent a simple, fully passive approach which could be used in conjunction with the standard actuated spoiler configuration under supersonic conditions.

- The attenuation from resonant arrays can be tuned to the different modes within a cavity. This targeted approach can either be used to attenuate a single mode or through a combined configuration through which multiple modes can be attenuated simultaneously. The attenuation from individual resonant arrays can be improved, to include a 7dB decrease in the OASPL and up to 15dB of peak modal attenuation at multiple modes simultaneously, through a combined configuration where one array was placed at the cavity front wall and another at the rear wall. This improvement in performance brings the attenuation level provided by resonant array configurations into line with spoiler devices, which typically provide modal attenuations coupled with a decrease in the broadband noise signature, and could represent an alternative to the typical spoiler configurations.

- The highest levels of attenuation were exhibited by configurations with an array installed into either the front or rear wall of the cavity. Little or no attenuation was exhibited by arrays when installed into the cavity ceiling or sidewalls. A consequence of this is that a certain length of the cavity will be required to house the resonant array and this length is expected to be around 10% of the cavity length.

6.2.2 Attenuation performance from other palliative approaches

- Porous meshes have demonstrated reasonable levels of modal attenuation under both transonic and supersonic conditions. Typically, the attenuation was for higher order modes and up to 12dB peak attenuation was provided at the third mode (3.2kHz) within the small scale cavity at Mach 0.95. At Mach 1.5 the third mode (1.9kHz) was attenuated by 7dB. To target lower frequencies would require a larger volume within the mesh device to meet the quarter wavelength condition ($\lambda/4 \approx 1$m for 80Hz mode). Therefore, it is unlikely that this will be viable for the low frequency modes expected within a full scale weapon bay cavity.

- Acoustic foam provided up to 13dB of modal attenuation at Mach 0.90 when installed into the cavity rear wall. When other surfaces, such as the ceiling or side walls, were treated individually with the foam, the attenuation was reduced to 9dB. This attenuation was limited to the third mode (3.2kHz) and higher frequencies and to target lower frequencies a thicker section of foam would be required. It is unlikely that this would be possible for the low frequencies expected within full scale weapon bays, due to the space constraints within the bay ($\lambda/4 \approx 1$m for 80Hz mode).

- The effect of steady mass injection and removal from the cavity end walls was investigated as a possible palliative mechanism at Mach 0.90. Both high levels of flow injection and removal through a porous mesh faceplate provided no increase in attenuation over the datum mesh case with no flow. It is therefore unlikely that this method can be used to successfully attenuate the cavity modes.

6.3 Design recommendations for resonant arrays

- Two mechanisms through which resonant arrays can be designed to attenuate cavity modes have been discussed. The first of these mechanisms is the typical approach used by resonant absorbers where energy is absorbed through viscous losses and vortex shedding within the devices. The second mechanism considers destructive interference from out-of-phase reflections to attenuate the standing waves associated with the Rossiter modes within the cavity. These two mechanisms are not mutually exclusive. However, the transonic third mode and all modes within the supersonic tests are more receptive to the out-of-phase mechanism compared with the second mode within the transonic cavity.

- To design the resonant arrays to operate within the high SPL environment of a cavity an analytical model was required. Whilst there are numerous models for resonant array design under low and medium SPL condition, there are relatively few which are acceptable for use under the high SPL conditions exhibited within a cavity, and none which accurately model the increases in resistance due to high SPLs. Therefore, an empirical model was developed which took into account the effects of the high SPL environment. This model provides better estimates of the resistance values of the arrays and enabled a series of arrays to be designed based on their effective resistance properties for both attenuation mechanisms presented within this work, where high resistance arrays attenuate through the viscous mechanism and low resistance arrays attenuate through the phase change mechanism.

- To achieve a high attenuation level under transonic conditions, arrays require a different level of resistance depending on which mode they are designed to attenuate. For both cavity modes used within this study the second and third modes exhibited the highest SPLs and were the primary targets for attenuation. For the second mode the arrays require a resistance in the range $0.25<Re(Z)^*<0.40$ and for third mode the arrays require a resistance of $Re(Z)^*<0.1$ to provide a high level of attenuation. Under supersonic conditions, both the second and third modes could be effectively attenuated by arrays which demonstrated attenuation levels of $Re(Z)^*<0.1$.

6.4 Applicability to full sized operational weapon bay cavities

- The potential for resonant arrays to be used as palliatives within a full sized operational weapon bay cavity has been demonstrated through a series of low frequency impedance tube tests. Arrays designed to target the second and third modes of a 4m long full scale cavity provided reasonable absorption profiles at the required frequencies. Whilst the tested arrays do not represent the ideal cases for attenuation, they indicate that resonant arrays can operate at the low frequencies expected within full scale weapon bay cavities.

- An operational weapon bay will not be an empty clean cavity and will be partially occupied by clutter and stores which will affect the modal properties of the cavity. When stores are installed the modal frequencies are expected to reduce by around 10% and the peak SPL is also reduced by around 5% [119]. If resonant arrays are designed to take this frequency shift into account then the carriage of stores is not expected to affect the attenuation performance.

- The small scale wind tunnel investigations, combined with the high SPL impedance tube tests, have demonstrated that the high SPL environment within open cavity flow is not an issue that will prevent the successful operation of resonant arrays as palliative devices.

- An aircraft may have to operate its weapon bay cavity at various points within the flight envelope and it is therefore important that palliatives are able to provide attenuation over a wide range of Mach numbers and at different altitudes. The frequency changes due to minor changes in conditions are expected to be within the bandwidth of a resonant array. However, at higher supersonic Mach numbers the modal frequencies may increase by up to 50% compared with the transonic frequencies. This variation in modal frequency is too large to be covered by a single array. Therefore, either multiple arrays are required for attenuation at both subsonic and supersonic Mach numbers, or only the supersonic case is targeted as other palliative approaches can be less effective within this regime.

6.5 Recommendations for further work

This work has covered a wide range of both analytical and experimental investigations into cavity flows and their control. However, there are areas which would benefit from further investigation and these are outlined below.

- The reliability of the initial analytical model used for the design of palliatives throughout this work was investigated under both low and high SPL conditions. It demonstrated reasonable reliability under the low SPL for which it was designed and poor reliability for resistance prediction under high SPL conditions. A new, more general approach, to calculate the resistance of arrays under high SPL conditions has been proposed and it demonstrates good reliability for the limited arrays tested. Further investigation into the relationship between the unsteady Reynolds number (Re_ω) and the array resistance (Re(Z)*) is required to verify the new model under high SPL conditions. This would be useful for cavity and gas turbine applications where the SPL is typically higher than room environments.

- Two attenuation mechanisms for resonant arrays have been discussed. These involve either low Re(Z)*, which attenuates through destructive interference or a prescribed Re(Z)* level which absorbs energy directly from the cavity flow. Under transonic conditions the second mode was best attenuated through the latter targeted Re(Z)* approach and the third mode through the former interference approach. However, under supersonic conditions both the second and third modes were successfully attenuated through the low Re(Z)* approach. Further investigation is required to ascertain whether similar levels of high attenuation could be achieved for the transonic second mode from arrays which demonstrate low Re(Z)*.

- Within this study two wind tunnel facilities were used to perform the cavity measurements, one small scale ($1/40^{th}$) and one medium scale ($1/20^{th}$). The medium scale model facility provided the opportunity to measure the mode shapes across the ceiling of the cavity, however this was not available for the small scale cavity. Measurement of the mode shapes within the small scale cavity would allow for a comparison with shapes calculated through an analytical approach and those measured in the medium scale facility. This comparison may reveal discrepancies between the two flowfields and this may explain why certain modes are sensitive to the different attenuation approaches.

- The feasibility of resonant arrays for full scale weapon bay cavities has been investigated through the use of a low frequency impedance tube. However, the devices were designed with different design constraints than for a full scale cavity and therefore did not represent the best candidate designs for cavity palliatives. Further investigation of resonant arrays, designed with a specific Re(Z)* (*section 5.8),* using a low frequency impedance tube would provide further information on

the feasibility of realistic devices for full scale usage. It is likely that a trade-off will exist between the space available within the cavity for the array and the porosity (ε) of the array faceplate required to provide the ideal level of resistance (Re(Z)*).

- Additionally, a numerical investigation of the resonant arrays characteristics under high SPL conditions could be used alongside the large scale impedance tube investigations. This would allow for the characteristics of a full scale array to be investigated under a wider range of high SPL conditions, which were similar when compared with a full scale cavity.

- Further testing opportunities at full scale would provide information about how designs for use within a full scale cavity, perform at the low modal frequencies expected within a full scale cavity. This testing could take place as part of a flight test where the effects of the various stages of the flight envelope on the attenuation could also be assessed. Alternatively, a full scale wind tunnel test would provide sufficient data to comment on the performance of designs for full scale weapon bay cavities.

- Whilst this study has combined numerous data analysis techniques, only unsteady pressure data were taken in the experimental tests. Alternative measurement techniques, such as Particle Image Velocimetry (PIV), could be used to support the unsteady pressure findings. A PIV approach could be used to investigate the characteristic speed of the vortex convection over the cavity and compare this value with those obtained through the correlation approach detailed in the current study. This would then provide evidence in support of the correlation approach.

- The development of the correlation analysis within the current study has provided a method to investigate the fundamental characteristics of cavity flows. This method can be used with numerical data to investigate whether the numerical solution has correctly modelled all of the fundamental flow features within the cavity, such as f_a and f_b. Previously, only the spectral characteristics were considered for validation and this correlation approach would provide further evidence for the reliability of numerical approaches as it provides a fundamental breakdown of the flowfield.

Overall, the newly developed palliative devices, based on Helmholtz type resonators, have demonstrated a good level of attenuation under both transonic and supersonic conditions. The supersonic attenuation results represent a major benefit over previous palliative techniques and it is under these conditions where the devices are likely to be adopted. The preliminary investigation of the full scale devices indicate that full scale arrays are viable and could be used to attenuate the modes within a full scale operational weapon bay cavity.

7 References

[1] Rossiter, J. (1966). Wind-Tunnel Experiments on the Flow over Rectangular Cavities at Subsonic and Transonic Speeds. *ARC-R&M-3438* .

[2] ESDU. (2006). Aerodynamics and aero-acoustics of rectangular planform cavities. Part II: Unsteady flow and aero-acoustics 04023.

[3] JSF.mil. (2012, 11 15). *www.jsf.mil.* Retrieved from http://www.jsf.mil/gallery/gal_photo_sdd_f35atest.htm

[4] Heller, H., & Bliss, D. (1975). *Aerodynamically induced pressure oscillations in cavities: Physical mechanisms and suppression concepts.* AFFDL TR-74-133.

[5] Gad-el-Hak, M. (2000). *Flow Control: Passive, Active, and Reactive flow management.* Cambridge University Press.

[6] ESDU. (2009). Aerodynamics and aero-acoustics of rectangular planform cavities. Part IIIB: Alleviation of unsteady flow effects - acoustic suppression using passive devices 08012.

[7] Shaw, L., & Shimovetz, R. (1994). *Weapons bay acoustic environment AGARD-CP-549.*

[8] Nayyar, P., Barakos, G., & Badcock, K. (2005). *Analysis and Control of Weapon Bay Flows.*, RTO-MP-AVT-123. NATO RTO, Budapest. Retrieved from http://www.cfd4aircraft.com/Papers/conference/AVT_nayyar_24.pdf

[9] Tracy, M., & Plentovich, E. (1993). *Characterization of cavity flow fields using pressure data obtained in the Langley 0.3-meter transonic cryogenic tunnel.* NASA TM 4436.

[10] Stallings, R., & Wilcox, F. (1987). *Experimental cavity pressure distributions at supersonic speeds.* NASA TP-2683.

[11] Plentovic, E. B., Stallings, R. L., & Tracey, M. B. (1993). Experiemental Cavity Pressure Measurements at Subsonic and Transoinc Speeds. *NASA Technical Paper 3358* .

[12] Taborda, N., Bray, D., & Knowles, K. (2001). Passive control of cavity resonance in tandem configurations. *31st AIAA Fluid Dynamics Conference & Exhibit.* Anaheim, California: AIAA 2001-2770.

[13] ESDU. (2004). *Aerodynamics and aero-acoustics of rectangular planform cavities Part I: Time-averaged flow.* ESDU 02008.

[14] Tracy, M., & Plentovich, E. (1997). *Cavity unsteady-pressure measurements at subsonic and transonic speeds.* NASA TP-3669.

[15] Delprat, N. (2006). Rossiter's formula: A simple spectral model for a complex amplitude modulation process? *Physics of fluids , vol 18*.

[16] Knowles, K., Khanal, B., Bray, D., & Geraldes, P. (2010). Passive control of cavity instabilities and noise. *27th International congress of the aeronautical sciences.*

[17] Dix, R., & Bauer, R. (2000). *Experimental and theoretical study of cavity acoustics AEDC-TR-99-4.* Arnold Engineering Development Center.

[18] Krishnamurty, K. (1955). *Acoustic radiation from two-dimensional rectangular cutouts in aerodynamic surfaces.* NACA TN-3487.

[19] Gloerfelt, X., Bogey, C., Bailly, C., & Juve, D. (2002). Aerodynamic noise induced by laminar and turbulent boundary layers over rectangular cavities. *8th AIAA/CEAS Aeroacoustics conference & exhibit.* Breckenridge, California: AIAA 2002-2476.

[20] Heller, H., Holmes, D., & Covert, E. (1971). Flow-induced pressure oscilations in shallow cavities. *Journal of Sound and Vibration , vol: 18* (iss: 4).

[21] Ahuja, K., & Mendoza, J. (1995). *Effects of cavity dimensions, boundary layer, and temperature on cavity noise with emphasis on benchmark data to validate aeroacoustic codes.* NASA Contractor report 4653.

[22] Yang, D., Fan, Z., & Luo, X. (2009). Effect of free-stream boundary layer thickness on aeroacoustic characteristics of open cavity flow. *10th International conference on fluid control, measurements, and visualization.* Moscow, Russia: Flucome.

[23] Unalmis, O. (2004). Cavity oscillation mechanisms in high speed flows. *AIAA Journal , vol: 42* (iss: 10), pp: 2035-2041.

[24] Tracey, M., Plentovic, E., & Chu, J. (1992). *Measurements of fluctuating pressure in a rectangular cavity in transonic flow at high reynolds number.* NASA TM-4363.

[25] Hamed, A., Basu, D., & Das, K. (2003). Effect of reynolds number on the unsteady flow and acoustic fields of supersonic cavity. *4th ASME/JSME Joint Fluids Engineering Conference.* Honolulu, Hawaii: FEDSM2003-45473.

[26] Bilanin, A., & Covert, E. (1973). Estimation of possible excitation frequencies for shallow rectangular cavities. *AIAA Journal , vol: 11*, pp: 347-351.

[27] Block, P. (1976). *Noise response of cavities of varying dimensions at subsonic soeeds.* NASA TN D-8351.

[28] Chaplin, R., & Birch, T. (2012). The aero-acoustic environment within the weapons bay of a generic UCAV. *30th AIAA Applied Aerodynamics Conference.* New Orleans, Louisiana: AIAA 2012-3338.

[29] Ukeiley , L., Ponton, M., Seiner, J., & Jansen, B. (2002). Suppression of pressure loads in cavity flows AIAA 2002-0661.

[30] Schmit, R., McGaha, C., Tekell, J., Grove, J., & Stanek, M. (2009). Performance results for the optical turbulence reduction cavity AIAA 2009-702.

[31] Doran, D. (2006). Experimental investigation of transonic cavity flow control. *Cranfield University MSc Thesis* .

[32] Stanek, M., Ross, J., Odedra, J., & Peto, J. (2003). High frequency acoustic suppression - The mystery of the rod in crossflow revealed AIAA 2003-0007.

[33] Agmen, K. (2007). Experimental Investigation of Transonic Cavity Flows. *Cranfield University MSc Thesis* .

[34] Lavoix, P. (2004). *Experimental Survey of Non-Rectangular Cavity Flows.* MSc thesis, Cranfield University.

[35] Usieto, P. V. (2008). Transonic Cavity Aerodynamics. *MSc Thesis, Cranfield University* .

[36] Shaw, L., Clark, R., & Talmadge, D. (1988). F-111 Generic weapons bay acoustic environment. *Journal of Aircraft , vol: 25* (iss: 2).

[37] Lai, H., & Luo, K. (2008). A conceptual study of cavity aeroacoustics control using porous media inserts. *Flow Turbulence Combust , vol: 80*.

[38] Hsu, J., & Ahuja, K. (1996). Cavity Noise Control Using Helmholtz Resonators. *AIAA 96-1675* .

[39] Cattafasta III, L., Williams, D., Rowley, C., & Alvi, F. (2003). Review of active control of flow-induced cavity resonance. *AIAA paper 2003-3567* .

[40] Lawson, S., & Barakos, G. (2011). Review of numerical simulations for high-speed, turbulent cavity flows. *Progress in Aerospace Sciences , vol: 47*, pp: 186-216.

[41] Clark, R. (1979). *Evalutation of F-111 weapon bay aero-acoustic and weapon bay separation improvement techniques.* AFFDL-TR-79-3003.

[42] Barakos, G., Lawson, S., Steijl, R., & Nayyar, P. (2009). Assessment of flow control devices for transonic cavity flows using DES and LES. *IUTAM Symposium on Unsteady Separated Flows.* Springer Science+Business Media B.V.

[43] Kaufman II, L., Maciulaitis, A., & Clark, R. (1983). *Mach 0.6 to 3.0 flows over rectangualr cavities.* AFWAL-TR-82-3112.

[44] Szepessy, S., & Bearman, P. (1992). Aspect ratio and end plate effects on vortex shedding from a circular cylinder. *Journal of Fluid Mechanics , vol: 234*, pp: 191-217.

[45] Stanek, M., Raman, G., Ross, J., Odedra, J., Peto, J., Alvi, F., et al. (2002). High frequency acoustic suppression - The role of mass flow, the notion of superposition and the role of inviscid instability -- A new model (Part II). AIAA 2002-2404.

[46] Smith, B., Welterlen, T., Maines, B., Shaw, L., Stanek, M., & Grove, J. (2002). Weapons bay acoustic suppression from rod spoilers. *40th AIAA Aerospace sciences meeting and Exhibit.* Reno, Nevada: AIAA 2002-0662.

[47] Shaw, L. (1982). Full scale flight evaluation of suppression concepts for flow-induced fluctauating pressures in cavities. *AIAA 20th Aerospace Sciences Meeting.* Orlando, Florida: AIAA 82-0329.

[48] Ukeiley, L., Ponton, M., Seiner, J., & Jansen, B. (2003). Suppression of pressure loads in resonating cavities through blowing (AIAA 2003-181). *41st Aerospace Sciences Meeting and Exhibit.* Reno, Nevada: AIAA.

[49] MacManus, D. G., & Doran, D. S. (2008). Passive control of transonic cavity flow. *Journal of Fluids Engineering , vol: 130.*

[50] Cox, T. J., & D'Antonio, P. (2004). *Acoustic Absorbers and Diffusers.* Spon Press.

[51] Shaw, L. (1985). Suppression of the flow induced acoustic environment in an irregularly shaped cavity with an opening exposed to subsonic flow. *Journal of the Acoustical Society of America , vol: 77* (iss: S1).

[52] Cattafesta III, L., Song, Q., Williams, D., Rowley, C., & Farrukh, A. (2008). Active control of flow-induced cavity oscilations. *Progress in Aerospace Sciences* (iss: 44), pp 479-509.

[53] Rowley, C., Juttijudata, V., & Williams, D. (2005). Cavity flow control simulations and experiments (AIAA 2005-292). *43rd AIAA Aerospace sciences meeting and exhibit.* Reno, Nevada: AIAA.

[54] Kergerise, M., Cattafesta III, L., & Ha, C. (2002). Adaptive indentification and control of flow induced cavity oscilations (AIAA 2002-3158). *1st Flow control conference.* St Louis, Missouri: AIAA.

[55] Kook, H., Mongeau, L., & Franchek, M. A. (2002). Active Control of Pressure Fluctuations Due To Flow Over Helmholtz Resonators. *Journal of Sound and Vibration , vol: 255* (iss: 1), pp: 61-76.

[56] Sarohia, V., & Massier, P. (1977). Control of cavity noise. *Journal of Aircraft , vol: 14* (iss: 9), pp: 833-7.

[57] Heller, H., & Bliss, D. (1975). The physical mechanism of flow-induced pressure fluctuations in cavities and concepts for their suppression. *AIAA 75-491* .

[58] Sarno, R., & Franke, M. (1994). Suppression of flow induced pressure oscilations in cavities. *Journal of Aircraft , vol: 31* (iss: 1), pp: 90-96.

[59] Lamp, A., & Chokani, N. (1999). *Control of cavity resonance using steady and oscillatory blowing.* Raleigh, North Carolina: North Carolina State University.

[60] Zhuang, N., Alvi, F., & Shih, C. (2005). Another look at supersonic cavity flows and their control. *11th AIAA/CEAS Aeroacoustics conference.* Monterey, California: AIAA 2005-2803.

[61] Cabell, R., Kergerise, M., Cox, D., & Gibbs, G. (2002). Experimental feddback control of flow induced cavity tones. *8th AIAA/CEAS Aeroacoustics conference and exhibit.* Breckenridge, Colorado: AIAA 2002-2497.

[62] Debiasi, M., & Samimy, M. (2003). An experimental study of the cavity flow for closed-loop flow control. *33rd AIAA Fluid dynamics conference and exhibit.* Orlando, Florida: AIAA 2003-4003.

[63] Cattafesta III, L., Garg, S., Choudhari, M., & Li, F. (1997). Active control of flow-induced cavity resonance. *28th AIAA fluid dynamics conference/4th AIAA shear flow control conference.* Snowmass Village, Collorado: AIAA 97-1804.

[64] Kergerise, M., Cabell, R., & Cattafesta III, L. (2007). Real-time feedback control of flow-induced cavity tones --- Part 2: Adaptive control. *Journal of Sound and Vibration , vol: 307*, pp: 924-940.

[65] Helmholtz, H. (1895). *On the sensations of tone as a physiological basis for the theory of music (Third edition).* London: Green and Co.

[66] Landels, J. (1967). Assisted resonance in ancient theatres. *Greece and Rome , vol: 14* (iss: 1), pp: 80-94.

[67] Rindel, J. (2011). Echo problems in ancient theatres and a comment to the "sounding vessels" described by Vitruvius. *The acoustics of ancient theatres conference.* Patras.

[68] Brüel, P. (2005). *Episodes and Achievements within Acoustics before 1954.* Danish Acoustical Society.

[69] Godman, R. (2008). *The Enigma of Vitruvian Resonating Vases and the Relevance of the Concept for Today.* Faculty for the Creative and Cultural Industries. University of Hertfordshire.

[70] D'Antonio, P., & Cox, T. J. (2005). *Technical bulletin on the design of microperforated transparent absorbers.* Upper Markboro, MD: RPG Diffuser Systems Inc.

[71] RPG Diffusor Systems. (2012, 10 16). *Diffusorblox - acoustic products*. Retrieved from http://www.rpgeurope.com/products/product/diffusorblox.html

[72] Gilford, C. (1951). Helmholtz resonators in the acoustic treatment of broadcasting studios. *British Journal of Applied Physics , vol :3*.

[73] Bellucci, V., Flohr, P., Pascherit, C., & Magni, F. (2004). On the use of helmholtz resonators for damping acoustic pulsations in industrial gas turbines. *Journal of Engineering for Gas Turbines and Power , vol: 126*, pp: 271-275.

[74] Zhao, D., & Morgans, A. (2009). Tuned passive control of combustion instabilities using multiple Helmholtz resonators. *Journal of sound and vibration , vol 320*, pp 744-757.

[75] Kempton, A. (n.d.). *Acoustic liners for modern aero-engines.* Retrieved January 2nd, 2013, from http://www.win.tue.nl/ceas-asc/Workshop15/CEAS-ASC_XNoise-EV_K1_Kempton.pdf

[76] Mangiarotty, R. (1971). The Reduction of Aircraft Engine Fan-Compressor Noise Using Acoustic Linings. *Journal of Sound and Vibration , vol: 18* (iss: 4), pp: 565-576.

[77] Reed, T. (2002). Assesment and treatment of wall boundary layers in the cranfield college of Aeronautics 2.5" transonic wind tunnel . *Cranfield University MSc Thesis* .

[78] Tracy, M. B., & Plentovich, E. B. (1992). Measurements of Fluctuating Pressure in a Rectangular Cavity in Transonic Flow at High Reynolds Numbers. *NASA TM 4363* .

[79] Hankey, W., & Shang, J. (1979). The numerical solution to pressure oscillations in an open cavity. *AIAA 79-0136* .

[80] Schlichting, H. (1955). *Boundary layer theoery.* Permagon Press Ltd.

[81] Taylor, J. R. (1997). An Introduction To Error Analysis (2nd Edition). *Sausalito (CA USA): University Science Books* .

[82] Schmit, R., Semmelmayer, F., Haverkamp, M., & Grove, J. (2001). Fourier analysis of high speed shadowgraph images around a Mach 1.5 cavity flow field, AIAA 2011-3961.

[83] Saladin, J. (2006). *Shakedown & determination of tunnel control setting for refurbished trisonic gasdynamic facility (TGF).* AFRL-VA-WP-TR-2007-3015.

[84] (2001). *BS EN ISO 10534-2 Acoustocs - Determination of sound absorption coefficient and impedance in impedance tube. Part 2: Transfer-function method.* British Standard Institute.

[85] (2001). *BS EN ISO 10534-2 Acoustics - Determination of sound absorption coefficient and impedance in impedance tube. Part 2: Transfer-function method.* British Standard Institute.

[86] (ASTM), A. S. *ASTM E1050 - 10 Standard Test Method for Impedance and Absorption of Acoustical Materials Using A Tube, Two Microphones and A Digital Frequency Analysis System.*

[87] Brüel & Kjær. (n.d.). *Portable Impedance Meter System - Type 9737 - Brüel & Kjær*. Retrieved June 7th, 2012, from www.bksv.com/doc/bn0293.pdf

[88] Shaw, L., & Shimovetz, R. (1994). Weapons bay acoustic environment. *AGARD-CP-549* .

[89] Delprat, N. (2006). Rossiter's formula: A simple spectral model for a complex amplitude modulation process. *Physics of Fluids 071703-2 , 18*.

[90] Delprat, N. (2010). Low-frequency components and modulation processess in compressible cavity flows. *Journal of sound and vibration , vol 329*.

[91] Malone, J., Debiasi, M., Little, J., & Samimy, M. (2009). Analysis of the spectral relationships of cavity tones in subsonic resonant cavity flows. *Physics of Fluids 055103 , 21*.

[92] Ukeiley, L., Ponton, M., Seiner, J., & Jansen, B. (2004). Suppression of pressure loads in cavity flows. *AIAA journal , vol: 44* (iss: 1).

[93] Murray, N., Sällström, E., & Ukeiley, L. (2009). Properties of subsonic open cavity flow fields. *Physics of Fluids , vol: 21*.

[94] Henderson, J. (2001). *Investigation of cavity flow aerodynamics using computational fluid dynamics.* University of Glasgow, PhD Thesis.

[95] Dupère, I., & Dowling, A. (2005). The use of helmholtz resonators in a practical combustor. *Journal of Engineering for Gas Turbines and Power , vol: 127*.

[96] Rossiter, J. (1966). Wind-tunnel experiments on the flow over rectangular cavities at subsonic and transonic speeds. *ARC-R&M-3438* .

[97] Cox, T., & D'Antonio, P. (2004). Acoustic Absorbers and Diffusers. *London: Spon Press* .

[98] de Bedout, J. (1996). *Adaptive passive noise control with self tuning helmholtz resonators.* Purdue University Masters Thesis.

[99] Tayong, R., & Leclaire, P. (2010). Hole interaction effects under high and medium sound intensities for micro perforated panels design. *10eme Congres Francais d'Acoustique.* Lyon.

[100] Knowles, K., Ritchie, S., & Lawson, N. (June 2007). An experimental and compuational investigation of a 3D, l/h=5 transoninc cavity flow. *3rd International Symposium on Integrating CFD and Experiments in Aerodynamics.* U.S. Air Force Academy, CO, USA.

[101] Sun, X., Jing, X., Zhang, H., & Shi, Y. (2002). Effect if grazing-bias flow interaction on acoustic impedance of perforated plates. (557-573, Ed.) *Journal of Sound and Vibration , vol: 254* (issue: 3), pp.

[102] Pratt & Whitney Aircraft. (1967). *A study of the suppression on combustion osicllations with mechanical damping devices (NASA contract# NA$8-11038).*

[103] Guo, Y., & Åbom, M. (2006). *Acoustic properties of new design elements for cooling systems -- micro-perforated panels.* European Commission DG Research.

[104] Dickey, N., Selamet, A., & Novak, J. (2000). The effect of high-amplitude sound on the attenuation of perforated tube silencers. *Journal of the Acoutic Society of America , Vol: 108* (Iss: 3).

[105] Schook, R. (2000). *Bypass transition experiments in subsonic boundary layers.* Technishe Universiteit Eindhoven.

[106] Guess, A. (1975). Calculation of perforated plate liner parameters from specified acoustic resistance and reactance. *Journal of Sound and Vibration , vol: 40* (iss: 1).

[107] Maa, D. (1994). Microperforated panel at high sound intensity. *Proceeding of internoise.* Yokohama.

[108] Tayong, R., & Leclaire, P. (2010). Hole interaction effects under high medium sound intensities for micro-perforated panels design. *10ème Congrès Français d'Acoustique.* Lyon.

[109] Roberts, D., & MacManus, D. (2012). Passive attenuation of transonic cavity aero-acoustics. *Journal of Fluids Engineering , (In Press).*

[110] Rice, E. (1973). *A model for the pressure excitation spectrum and acoustic impedance of sound absorbers in the presence of grazing flow.* NASA TM-X-71418.

[111] Rao, N., & Munjal, M. (1986). Experimental evalutation of impedance of perforates with grazing flow. *Journal of Sound and Vibration , vol: 108* (iss: 2).

[112] Ahuja, K., Cataldi, P., & Gaeta Jr, R. (2001). *Sound Absorption of a 2DOF Resonant Liner with Negative Bias Flow.* NASA CR-2000-210637.

[113] Williams, D., Rowley, C., Colonius, T., Murray, R., MacMartin, D., Fabris, D., et al. (2002). Model-based control of cavity oscillations -- Part 1: Experiments AIAA 2002-0971.

[114] Lusseyran, F., Pastur, L., & Letellier, C. (2008). Dynamical analysis of an intermittency in an open cavity flow. *Physics of Fluids , vol: 20*.

[115] Kergerise, M., Spina, E., Garg, S., & Cattafesta III, L. (2004). Mode-switching and nonlinear effects in compressible flow over a cavity. *Physics of Fluids , vol: 16* (iss: 3).

[116] Barakos, G., Lawson, S., Steijl, R., & Nayyar, P. (2009). Numerical simulations of high speed turbulent cavity flows. *Flow Turbulence Combust , vol: 89*.

[117] Smith, D., Shaw, L., Talmadge, R., & Seely, D. (1974). *Aero-acoustic environment of rectangular cavities with length to depth ratios of five and seven.* AFFDL-TM-74-79-FYA.

[118] Kinsler, L., Frey, A., Coppens, A., & Sanders, J. (2000). *Fundamentals of Acoustics (4th edition).* John Wiley & Sons, Inc.

[119] Bartel, H., & McAvoy, J. (1981). *Cavity oscillation in cruise missile carrier aircraft.* AFWAL-TR-81-3036.

[120] Raytheon Missile Systems. (n.d.). *AMRAAM Advanced medium-range air-to-air missile.* Retrieved June 20th, 2011, from http://www.raytheon.com/capabilities/products/stellent/groups/rms/documents/content/cms01_054563.pdf

Appendices

A Design spaces for all apparatus

This appendix will describe the design space available for each of the experimental facilities used within this study. The design space is defined as the volume available for palliative installation in the case of wind tunnel investigations or the test samples for the impedance tube tests. The description is limited to the external dimensions and will not provide detailed information about the design of the palliatives. *Figure A 1* shows the external dimension limits for a resonant array to be installed into a cavity. In *Figure A 1* and *Figure A 2* h is the cavity height, w is the cavity with and t+L relate the maximum sum of the faceplate thickness and backing length for an array. The sketches in *Figure A 1* represent the format in which the design spaces for the various experimental facilities are represented in the following sections.

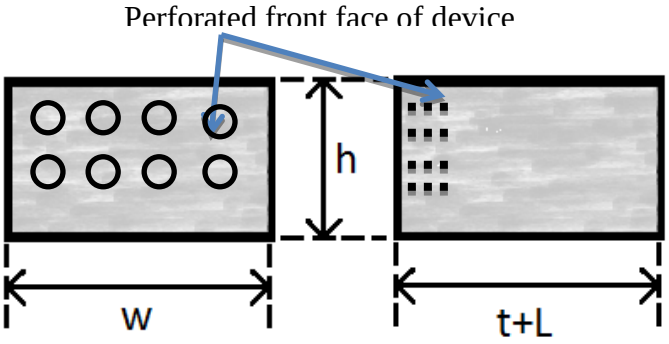

Figure A 1 – Sketch of resonant array palliative external dimensions to demonstrate layout for following sections

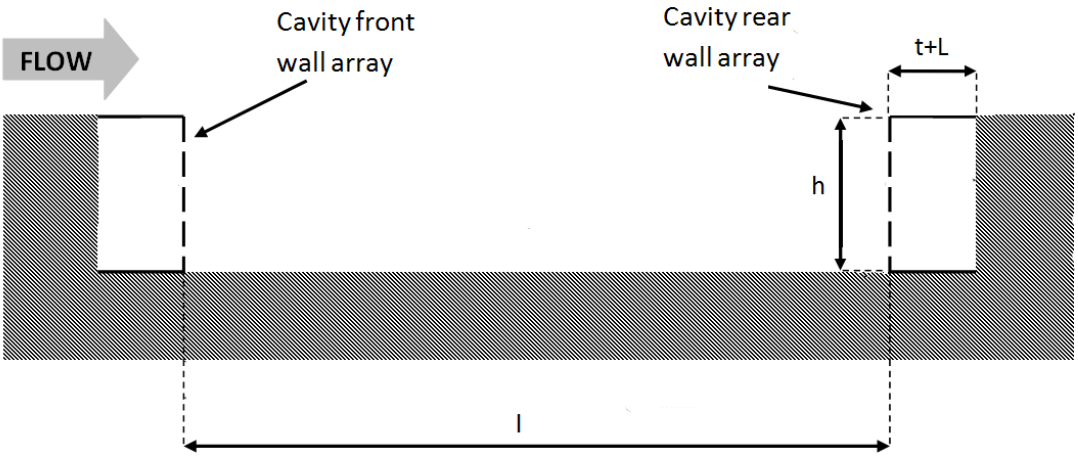

Figure A 2 – Side view of model cavity with resonant arrays installed within the end walls. External limits to design space shown.

A.1 Cranfield University 2.5" wind tunnel

Two builds were used for the small scale wind tunnel testing conducted at Cranfield and each build has different design constraints for the palliatives. The following sections discuss the design constraints placed on the array designs for both small scale cavity builds. Build 1 only allowed for arrays to be installed at the front and rear wall, whereas Build 2 allowed arrays to be installed into the front, rear, side and ceiling walls of the cavity (*Figure A 5*).

A.1.1 Build 1

Within Build 1 palliatives can only be installed in either the front or rear wall of the cavity (*Figure A 2*) and the maximum external dimensions for the arrays are shown in *Figure A 3*.

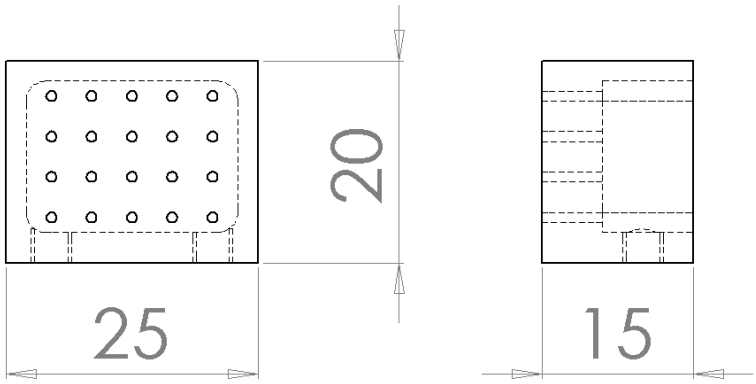

Figure A 3 – Design space for end wall arrays to be installed into Build 1 cavity. (Dimensions in millimetres)

A.1.2 Build 2

Within Build 2 palliatives can be installed into the front, rear, side or ceiling of the cavity (*Figure A 5*). This required to the cavity to be moved to the side wall of the wind tunnel test section (*Figure A 4*). The cavity is located at the same streamwise position within the working section and the dimensions are the same as Build 1. The external dimensions within which an array can be installed are defined in *Figure A 6* to *Figure A 8*.

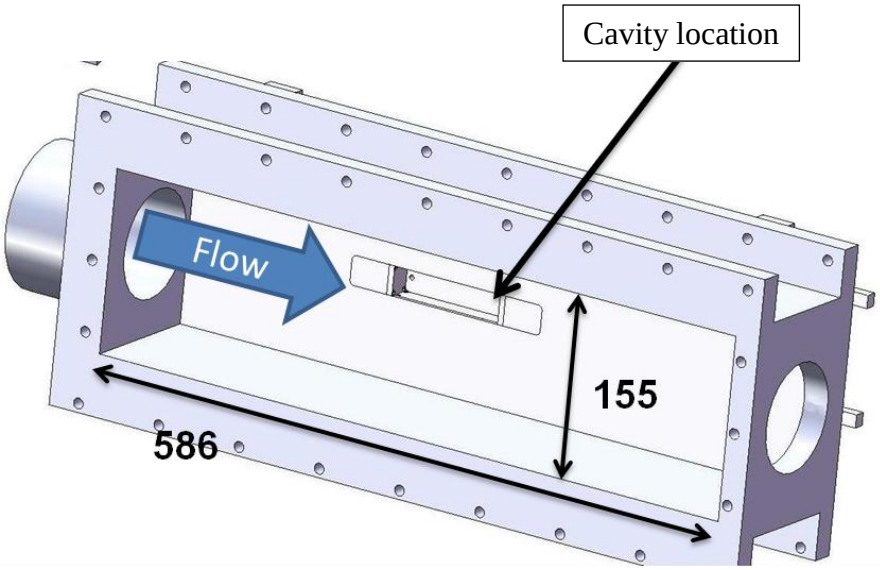

Figure A 4 – Sketch of the build 2 cavity installed into the side wall of the Cranfield 2.5" tunnel working section

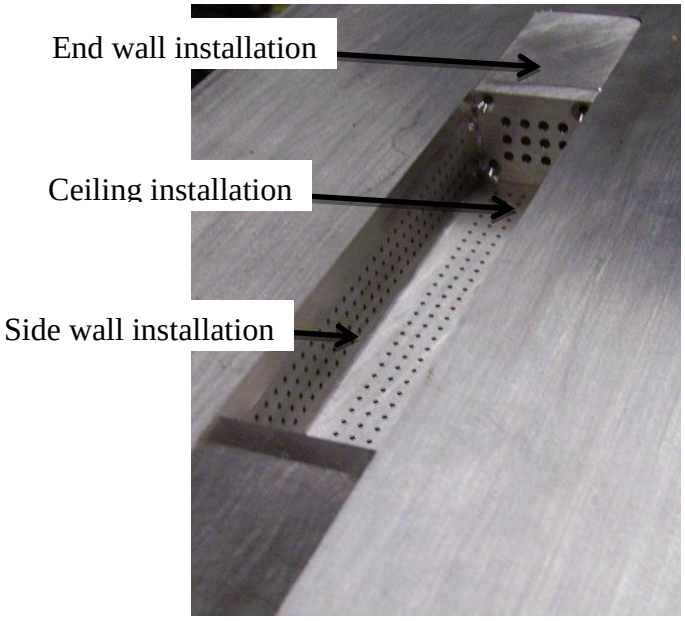

Figure A 5 – Various arrays installed into Build 2 cavity model.

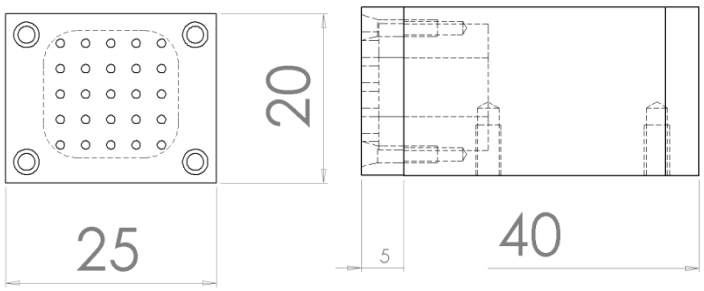

Figure A 6 – Design space for end wall arrays to be installed into Build 2 cavity. (Dimensions in millimetres)

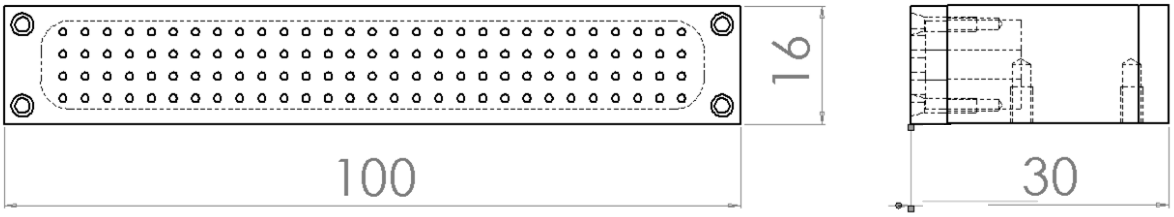

Figure A 7 – Design space for side wall arrays to be installed into Build 2 cavity. (Dimensions in millimetres)

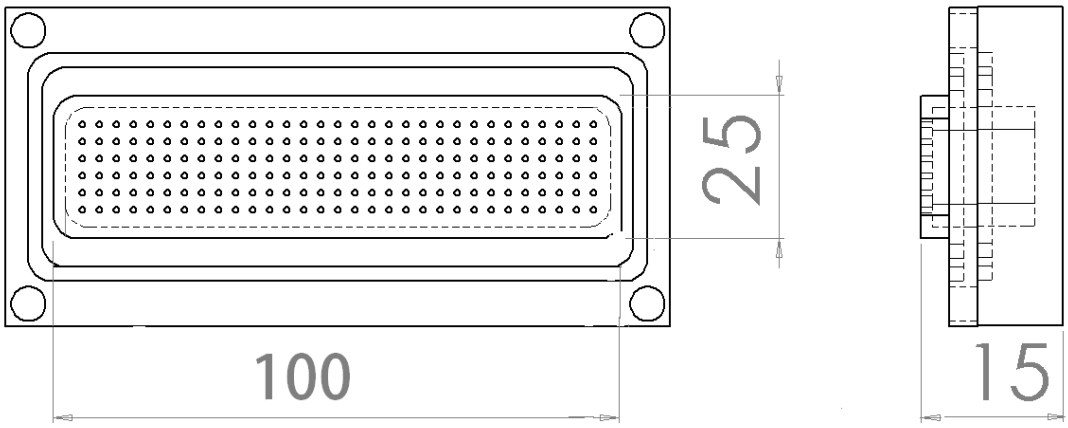

Figure A 8 – Design space for ceiling arrays to be installed into Build 2 cavity. (Dimensions in millimetres)

A.2 AFRL Tri-sonic gasdynamics facility

The Tri-sonic gasdynamics facility (TGF) ADDICT model provided to opportunity to investigate the performance of resonant arrays within a 1/20th scale cavity. The cavity model had space at both the front and rear wall to install resonant arrays (*Figure A 9*). The maximum space available to install the devices into the ADDICT cavity model is shown in *Figure A 10*. The build was constructed in such a way so that the front and rear wall arrays were identical and the maximum design space available at the end walls is shown in *Figure A 10*.

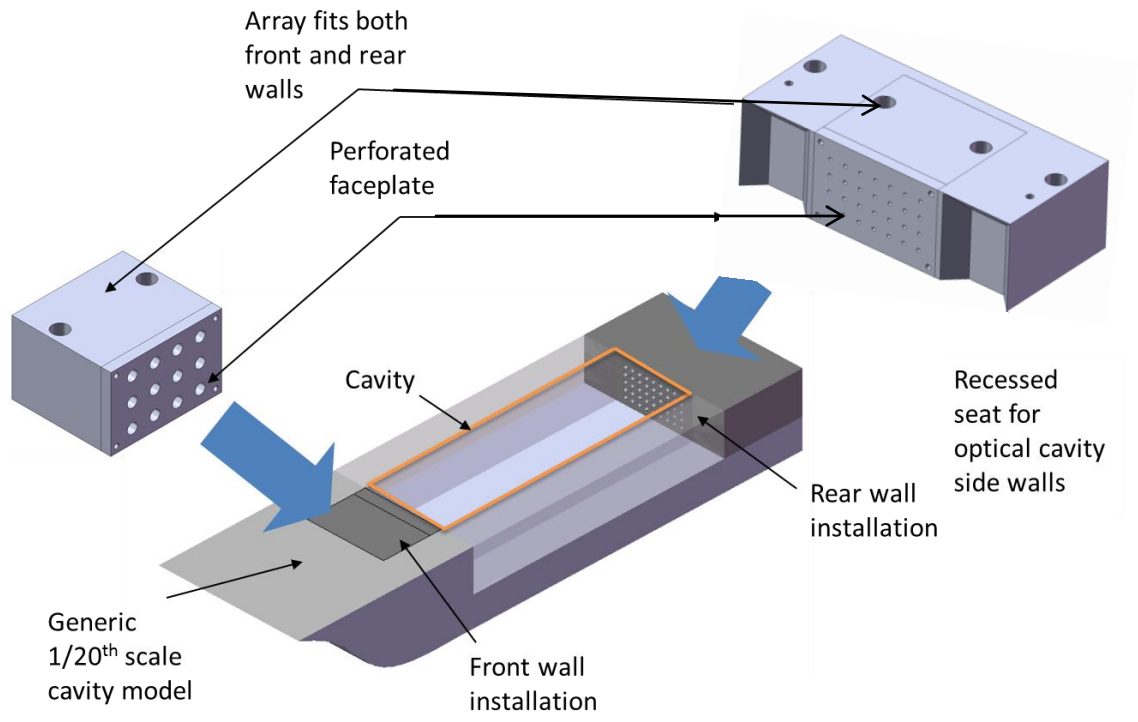

Figure A 9 – Resonant array installation into the ADDICT cavity model used within the TGF tunnel

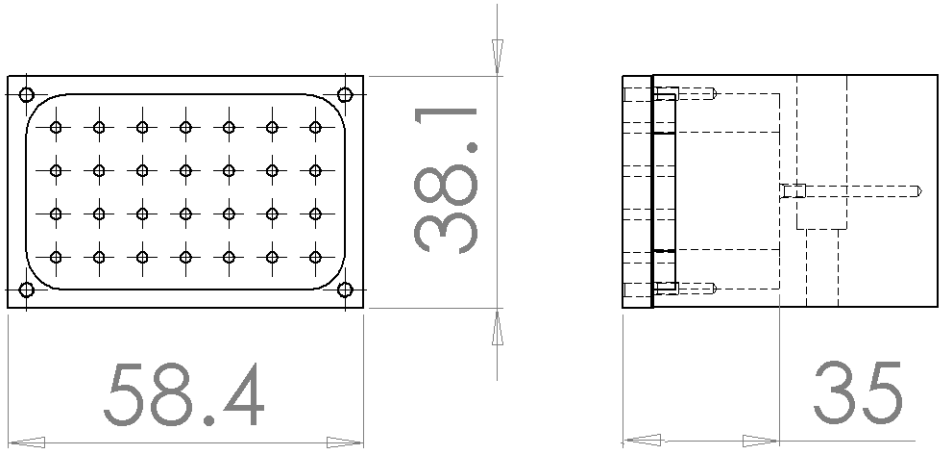

Figure A 10 – Design space for end wall arrays to be installed into the TGF ADDICT cavity model. (Dimensions in millimetres)

A.3 Large scale impedance tube

To investigate the acoustic properties of a series of resonant arrays designed for the low frequencies expected within a full scale weapon bay cavity a large scale impedance tube was used. The arrays were designed to be compatible with the current set up of this device which allowed for a 2mm thick faceplate with a maximum height and width of 500mm (*Figure A 11*). The backing volume provided by the current set up of this device provided a length of L=68mm.

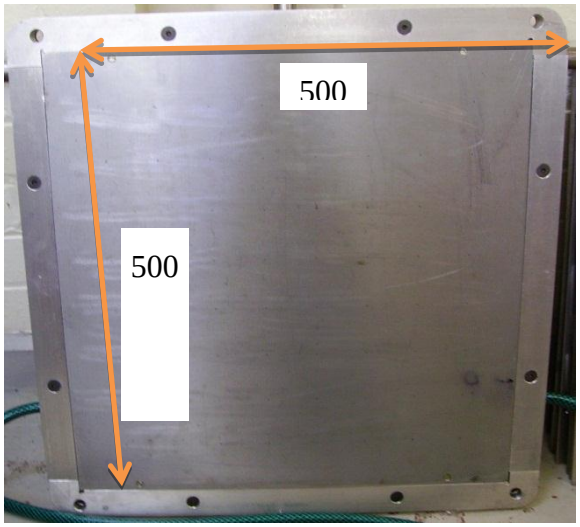

Figure A 11 – Faceplate for large scale impedance tube tests. (Dimensions in millimetres)

A.4 Medium scale impedance tube

To investigate the acoustic properties of a series of arrays a medium scale impedance was used (*Figure A 12*). The resonant arrays were formed from a separate faceplate and backing volume component which were secured to the end of the impedance tube (*Figure A 12* and *Figure A 13*). The overall dimensions of the resonant array component are shown in *Figure A 13*.

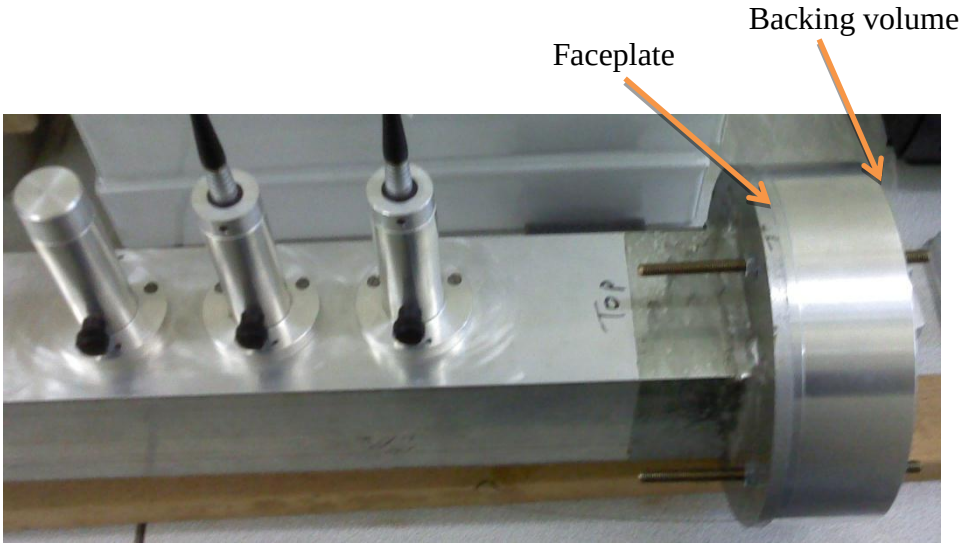

Figure A 12 – Components for medium scale impedance tube testing

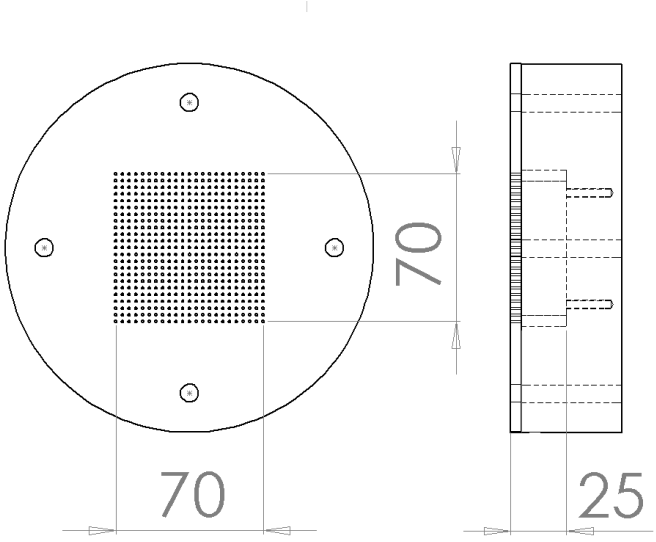

Figure A 13 – Design space for resonant array sample to be used with the medium scale impedance tube. (Dimensions in millimetres)

A.5 Small scale, high SPL impedance tube

To investigate how the high SPL environment within a cavity affects the fundamental acoustic properties of a resonant array a series of tests were carried out with small scale arrays and a high SPL impedance meter. The small scale arrays were formed from a separate faceplate and backing volume (*Figure A 14*). The frequency of the device could be varied through the insertion of a tuning insert into the device's backing volume (*Figure A 14*). This enabled the effect of frequency on the fundamental properties to be investigated, which has not previously been assessed in the literature. The overall dimensions of the resonant array used for these high SPL tests are given in *Figure A 15*.

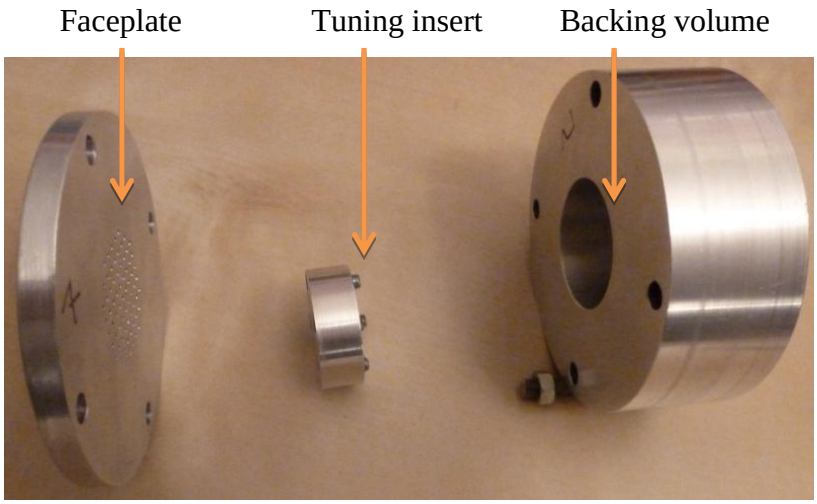

Figure A 14 – Components for small scale impedance tube testing

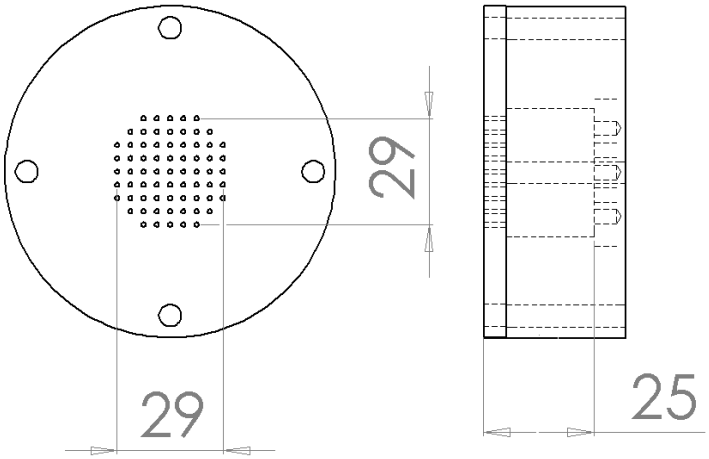

Figure A 15 – Design space for resonant array sample to be used with the small scale impedance meter. (Dimensions in millimetres)

B Build 2 validation

To facilitate the installation of resonant arrays into the sidewalls and ceiling of a model cavity a new cavity build was designed and commissioned. This new cavity is referred to as Build 2 (see *Appendix A.1.2*) and was installed into the sidewall of the Cranfield 2.5" wind tunnel working section. The cavity has the same dimensions as the previous test cavity (Build 1), but the modal characteristics were expected to differ slightly due to the changes in approaching flow conditions between the working section ceiling and side wall. Therefore, the characteristics of the Build 2 cavity need to be assessed and validated to ensure that they are appropriate for the cavity palliative tests. The following sections discuss the approaches used for the validation process.

B.6 Spectral comparisons between Build 1 and Build 2

The most important characteristic required by the Build 2 cavity was that it exhibited the large amplitude modal peaks which are typical of open flow type cavities and *Figure B 1* shows that this is indeed the case. As with the Build 1 cavity, the Build 2 cavity spectrum exhibits three discrete modal peaks at around 800Hz, 1900Hz, and 3200Hz for Mach 0.90 freestream flow. The frequencies of the first and third Rossiter modes for the Build 2 cavity are within 1% of those exhibited by the Build 1 cavity and remain within 5% of those calculated by the Rossiter equation (*Equation 1*) (*Figure B 1*). The frequency of the second mode within the Build 2 spectrum is within 5% of the Build 1 case. For all the modes within the Build 2 spectrum the amplitudes are within 4% of the Build 1 case. The difference in modal frequencies and amplitudes are caused by the different properties of the approaching boundary layers over the cavity ceiling and side wall (see *section 3.1.3*) and are not thought to be sufficient to affect the performance of the resonant arrays. Therefore the modal characteristics of Build 2 are acceptable for the investigation of palliative performance within the sidewalls and ceiling of the model cavity.

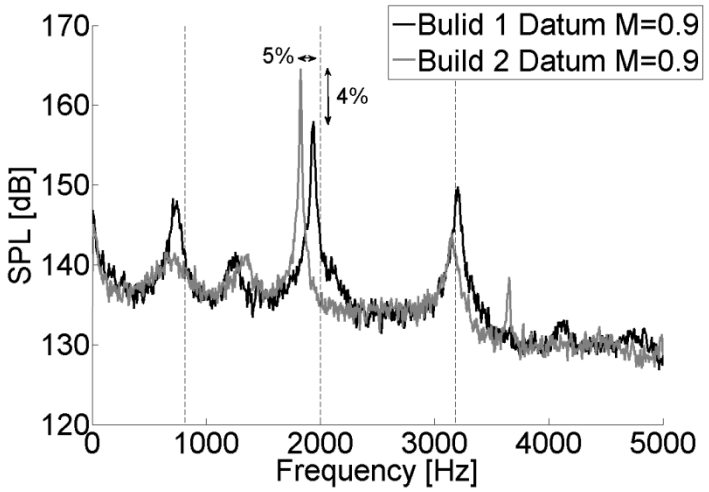

Figure B 1 – Comparison between the datum spectra from the Build 1 and Build 2 cavities installed into the Cranfield 2.5" wind tunnel at Mach 0.9.

B.7 Flow visualisation over the Build 2 cavity location

A further analysis of the Build 2 configuration was conducted using flow visualisation over the location of the cavity. The flow visualisation was conducted in the absence of the cavity and was intended to investigate the flow directionality over the cavity location. As the Build 2 cavity is located on the side wall it was not known if the flow would travel in a parallel direction to the cavity length. Any non-parallel flow would create a cavity under yaw conditions which may affect the modal generation process. The results of the flow visualisation are shown in *Figure B 2* where the flow can be seen to travel in a direction parallel to the cavity length over the cavity location. Therefore, the location of the Build 2 cavity on the side wall of the wind tunnel working section is acceptable for the investigation of the palliative performance.

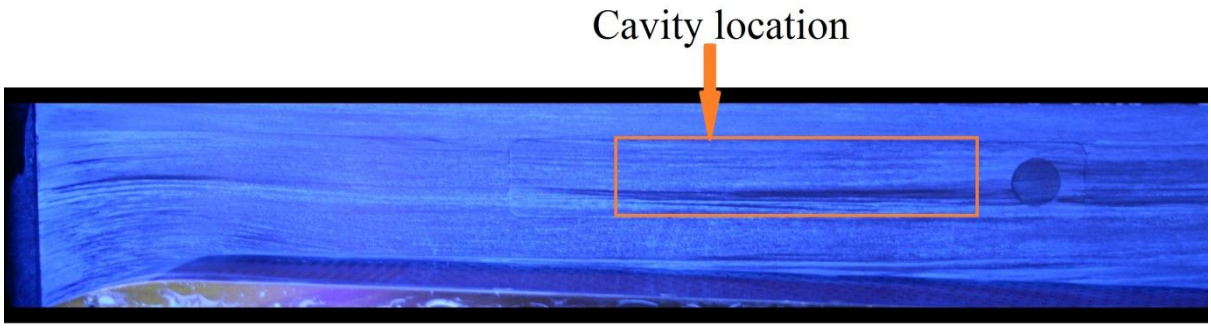

Figure B 2 – Oil flow visualisation of flow over Build 2 liner in the absence of the cavity.

C Uncertainty analysis

This appendix sets out the methods used for the calculation of uncertainties within the experimental wind tunnel facilities used within this study.

3

C.1 Cranfield University 2.5" transonic wind tunnel

C.1.1 Boundary layer

The boundary layer within the tunnel working section was measured using a Pitot tube connected to a Moore and Wright micrometer. This device has a quoted measurement resolution of 0.01 mm. The initial probe position was zeroed using a sheet of paper which was placed between the probe tip and the wind tunnel liner. The thickness of the sheet of paper was estimated at 0.1 mm from an average of a sample of 100 sheets with an uncertainty of ± 0.005mm. Inaccuracy due to the shape of the probe head was assumed to be a maximum of ±0.05mm. Therefore the combined uncertainty of this process yields a total uncertainty of the boundary layer measurements of 0.065mm.

C.1.2 Pressure measurements

The uncertainties of the pressure measurements from the various transducers as given by the manufacturers are presented in *Table C 1*. All of the transducers were statically calibrated using linear regression with a zero constant. The standard uncertainty for all of the points was then calculated and given as a percentage of the calibration constant (linear regression gradient) and shown in *Table C 2*. The data acquisition card used for this study had a 16-bit resolution. Therefore over the voltage range of each of the transducers the pressure resolution varied as shown in *Table C 3*.

Measurement	Manufacturer uncertainty
Setra (Total)	± 0.14 %
Druck (Static)	± 0.1 %
Kulite (Unsteady)	± 0.1 %
Atmospheric	± 0.01 %
Temperature	± 0.05 °C

Table C 1 – Measurement manufacturer uncertainty (combined linearity and hysteresis)

Transducer	Linear regression uncertainty as % of calibration constant
Setra (Total)	± 0.1
Druck (Static)	± 0.02
Kulite 1	± 0.09
Kulite 2	± 0.07
Kulite 3	± 0.08
Kulite 4	± 0.08

Table C 2 – Linear regression uncertainty for pressure transducers as % of their calibration constant

Transducer	Voltage range (V)	Resolution (mV)
Setra	0 – 24	0.37
Druck	0 -- 12	0.18
Kulite	0 – 10	0.15

Table C 3 – Voltage resolution due to DAQ card for pressure transducers by type.

C.1.3 Uncertainty of pressure measurements

Pressure measurements from all of the transducers are found by multiplying the voltage output (*v*) by the linear regression calibration coefficient (*c*) and atmospheric pressure is then added to give an absolute pressure value (*Equation C 1*). This process introduces uncertainty from the manufacturers uncertainty (*m*), linear regression uncertainty (*l*) and instrumentation resolution uncertainty (*i*). These values must be taken into account and are summed in quadrature as per *Equation C 2* to give the total uncertainty as a fraction of the measured value. *Equation C 2* only takes into account the systematic uncertainty for the measurement process of a single value. In reality the recorded value is taken from an average of a large sample. For the case of the total and static pressure 2000 samples are taken at a rate of 20 kHz. The uncertainty of this process can then be found from the standard deviation of the sample as given by *Equation C 3* where N is the number of samples. The numerical calculations using typical values for each of the measurements now follow. In each case it is noted that the resultant uncertainty will be the greatest possible scenario.

$$p = vc + p_{atm} \qquad \textbf{Equation C 1}$$

$$\frac{\Delta p}{p} = \sqrt{m^2 + i^2 + l^2} + p_{atm} \qquad \textbf{Equation C 2}$$

$$\sigma_{\bar{p}} = \frac{2\sigma_p}{\sqrt{N}} \qquad \textbf{Equation C 3}$$

C.1.4 Total pressure systematic uncertainty

The uncertainty caused by the voltage resolution of the 16-bit DAQ system (i) is found by dividing the voltage resolution of the transducer over its operational range by a typical voltage value as shown below:

$i = 0.37 \times 10^{-3} / 0.57098 = 0.006\%$

The linear regression uncertainty from the calibration process (l) and the manufactures quoted uncertainty (m) are shown below:

$l = 0.1\%$

$m = 0.14\%$

These uncertainties are then combined in quadrature as per *Equation C 2* to yield the uncertainty of the measurements as a fraction of a typical measurement value as shown below:

$$\Delta p_0/p_0 = (0.14^2 + 0.006^2 + 0.1^2)^{0.5} + 0.01 = 0.17\% + 0.01\%$$

A typical value for the total pressure (P_0) can then be calculated from a recorded voltage value using *Equation C 1*. This can then be multiplied by $\Delta p_0/p_0$ to provide an absolute estimate of the total pressure uncertainty:

$$P_0 = 0.0017 \times 0.57 \times 1367 = 1.32 \text{ Pa}$$

The absolute uncertainty of the atmospheric pressure measurement can be estimated from the manufactures quoted uncertainty for the barometer:

$$p_{atm} = 0.0001 \times 101083 = 10.1 \text{ Pa}$$

The uncertainty for both the total pressure (P_0) and the atmospheric pressure (Patm) are then combined in quadrature to provide the absolute uncertainty for the absolute total pressure (P_0):

$$\Delta p_0 = (10.1^2 + 1.32^2)^{0.5} = 10.2 \text{ Pa}$$

This value can then be expressed as a percentage of a typical total pressure value and this then yields a representative value for the uncertainty of the total pressure measurements:

$$\Delta p_0/p_0 = 10.2/99189 = \underline{0.01\ \%}$$

C.1.5 Total pressure averaging uncertainty

The uncertainty associated with the averaging process was found from the standard deviation over all of the values taken within a data set. The uncertainty was multiplied by 2 to give a 95% confidence interval. This resulted in an uncertainty of 0.09 Pa which is 9.6×10^{-5} % of a typical value. Therefore it is assumed that the uncertainty of the total pressure measurements is solely due to the systematic uncertainty. This yields a final value for the uncertainty of ± 0.01 %.

C.1.6 Static pressure systematic uncertainty

A similar process was conducted for the static pressure measurement system and this is set out below. This process results in a systematic uncertainty for the static pressure measurements of 0.8%.

$v = 0.18 \times 10^{-3} / 0.326 = 0.006\ \%$

$c = 0.02\ \%$

$m = 0.1\%$

$\Delta p/p = (0.1^2 + 0.006^2 + 0.02^2)^{0.5} + 0.01\% = 0.1 + 0.01$

$p = 0.01 \times 0.316 \times 146450 = 462\ Pa$

$p_{atm} = 10.1\ Pa$

$\Delta p = (462^2 + 10.1^2)^{0.5} = 462$

$\Delta p/p = 462/58053 = 0.8\ \%$

C.1.7 Uncertainty due to static pressure averaging process

The uncertainty over an entire data sample with a 95% confidence interval is found to be ± 0.0005%. It was therefore assumed that the total uncertainty of the measurements for the static pressure were solely due to the systematic uncertainties introduced into the measurement system.

C.1.8 Uncertainty of Mach number measurement

Mach number within the tunnel is calculated using the ratio of the total (P_0) to static (p) pressure using the isentropic relationship shown in *Equation C 4.* Therefore to calculate the upper and lower bounds the extreme values based on the uncertainties of the static and total pressure are found. Using the uncertainties for the total and static pressure measurement systems of $\Delta p_0 = \pm 0.01\%$ and $\Delta p = \pm 0.8\%$ upper and lower estimates of the Mach number could be found. From these a Mach number range could then be found and this meant the Mach number could be quoted to ±0.01.

$$M = \sqrt{\frac{2}{\gamma - 1}\left[\left(\frac{\overline{p}_0}{\overline{p}}\right)^{\frac{\gamma-1}{\gamma}} - 1\right]} \qquad \textbf{Equation C 4}$$

3.1.9 OASPL uncertainty

OASPL is calculated in the time domain using *Equation C 5* which allows for the uncertainty to be found analytically. The uncertainty for the OASPL value depends on the uncertainty for the fluctuating pressure returned from the unsteady pressure transducers. Again the pressure value returned from the transducer is the product of the

voltage output and the calibration coefficient plus the atmospheric pressure *Equation C 1*. The systematic uncertainties for the measurement system can be added in quadrature to give an uncertainty for the steady pressure output, this is then doubled to provide an estimate for the unsteady pressure uncertainty. This unsteady uncertainty is then converted to a percentage using a typical peak value of fluctuating pressure (3300Pa), the uncertainty is doubled to give a 95% confidence interval. The percentage uncertainty is then converted to decibels using *Equation C 6*.

$$OASPL = 20\log\left(\frac{\overline{p}'^2}{p_{ref}^2}\right) \qquad \textbf{Equation C 5}$$

$$error(dB) = 10\log\left(1+\frac{\%error}{100}\right) \qquad \textbf{Equation C 6}$$

Following a similar process to the total and static pressure measurements the uncertainty for the unsteady pressure transducers can be estimated from the various quoted uncertainties. The linear regression uncertainty from the calibration process (l) and the manufactures quoted uncertainty (m) are shown below:

v = 1.5x10^{-4}/1.239 = 0.012% (1.239 = Transducer voltage value for datum run at M=0.9)

c = 0.09% (at worst)

m = 0.1%

These uncertainties are then combined in quadrature as per *Equation C 2* to yield the uncertainty of the measurements as a fraction of a typical measurement value as shown below:

$\Delta p/p = (0.1^2 + 0.012^2 + 0.09^2)^{0.5} = 0.135\%$

A typical value for the steady pressure (p) can then be calculated from a recorded voltage value using *Equation C 1*. This can then be multiplied by $\Delta p/p$ to provide an absolute estimate of the total pressure uncertainty:

p = 0.00 135 x 1.239 x 29878 ≈ 50Pa (29878 is the maximum calibration coefficient)

The absolute uncertainty of the atmospheric pressure measurement can be estimated from the manufactures quoted uncertainty for the barometer:

p_{atm} = 0.0001 x 101083 = 10.1Pa (101083 is typical p_{atm} value)

The uncertainty for both the steady pressure (p) and the atmospheric pressure (Patm) are then combined in quadrature to provide the absolute uncertainty for the absolute steady pressure (p):

$$\Delta p = (50^2 + 10.1^2)^{0.5} = 51\text{Pa}$$

This value is then doubled to account for the unsteady nature of the measurements. The unsteady pressure p' is the sum of a fluctuating pressure (p_{fluc}) and a time averaged pressure (p_{ave}) where the assumption of $p_{fluc} = p_{ave}$ is made as an estimate of the greatest p_{fluc} value. Therefore, the absolute uncertainty of the unsteady pressure is:

$$\Delta p' = 102 \text{ Pa}$$

This value can then be expressed as a percentage of a typical unsteady pressure value and this then yields a representative value for the uncertainty of the unsteady pressure measurements:

$$\Delta p'/p' = 102/3300 = 0.03 \text{ (3300Pa typical value for p')}$$

This uncertainty is then multiplied by a factor of 2 to provide a 95% confidence interval. The final value is then converted into decibels using *Equation C 6*. This results in an OASPL uncertainty of ±0.25dB.

Multiply by 2 for 95% confidence interval = 0.06

OASPL uncertainty = 10log(1+0.06) = ±0.25dB uncertainty for OASPL

C.1.10 SPL uncertainty

The uncertainty in the reported SPL values cannot be found analytically due to the sampling technique used. Therefore a statistical estimate of the uncertainty was used. In the process of finding the SPL it is necessary to calculate the average power spectral density (PSD) value across all of the 31 blocks into which the total sample size was split. Therefore a standard deviation across these block values was calculated at a typical modal frequency value. This value was taken to be 2kHz as this is the main area of interest to this study due to the second mode exhibiting the highest modal intensity within the SPL spectra. Once the standard deviation of the blocks was found the averaged uncertainty at the frequency of 2kHz was found using *Equation C 7*. This averaged uncertainty in the PSD value was then added to a typical PSD value to give the maximum value. The difference between the typical SPL value and that resulting from the maximum PSD was then found in decibels, this was shown to be 2.2dB. Because of this relatively large estimate for the statistical SPL uncertainty it was assumed that other uncertainty sources such as that from the transducers or repeatability are negligible.

$$\bar{\sigma}_x = \frac{2\sigma_x}{\sqrt{n^o blocks}}$$ **Equation C 7**

C.1.11 Repeatability

To ensure that results could be reproduced 4 datum cavity test cases were taken for further investigation. Between each of these cases the equipment had been altered and the wind tunnel set up had been changed and returned to its original configuration. This process was designed to show that such changes do not greatly affect the final outcome of any tests undertaken. The standard deviation across the 4 tests was calculated to provide the uncertainty due to the test procedure which is not covered in the previous investigation.

Minor discrepancies are expected due to uncertainty introduced from factors, such as the positioning of the throttle wheel and due to slight variations in the operating Mach number introduced by the varying pressure within the vacuum tank. It is noted that the sample size of 4 is not large enough to provide a statistically significant result. However, from previous investigations [31] [33] [35] the tunnel and experimental set up are known to give good repeatability.

Across the 4 test runs the standard deviation for the measured Mach number yields an uncertainty of ±0.001. This repeatability uncertainty takes into account any uncertainties from the total and static pressure measurements. Over the 4 test runs the standard deviation of the OASPL values was found to give an uncertainty of ±0.12dB. This is less than half of the uncertainty calculated through the analytical method. Therefore it can be assumed that any uncertainty introduced from equipment changes or test procedures will be negligible compared to the uncertainty of the measurement system. The standard deviation over the 4 test runs for the SPL yields an uncertainty of ±0.44dB. This is an order of magnitude smaller than the statistical uncertainty calculated for the sampling method.

Therefore it can again be assumed that any uncertainty introduced from equipment changes or from the test procedure will be negligible. This uncertainty is combined with the statistical uncertainty to produce an overall uncertainty of the SPL values of ±2.6dB.

C.2 AFRL Tri-sonic Gas dynamics Facility

For the transducers within the TGF only the uncertainties, which combine non-linearity, hysteresis, and repeatability, are given in *Table C 4*. These uncertainty values will be used to provide estimates of the uncertainty placed on the steady and unsteady pressure measurements from the TGF. The calculation technique will follow the same process as set out in *Appendix C.1.2 to C.1.10*. The resultant estimates for the uncertainty of the TGF measurements are given in *Table C 5*.

Measurement	Manufacturer uncertainty
(Total)	± 0.1 %
(Static)	± 0. 1%
(Unsteady)	Max ± 0.93 %
Atmospheric	± 0.1 %
Temperature	± 0.1 °C

Table C 4 – Measurement manufacturer uncertainties for the TGF transducers.

Measurement	Calculated uncertainty estimate
Mach number	±0.6%
OASPL	±0.16dB
SPL	±3.7dB

Table C 5 – Calculated uncertainty estimates for the TGF transducers.